

Electrical discharges in planetary upper atmospheres: thermal and chemical effects



Universidad de Granada

Francisco Carlos Parra Rojas

Department of Solar System

Instituto de Astrofísica de Andalucía

Física y Ciencias del Espacio

A thesis submitted for the degree of

Philosophiæ Doctor (PhD)

2015 June

Examination date: June 18, 2015

Thesis supervisors:

Dr. D. Francisco J. Gordillo Vázquez Dr. D. Alejandro Luque Estepa

© Francisco C. Parra Rojas

ISBN: 978-84-606-7924-0

Cover design: María Passas Varo and Francisco C. Parra Rojas.

Cover picture: Sprite over the Mediterranean Sea. Photography by Oscar van der Velde, Castellgalí, Catalonia, Spain.

Some of the figures included in this document have been previously published in *Journal of Geophysical Research - Space Physics* and *Icarus*.

1. Reviewer:

2. Reviewer:

Day of the defense: June 18, 2015

Signature from the head of the PhD committee:

Abstract

A one-dimensional electrochemical model is developed to describe, in a self-consistent way, the response of the Earth mesosphere to different types of lightning discharges between 50-87 km of altitude. This model is applied to the case of sprite halos, one of the most common types of Transient Luminous Events (TLE). We have studied the time-altitude evolution of more than 20 chemical species. Our model predicts an increase of up to 70 cm^{-3} in the electron density from ambient electron density values between 55-81 km of altitude in the +CG lightning cases and a negligible mesospheric electron density perturbation in the -CG lightning case. For all the +CG and some -CG (200 kAkm) cases considered, the model also shows an enhancement of several orders of magnitude in the concentration of ground state negative (O^- , O_2^- , NO_2^-) and positive (O_2^+ , O_4^+) ions and electronically excited positive ions such as $\text{N}_2^+(\text{A}^2\Pi_u)$ responsible for the N_2^+ Meinel emissions and $\text{N}_2^+(\text{B}^2\Sigma_u^+)$. On the other hand, for the first positive group of N_2 the calculated emission brightness exceeds 1 MR for a halo of 100 km of diameter at an altitude of 77 km for all the CG lightning discharges studied (except for the -CG case with 100 kAkm current peak) and for relatively lower altitudes when +CG lightning are considered. Moreover, the calculated concentration of the metastables $\text{N}_2(\text{A}^3\Sigma_u^+)$ and $\text{O}(^1\text{D})$ exhibit an enormous enhancement (of more than ten orders of magnitude) over their ambient values that, for +CG, remains high (5-7 orders of magnitude above ambient values) for long times (up to 500 s), below 55 km.

We have studied laboratory low pressure ($0.1 \text{ mbar} \leq p \leq 2 \text{ mbar}$) glow air discharges by optical emission spectroscopy to discuss several spectroscopic techniques that could be implemented by field spectrographs, depending on the available spectral resolution, to experimentally quantify the gas temperature associated to TLEs occurring at different altitudes including blue

jets, giant blue jets and sprites. Laboratory air plasmas have been analysed from the near UV (300 nm) to the near IR (1060 nm) with high (up to 0.01 nm) and low (2 nm) spectral resolution commercial grating spectrographs and by an inhouse intensified CCD grating spectrograph that we have recently developed for TLE spectral diagnostic surveys with $\simeq 0.45$ nm spectral resolution. We discuss the results of lab tests and comment on the convenience of using one or another technique for rotational (gas) temperature determination depending on the altitude and available spectral resolution. Moreover, we compare available low resolution ($3 \text{ nm} \leq \Delta\lambda \leq 7 \text{ nm}$) N_2 1PG field recorded sprite spectra at 53 km ($\simeq 1 \text{ mbar}$), and resulting vibrational distribution function (VDF), with 1 mbar laboratory glow discharge spectrum ($\Delta\lambda = 2 \text{ nm}$) and synthetic sprite spectra from models. We found that while the relative population of $\text{N}_2(B^3\Pi_g, v = 2 - 7)$ in sprites and laboratory produced air glow plasmas are similar, the $\text{N}_2(B^3\Pi_g, v = 1)$ vibrational level in sprites is more efficiently populated (in agreement with model predictions) than in laboratory air glow plasmas at similar pressures.

Concerning sprites, a one-dimensional self-consistent model has also been developed to study the chemical and thermal effects of a single sprite streamer in the Earth mesosphere. We have used sprite streamer profiles with three different driving current durations (5 ms, 50 ms and 100 ms) between 50 and 80 km of altitude and considering a kinetic scheme of air with 20 chemical species. Our model predicts strong increases in practically all the concentrations of the species studied at the moment of the streamer head passage. Moreover, their densities remain high during the streamer afterglow phase. The electron concentration can reach values of up to 10^8 cm^{-3} in the three cases analysed. The sprite model also predicts an important enhancement, of several orders of magnitude above ambient values, of nitrogen oxides (NO_x and N_2O) and the considered metastables molecular species ($\text{N}_2(A^3\Sigma_u^+)$, $\text{O}_2(a^1\Delta_g)$, $\text{O}_2(b^1\Sigma_g^+)$). Metastables are capable of storing energy for relatively long time (hundreds of seconds). On the other hand, we found that the $4.26 \mu\text{m}$ IR emission brightness of CO_2 can reach 10 GR at low altitudes ($< 65 \text{ km}$) for the cases of intermediate (50 ms) and long (100 ms) driving currents. These results suggest the possibility of detecting

sprite IR emissions from space with the appropriate instrumentation. Moreover, according to our model, the Meinel emission brightness of N_2^+ could also reach 1 MR below 50 km. Finally, we found that the thermal impact of sprites in the Earth mesosphere is proportional to the driving current duration. This produces variations of up to 30 K (in the extreme case of a 100 ms driving current) at low altitudes (< 55 km) and at about 10 seconds after the streamer head.

Finally, we have also studied the chemical effects of intracloud lightnings with different Charge Moment Change (CMC) and with different ambient electron density profiles on the lower ionosphere of Saturn. We have developed a self-consistent kinetic model that allows us to estimate the time- and altitude-dependence of the electric field and the chemical species included in our model as well as photon emissions. We have tested two ambient electron density profiles on Saturn and found that the conservative estimation of lightning $\text{CMC} = 10^5$ C km could lead to faint halos and possibly sprites if the base of the ionosphere is located at 1000 km of altitude over the 1-bar reference level. If the base of the ionosphere is at 600 km above the 1-bar level, then only the extreme case of 10^6 C km could produce considerable ionization, halos and possibly sprites. We also found that H_3^+ ions are rapidly produced from the parent H_2^+ ions through the reaction $\text{H}_2^+ + \text{H}_2 \rightarrow \text{H}_3^+ + \text{H}$, so that H_3^+ becomes the dominant ion in all the cases considered. The resulting light emissions, mainly in the blue and ultraviolet spectral region, are below the detection threshold of Cassini.

Resumen

En la tesis se ha desarrollado un modelo electroquímico unidimensional que describe, de forma autoconsistente, la respuesta de la mesosfera de La Tierra a diferentes tipos de descargas eléctricas asociadas a rayos entre 50 km y 85 km de altitud. Este modelo se ha aplicado al caso de halos de sprites, uno de los tipos de Eventos Lumínicos Transitorios (TLEs) más conocidos y frecuentes. Hemos estudiado la evolución en tiempo y altura de más de 20 especies químicas. Nuestro modelo predice un incremento de hasta 70 cm^{-3} en la densidad de electrones desde valores ambientales de la densidad de electrones entre 55-81 km de altitud para el caso de un rayo positivo (+CG) y una perturbación despreciable en la concentración mesosférica de electrones en el caso de un rayo negativo (-CG). Para todos los casos de rayos +CG y algunos rayos -CG (200 kAkm) estudiados, el modelo también muestra aumentos de varios órdenes de magnitud en la concentración de iones negativos (O^- , O_2^- , NO_2^-) y positivos (O_2^+ , O_4^+) en el estado fundamental, e iones positivos electrónicamente excitados como $\text{N}_2^+(\text{A}^2\Pi_u)$ responsable de la emisión Meinel del N_2^+ y el $\text{N}_2^+(\text{B}^2\Sigma_u^+)$. Por otra parte, para el primer positivo del N_2 , el brillo de emisión calculado excede en 1 MR para un halo de 100 km de diámetro a una altitud de 77 km y para todos los casos de rayos CG estudiados (excepto para el caso de un rayo -CG con 100 kAkm de pico de corriente) y a alturas relativamente bajas cuando consideramos rayos +CG. Además, las concentraciones calculadas de especies metaestables como $\text{N}_2(\text{A}^3\Sigma_u^+)$ y $\text{O}(^1\text{D})$ exhiben enormes aumentos (de más de diez órdenes de magnitud) sobre sus valores ambientales que, para rayos +CG, se mantienen en valores altos (5-7 órdenes de magnitud sobre valores ambientales) un largo tiempo (hasta 500 s), por debajo de 55 km.

Por otra parte, hemos estudiado espectroscópicamente descargas eléctricas tipo “glow” producidas en aire y generadas en el laboratorio a baja presión ($0.1 \text{ mbar} \leq p \leq 2 \text{ mbar}$). Hemos discutido algunas técnicas espectroscópicas que podrían ser implementadas en espectrógrafos de campo de forma que dependiendo de la resolución espectral disponible nos permitieran cuantificar la temperatura del gas asociada a TLEs (incluyendo blue jets, giant blue jets y sprites) que ocurren a diferentes altitudes. Los plasmas de aire generados en laboratorio han sido analizados desde el ultravioleta cercano (300 nm) hasta el infrarrojo cercano (1060 nm) con alta (hasta 0.01 nm) y baja (2 nm) resolución espectral y por un espectrógrafo CCD intensificador que hemos desarrollado recientemente en el grupo para el estudio de las características espectrales de TLEs con $\simeq 0.45 \text{ nm}$ de resolución espectral. Hemos discutido los resultados de los trabajos de laboratorio y comentado la conveniencia de usar una u otra técnica para la determinación de la temperatura rotacional (gas) dependiendo de la altitud y de la resolución espectral disponible. Por otra parte, hemos comparado los espectros del 1PN_2 obtenidos a baja resolución espectral ($3 \text{ nm} \leq \Delta\lambda \leq 7 \text{ nm}$) a 53 km de altitud ($\simeq 1 \text{ mbar}$) y su función de distribución vibracional (VDF), con espectros de descargas tipo glow realizadas en laboratorio a 1 mbar ($\Delta\lambda = 2 \text{ nm}$) y con espectros sintéticos de sprites obtenidos con modelos. Hemos encontrado que mientras la población relativa de $\text{N}_2(\text{B}^3\Pi_g, v = 2-7)$ en sprites y en plasmas de aire tipo glow producidos en laboratorio son similares, el nivel vibracional $\text{N}_2(\text{B}^3\Pi_g, v = 1)$ para sprites es más eficientemente poblado (en concordancia con predicciones de modelos) que en los plasmas de aire tipo “glow” producidos en laboratorio a presiones similares. En relación con el estudio de sprites, se ha desarrollado un modelo unidimensional autoconsistente para el estudio de los efectos químicos y térmicos de un filamento (streamer) de sprite en la mesosfera terrestre. Para ello, hemos usado perfiles de corriente de streamers de sprites con tres duraciones de afterglow diferentes (5 ms, 50 ms y 100 ms) entre 50 y 80 km de altitud considerando un esquema cinético de plasma de aire con más de 90 especies químicas. Nuestro modelo predice fuertes aumentos en prácticamente todas las densidades de las especies estudiadas en el instante del paso de la cabeza

del streamer. Por otra parte, dichas densidades se mantienen en valores relativamente altos durante la fase de “afterglow” del streamer. La concentración de electrones puede alcanzar valores de hasta 10^8 cm^{-3} en los tres casos analizados. El modelo también predice un importante aumento, de algunos órdenes de magnitud sobre el valor ambiental, de las concentraciones de óxidos de nitrógeno (NO_x y N_2O) y de las especies metaestables consideradas ($\text{N}_2(\text{A}^3\Sigma_u^+)$, $\text{O}_2(\text{a}^1\Delta_g)$ y $\text{O}_2(\text{b}^1\Sigma_g^+)$). Las especies metaestables son capaces de almacenar energía un tiempo relativamente largo (cientos de segundos).

Por otra parte, hemos encontrado que el brillo de emisión en IR a $4.26 \mu\text{m}$ del CO_2 puede alcanzar 10 GR a bajas altitudes ($< 65 \text{ km}$) para los casos de duración intermedia (50 ms) y larga (100 ms) del “afterglow” de corriente. Estos resultados sugieren la posibilidad de detectar emisión infrarroja de sprites desde el espacio con la instrumentación adecuada. Además, acorde con nuestro modelo, el brillo de emisión Meinel del N_2^+ podría alcanzar también 1 MR por debajo de 50 km. Finalmente, hemos encontrado que el impacto térmico local de sprites en la mesosfera terrestre es proporcional a la duración del “afterglow” de corriente. Este produce variaciones de hasta 30 K (en el caso extremo de 100 ms de afterglow de corriente) a bajas altitudes ($< 55 \text{ km}$) y 10 segundos después del paso de la cabeza del streamer.

Por último, hemos estudiado los efectos químicos de rayos intranube con diferentes momentos de carga (CMC) y con diferentes perfiles de densidad de electrones en la baja ionosfera de Saturno. Hemos desarrollado un modelo cinético autoconsistente unidimensional el cual puede estimar la dependencia en tiempo y en altura del campo eléctrico y las especies químicas consideradas así como la emisión de fotones. Hemos probado dos perfiles de densidad de electrones ambiental encontrando que con la estimación más conservadora de CMC de un rayo, esto es 10^5 C km , se podrían producir halos débiles y posiblemente sprites si la base de la ionosfera esta situada a 1000 km sobre la presión de referencia de 1 bar. Si la base de la ionosfera esta situada a 600 km sobre el nivel de 1 bar, entonces solo el caso extremo de 10^6 C km de CMC podría producir una considerable

ionización, halos y posiblemente sprites. También hemos encontrado que el ion H_3^+ es producido rápidamente a partir del H_2^+ a través del proceso $H_2^+ + H_2 \rightarrow H_3^+ + H$, con lo que el H_3^+ llega a ser el ion más dominante en todos los casos considerados. La luz emitida por halos o sprites, principalmente en azul y ultravioleta estaría por debajo del umbral de detección de la nave Cassini que ha detectado rayos en la atmósfera de Saturno.

To Juan Pablo and Manolita.

Acknowledgements

Me gustaría dedicar este trabajo, ante todo a mis padres Fulgencio Parra y María Rojas, porque sin su esfuerzo y sacrificio nunca jamás hubiese llegado a este punto de mi vida. También al resto de mi familia, siempre atentos a mis progresos científicos. Especialmente, quisiera dedicar mi tesis a mi tía Manolita y a mi primo Juan Pablo (D.E.P.), las dos personas que más han influido en mi vida, que nunca vacilaron en apoyarme en los momentos difíciles y que siempre me alentaron a realizar mis sueños. Aquello que vive en nuestro recuerdo nunca muere. A todos ellos, por todo esto, GRACIAS.

First and foremost, I would like to express my sincere gratitude to my advisors Dr. Francisco J. Gordillo Vázquez and Dr. Alejandro Luque for their continuous support during my Ph.D thesis and research, for their patience, motivation, enthusiasm, and immense knowledge. Their guidance has helped me during my research and writing of this thesis. I could not have imagined having better advisors and mentors.

Besides, I would like to thank the rest of the TRAPPA group, specially Maria Passas. I have learned a lot with her, mainly Matlab and, why not say it, I have also laughed a lot. She is an excellent professional and colleague.

I must also acknowledge Dr. Sergey Pancheshnyi, without whose invaluable help I would have never been able to complete the thermal studies of sprites. My short stay in the Laplace Lab. in Toulouse was very helpful and constructive. I am thankful to Dra. Isabel Tanarro, Dr. Victor J. Herrero and Dra. Esther Carrasco of the IEM (Madrid). Despite the 480 volts (80 mA) that swept my arm, I am very satisfied with my stay in Madrid where we perform a lot of experiments in the hollow cathode reactor with very interesting results. I am also indebted with Dr. Milan Šimek, Dr. Tomáš

Hoder and small Vacláv (české pivo, český holky, svíčková, to miluju). I'll never forget Prague, the Czech beer and the great streamers plasma reactor adventure. I also acknowledge Dra. Maia Leire Garca Comas (IAA-CSIC) for providing CO₂ radiative decay data values.

I would like to thank my colleagues of the Institute for Astrophysics of Andalusia (Granada), specially to: Pablo Ramírez, Naim Ramírez, Jesus Muñoz, Estefanía Casal, Javi Madrona, Rubén Sánchez, Rubén Herrero, Zaira Modroño, Fran Pozuelos, Estela Fernández, Jesus Escobar, Javi Blasco, Eduardo Duarte, Carolina Casadio, Gabriella Gilli (la mia amata sorellina), Sergio, Joserra, Goro (R.I.P.), Toño, Jonathan, Sandra, Juan Carlos and Dominika. I owe special thanks to Isa Egea because without her I would have never got here. I have enough reasons to think it. To my greatest friends Aythami Jurado (mobil-breaker), Jorge Abreu (El zanjás), Guillermo Carbajosa (Rapidmind), Juan Ontiveros (Onti) and the old members of M.I.L.F., the best heavy metal band in history. I really enjoyed playing songs of Metallica, ACDC, Black Sabbath, Steppenwolf, Dio, etc with them. And to Wacken and Sonisphere. Last but not least, to Silvia Pérez the biggest and strongest Dirac delta of my life.

Finally, this research has been made possible with the financial assistance of the Spanish Ministry of Science and Innovation (MICINN) under project AYA2009-14027-C05-02 and FPI grant BES-2010-042367. Thanks also to the University of Granada for allowing me to get a Ph.D. in the Physics and Space Science program.

Fran Parra

Contents

List of Figures	xi
List of Tables	xxix
1 Introduction	1
1.1 The atmosphere of the Earth	1
1.1.1 Definition and origin	1
1.1.2 Composition of the atmosphere	3
1.1.3 Vertical structure	4
1.2 Lightning	9
1.3 Transient Luminous Events	15
1.3.1 Blue Jets and Blue Starters	16
1.3.2 Gigantic Jets	18
1.3.3 Sprites and Halos	18
1.3.4 ELVES	20
1.3.5 Other TLEs	20
1.3.6 Non-Luminous emissions	21
1.4 Scientific contributions	22
1.5 Organization of the thesis	24
2 Sprite Halos	25
2.1 State of the art	25
2.2 Model	30
2.2.1 Model description	30
2.3 Results and discussion	37
2.3.1 Reduced electric field	39

CONTENTS

2.3.2	Negatively charged species	42
2.3.3	Positively charged species	51
2.3.4	Excited species	58
2.3.5	Neutral species	75
2.3.6	High current moment (500 kAkm) case	77
2.4	Laboratory experiments	85
2.4.1	Experimental set-up for hollow cathode discharges in air	85
2.4.2	Brief description of GRASSP	88
2.4.3	Gas temperature determination by spectral analysis of low pressure air and N ₂ plasmas	89
2.4.3.1	Rotational structure of N ₂ ⁺ (B ² Σ _u ⁺ , v' = 0 → X ² Σ _g ⁺ , v'' = 0)	89
2.4.3.2	Subband head peaks of N ₂ (B ³ Π _g , v' → A ³ Σ _u ⁺ , v'') vibrational transitions	90
2.4.3.3	Spectral fitting of N ₂ (B ³ Π _g , v' → A ³ Σ _u ⁺ , v'') rovibronic bands	94
2.4.4	Experimental quantification of vibrational distribution functions	97
2.4.5	Results and discussion	97
3	Sprites	111
3.1	State of the art	111
3.2	Model	116
3.2.1	Model description	116
3.3	Results and discussion	122
3.3.1	Reduced Electric Field	122
3.3.2	Electron density and O ⁻	126
3.3.3	N(² D) and NO	129
3.3.4	N ₂ ⁺ (A ² Π _u) and N ₂ ⁺ (B ² Σ _u ⁺)	131
3.3.5	NO ₂ and NO ₃	133
3.3.6	Metastable excitations of atomic oxygen	136
3.3.7	Atomic oxygen and ozone	138
3.3.8	Molecular oxygen metastables	139
3.3.9	Atomic nitrogen	142

3.3.10 N ₂ O	142
3.3.11 N ₂ O ₂ ⁺	144
3.3.12 N ₂ (A ³ Σ _u ⁺)	145
3.3.13 Optical emission brightness	146
3.3.14 Energy balance	156
4 Electrical discharges on Saturn	165
4.1 State of the art	165
4.2 A brief description of the model	171
4.3 Results	175
5 Conclusions	183
Appendix A Some constants for atmospheric sciences	191
Appendix B Vibrational modes and statistical weights of CO₂	193
Appendix C Formation enthalpies of the chemical species considered	195
Appendix D The correction factor of T_{gas}	199
Appendix E Kinetic model for electrical discharges in the Earth's atmosphere	203
E.1 Chemical species	203
E.2 Types of reactions	205
E.3 Reaction rates	206
E.4 EEDF and cross section dependent processes	210
E.5 Electronic temperature dependent processes	212
E.5.1 Ionization and dissociative ionization	212
E.5.2 Dissociation	213
E.5.3 Attachment	213
E.5.4 Recombination	214
E.6 Molecular nitrogen kinetics	215
E.6.1 Vibrational-Vibrational processes (VV)	215
E.6.2 Vibrational-Translational processes (VT)	215
E.7 Molecular oxygen kinetics	217

CONTENTS

E.7.1	Vibrational-Translational processes (VT)	217
E.8	Heavy particle kinetics	218
E.8.1	Electronically excited species	218
E.8.2	Ground neutrals	220
E.9	Ionic kinetics	222
E.9.1	Ion-Ion recombination	222
E.9.2	Positive ions	223
E.9.3	Negative ions	225
E.10	Carbon dioxide kinetics	226
E.10.1	Vibrational-Translational processes (VT)	226
E.10.2	Vibrational-Vibrational processes (VV)	229
E.11	Ionization processes due to galactic cosmic rays	230
E.12	Rotational deexcitation processes	230
E.13	Radiative decay processes	231
E.14	Processes only included in the model of halos	236
Appendix F Kinetic model for electrical discharges in Saturn's atmosphere		237
F.1	Species	237
F.2	Reaction rates	238
F.3	EEDF and cross section dependent processes	239
F.4	Electronic temperature dependent processes	240
F.4.1	Ionization process	240
F.4.2	Dissociation processes	240
F.4.3	Attachment and dissociative attachment processes	240
F.4.4	Excitation/De-excitation processes	241
F.4.5	Detachment process	241
F.4.6	Recombination and dissociative recombination processes	242
F.5	Heavy particle kinetics	243
F.5.1	Ground neutral processes	243
F.5.2	Electronically excited neutral including Penning ionization processes	243
F.5.3	Vibrational-vibrational processes (VV)	244

CONTENTS

F.5.4	Vibrational-translational processes (VT)	244
F.6	Ionic kinetics	245
F.6.1	Ion-Ion recombination processes	245
F.6.2	Positive ion processes	246
F.6.3	Negative ion processes	246
F.7	Radiative decay processes	247
	References	249

CONTENTS

List of Figures

1.1	The Iberian peninsula taking by an astronaut aboard the International space Station. This photograph from space also shows the airglow, a faint green arc seen along the horizon that's caused by chemical reactions among the gas molecules of Earth's upper atmosphere (Courtesy of NASA).	2
1.2	The plot shows the total number density profile (thin solid line) of the atmosphere in cm^{-3} and those of five species, namely, N_2 (dotted line), O_2 (dash-dot-dot-dotted line), H_2O (dashed line), CO_2 (long-dashed line), and O_3 (dash-dotted line). Temperature (thick line up to 80 km) and mixing ratios of the different species are those of Earth. The thickest horizontal line shows the position of the cloud layer [Ehrenreich et al., 2006].	5
1.3	Vertical structure of the Earth's atmosphere. The solid yellow line is the global (averaged over all latitudes except the polar ones) vertical gradient of the air temperature and the dotted red line is the vertical gradient in the polar regions.	7
1.4	Boreal aurora captured in Nordresia, Norway by Ivar Næss on December 9, 2013. The green color is due to the radiative deexcitation of the atomic oxygen present in the ionosphere.	8
1.5	A far ultraviolet (FUV) photograph reveals the geocorona, a halo of low density hydrogen which surrounds the Earth. The photograph was taken by astronaut John W. Young, Apollo 16 mission commander, during the first spacewalk of his trip to the moon on April 21, 1972.	9
1.6	Positive cloud-to-ground lightning captured by Kara Swanson in the coast of the Bahamas.	10

LIST OF FIGURES

1.7	The charge structure of two simple thunderstorms, the types of lightnings and the locations where lightning can occur. Courtesy of British Encyclopedia.	11
1.8	The four types of cloud-to-ground lightning flashes defined through the direction of leader propagation and the charge of the initiating leader [Dwyer and Uman, 2014].	12
1.9	Detailed development of a negative cloud-to-ground lightning discharge from the first electrical breakdown to the second return stroke. Adapted from Uman [2001] by Dwyer and Uman [2014].	13
1.10	Lightning related Transient Luminous Events (TLEs). The picture shows the most common TLEs produced in the Earth atmosphere. Courtesy of Maria Passas.	16
1.11	Blue Jet captured by Patrice Huet, La Réunion in 1997 above a thundercloud system.	17
1.12	Evolutionary stages of a Gigantic Jet recorded from Puerto Rico in 2001 [Pasko et al., 2002].	19
1.13	Images of sprites, sprite halo and elve captured by Maria Passas using GRASSP from the Calar-Alto Observatory, Almería, Spain (2013).	20
2.1	Altitude variation of the initial ambient densities of N_2 (solid blue line), O_2 (dashed purple line), Ar (dotted black line) and CO_2 (dashed dotted red line) taken from the Whole Atmosphere Community Climate Model (WACCM) under the nighttime conditions. The solid black line is the gas temperature variation with altitude taken from WACCM.	33
2.2	Altitude variation of the initial ambient densities where the dashed lines are the ones (before the relaxation stage) taken from WACCM, and the solid lines are the initial ambient densities obtained after the relaxation stage.	34
2.3	Altitude variation of the initial ambient densities where the dashed lines are the initial (before the relaxation stage) ambient densities extracted from WACCM, and the solid lines are the initial ambient densities obtained after the relaxation stage.	35

2.4	Variation of the initial ambient electron density with altitude taken from Hu et al. [2007].	36
2.5	Altitude variation of the negatively charged species considered in our model, as obtained after the relaxation stage.	37
2.6	Altitude variation of the positively charged species considered in our model, as obtained after the relaxation stage.	38
2.7	Altitude variation of the neutral excited species considered in our model, as obtained after the relaxation stage.	39
2.8	Time dependence of the various lightning electrical signals implemented in the model. All signals are triangular with 2 ms width. -CG lightnings (solid green line for 200 kAkm of current peak and dashed dotted blue line for 100 kAkm of current peak) have a negligible current moment beyond 2 ms. +CG lightnings (dashed black line for 200 kAkm of current peak and dotted violet line for 100 kAkm of current peak) have a continuous current moment of 20 kAkm from 2 ms to 100 ms. Beyond 100 ms the current moment is considered negligible.	40
2.9	Time dependence of the charge moment change (CMC) for the different lightning electrical signals implemented in the model. -CG lightnings (solid red line for 200 kAkm of current peak and solid black line for 100 kAkm of current peak) have a negligible current moment beyond 2 ms (see Figure 2.8). +CG lightnings (solid green line for 200 kAkm of current peak and solid blue line for 100 kAkm of current peak) have a continuous current moment of 20 kAkm from 2 ms to 100 ms (see Figure 2.8). Beyond 100 ms the current moment is considered negligible. Finally, the solid pink line shows the charge moment change of a realistic +CG lightning measured by Gamerota et al. [2011].	41
2.10	Time dependence of the measured (empirical) electrical signal used in the model, extracted from Gamerota et al. [2011], corresponding to a real +CG lightning discharge. The lightning discharge signal was obtained from ELF data recorded in Yucca Ridge Field Station (40.702N-105.031E) on July 3, 2008. The frequency range of the station covers from a few Hz up to 25 kHz. The authors do not specify the particular signal resolution used for these measurements.	42

LIST OF FIGURES

2.11	Altitude-time evolution of the reduced electric field due to cloud-to-ground lightnings with (a) realistic current moment, (b) 100 kAkm peak current moment and 20 kAkm continuous current moment, (c) 200 kAkm peak current moment and 20 kAkm continuous current moment, (d) 100 kAkm peak current moment and (e) 200 kAkm peak current moment.	43
2.12	Altitude-time evolution of the electron density due to cloud-to-ground lightnings with (a) realistic current moment, (b) 100 kAkm peak current moment and 20 kAkm continuous current moment, (c) 200 kAkm peak current moment and 20 kAkm continuous current moment, (d) 100 kAkm peak current moment and (e) 200 kAkm peak current moment.	44
2.13	Altitude-time evolution of the O^- density due to cloud-to-ground lightnings with (a) realistic current moment, (b) 100 kAkm peak current moment and 20 kAkm continuous current moment, (c) 200 kAkm peak current moment and 20 kAkm continuous current moment, (d) 100 kAkm peak current moment and (e) 200 kAkm peak current moment.	47
2.14	Altitude-dependent behaviour of the concentration of O^- under the conditions of a single sprite halo event generated by a -CG lightning with 200 kAkm peak current moment for three different altitudes. The dashed blue line is for an altitude of 67 km, the dotted red line indicates O^- density at 60 km and the solid black line corresponds to the case of an altitude of 53 km.	49
2.15	Altitude-time evolution of the O_2^- density due to cloud-to-ground lightnings with (a) realistic current moment, (b) 100 kAkm peak current moment and 20 kAkm continuous current moment, (c) 200 kAkm peak current moment and 20 kAkm continuous current moment, (d) 100 kAkm peak current moment and (e) 200 kAkm peak current moment.	50
2.16	Altitude-time evolution of the NO_2^- density due to cloud-to-ground lightnings with (a) realistic current moment, (b) 100 kAkm peak current moment and 20 kAkm continuous current moment, (c) 200 kAkm peak current moment and 20 kAkm continuous current moment, (d) 100 kAkm peak current moment and (e) 200 kAkm peak current moment.	52

2.17 Altitude-time evolution of the O_2^+ density due to cloud-to-ground lightnings with (a) realistic current moment, (b) 100 kAkm peak current moment and 20 kAkm continuous current moment, (c) 200 kAkm peak current moment and 20 kAkm continuous current moment, (d) 100 kAkm peak current moment and (e) 200 kAkm peak current moment.	53
2.18 Altitude-time evolution of the O^+ density due to cloud-to-ground lightnings with (a) realistic current moment, (b) 100 kAkm peak current moment and 20 kAkm continuous current moment, (c) 200 kAkm peak current moment and 20 kAkm continuous current moment, (d) 100 kAkm peak current moment and (e) 200 kAkm peak current moment.	55
2.19 Altitude-time evolution of the N_2^+ density due to cloud-to-ground lightnings with (a) realistic current moment, (b) 100 kAkm peak current moment and 20 kAkm continuous current moment, (c) 200 kAkm peak current moment and 20 kAkm continuous current moment, (d) 100 kAkm peak current moment and (e) 200 kAkm peak current moment.	56
2.20 Altitude-time evolution of the N_4^+ density due to cloud-to-ground lightnings with (a) realistic current moment, (b) 100 kAkm peak current moment and 20 kAkm continuous current moment, (c) 200 kAkm peak current moment and 20 kAkm continuous current moment, (d) 100 kAkm peak current moment and (e) 200 kAkm peak current moment.	57
2.21 Altitude-time evolution of the O_4^+ density due to cloud-to-ground lightnings with (a) realistic current moment, (b) 100 kAkm peak current moment and 20 kAkm continuous current moment, (c) 200 kAkm peak current moment and 20 kAkm continuous current moment, (d) 100 kAkm peak current moment and (e) 200 kAkm peak current moment.	58
2.22 Altitude-time evolution of the $N_2(A^3\Sigma_u^+)$ density due to cloud-to-ground lightnings with (a) realistic current moment, (b) 100 kAkm peak current moment and 20 kAkm continuous current moment, (c) 200 kAkm peak current moment and 20 kAkm continuous current moment, (d) 100 kAkm peak current moment and (e) 200 kAkm peak current moment.	60

LIST OF FIGURES

2.23	Altitude-time evolution of the $N_2(B^3\Pi_g)$ density due to cloud-to-ground lightnings with (a) realistic current moment, (b) 100 kAkm peak current moment and 20 kAkm continuous current moment, (c) 200 kAkm peak current moment and 20 kAkm continuous current moment, (d) 100 kAkm peak current moment and (e) 200 kAkm peak current moment.	61
2.24	Altitude-time evolution of the first positive band system ($1PN_2$) emission brightness due to cloud-to-ground lightnings with (a) realistic current moment, (b) 100 kAkm peak current moment and 20 kAkm continuous current moment, (c) 200 kAkm peak current moment and 20 kAkm continuous current moment, (d) 100 kAkm peak current moment and (e) 200 kAkm peak current moment.	63
2.25	Altitude-time evolution of the $N_2(C^3\Pi_u)$ density due to cloud-to-ground lightnings with (a) realistic current moment, (b) 100 kAkm peak current moment and 20 kAkm continuous current moment, (c) 200 kAkm peak current moment and 20 kAkm continuous current moment, (d) 100 kAkm peak current moment and (e) 200 kAkm peak current moment.	64
2.26	Altitude-time evolution of the second positive band system ($2PN_2$) emission brightness due to cloud-to-ground lightnings with (a) realistic current moment, (b) 100 kAkm peak current moment and 20 kAkm continuous current moment, (c) 200 kAkm peak current moment and 20 kAkm continuous current moment, (d) 100 kAkm peak current moment and (e) 200 kAkm peak current moment.	65
2.27	Altitude evolution of the emission brightness due to a positive cloud-to-ground lightning discharge with different current peaks as would be measured by a 30 fps camera. The red symbols correspond to the first positive band system and the blue symbols correspond to the second positive band system.	66
2.28	Altitude evolution of the emission brightness due to a positive cloud-to-ground lightning discharge with different current peaks as would be measured by a 1000 fps camera. The red symbols correspond to the first positive band system and the blue symbols correspond to the second positive band system.	67

2.29	Altitude-time evolution of the $N_2^+(A^2\Pi_u)$ density due to cloud-to-ground lightnings with (a) realistic current moment, (b) 100 kAkm peak current moment and 20 kAkm continuous current moment, (c) 200 kAkm peak current moment and 20 kAkm continuous current moment, (d) 100 kAkm peak current moment and (e) 200 kAkm peak current moment.	68
2.30	Altitude-time evolution of the $N_2^+(B^2\Sigma_u^+)$ density due to cloud-to-ground lightnings with (a) realistic current moment, (b) 100 kAkm peak current moment and 20 kAkm continuous current moment, (c) 200 kAkm peak current moment and 20 kAkm continuous current moment, (d) 100 kAkm peak current moment and (e) 200 kAkm peak current moment.	69
2.31	Altitude-time evolution of the $N(^2D)$ density due to cloud-to-ground lightnings with (a) realistic current moment, (b) 100 kAkm peak current moment and 20 kAkm continuous current moment, (c) 200 kAkm peak current moment and 20 kAkm continuous current moment, (d) 100 kAkm peak current moment and (e) 200 kAkm peak current moment.	70
2.32	Altitude-time evolution of the $O(^1D)$ density due to cloud-to-ground lightnings with (a) realistic current moment, (b) 100 kAkm peak current moment and 20 kAkm continuous current moment, (c) 200 kAkm peak current moment and 20 kAkm continuous current moment, (d) 100 kAkm peak current moment and (e) 200 kAkm peak current moment.	72
2.33	Altitude-time evolution of the $O(^1S)$ density due to cloud-to-ground lightnings with (a) realistic current moment, (b) 100 kAkm peak current moment and 20 kAkm continuous current moment, (c) 200 kAkm peak current moment and 20 kAkm continuous current moment, (d) 100 kAkm peak current moment and (e) 200 kAkm peak current moment.	73
2.34	Altitude-time evolution of the $O_2(a^1\Delta_g)$ density due to cloud-to-ground lightnings with (a) realistic current moment, (b) 100 kAkm peak current moment and 20 kAkm continuous current moment, (c) 200 kAkm peak current moment and 20 kAkm continuous current moment, (d) 100 kAkm peak current moment and (e) 200 kAkm peak current moment.	74

LIST OF FIGURES

2.35	Altitude-time evolution of the $O_2(b^1\Sigma_g^+)$ density due to cloud-to-ground lightnings with (a) realistic current moment, (b) 100 kAkm peak current moment and 20 kAkm continuous current moment, (c) 200 kAkm peak current moment and 20 kAkm continuous current moment, (d) 100 kAkm peak current moment and (e) 200 kAkm peak current moment.	76
2.36	Altitude-time evolution of the N density due to cloud-to-ground lightnings with (a) realistic current moment, (b) 100 kAkm peak current moment and 20 kAkm continuous current moment, (c) 200 kAkm peak current moment and 20 kAkm continuous current moment, (d) 100 kAkm peak current moment and (e) 200 kAkm peak current moment.	77
2.37	Altitude-time evolution of the O density due to cloud-to-ground lightnings with (a) realistic current moment, (b) 100 kAkm peak current moment and 20 kAkm continuous current moment, (c) 200 kAkm peak current moment and 20 kAkm continuous current moment, (d) 100 kAkm peak current moment and (e) 200 kAkm peak current moment.	78
2.38	Altitude-time evolution of the reduced electric field ((a)-(b)) and electron density ((c)-(d)) due to cloud-to-ground lightnings. The plots in the left correspond to -CG lightnings and the plots in the right correspond to +CG lightnings both with 500 kAkm peak current moment.	80
2.39	Altitude-time evolution of the N_2^+ density ((a)-(b)) and the O_2^+ density ((c)-(d)) due to cloud-to-ground lightnings. The plots in the left correspond to -CG lightning and the plots in the right correspond to +CG lightning both with 500 kAkm peak current moment.	82
2.40	Altitude-time evolution of the $N_2(B^3\Pi_g)$ density ((a)-(b)) and the first positive band system (1PN ₂) emission brightness ((c)-(d)) due to cloud-to-ground lightnings. The plots in the left correspond to -CG lightning and the plots in the right correspond to +CG lightning both with 500 kAkm peak current moment. The mistake at 80 km of altitude in the case of -CG discharges (Plots (a) and (c)) is due to numerical fluctuations.	83
2.41	Altitude-time evolution of the N_2O density ((a)-(b)) variation due to cloud-to-ground lightnings. The plot in the left correspond to -CG lightning and the plot in the right correspond to +CG lightning both with 500 kAkm peak current moment.	85

2.42	Experimental set up (panel A) of the DC hollow cathode discharge used for spectroscopic diagnostics and an image (panel B) of the generated air plasma where a more intense pink light emission can be seen in the center of the discharge	87
2.43	Boltzmann plots ($\ln F$ vs $J'(J'+1) = (J'' + 1)(J'' + 2)$, see equation (2.13)) of the rotational R - branch ($\Delta J = +1$) transitions involving even (square symbols and blue line) and odd (circles and red line) J'' of $N_2^+(B^2\Sigma_u^+, v' = 0, J' \rightarrow X^2\Sigma_g^+, v'' = 0, J'')$ in a 1.5 mbar ($\simeq 48$ km) DC hollow cathode discharge in air. The rotational (gas) temperatures resulting from the even and odd J'' are 474 K and 426 K, respectively. The $N_2^+(B^2\Sigma_u^+, v' = 0, J' \rightarrow X^2\Sigma_g^+, v'' = 0, J'')$ spectrum was recorded with the Jobin-Yvon spectrometer using the CCD and the 1800 grooves/mm grating providing a spectral resolution of 0.023 nm	91
2.44	Rotational (gas) temperatures measured in the hollow cathode discharge: (Panel A) derived with the Boltzmann plot of the $N_2^+(B^2\Sigma_u^+)$ (solid line, right triangle FM-0.010 nm; pentagon CCD-0.02 nm; star CCD-0.034 nm) and the sub-band head peak methods applied to the $N_2 - 1PG$ band (dashed line, left triangle (3,0)-0.25 nm; square (3,0)-0.43 nm; down-triangle (2,0)-0.25 nm; circle (2,0)-0.43 nm). (Panel B) derived from the analysis of sub-band head peaks (3,0) and (2,0) recorded (each of them) with two spectral resolutions (0.25 nm and 0.43 nm) (dashed line and symbols correspond to the same data that in panel A) and from spectral fitting methods (solid line, left triangle (3,0)-0.25 nm; square (3,0)-0.43 nm; down-triangle (2,0)-0.25 nm; circle (2,0)-0.43 nm) for different pressures.	100
2.45	Spectral fitting (dashed blue line) of laboratory measured (solid red line) spectra of the (3,0) rovibronic transitions of $N_2(B^3\Pi_g \rightarrow A^3\Sigma_u^+)$ using 0.43 nm spectral resolution for 0.11 mbar (panel A resulting in $T_{gas} = 386$ K), 1 mbar (panel B resulting in $T_{gas} = 353$ K), 1.5 mbar (panel C resulting in $T_{gas} = 340$ K) and 2 mbar (panel D resulting in $T_{gas} = 334$ K). The spectra shown in panels A - D were recorded in the laboratory hollow cathode air discharge.	101

LIST OF FIGURES

- 2.46 Spectral fitting (dashed blue line) of laboratory measured (solid red line) spectra of the (2,0) rovibronic transitions of $N_2(B^3\Pi_g \rightarrow A^3\Sigma_u^+)$ using 0.43 nm spectral resolution for 0.11 mbar (panel A resulting in $T_{gas} = 365$ K), 1 mbar (panel B resulting in $T_{gas} = 343$ K), 1.5 mbar (panel C resulting in $T_{gas} = 334$ K) and 2 mbar (panel D resulting in $T_{gas} = 321$ K). The spectra shown in panels A - D were recorded in the laboratory hollow cathode air discharge. 102
- 2.47 Panel A shows instrument efficiency corrected partial spectra of N_2 1PG band in a hollow cathode air discharge (solid line) at 0.23 mbar recorded by a commercial spectrograph (Jobin Yvon-HORIBA FHR 1000) and of a commercial air discharge lamp (dashed line) at 0.2 mbar taken with GRASSP. Panels B and C show the spectral fitting (solid line) of, respectively, the experimentally recorded (circles) (5,3) and (5,2) rovibronic band transition spectra of N_2 1PG in the commercial air lamp as recorded by GRASSP. The gas temperatures obtained by the (5,3) (panel B) and (5,2) (panel C) fits of the commercial air lamp N_2 1PG experimental spectrum taken by GRASSP are 524 K and 656 K, respectively. The gas temperature obtained in the hollow cathode discharge at 0.23 mbar is $\simeq 380$ K (see Figure 3). The spectral resolution used in both cases (hollow cathode and commercial lamp) is 0.43 nm. 104

- 2.48 Panel A shows a comparison of the VDF of $N_2(B^3\Pi_g)$ derived from the N_2 1PG instrument corrected sprite emission spectrum at 53 km ($\simeq 1$ mbar) using $\Delta\lambda = 7$ nm [Bucsela et al., 2003] and $\Delta\lambda = 3$ nm [Kanmae et al., 2007], from the N_2 1PG spectrum of a hollow cathode air discharge generated at 1 mbar ($\simeq 53$ km) recorded with $\Delta\lambda = 2$ nm and from a kinetic model to predict the VDF of $N_2(B^3\Pi_g)$ in sprites at 74 km [Luque and Gordillo-Vázquez, 2011, Gordillo-Vázquez et al., 2011, 2012]. In panel B we see a comparison between the VDF of $N_2(B^3\Pi_g)$ recorded from the instrument corrected N_2 1PG sprite emission spectra at 74 km using $\Delta\lambda = 3$ nm [Kanmae et al., 2007], from a kinetic model to predict the VDF of $N_2(B^3\Pi_g)$ in sprites and halos at, respectively, 74 km and 80 km [Luque and Gordillo-Vázquez, 2011, Gordillo-Vázquez et al., 2011, 2012] and from the N_2 1PG spectrum of a hollow cathode air discharge generated at 0.11 mbar ($\simeq 70$ km) recorded with $\Delta\lambda = 2$ nm. The VDF is normalized to the sum of the populations from $v' = 2$ to $v' = 6$ 108
- 2.49 Panel A shows a comparison of the instrument corrected N_2 1PG spectra recorded from sprites at 53 km using $\Delta\lambda = 3$ nm (circles) [Kanmae et al., 2007] and $\Delta\lambda = 7$ nm (blue dashed line [Bucsela et al., 2003], from a laboratory hollow cathode air discharge (green solid line) generated at 1 mbar ($\simeq 53$ km) recorded with $\Delta\lambda = 2$ nm and a transmission corrected synthetic sprite spectrum (dotted line) for a sprite at 74 km calculated with a kinetic model of sprites and halos assuming $\Delta\lambda = 3$ nm [Gordillo-Vázquez et al., 2012]. All spectra in panel A are normalized to the (2,0) transition at 773.2 nm while experimental spectra (green solid line) in panels B and C are normalized to the oxygen 777 nm line. Panel B shows the spectral fit (blue dashed line), using $T_{gas} = 385$ K, to the N_2 1PG spectrum recorded in a hollow cathode air discharge generated at 0.11 mbar ($\simeq 70$ km) recorded with $\Delta\lambda = 2$ nm. Panel C shows the spectral fit (blue dashed line), using $T_{gas} = 356$ K, to the N_2 1PG spectrum recorded in a hollow cathode air discharge generated at 1 mbar ($\simeq 53$ km) recorded with $\Delta\lambda = 2$ nm. 109

LIST OF FIGURES

3.1	Dependence of $\mu_e N$, where μ_e is the electron mobility and N is the gas density, with the reduced electric field in dry air. The solid red line is the power fit with a correlation coefficient of 0.9808.	120
3.2	Time evolution of the current density of a sprite streamer at 75 km of altitude. The black, red and blue lines are for driving currents of 5 ms, 50 ms and 100 ms, respectively. Label A corresponds to the streamer head, B corresponds to the driving current and C (black, red and blue) is associated to the post-afterglow stage.	121
3.3	Altitude-time evolution of the reduced electric field (top panel) and current density (bottom panel) due to a single sprite streamer with a driving current of 5 ms ((a)-(d)), 50 ms ((b)-(e)) and 100 ms ((c)-(f)).	123
3.4	Altitude evolution of the maximum reduced electric field (black line) and maximum streamer current density (blue line).	124
3.5	Reduced electric field (black solid line) and current density (blue dotted line) temporal behaviour of a single sprite streamer at 50 km of altitude with a driving current duration of 50 ms.	125
3.6	Altitude-time evolution of the reduced electric field oscillations during the driving current (50 ms duration) and between 54 and 62 km of altitude. The black line shows the upward movement of the possible crawlers [Moudry, 2003].	127
3.7	Altitude-time evolution of the electron density (upper plots) and O^- density (lower plots) due to a single sprite streamer with a driving current of 5 ms ((a)-(d)), 50 ms ((b)-(e)) and 100 ms ((c)-(f)).	130
3.8	Altitude-time evolution of the $N(^2D)$ density (upper plots) and NO density (lower plots) due to a single sprite streamer with a driving current of 5 ms ((a)-(d)), 50 ms ((b)-(e)) and 100 ms ((c)-(f)).	132
3.9	Altitude-time evolution of the $N_2^+(A^2\Pi_u)$ density (upper plots) and $N_2^+(B^2\Sigma_u^+)$ density (lower plots) due to a single sprite streamer with a driving current of 5 ms ((a)-(d)), 50 ms ((b)-(e)) and 100 ms ((c)-(f)).	133
3.10	Altitude-time evolution of the NO_2 density (upper plots) and NO_3 density (lower plots) due to a single sprite streamer with a driving current of 5 ms ((a)-(d)), 50 ms ((b)-(e)) and 100 ms ((c)-(f)).	135

LIST OF FIGURES

3.11 Altitude-time evolution of the $O(^1D)$ density (upper plots) and $O(^1S)$ density (lower plots) due to a single sprite streamer with a driving current of 5 ms ((a)-(d)), 50 ms ((b)-(e)) and 100 ms ((c)-(f)).	137
3.12 Altitude-time evolution of the O density (upper plots) and O_3 density (lower plots) due to a single sprite streamer with a driving current of 5 ms ((a)-(d)), 50 ms ((b)-(e)) and 100 ms ((c)-(f)).	140
3.13 Altitude-time evolution of the $O_2(a^1\Delta_g)$ density (upper plots) and $O_2(b^1\Sigma_g^+)$ density (lower plots) due to a single sprite streamer with a driving current of 5 ms ((a)-(d)), 50 ms ((b)-(e)) and 100 ms ((c)-(f)).	141
3.14 Altitude-time evolution of the atomic nitrogen density (N) due to a single sprite streamer with 5 ms (a), 50 ms (b) and 100 ms (c) driving current.	143
3.15 Altitude-time evolution of the N_2O density due to a single sprite streamer with 5 ms (a), 50 ms (b) and 100 ms (c) driving current.	144
3.16 Altitude-time evolution of the $N_2O_2^+$ ion density due to a single sprite streamer with 5 ms (a), 50 ms (b) and 100 ms (c) driving current.	145
3.17 Altitude-time evolution of the metastable $N_2(A^3\Sigma_u^+)$ due to a single sprite streamer with 5 ms (a), 50 ms (b) and 100 ms (c) driving current.	147
3.18 Altitude-time evolution of the $N_2(B^3\Pi_g)$ density (upper plots) and the first positive band system ($1PN_2$) emission brightness (lower plots) due to a single sprite streamer with a driving current of 5 ms ((a)-(d)), 50 ms ((b)-(e)) and 100 ms ((c)-(f)).	148
3.19 Altitude-time evolution of the $N_2(C^3\Pi_u)$ density (upper plots) and the second positive band system ($2PN_2$) emission brightness (lower plots) due to a single sprite streamer with a driving current of 5 ms ((a)-(d)), 50 ms ((b)-(e)) and 100 ms ((c)-(f)).	149
3.20 Altitude-time evolution of the $4.26\ \mu\text{m}$ (upper plots) and $14.9\ \mu\text{m}$ (lower plots) infrared emission brightness of CO_2 due to a single sprite streamer with a driving current of 5 ms ((a)-(d)), 50 ms ((b)-(e)) and 100 ms ((c)-(f)).	152
3.21 Altitude-time evolution of the Meinel ($N_2^+(A^2\Pi_u) \rightarrow N_2^+(X^2\Sigma_g^+)$) emission brightness due to a single sprite streamer with 5 ms (a), 50 ms (b) and 100 ms (c) driving current.	153

LIST OF FIGURES

3.22	Altitude dependence of the emission brightness due to a single sprite streamer with 50 ms driving current as would be measured by a 33 fps camera. The red, blue and purple lines correspond, respectively, to the first and second positive band systems of N_2 and to the Meinel band of N_2^+ . The black and green lines correspond to the 4.26 μm IR and 14.9 μm IR bands of CO_2	154
3.23	Altitude dependence of the emission brightness due to a single sprite streamer with 50 ms driving current as would be measured by a 1000 fps camera. The red, blue and purple lines correspond, respectively, to the first and second positive band systems of N_2 and to the Meinel band of N_2^+ . The black line corresponds to the 4.26 μm IR band of CO_2 . We have not included the integrated emission brightness of the 14.9 μm IR band because our model has not enough temporal resolution at these timescales.	155
3.24	Altitude-time evolution of the gas temperature variation due to a single sprite streamer with (a) 5 ms, (b) 50 ms and (c) 100 ms of driving current.	156
3.25	Altitude evolution of the maximum value of the gas temperature. The solid black, red and blue lines are for driving currents of, respectively, 5 ms, 50 ms and 100 ms.	157
3.26	Temporal evolution of the gas temperature (blue line) and the reduced electric field (black line) at 50 km of altitude for the 50 ms driving current.	158
3.27	Time-dependent distribution of the energy density dissipated by a single sprite streamer with 50 ms driving current at an altitude of 50 km. . . .	159
3.28	Time-integrated contribution to gas temperature of each energetic channel in the afterglow stage (red bars) and in the post-afterglow stage (green bars) after the streamer head at 50 km of altitude and for the 50 ms driving current. Note that a negative sign of the temperature contribution corresponds to the temperature absorbed by the gas in non-thermal processes.	160
3.29	Electron energy loss fractions through electron-impact collision processes producing species above 50 km of altitude for a 50 ms driving current during the afterglow stage. Note that in $\text{O}_2(v)$ and $\text{N}_2(v)$ we have taken into account all the vibrational levels considered.	161

3.30	Fractions of electron energy partitioned into the excitation, ionization and dissociation of molecules. These values are calculated at 50 km of altitude for a 50 ms driving current considering the afterglow and post-afterglow stages. Note that in $O_2(v)$ and $N_2(v)$ we have taken into account all the vibrational levels considered.	162
3.31	Time-integrated contribution of different kinetic processes to gas heating up to 33.6 s at 50 km of altitude for a 50 ms driving current during the post-afterglow stage.	163
4.1	The set of VLF pulses recorded by Venera 12 on the Venus surface, 30 min after landing [Ksanfomaliti, 1980].	166
4.2	Dark-side multiple-image view of Jupiter captured by Voyager 1 in 1979 from a distance of 320000 km. The blue arc of the limb is an aurora in the north pole of Jupiter. The white spot clusters are lightning flashes in jovian thunderstorms [Smith et al., 1979]	167
4.3	Images of Uranus at K' band ($2.2 \mu\text{m}$) obtained with the 10-m Keck telescope on UT 5 and 6 August 2014 [de Pater et al., 2015]	167
4.4	(a) NASA's Cassini spacecraft captured the first lightning flashes on Saturn when it took these images on Nov. 30, 2009 [Dyudina et al., 2013]. (b) The huge storm churning through the atmosphere on Saturn's northern hemisphere (Dic. 10, 2009) overtakes itself as it encircles the planet in this true-color view from NASA's Cassini spacecraft [Fischer et al., 2011].	168
4.5	(a) The electrostatic field above a Venusian charge configuration placed at 50 km over the surface with different values of total charge. (b) The electrostatic field above a Jovian thundercloud possessing a negative charge located 30 km below the 1-bar pressure level for different values of total charge. When the conventional breakdown field (solid blue line) crosses the electric field, a sprite can potentially occur [Yair et al., 2009].	170

LIST OF FIGURES

4.6	Top: Time evolution of the electric field at 700 km of altitude above the 1-bar pressure level due to a lightning discharge with a charge moment change of $M = 10^5$ C km located at -110 km below the 1-bar pressure level on the Saturn's atmosphere. Bottom: Time evolution of the electric field at 70 km of altitude over a thunderstorm due to a cloud-to-ground discharge located on Earth induced by a charge moment change of $M = 10^2$ C km. The center of the dipole is at 0 km. The dotted blue and green lines represent the static and induction components of the electric field and the solid black line represents the total electric field applied, all of them calculated through equation (4.2) [Dubrovin et al., 2014].	172
4.7	Density profiles of the neutral background gas (solid red line) and the ambient free electrons (solid blue lines) used in our simulations. The neutral gas density was obtained by Festou and Atreya [1982] by interpolating two sets of measurements. [Luque et al., 2014].	175
4.8	Temporal evolution of the reduced electric field (E/N), electron and ion concentration calculated with the kinetic model for $M = 10^5$ C km (profiles (a) and (b)) and with $M = 10^6$ C km (profile (b)). The plots have been calculated for altitudes where the electron density reaches its maximum value, that is, 750 km (panels (a) and (b)), 700 km (panels (c) and (d)) and 500 km (panels (e) and (f)). The panels (a) and (b) show results for the profile (a) and the panels (c), (d), (e) and (f) for the profile (b).	177
4.9	Altitude-dependent instantaneous number of UV continuum (left hand side panels) and Fulcher band (right hand side panels) photons $\text{cm}^{-3} \text{s}^{-1}$, calculated with the kinetic model for the same CMC and ambient electron density profiles as in Figure 4.8.	180
4.10	Altitude-dependent cumulative number of UV continuum (left hand side panels) and Fulcher band (right hand side panels) photons cm^{-3} , calculated with the kinetic model for the same CMC and ambient electron density profiles as in Figure 4.8.	181
4.11	Altitude-dependent cumulative number of Balmer band (left hand side panels) photons cm^{-3} and $H(n=3)$ density (right hand side panels) in cm^{-3} , calculated with the kinetic model for the same CMC and ambient electron density profile as in Figure 4.8.	182

LIST OF FIGURES

D.1	Variation of the correction parameter (k_{corr}) with altitude taken from the thermal relaxation stage of the model.	202
E.1	Variation of the cosmic rays constant (CRC) with altitude taken from the electronic relaxation stage of the model.	208

LIST OF FIGURES

List of Tables

1.1	Composition of the Earth's atmosphere below 100 km [Wallace and Hobbs, 2006]	6
2.1	I ₁ , I ₂ , I ₃ and I ₄ sub-band peak positions (nm) of the (0,0), (1,0), (2,0) and (3,0) bands of the N ₂ - 1PG	92
2.2	Wavelengths and $J'(J' + 1) = (J'' + 1)(J'' + 2)$ values for the R branch ($\Delta J = +1$) rotational transitions of the (0,0) vibrational band of the first negative system of N ₂ ⁺ (B ² Σ _u ⁺)	99
A.1	Some constant for atmospheric sciences	191
B.1	Statistical weights of vibrational levels of the ground electronic state of CO ₂	194
C.1	Potential energies of the species <i>i</i>	196
E.1	Ground neutrals considered	203
E.2	Electrons and negative ions considered	203
E.3	Excited neutrals considered	204
E.4	Positive ions considered	204
E.5	Different types of reactions considered	205
E.6	EEDF and cross section dependent processes	210
E.7	Ionization and dissociative ionization processes	212
E.8	Dissociation processes	213
E.9	Attachment processes	213
E.10	Recombination processes	214

LIST OF TABLES

E.11	Vibrational-Vibrational processes (VV)	215
E.12	Vibrational-Translational processes (VT)	215
E.13	O ₂ chemistry: vibrational-translational processes (VT)	217
E.14	Electronically excited species	218
E.15	Ground neutral species	220
E.16	Ion-Ion recombination processes	222
E.17	Positive ion processes	223
E.18	Negative ion processes	225
E.19	Vibrational-Translational processes	226
E.20	Vibrational-Vibrational processes	229
E.21	Galactic cosmic rays ionization	230
E.22	Rotational deexcitation processes	230
E.23	Radiative decay processes	231
E.24	Processes only included in the model of halos	236
F.1	Ground neutrals considered	237
F.2	Excited neutrals considered	237
F.3	Electrons and negative ions considered	238
F.4	Positive ions considered	238
F.5	EEDF and cross section dependent processes	239
F.6	Ionization process	240
F.7	Dissociation processes	240
F.8	Attachment and dissociative attachment processes	240
F.9	Excitation/de-excitation processes	241
F.10	Detachment process	241
F.11	Recombination and dissociative recombination processes	242
F.12	Ground neutral processes	243
F.13	Electronically excited neutral including Penning ionization processes	243
F.14	Vibrational-vibrational processes	244
F.15	Vibrational-translational processes	244
F.16	Ion-Ion recombination processes	245
F.17	Positive ion processes	246
F.18	Negative ion processes	246

LIST OF TABLES

F.19 Radiative decay processes 247

LIST OF TABLES

1

Introduction

“I’ve seen things you people wouldn’t believe: Attack ships on fire off the shoulder of Orión. I’ve watched c-beams glitter in the dark near the Tannhäuser Gate. All those ... moments will be lost in time, like tears...in rain. Time to die.”

– Roy Batty, *Blade Runner*

1.1 The atmosphere of the Earth

1.1.1 Definition and origin

The atmosphere is a gaseous layer that surrounds some planets and other celestial bodies. The Earth’s atmosphere is constituted by a gas mixture (air) and it presents in its composition nitrogen (78 %), oxygen (21 %), and some minor components like carbon dioxide (necessary for photosynthesis), and water vapor whose condensation leads to precipitation and thus supplies freshwater. The whole atmosphere acquires a characteristic blue coloration due to the dispersion (Rayleigh scattering) of sunlight by air molecules. The Earth’s atmosphere regulates temperature and radiations from the Sun. Some decades ago, scientists considered that the primitive atmosphere must be reducing, that is, that it lacked free oxygen and it was composed by NH_3 , CH_4 and H_2 . A lot of data collected during the seventies changed this idea. The primitive atmosphere consisted probably in common gases in the Solar System: Hydrogen (H) and Helium (He). Due to its low atomic weight these light chemical species were lost to space.

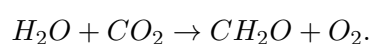
1. INTRODUCTION



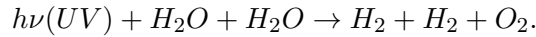
Figure 1.1: The Iberian peninsula taking by an astronaut aboard the International space Station. This photograph from space also shows the airglow, a faint green arc seen along the horizon that's caused by chemical reactions among the gas molecules of Earth's upper atmosphere (Courtesy of NASA).

Nowadays it is believed that the primitive atmosphere originated from the incessant volcanic activity and cooling of magma in the early stages of the planet formation. This must have been a slightly reducing atmosphere formed mainly by water vapor, N_2 , CO_2 , SO_2 and Cl_2 . Cooling of the primitive atmosphere allowed the condensation and precipitation of the water vapor to form the oceans. A portion of CO_2 was dissolved in water droplets joining the ocean.

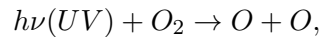
Between 2500 and 2000 million years ago, free oxygen emerged in the atmosphere due to the first photosynthetic organisms. These anaerobic bacteria (cyanobacteria) in the ocean began to produce O_2 through the photosynthetic reaction



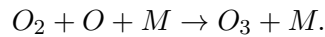
Another possible oxygen source could have been the photodissociation of hydrogen by ultraviolet (UV) radiation



The oxygen present in the primitive atmosphere was initially consumed in the oxidation of rocks. However, 600 million years ago, the level of O_2 had reached between 1-10 % of the present values. This amount was sufficient to form the ozone layer in the stratosphere through the reactions



and



The creation of the ozone layer allowed living organisms to flourish in the ocean's surface and, eventually, to go on land (400 million years ago). Subsequent changes in the atmosphere mainly consist in variations in the CO_2 concentration related to the glaciations, the existence of the biosphere and the human activity [Wallace and Hobbs, 2006].

1.1.2 Composition of the atmosphere

The atmosphere is formed by a gas mixture called air, and a number of solid and liquid particles in suspension called aerosols. The air is composed of different gases (Table 1.1):

- **Majority:** Nitrogen (N_2) with a proportion of 78 %, oxygen (O_2) with a proportion of 20.9 %, argon (Ar) with a proportion of 0.93 % and carbon dioxide (CO_2) with a proportion of 0.03 %.
- **Minority:** constitute the remaining 0.14 % and their proportions are so small that they are measured in parts per million (ppm). These include carbon monoxide (CO), ozone (O_3), hydrogen (H_2) and helium (He).
- **Variables:** there are other components whose proportion varies, such as water vapor or atmospheric pollutants.

1. INTRODUCTION

In Figure 1.2 we can see the density vertical distribution of the main species present in the atmosphere from the ground to the lower ionosphere (85 km of altitude). Up to 80 km of altitude, the atmospheric composition is uniform due to the air turbulence, so it is called homosphere. Above 80 km of altitude, the composition of the gases is not uniform (heterosphere) so that several layers can be differentiated according to the predominant gas component:

- Sodium layer: between 80-105 km.
- Nitrogen layer: between 80-500 km.
- Atomic oxygen layer: between 200-1000 km.
- Helium layer: between 1000-3500 km.
- Atomic hydrogen layer: from 3500 km.

Aerosols are solid and liquid particles of submicron size. Their atmospheric lifetime is small, around 5 days, but they have a great importance in the atmosphere: they trigger the rain, have high reflectivity and are the key component in heterogeneous (gas-surface) chemical reactions. The aerosols can have a natural origin, being generated by the volcanos, the wind or forest fires, or an anthropogenic origin.

1.1.3 Vertical structure

Using as criterion the temperature and its variations with respect to the altitude, the Earth's atmosphere can be divided in a set of horizontal layers (see Figure 1.3) that from bottom to top are the following:

Troposphere

The troposphere is the lowest layer in the atmosphere and the one of greatest environmental importance since virtually all weather phenomena take place in it: cloud formation, rain, etc. It contains 75 % of the mass of the atmosphere and most of the water vapor and carbon dioxide. The troposphere has a first part influenced by the Earth's surface. This first stratum is called "planetary boundary layer" (or "dirty layer") where there is a continuous friction with the ground surface and an elevation of the air when heated. This layer can have a thickness of 600-800 m although it depends

1.1 The atmosphere of the Earth

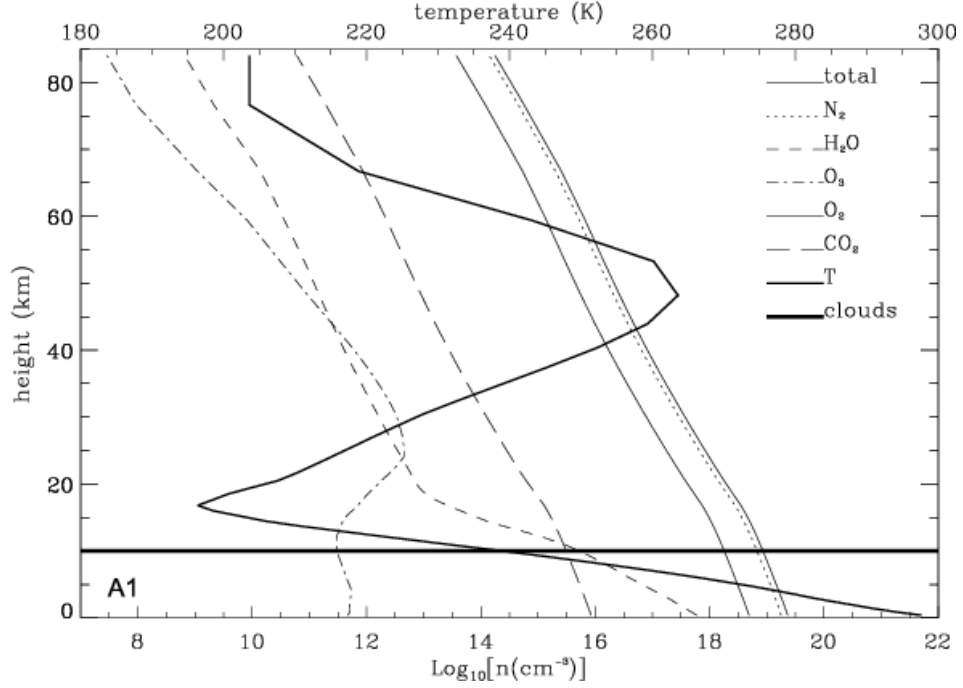


Figure 1.2: The plot shows the total number density profile (thin solid line) of the atmosphere in cm^{-3} and those of five species, namely, N_2 (dotted line), O_2 (dash-dot-dot-dotted line), H_2O (dashed line), CO_2 (long-dashed line), and O_3 (dash-dotted line). Temperature (thick line up to 80 km) and mixing ratios of the different species are those of Earth. The thickest horizontal line shows the position of the cloud layer [Ehrenreich et al., 2006].

on the topography, the wind force, the heating grade of the surface, etc. As we ascend in the troposphere, we can note an average drop in temperature at a rate of $6.5\text{ }^\circ\text{C}/\text{km}$. The atmosphere is heated mainly due to the heat transfer from the surface, therefore the temperature decreases with the altitude in the troposphere (except in the cases of thermal inversion). The upper limit of the troposphere is called tropopause, and it is where the temperature reaches a minimum value of $-70\text{ }^\circ\text{C}$, at which the temperature stops decreasing. The tropopause altitude is not constant but it has a maximum value in the equator (at about 16 km of altitude) and a minimum value at the poles (at about 8 km of altitude).

1. INTRODUCTION

Table 1.1: Composition of the Earth's atmosphere below 100 km [Wallace and Hobbs, 2006]

Constituent	Molecular weight	Content
Nitrogen (N ₂)	28.013	78.08 %
Oxygen (O ₂)	32.00	20.95 %
Argon (Ar)	39.95	0.93 %
Water vapor (H ₂ O)	18.02	0 - 5 %
Carbon dioxide (CO ₂)	44.01	380 ppm
Neon (Ne)	20.18	18 ppm
Helium (He)	4.00	5 ppm
Methane (CH ₄)	16.04	1.75 ppm
Krypton (Kr)	83.8	1 ppm
Hydrogen (H ₂)	2.02	0.5 ppm
Nitrous oxide (N ₂ O)	56.03	0.3 ppm
Ozone (O ₃)	48.00	0 - 0.1 ppm

Stratosphere

The stratosphere extends from the tropopause up to 50 km of altitude approximately, in the stratopause. In this layer we can find most of the ozone of the atmosphere, concentrated between 20 and 25 km of altitude (see Figure 1.2) (ozonosphere). In the stratopause, the temperature peaks at about 0 °C (sometimes reaching 15 °C), associated to the absorption of solar ultraviolet radiation by ozone. There is no vertical circulation in the stratosphere, although the horizontal fluxes can reach 200 km/h (this feature give its name to this layer). The horizontal winds facilitate the global spreading of any substance that reaches the stratosphere, which is what happens with ozone-depleting chlorofluorocarbons (CFCs).

Mesosphere

Above the stratopause and up to 80 km, approximately, we can distinguish another layer called mesosphere whose upper limit is the mesopause. In this layer, the temperature falls with altitude to less than -80 °C. This is the region where the ice-crystal noctilucent clouds and sprites (associated with lightning) are observed. The mesosphere contains only 0.1 % of the total mass of the atmosphere. This is the reason why planes and

1.1 The atmosphere of the Earth

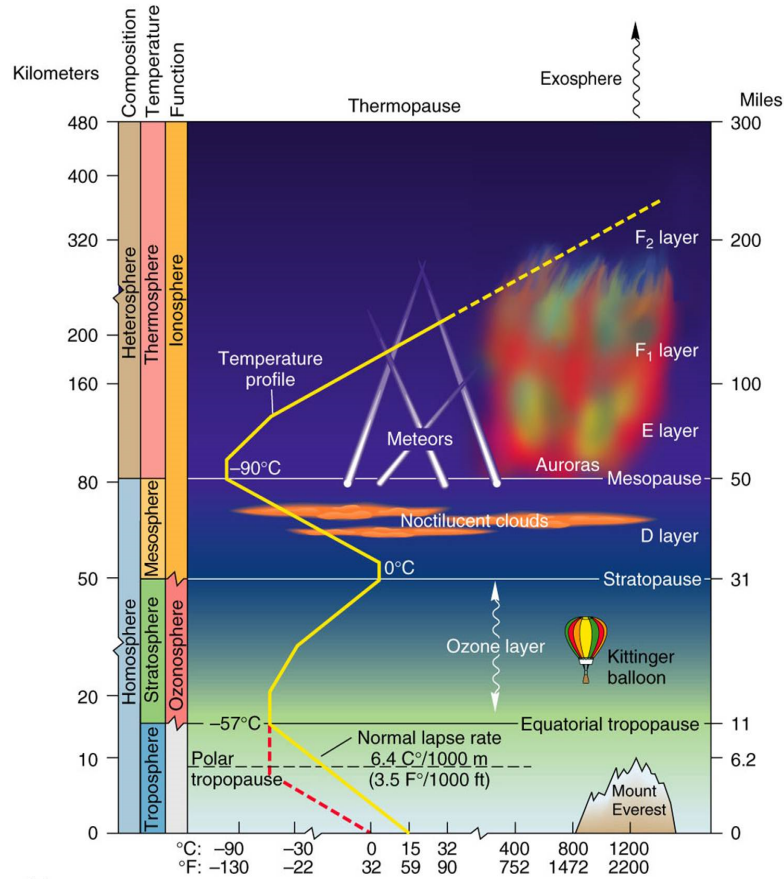


Figure 1.3: Vertical structure of the Earth’s atmosphere. The solid yellow line is the global (averaged over all latitudes except the polar ones) vertical gradient of the air temperature and the dotted red line is the vertical gradient in the polar regions.

balloons can not reach it due to its low density, but it has too much density for satellites. Due to its difficult access, the mesosphere is not well known and for that reason it is sometimes called “ignorosphere”. Despite its low mass, the mesosphere is a very important layer due to the existence of turbulent flows and atmospheric waves as well as ionization and chemical reactions taking place in it. In the upper mesosphere there is also a region of the ionosphere called D layer. The D layer is only present during daytime due to ionization of NO by Lyman-alpha radiation from the Sun. At nighttime this ionization disappears and the conductivity decreases due to recombination between free electrons and ions.

1. INTRODUCTION

Ionosphere (or Thermosphere)

The ionosphere extends from the mesopause (~ 80 km) to the thermopause between 600-800 km of altitude, where the exosphere begins. Sometimes, the ionosphere is also called thermosphere due to the coinciding intervals of both layers. The term thermosphere is based simply on the vertical temperature profile while the criterion for designating the ionosphere refers to the remarkable presence of ions. In the thermosphere and the exosphere the densities are extremely low and the gases are not well-mixed, so these layers are also called heterosphere. The composition of the thermosphere is mainly molecular and atomic nitrogen and oxygen up to about 200 km of altitude, while above 200 km the predominant chemical species is atomic oxygen. Due to the solar ultraviolet absorption of the molecular and atomic oxygen, the temperature rises again to about 1000 °C. The UV, X and γ radiations from the Sun, strongly ionize oxygen atoms and nitrogen molecules above 100 km of altitude. The deexcitation of these species during the night is the responsible of a weak greenish emission called air-glow (or nightglow) (see Figure 1.1). The interaction of the solar wind with the polar ionosphere produces the famous (boreal and austral) auroras (see Figure 1.4). It is



Figure 1.4: Boreal aurora captured in Nordresia, Norway by Ivar Næss on December 9, 2013. The green color is due to the radiative deexcitation of the atomic oxygen present in the ionosphere.

also in the ionosphere where radio waves from the Earth are reflected facilitating the communication between continents.

Exosphere

The exosphere is the last layer of the atmosphere and it extends from the thermopause to space. The exosphere is composed by atoms of hydrogen and helium whose far-ultraviolet (FUV) scattering from the Sun produces the geocorona emission (see Figure 1.5).

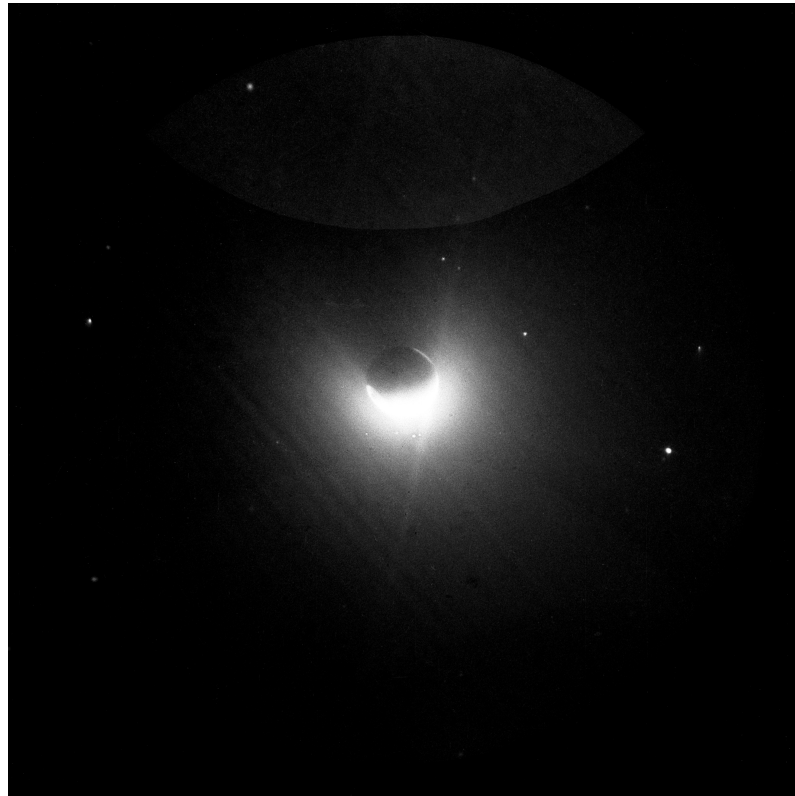


Figure 1.5: A far ultraviolet (FUV) photograph reveals the geocorona, a halo of low density hydrogen which surrounds the Earth. The photograph was taken by astronaut John W. Young, Apollo 16 mission commander, during the first spacewalk of his trip to the moon on April 21, 1972.

1.2 Lightning

We can define lightning as a very longitudinal electrical discharge which is produced in a cloud as a consequence of stormy activity (see Figure 1.6). Early scientific studies related to lightning were carried out by Benjamin Franklin in the eighteenth century

1. INTRODUCTION

with rudimentary instrumentation (the famous kite experiment). He demonstrated that some clouds are electrically charged and that lightning stroke are huge electrical discharges [Cohen, 1941]. In the last century, lightning research was relaunched by, among others, C.T.R. Wilson, Nobel Prize winner in 1927. Wilson could estimate the charge distribution inside the cloud as well as the individual charge involved in the lightning discharge [Wilson, 1921, 1920]. In the second half of the twentieth century, with the development of new techniques of data acquisition and analysis and largely driven by the motivation of minimizing lightning damages to aircraft and ground-based instalations, progress was made in the understanding of these natural phenomena.



Figure 1.6: Positive cloud-to-ground lightning captured by Kara Swanson in the coast of the Bahamas.

Within a thunderstorm, the primary charge transfer process is collisions between soft hail (graupel) particles and small crystals of ice. After charge has been transferred to the particles, the positively charged ice crystals are carried to the top part of the thunderstorm, to an altitude near 10 km (in template summer storms); while the negatively charged hails are placed at a height of 6-8 km [MacGorman and Rust, 1998].

The lightning discharges can be divided into two categories: (1) those that go from the cloud to the ground and (2) those that do not. The latter group are called cloud discharges and they can occur totally within a single cloud (intracloud lightning), between clouds (intercloud lightnings) and from cloud to surrounding air (cloud-to-

air lightning) (see Figure 1.7). There are four types of lightning flashes that occur

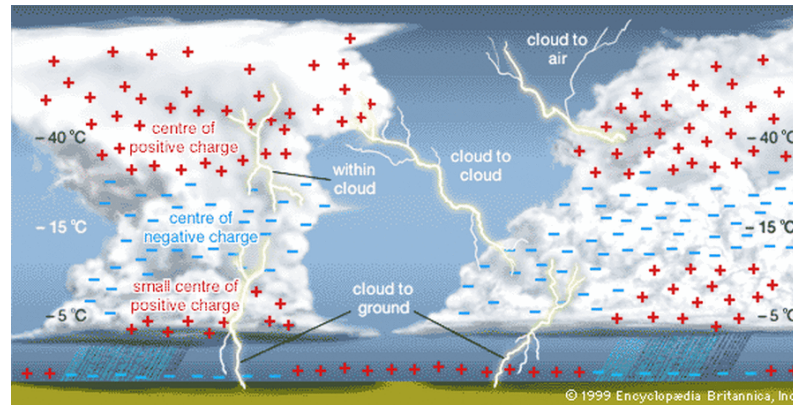


Figure 1.7: The charge structure of two simple thunderstorms, the types of lightnings and the locations where lightning can occur. Courtesy of British Encyclopædia.

between the cloud and the ground (CG) which are differentiated by the leader electric charge and its direction of propagation. About 90 % of the CG flashes are initiated by negatively charged leaders in downward propagation (the so-called negative cloud-to-ground lightning, or -CG), as shown in Figure 1.8a. Most of the remaining 10 % of the lightning discharges between the cloud and the ground are initiated by positively charged leaders with downward propagation (positive cloud-to-ground lightning, or +CG), as shown Figure 1.8c. The remaining types of (ground-to-cloud) lightning are very rare and are initiated usually from mountain tops, tall man-made towers and other tall objects (see Figures 1.8b, d). The most common downward electrical discharge is the negative cloud-to-ground flash, which begins with a local discharge between the bottom of the main negative charge region within the cloud and the small lower positive charge region beneath. The free electrons move to the lower positive region, neutralizing a significant fraction of the positive charge and continue their journey towards the ground. The physical mechanism for moving the charges to the ground is called “stepped leader”. The stepped leader’s movement from cloud to ground is not continuous, but rather it moves downward in discrete luminous segments (steps) of tens of meters length [Dwyer and Uman, 2014]. The time between luminous steps is about $50 \mu\text{s}$ when they are close to the cloud and about $10 \mu\text{s}$ when the segments are near the ground. The average downward velocity of the stepped leader from the cloud to the ground is about $2 \times 10^5 \text{ m/s}$ so that it takes the trip in 20 ms approximately.

1. INTRODUCTION

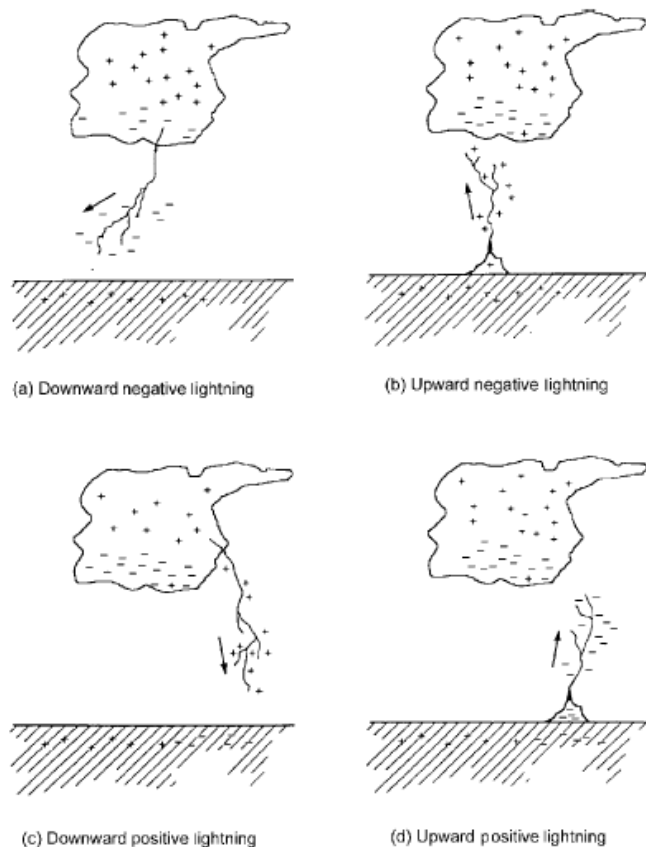


Figure 1.8: The four types of cloud-to-ground lightning flashes defined through the direction of leader propagation and the charge of the initiating leader [Dwyer and Uman, 2014].

A typical stepped leader has 5 C of negative charge distributed along its body when it is close to ground and an average current of 100-200 A must flow during the leader process [Dwyer and Uman, 2014].

When the stepped leader is close to ground, its relatively large negative charge attracts the positive charge concentrated in the ground (mainly at elevated objects), generating a positive upward discharge from ground to leader. When the two (positive and negative) electrical discharges contact each other, they produce the primary lightning current channel between cloud and ground. Since the negative charges of the leader are very close to the ground, they move violently into the Earth, causing a large flow of current to ground and producing a great luminosity at the bottom of the leader channel. Inside the luminous channel, the current flows continuously upward with a

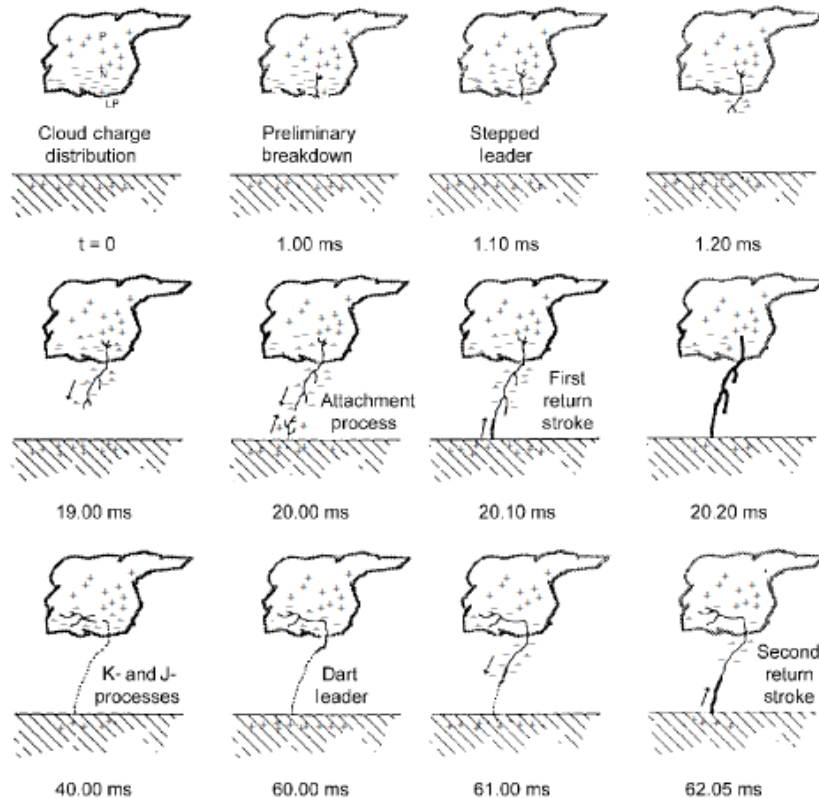


Figure 1.9: Detailed development of a negative cloud-to-ground lightning discharge from the first electrical breakdown to the second return stroke. Adapted from Uman [2001] by Dwyer and Uman [2014].

typical velocity between one-third and one-half of the speed of light. This process is called “return stroke”. In Figure 1.9, it occurs between 20.10 ms and 20.20 ms after the lightning initiation. This phase is the responsible of the strong brightness of the main channel and the heating of the surrounding air (the highest temperature recorded is 30000 °C). The sudden expansion of the heated air produces most of the thunder we hear. After the first stroke the current has ceased to flow, the luminous flash can finish in which case the discharge is called “single-stroke flash”. However, 80 % of the lightning produced in temperate regions exhibit between 3 and 5 strokes separated 40 ms from each other in time [Uman, 2001].

Sometimes, the residual channel of the first stroke is crossed down by another leader which seems to move continuously, this is so-called “dart leader”. Between the end of the first stroke and the beginning of the dart leader the J- and K-processes can

1. INTRODUCTION

occur. The J-process is a charge redistribution into the cloud, taking place in tens of milliseconds as a consequence of the previous return stroke. This process is often viewed like a relatively slow positive leader which extends from the origin of the lightning discharge in the negatively charged region into the cloud. The K-process is a relatively fast backward motion streamer which begins in the tip of the positive leader and it propagates to the flash origin [Rakov and Uman, 2003].

The dart leader moves downward into the leader stroke channel and deposits the negative charge along the channel about 60 ms after the lightning initiation. The dart leader trip to ground is produced in a few milliseconds but transports less charge than the stepped leader so the subsequent return stroke will have less charge than the first return stroke. The first stroke currents are typically 30 kA in a few microseconds, while the currents of subsequent strokes can be between 10-15 kA in 0.1 microseconds.

There are three possible modes of charge transfer between the cloud and the ground in a lightning discharge. In negative subsequent strokes these three modes are represented by [Rakov and Uman, 2003]:

- In a leader-return-stroke sequence, the downward leader develops a conductive path between the charge source into the cloud and the ground depositing negative charge along the path. The following return-stroke travels through this path from the ground to the charge source into the cloud and neutralizes the negative leader charge.
- The continuous lightning current can be seen as a quasi-stationary arc between the charge source and the ground. This continuous current can be tens to hundreds of amperes and with a duration up to hundreds of milliseconds.
- The M-component of a lightning discharge can be viewed as perturbations in the continuous current and in the channel luminosity. The spatial front length of the M-component waves can be up to one kilometer while for dart-leader and return-strokes waves it can be of the order of 10 and 100 meters, respectively.

About 10 % of the cloud-to-ground lightning strokes have positive polarity, that is, they are originated in the upper positive charge region of the cloud. The stepped leader of a positive lightning is optically almost undistinguishable from that of the negative stepped leader. However, the +CG return stroke can exhibit current peaks of 300 kA

(three times higher than -CG return stroke). Positive cloud-to-ground lightning flashes generally have a single return stroke followed by a relatively long period of continuous current. In upward lightning, the first leader propagates from ground to cloud. When the leader contacts the cloud, nearly half of the ground-to-cloud lightning flashes can present subsequent return strokes with the same features of the CG return strokes.

The so-called CIDs (Compact Intracloud Discharges) can also occur inside the clouds [Smith et al., 1999]. CIDs are vertical and short electrical discharges (about 1 km length) in the upper region of the cloud accompanied by copious VHF (Very High Frequency) radiation and visible light. Ball lightnings are the weirdest electrical phenomena in thunderclouds. There are almost 5000 ball lightning observations but no theory so far can explain them satisfactorily. Ball lightnings are red or yellow sphere-like plasma structures with a size comparable to that of a grapefruit. Their duration may be of up to few seconds and they often occur just after a cloud-to-ground lightning.

1.3 Transient Luminous Events

In the summer of 1989 several US researchers, supervised by J. R. Winkler, recorded a few bright flashes [Franz et al., 1990] at 50 km of altitude above very far thunderclouds. They had performed the first detection of mesospheric plasmas (50-90 km of altitude) hypothesized in 1925 by the scottish Nobel prize C.T.R. Wilson [Wilson, 1925, 1956] although since the late nineteenth century several witnesses reported observations of very fast transient luminous phenomena above thunderstorm systems [Toynbee, 1886, Everett, 1903]. Wilson [1925] thought that as one ascends into the atmosphere, the density of the air decreases, therefore less collisions will be undergone by free electrons and they will gain energy from an imposed electric field more easily. The electric field created by the charge inside the cloud decreases slowly with height while the atmospheric density decays much faster (exponentially). Therefore, there will be a height at which free electrons gain so much energy from the electric field that they can easily ionize oxygen and nitrogen molecules releasing new electrons. The resultant avalanche multiplies the number of free electrons and starts an electrical discharge. This mechanism offers us a first explanation for the formation of some TLEs, particularly that of sprites which are the most frequently observed. However, there are many kinds of TLEs (see Figure 1.10) occurring at different altitudes, whose generation mechanisms

1. INTRODUCTION

are not well known nor their influence in the atmosphere properties quantified. Since the summer of 1989, many different types of transient upper atmospheric electrical discharges have been discovered. Nowadays these electrical discharges are generally called *Transient Luminous Events* (TLE) which occur from the upper troposphere to the lower ionosphere. The names of most of TLEs have been inspired by W. Shakespeare’s “A Midsummer Night’s Dream” due to their elusive and mysterious nature.

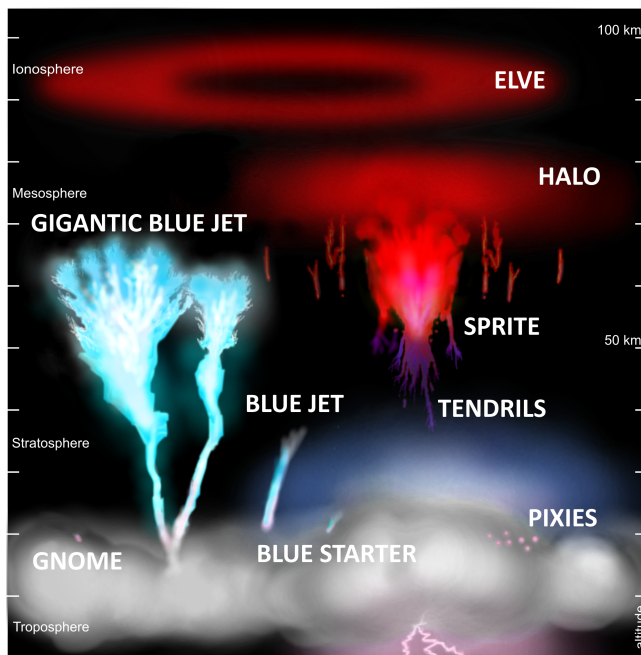


Figure 1.10: Lightning related Transient Luminous Events (TLEs). The picture shows the most common TLEs produced in the Earth atmosphere. Courtesy of Maria Passas.

1.3.1 Blue Jets and Blue Starters

The first publications about the detection of bluish streamer-like electrical discharges from the upper side of thunderclouds (see Figure 1.11), between 15-18 km of altitude, date back from the summer of 1994 in Arkansas [Wescott et al., 1995]. However, in 1989, a similar phenomena was accidentally captured from the Space Shuttle [Boeck et al., 1995]. These discharges are called *Blue Jets* and can reach up to 40 km of altitude from the top of the initial stage thundercloud while a lot of negative cloud-to-ground lightnings are occurring (see Figure 1.11). Blue jets usually have a duration of about 200-300 ms. Present theories describe Blue Jets as streamer-like electrical

discharges with positive polarity, that is, they have a positive charge concentration in the streamer head. Blue jets can propagate upward at 100 km/s and typically exhibit a conic-like structure with an angle of about 15 degrees [Wescott et al., 1995, Lyons et al., 2003, Wescott et al., 1998, 2001]. In 1998, Wescott et al. [1998] used TV images obtained with two different filters (red and blue) to conclude that significant ionization of N_2^+ was required to match the available observations of blue jets.



Figure 1.11: Blue Jet captured by Patrice Huet, La Réunion in 1997 above a thundercloud system.

The first results about *Blue Starters* were published in 1996 [Wescott et al., 1996]. Blue Starters seem to be the first stages of Blue Jets since they only propagate up to 25 km of altitude and exhibit a streamer-like appearance with velocities between

1. INTRODUCTION

27-153 km/s [Wescott et al., 1996]. Blue Starters (also blue jets) are very difficult to observe from the ground due to Rayleigh scattering of blue light [Wescott et al., 1998, Heavner, 2000]. Blue Starters are no related to any particular type of lightning but when they occur the rate of -CG flashes decreases abruptly during 3 seconds after the event, followed by the resumption of lightning activity [Wescott et al., 1996].

1.3.2 Gigantic Jets

Gigantic Jets (see Figure 1.12), which were discovered in 2002 [Pasko et al., 2002], emerge from the top of the thundercloud (10-20 km of altitude) and they can reach the lower ionosphere (90 km of altitude) and connect electrically both the troposphere and the ionosphere [Pasko, 2003, Su et al., 2003]. Both blue jets and gigantic jets play an important role in the global electric circuit which maintains a potential difference of several hundreds of thousands of volts between the ground and the terrestrial ionosphere.

The polarity of Gigantic Jets (GJ) is usually negative [Krehbiel et al., 2008], they are not associated to any particular type of lightning and it has been speculated that they may be responsible of the lightning-related X-ray and γ -ray emissions [Fishman et al., 1994, Moore et al., 2001, Dwyer, 2005, Smith et al., 2005, Moss et al., 2006] detected from the space. The average upward velocities of Gigantic Jets are between 5×10^4 m/s in the lower side and 2.7×10^5 in their upper side [Uman, 2001]. Su et al. [2003] classified Gigantic Jets in two categories depending of their morphology: *Tree Jets* and *Carrot Jets*, and distinguished three different evolutive stages: *leading jet* (Figures 1.12a-b), *fully developed jet* (Figures 1.12c-d) and *trailing jet* (Figures 1.12e-i).

1.3.3 Sprites and Halos

Sprites are the most commonly observed TLEs. In fact, the first detected TLE in 1989 was a sprite, which is a huge and short (a few milliseconds) electrical discharge produced by a positive cloud-to-ground lightning. In a first approximation, it can be considered as being produced at a given height where the dipolar electric field generated by an intense +CG discharge is higher than the dielectric breakdown field of the air [Pasko et al., 1998]. Sprites usually cover heights between 85 km and 40-45 km, it is common to observe at their top (above 70 km of altitude) a diffuse optical

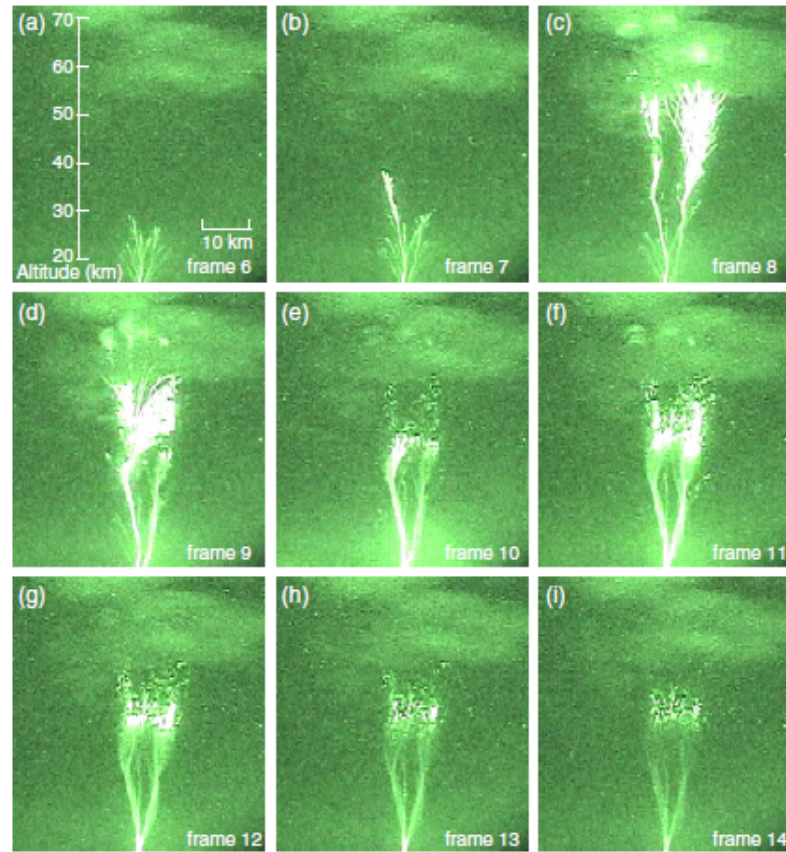


Figure 1.12: Evolutive stages of a Gigantic Jet recorded from Puerto Rico in 2001 [Pasko et al., 2002].

emission (glow-like discharge) while in the lower region (below 70 km of altitude) they have a filamentary structure (streamer-like) (see Figure 1.13a, 1.13c and 1.13d). The optical emissions of sprites are mainly in the red and in the blue spectral range due to the radiative deexcitation of the first (1PN_2) and second (2PN_2) positive systems of molecular nitrogen, respectively.

With sprites, *halos* are another common type of TLE. Halos are electrical discharges with red color and diffuse disc shape of 80-100 km of diameter that are produced at 80-85 km of altitude approximately (see Figure 1.13d). Halos can be associated with sprites or not and they are produced by both positive and negative cloud-to-ground lightning strokes.

1. INTRODUCTION

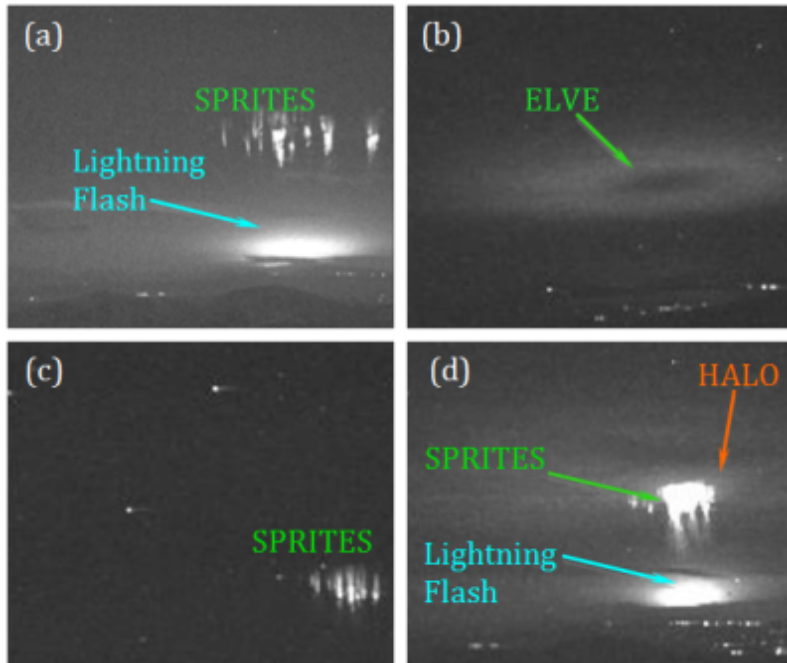


Figure 1.13: Images of sprites, sprite halo and elve captured by Maria Passas using GRASSP from the Calar-Alto Observatory, Almería, Spain (2013).

1.3.4 ELVES

Elves (Emissions of Light and Very Low Frequency Perturbations due to Electromagnetic Pulse Sources) are the faster TLEs detected to date and they were first postulated by Inan et al. [1991] and observed in 1992 by Boeck et al. [1992] from the Space Shuttle and by Fukunishi et al. [1996] from ground stations. Elves are electrical phenomena exhibiting a donut-like shape with a diameter between 100-300 km and located around 90-100 km of altitude (see Figure 1.13b). These elusive phenomena usually occur before sprites and they seem to be associated with the electron heating occurring in the lower ionosphere as a consequence of the EMPs (electromagnetic pulses) produced by very intense +CG lightning strokes [Inan et al., 1991].

1.3.5 Other TLEs

Trolls

A *Troll* is a reddish jet-like structure, very similar to a Blue Jet, which propagates upward from near the top of the cloud to 40-50 km of altitude and with an average

speed of 150 km/s. Trolls usually appear after *tendrils* in the larger sprites [Lyons et al., 2000].

Gnomes

Gnomes are probably a different manifestation of a blue jet but with a more compact shape (< 1 km). They can be located in the top of convective thunderclouds [Lyons et al., 2003].

Pixies

Pixies are pinpoints of light (about 100 m of diameter) with a duration of up to 10 ms which appear in the upper surface of a convective supercell [Lyons et al., 2003].

Smooth Crawlers

Smooth Crawlers are like beads of slowly varying luminosity moving upward with typical velocity of 10^4 m/s. They seem to have no apparent connection to clouds [Moudry, 2003].

Embers

An *Ember* is a small bead (< 2 km of diameter) which typically develops and brightens during 1 ms within decayed sprite tendrils (< 60 km of altitude) [Moudry, 2003].

Palm Trees

Another TLE with a very similar appearance of the Gigantic Jet is the *Palm Tree*. This is a single stem coming up from the cloud top and spreading out into a wider crown near 60-70 km of altitude [Moudry, 2003, Heavner, 2000]. Marshall and Inan [2007] estimated Palm Trees upward velocities at about 1.5×10^6 m/s.

1.3.6 Non-Luminous emissions

TIPPs

TIPPs (Trans-Ionospheric Pulse Pairs) are extremely intense pairs of VHF (Very High Frequency) pulses originating from thunderstorm regions, but some 10000 times

1. INTRODUCTION

stronger than sferics produced by normal lightning activity [Zuelsdorf et al., 1997]. They were first observed by the ALEXIS satellite [Massey and Holden, 1995].

TGFs

TGFs (Terrestrial Gamma Flashes) are gamma-ray bursts of short duration (1 ms) of terrestrial origin and first detected by the Compton Gamma Ray Observatory in 1994 [Fishman et al., 1994]. They occur in regions with high thunderstorm activity and their source seem to be located at altitudes < 30 km [Dwyer et al., 2012], though this is not yet well known.

1.4 Scientific contributions

During my PhD Thesis We have studied, both with numerical simulations and with laboratory experiments, the chemical and thermal evolution of the terrestrial atmosphere under the action of sprites and halos, including the analysis of spectral fingerprints of their laboratory electric discharge analogs.

First, We carried out simulations (using CSIC computer clusters in Granada (IAA) and Madrid) of the electrochemical impact of lightning flashes (synthetic and realistic [Gamerota et al., 2011]) with different polarities (+CG and -CG) and different current moment peaks (100 kAkm, 200 kAkm and 500 kAkm) between 50 km and 87 km of altitude [Parra-Rojas et al., 2013a]. In doing this, We previously carried out the relaxation of the statistical equilibrium equations to obtain the initial ion and neutral densities from the ambient neutral species provided by the WACCM model and the ambient electronic density by Hu et al. [2007]. In this relaxation stage, we also obtained the ionization and dissociative ionization rates of N_2 and O_2 by galactic cosmic rays that are consistent with the ambient electron density profile that has been used. After calculating the initial densities, we ran the simulations in a range of 37 altitudes in the Earth mesosphere for each of the different lightning cases considered. We employed a kinetic model with almost 100 chemical species and more than 900 processes based in the model by Gordillo-Vázquez [2008] and Gordillo-Vázquez [2010] solving the equations in a self-consistent way.

In 2012, we carried out laboratory studies of air plasmas under different pressures (ranging from 0.1 mbar to 2 mbar) in a hollow cathode reactor [Parra-Rojas et al.,

2013b]. We generated air halo-like plasmas to obtain their characteristic spectroscopic and thermal features with different spectral resolutions. We estimated the rotational (gas) temperature of the plasmas using non-invasive diagnostic techniques at different pressures and with three different spectral methods: a) analyzing the rotational structure of the (0,0) band of the first negative system of N_2^+ (1NN₂) [Herzberg, 1950], b) using the sub-band head peaks of the (3,0) vibrational transition of the first positive system of N_2 (1PN₂) [Simek and DeBenedictis, 1995] and c) using the spectral fitting of the rovibrational band of the 1PN₂.

We also performed simulations to understand the chemical and thermal impact of sprite streamers at different altitudes in the mesosphere (between 50 km and 80 km) using streamer current density profiles obtained with the streamer model proposed by Luque et al. [2008] and Luque and Ebert [2010]. The streamer current density profiles were extended with afterglows of 5 ms, 50 ms and 100 ms of duration, always within the observed values [Stenbaek-Nielsen and McHarg, 2008]. Similarly to the simulations of halos, we did a previous electronic relaxation to obtain the ambient initial densities of all the species. After the electronic relaxation, we also carried out a thermal relaxation of the energy equations to correct for some differences between WACCM and our model (regarding the number and type of species, etc...). The kinetic and thermal equations of our model were solved in a self-consistent way in each time step [Parra-Rojas et al., 2015].

Finally, we have studied the chemical effects of lightning flashes in the lower ionosphere of Saturn through a detailed self-consistent one-dimensional kinetic model. We have estimated the changes in the electron density, in the ion concentration and the photon emission. The electron density profiles have been obtained from two different models based in radio occultation measurements of the Cassini spacecraft. The first of them, by Moore et al. [2004] does not include a CH_x layer, so the base of Saturn's ionosphere is located around 900-1000 km over the 1-bar pressure altitude. The second model, by Galand et al. [2009] includes the CH_x layer and thus places the ionosphere around 600 km above the 1-bar level. With these two configurations of the ionosphere, we have studied the possibility of generation of sprites and halos in Saturn's upper atmosphere.

1.5 Organization of the thesis

The theoretical and experimental background of halos will be treated in chapter 2. Here, in the first section of the chapter, we will explain and describe the theoretical model employed to study the time-altitude dependence of the chemical species present in the Earth mesosphere. Most aspects of our experimental set-ups and measurement techniques are discussed in the second section of chapter 2. We show and explain the three methods used to obtain the rotational (gas) temperature of the air halo-like plasma generated inside a hollow cathode reactor.

Chapter 3 is devoted to the modeling of the chemical and thermal impact of sprites in the Earth mesosphere. In the first section we show the self-consistent model which we have used to study the chemical evolution of the mesosphere under the action of a sprite streamer. The second section of this chapter treats the contribution of a single sprite streamer to the possible local heating of the mesosphere. We discuss the different energetic channels and chemical mechanisms that can produce a variation of the gas temperature in the surrounding atmosphere after the sprite streamer passage.

In chapter 4 we investigate the effects of the electrical discharges and possible TLEs in the upper Saturnian atmosphere, using different electron density profiles and different charge moment changes of the parent lightning.

We conclude with chapter 5 where we summarize the most important results and conclusions and give ideas for future work.

Finally, we have added some appendices in which we show the chemical reactions employed in the halo and streamer models on the Earth and Saturn atmospheres. Other appendices describe the normal vibrational modes of the CO_2 molecule and explain how we obtained the statistical weights of the vibrational levels of CO_2 as well as the standard enthalpies of formation of the chemical species employed in the sprite model.

2

Sprite Halos

“And that, I think, was the handle-that sense of inevitable victory over the forces of Old and Evil. Not in any mean or military sense; we didn’t need that. Our energy would simply prevail. There was no point in fighting on our side or theirs. We had all the momentum; we were riding the crest of a high and beautiful wave. So now, less than five years later, you can go up on a steep hill in Las Vegas and look West, and with the right kind of eyes you can almost see the high-water mark-that place where the wave finally broke and rolled back.”

– Raoul Duke, *Fear and Loathing in Las Vegas*

2.1 State of the art

As we have explained in Section 1.3, sprite halos are flattened diffuse reddish flashes of light that usually appear between 75 km and 85 km associated with both positive and negative cloud-to-ground flashes (CG) [Barrington-Leigh et al., 2001]. Halos can spread to diameters of up to 100 km with a vertical width of up to 10 km. The generation mechanism is the same as that of sprites (quasielectrostatic electric field caused by thunderclouds [Pasko et al., 1996]) although the electric field causing halos is much lower than that associated with sprites, so halos are subtle and more difficult to observe.

It has been reported that lightning discharges affect the electron density and thus the electric conductivity in the mesosphere and ionosphere (Shao et al. [2013]). Moreover, the chemical disbalance caused by halos in the mesosphere is driven by the lightning

2. SPRITE HALOS

modified electron density. Several models have predicted the influence of thunderstorms on the chemical balance of the mesosphere, in particular the interaction of the EMP (electromagnetic pulses) caused by lightning-producing electron heating, ionization and dissociative attachment in the lower ionosphere, affecting the local conductivity and electron density (Taranenko et al. [1993], Fernsler and Rowland [1996], Pasko et al. [1997], Marshall et al. [2008], Cho and Rycroft [1998, 2001] and Lay et al. [2010]). In the study presented here, our goal is not only to quantify the influence of the mesospheric electric field generated by +CG and -CG lightning on the ambient electron density between 50 km and \simeq 90 km but, also, to analyze the dependence on time and altitude of the background chemical species densities under the action of sprite halo electric fields.

Previous studies based on the influence of Atmospheric Gravity Waves showed neutral density fluctuations between 60-90 km due to storm activity (Taylor and Hapgood [1988], Dewan et al. [1998], Sentman et al. [2003] and Yue et al. [2009]). In the case of the metastable species $O(^1D)$, Hiraki et al. [2004] proposed that the source mechanism of oxygen atoms $O(^1D)$ in the mesosphere due to sprite halo events during nighttime conditions was electron impact dissociation of O_2 molecules. They estimated an accumulated $O(^1D)$ production density of 10^4 cm^{-3} integrating in time during 1 ms and assuming a charge moment of 1000 Ckm. These authors also studied the dependence of the maximum $O(^1D)$ production density on the CG discharges with charge moment between 500 Ckm and 2000 Ckm at daytime and nighttime conditions. In our model, we present results of lightning discharges with 100 Ckm and 200 Ckm of charge moment for negative cloud-to-ground lightning discharges, and 2060 Ckm and 2160 Ckm for positive cloud-to-ground lightning discharges.

Sentman et al. [2008b] investigated, using plasmachemical simulations, the chemical response of the mesosphere (at 70 km of altitude) to the passage of a sprite streamer with $E_{max} = 5 E_k$, where E_k is the breakdown field of air. The results by Sentman et al. [2008b] showed strong increases in practically every relevant ambient chemical species. Particularly, the NO density presented a fractional enhancement of about 75% within the streamer channel. A comprehensive study of the kinetics of air plasmas under the influence of sprites was also presented by Gordillo-Vázquez [2008] where he studied the evolution of 77 chemical species for three different altitudes in the mesosphere subjected to an impulsive electric discharge similar to that of sprite streamers and including

the influence of water. Among other features, the model by Gordillo-Vázquez [2008] predicted local NO density enhancement for the three studied altitudes.

On the other hand, spectroscopic studies of TLEs started in the mid 1990s, when the simultaneous works by Mende et al. [1995] and Hampton et al. [1996] provided the first spectroscopic studies of the red N₂ first positive group (1PG) sprite optical emissions at standard video rate (40 fps) in the 550 nm - 840 nm spectral range at low (between 10 nm and 6 nm) spectral resolutions. In a paper published in 2001, Wescott et al. [2001] used a narrowband (1.25 nm) filter to measure the N₂⁺ first negative group (1NG) (0,1) band emission at 427.8 nm, which provided the first direct evidence for the ionization of blue starters and blue jets reaching a maximum altitude of about 40 km. In 2002, Morrill et al. [2002] also reported aircraft UV observations of the N₂⁺ 1NG (0,1) band at 427.8 nm and N₂ 2PG (0,0) band at 337.0 nm from sprites. The 1NG/2PG intensity ratios measured by Morrill et al. [2002] showed two distinct regions, above and below 55 km. They suggested a relative enhancement of ion emission below 55 km (region of sprite “tendrils”) based on high speed (1000 fps) video recordings by Moudry et al. [2002] showing that while sprite “tendrils” emissions last for ~ 1 ms, sprite “body” emissions occur during a longer time gap of ~ 10 ms and, as reported by Morrill et al. [2002], these time scales are consistent with ionization taking place during short times (~ 1 ms) at 40 - 55 km [Armstrong et al., 1998, Suszcynsky et al., 1998, Armstrong et al., 2000] and with longer neutral emissions dominating above 55 km [Morrill et al., 2002]. So, depending on the altitude, the species responsible for the TLE optical emissions change from being mostly excited neutrals (N₂(B³Π_g) and N₂(C³Π_u) for higher altitudes (55 km up to 85 km) to a balance at lower heights (55 km and below) between the emissions from excited neutrals (mainly N₂(C³Π_u)) and excited ions (N₂⁺(B²Σ_u⁺)).

The rotational temperature derived from the optical emissions produced by an excited electronic state of a diatomic molecule is a correct measurement of the gas temperature only if the rotational distribution of a given electronically excited state is thermalized, that is, if it follows a Boltzmann distribution of rotational levels of the ground electronic state. The latter occurs when the characteristic rotation-translation relaxation time is much smaller than the characteristic time of the primary deexcitation process (the radiative lifetime at sufficiently low pressure or the collisional quenching time at higher pressures [Lavrov et al., 2003]). The radiative lifetime of the highest

2. SPRITE HALOS

vibrational level ($v = 12$) of $N_2(B^3\Pi_g)$ is around $4 \mu\text{s}$ and the corresponding values of $v = 3, 2, 1,$ and 0 of $N_2(B^3\Pi_g)$ are, respectively, about $7.3, 8.5, 9.7$ and $12.1 \mu\text{s}$. On the other hand, the radiative lifetimes of $N_2^+(B^2\Sigma_u^+)$ and $N_2(C^3\Pi_u)$ are 60 ns and 40 ns , respectively. Assuming that $2 - 3$ collisions are usually enough to thermalize the rotational distributions of $N_2(B^3\Pi_g)$, $N_2(C^3\Pi_u)$ and $N_2^+(B^2\Sigma_u^+)$, we can determine the pressure dependent characteristic rotation-translation relaxation time of N_2 [Biloiu et al., 2007]. Therefore, due to these differences in radiative lifetimes, the low pressure (high altitude) limit for achieving thermalization (assuming $T_{gas} = 220 \text{ K}$) of the rotational manifold of the $N_2(B^3\Pi_g)$ changes with vibrational level. The highest altitude limit is in fact associated only with the $v' = 0$. Therefore, for the $(0, v'')$ bands of the $N_2(B^3\Pi_g \rightarrow A^3\Sigma_u^+)$ transition (N_2 1PG) it has a value around $\simeq 75 \text{ km}$ (0.03 mbar), whereas the highest altitude limit is $\simeq 68 \text{ km}$ (0.08 mbar) for the $(12, v'')$ bands of the N_2 1PG, 60 km (0.70 mbar) for $N_2^+(B^2\Sigma_u^+)$ and it is 50 km (1 mbar) for $N_2(C^3\Pi_u)$.

On the other hand, quenching rate coefficients of $N_2(B^3\Pi_g)$ by N_2 are $(1-8) \times 10^{-11} \text{ cm}^3 \text{ s}^{-1}$ for $v = 0 - 12$ [Piper, 1988]. Then, for the 0.03 mbar lowest pressure limit ($\simeq 75 \text{ km}$ altitude), the characteristic time of the quenching process, which is the other channel that competes with the deactivation of the $N_2(B^3\Pi_g)$ state, is roughly one order of magnitude longer than rotational-translational relaxation time. As we decrease in altitude, collisional (quenching) deactivation tends to dominate over radiative decay of $N_2(B^3\Pi_g)$, $N_2^+(B^2\Sigma_u^+)$ and $N_2(C^3\Pi_u)$. The quenching heights (h_q) indicate the altitudes above which quenching is negligible, while below h_q collisional deactivation begins to be severe. The values of h_q for $N_2(B^3\Pi_g)$, $N_2^+(B^2\Sigma_u^+)$ and $N_2(C^3\Pi_u)$ are around 53 km , 48 km and 30 km , respectively [Vallance, 1974]. For sufficiently high pressures (when quenching dominates), the rotational temperatures derived from surviving $N_2(B^3\Pi_g)$, $N_2^+(B^2\Sigma_u^+)$ or $N_2(C^3\Pi_u)$ optical emissions from some TLEs (like blue jets and/or giant blue jets) below h_q can only be considered reliable if collisional quenching times (τ_q) remain longer than rotational-translational relaxation times. The previous considerations can be useful as an indication of the emitting species in TLEs that could be tracked to determine the rotational (gas) temperature by spectroscopic means at different altitudes.

In the sprite halo kinetic model developed in section 2.2, we have calculated the variation of the concentrations of a large number of species under the influence of halos by self-consistently calculating electric field profiles and non equilibrium air plasma

kinetics (including the solution of the Boltzmann equation) for altitudes between 50 km and 85 km in the mesosphere.

In section 2.4 we present three main scientific goals: (a) To test hollow cathode (HC) air discharges as laboratory analog discharges of TLEs; (b) to test and compare three different spectroscopic techniques to quantify the rotational (gas) temperature in air discharges with the aim to use them in TLE spectral diagnosis and, (c) to test the capabilities of a recently inhouse developed field instrument called GRANada Sprite Spectrograph and Polarimeter (GRASSP), with a nominal spectral resolution of 0.45 nm, that we will use for TLE spectroscopic surveys in Europe.

We test three different methods of gas temperature determination that employ (a) the rotational R - branch ($\Delta J = +1$) of the vibrational transition (0,0) of the first negative system of $N_2^+(B^2\Sigma_u^+ \rightarrow X^2\Sigma_g^+)$ when the resolution of the spectrograph is high enough (0.005 nm - 0.05 nm) to resolve the rotational structure (this is the so called Boltzmann plot method [Herzberg, 1950]), (b) a method proposed by Simek and DeBenedictis [1995] based on the analysis of several peaks appearing in low lying vibrational transitions, specifically (3,0), (2,0), (1,0) and (0,0), of the first positive group of $N_2(B^3\Pi_g \rightarrow A^3\Sigma_u^+)$, or $N_2(B^3\Pi_g)$ 1PG, that can be used when medium (0.1 nm - 0.5 nm) resolution spectrographs are available, and (c) a method based on the numerical fitting of synthetic spectrum to the observed (measured) spectrum of the envelope of selected (v' , v'') bands of the $N_2(B^3\Pi_g)$ 1PG recorded with medium (0.1 nm - 0.5 nm) resolution spectrographs.

The spectra recorded in the laboratory will be used as a test for the GRANada Sprite Spectrograph and Polarimeter (GRASSP) instrument recently developed in our group in order to start spectroscopic field campaigns of TLEs in Spain as ground support to the Atmosphere Space Interaction Monitor (ASIM) mission of ESA and to the TARANIS mission of CNES, to be launched in June 2016 and 2017, respectively. In this sense, the spectra (corrected by instrument spectral response) of a 0.2 mbar air commercial discharge lamp taken by GRASSP will be compared with the spectra of air discharges produced at similar (0.23 mbar) pressure within DC hollow cathode reactors recorded by laboratory commercial spectrographs. After the gas temperature is obtained, we will be able to extract the vibrational distribution function (VDF) of $N_2(B^3\Pi_g)$ by fitting a synthetic spectrum of the $N_2(B^3\Pi_g)$ 1PG to the recorded/observed spectrum at low resolution (2 nm). The latter will be used to obtain partial ($1 \leq v \leq 7$) VDFs

2. SPRITE HALOS

of $N_2(B^3\Pi_g)$ in air plasmas produced in laboratory DC hollow cathode discharges (0.1 mbar - 2 mbar) that will be compared with the experimental $N_2(B^3\Pi_g)$ VDF in sprites derived by Bucselá et al. [2003] at 53 km ($\simeq 1$ mbar) and Kanmae et al. [2007] at 53 km and with theoretical predictions of $N_2(B^3\Pi_g)$ VDF in halos and sprites [Gordillo-Vázquez, 2008], [Gordillo-Vázquez, 2010, Luque and Gordillo-Vázquez, 2011, Gordillo-Vázquez et al., 2011, 2012]. Previous experimental and modeling works on the kinetics and vibrational level populations of N_2 triplet states were done to investigate N_2 emissions in low altitude auroras [Cartwright, 1978, Morrill and Benesch, 1996] and N_2 afterglow discharges [Piper, 1988, 1989].

2.2 Model

2.2.1 Model description

Generally, a halo has a convex, saucer-like shape, with its center descending to lower altitudes than its borders. Here we are neglecting this curvature and assuming instead a perfectly planar geometry that reduces the problem to one dimension. Furthermore, as discussed below, in 1D the total electric current conservation allows us to avoid dealing explicitly with space charges and the conduction current and, consequently, we can integrate the equations independently at each altitude. Hence the one-dimensional problem is further reduced to a series of zero-dimensional problems. The two main drawbacks of this computational simplification are that (a) we underestimate the peak electric fields at the center of the halo and (b) a planar model does not allow the formation and propagation of filamentary structures (streamers). Point (a) was discussed by Luque and Gordillo-Vázquez [2012], where they compared one-dimensional and two-dimensional results and showed that neglecting the enhancement of the electric field due to the curvature of the halo did not introduce qualitative changes. Point (b) limits the validity of the one-dimensional approach to high-altitudes and must be kept in mind in discussing the results that we present below. The kinetic model used here is an upgrade of the model by Gordillo-Vázquez [2008, 2010] (Appendix E), where we now use more than 80 species (neutral and excited ones) and over 800 chemical processes (excluding photochemical processes) including electron impact ionization and excitation of atomic and molecular species, whose rates depend on the EEDF (electron energy distribution

function) as well as processes involving vibrational excitation exchange, vibrational-vibrational (VV)-like and vibrational-translational (VT)-like. All these processes are shown in detail in one of the appendices included as supplementary material to this thesis.

The kinetic model solves the statistical balance equations

$$\frac{\partial n_i}{\partial t} = G_i - L_i, \quad (2.1)$$

which represents a set of differential equations, one for each species i (electrons, ions as well as excited and ground-state atoms and molecules) present in the air plasma. Equation (2.1) provides the evolution of the concentrations of chemical species (n_i) over time as a result of the difference between the rates of the processes that contribute to the generation (G_i) and loss (L_i) of species i . The balance equations (2.1) are coupled and solved together with the steady-state Boltzmann transport equation. In its general form, the Boltzmann equation reads

$$\left(\frac{\partial}{\partial t} + \frac{\mathbf{F}}{m} \cdot \nabla_{\mathbf{v}} + \mathbf{v} \cdot \nabla_{\mathbf{r}} \right) f(\mathbf{v}, \mathbf{r}, t) = \left(\frac{\partial f}{\partial t} \right)_{collisions}, \quad (2.2)$$

where $f(\mathbf{r}, \mathbf{v}, t)$ is the velocity distribution function of free electrons in the plasma at time t and velocity \mathbf{v} . Considering both steady state and spatial uniformity conditions, we can cancel the first and third terms in the sum on the left hand side. If we want to find the nonequilibrium $f(\mathbf{r}, \mathbf{v}, t)$ within an electric field, the previous equation will be

$$\frac{e\mathbf{E}(t)}{m_e} \cdot \nabla_{\mathbf{v}} f(\mathbf{v}, t) = \left(\frac{\partial f}{\partial t} \right)_{collisions}, \quad (2.3)$$

where the symbols e , m_e , $\mathbf{E}(t)$ and $\nabla_{\mathbf{v}}$ represent the electric charge and mass of the electron, the electric field in the mesosphere generated by a lightning discharge and the velocity gradient operator, respectively. The right hand side of equation (2.2) represents the variation rate of $f(\mathbf{v}, t)$ due to different collisions between electrons and heavy species including neutral molecules and atoms as well as ions. The electron-electron collisions are not taken into account due to low electron density, which makes the Coulomb interactions negligible. Inclusion in the model of the Boltzmann equation is a great advantage because, through this, we can calculate the electron velocity or energy distribution function and therefore the reaction rates of the processes driven by direct electron impact. We also impose as a condition the macroscopic electrical

2. SPRITE HALOS

neutrality of the plasma, that is, the net balance of electric charges in the plasma is zero

$$\sum_j n_j^+ = n_e + \sum_k n_k^-, \quad (2.4)$$

where n_j^+ , n_k^- and n_e represent, respectively, the concentrations of positive and negative ions and electrons in the plasma. In this occasion the model simulations were performed with the ZDPlasKin software developed by Pancheshnyi et al. [2008] that incorporates the BOLSIG+ solver to calculate the EEDF (Hagelaar and Pitchford [2005]). Although ZDPlasKin is a 0-dimensional solver, we have slightly modified it by including an electrostatic electric field equation (see equation (2.5) below) that is self-consistently solved with equations (2.1)-(2.4) in a range of altitudes covering the Earth mesosphere.

The simulation process basically consists of two stages. The first step is what we have called “relaxation” of the system of equations. Following Sentman et al. [2008b], in order to isolate the impact of a lightning-generated electric field, we first look for the chemical equilibrium of our kinetic scheme consistent with the ambient electron density profile. In this case we have chosen the ambient electron density estimated by Hu et al. [2007]. To do so, we searched, at each altitude, for the value of the cosmic-ray flux that, once the equations are evolved with a reduced electric field $E/N \sim 0$ for a long time $t \sim 10^6$ s, match the desired electron density. The dry air initial densities used at each altitude and under nighttime conditions, are taken from the Whole Atmosphere Community Climate Model (WACCM) for midlatitudes and are shown in Figure 2.1. Figures 2.2 and 2.3 show the altitude variation of the initial densities used in our model, where the dashed lines are the initial densities extracted from the Whole Atmosphere Community Climate Model (used to initiate the relaxation stage) and the solid lines are the densities of the same species obtained after the model relaxation stage. The densities obtained after the relaxation act as initial conditions for the halo simulations. The ambient electron density concentration n_e is shown in Figure 2.4 and is taken from Hu et al. [2007].

Figures 2.5, 2.6 and 2.7 show the altitude variation of the ambient initial densities of the negative, positive and neutral excited species, respectively. These initial densities

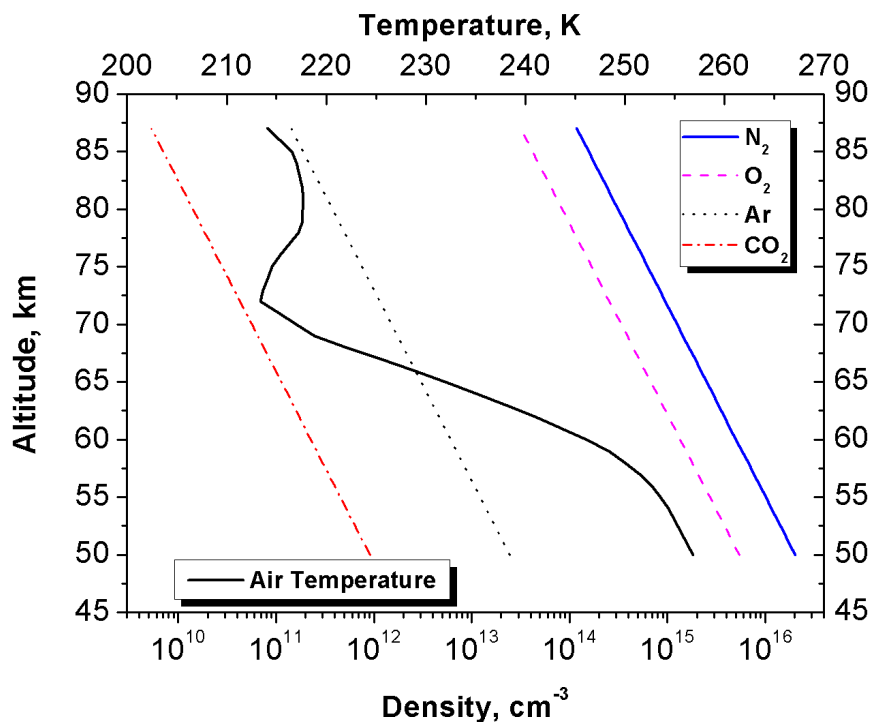


Figure 2.1: Altitude variation of the initial ambient densities of N_2 (solid blue line), O_2 (dashed purple line), Ar (dotted black line) and CO_2 (dashed dotted red line) taken from the Whole Atmosphere Community Climate Model (WACCM) under the nighttime conditions. The solid black line is the gas temperature variation with altitude taken from WACCM.

were obtained after the relaxation stage. We do not show the ambient initial density of other species because their initial density values are negligible.

Once the system of equations is relaxed, we implement the effect of -CG and +CG lightning strikes in the range of altitudes considered (50-85 km). To do this, we assume triangular shaped lightning current moments with different peak values as shown in Figure 2.8 with the corresponding charge moment changes shown in Figure 2.9.

Following Luque and Gordillo-Vázquez [2012], our model calculates the electric field E in the mesosphere associated with lightning by self-consistently solving equations (2.1), (2.3) and (2.4) coupled with

$$\epsilon_0 \frac{dE}{dt} = -\sigma E + J_T(t), \quad (2.5)$$

where σ is the electric conductivity and $J_T(t)$ is the total current given by Luque

2. SPRITE HALOS

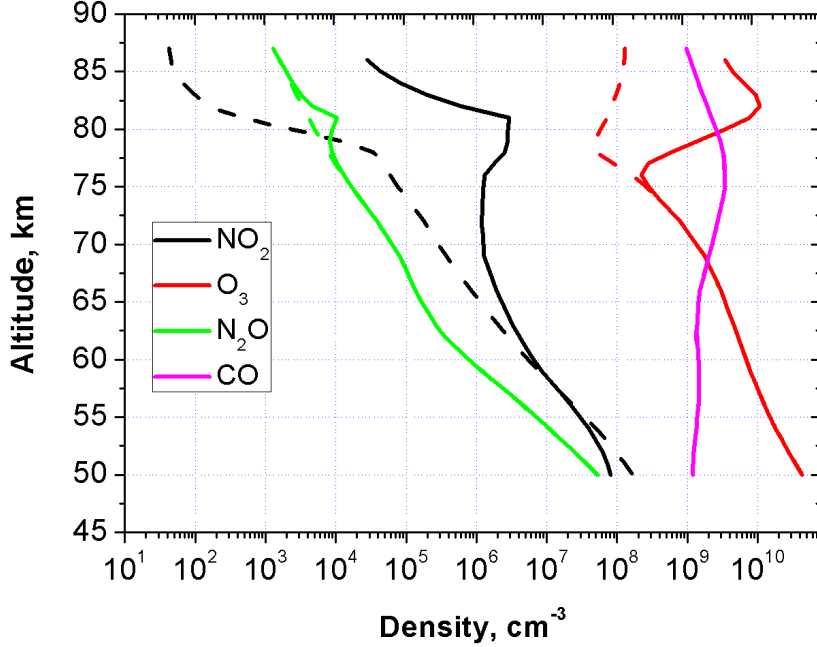


Figure 2.2: Altitude variation of the initial ambient densities where the dashed lines are the ones (before the relaxation stage) taken from WACCM, and the solid lines are the initial ambient densities obtained after the relaxation stage.

and Gordillo-Vázquez [2012] as

$$J_T(t) = \epsilon_0 \frac{\partial E_p}{\partial t} = \frac{hI(t)}{\pi} \left(\frac{1}{z_0^3} + \frac{1}{z_1^3} \right), \quad (2.6)$$

where E_p is the electric field created by the electric dipole $p = 2hQ$ (the cloud charge and its image with respect to the conducting surface of the Earth), which is approximately homogeneous in a layer over the thunderstorm between $z_0 = 60$ km and $z_1 = 80$ km, and where $hI(t)$ is the imposed current moment, h being the cloud altitude and $I(t)$ the lightning electric current liberated to the ground from the cloud. A more extended derivation of equation (2.6) is shown by Luque and Gordillo-Vázquez [2012]. The space charge is considered in the model in an implicit way through equation (2.5). This equation can be easily derived from the charge conservation equation

$$\frac{\partial q}{\partial t} = -\nabla \cdot (\sigma \mathbf{E}), \quad (2.7)$$

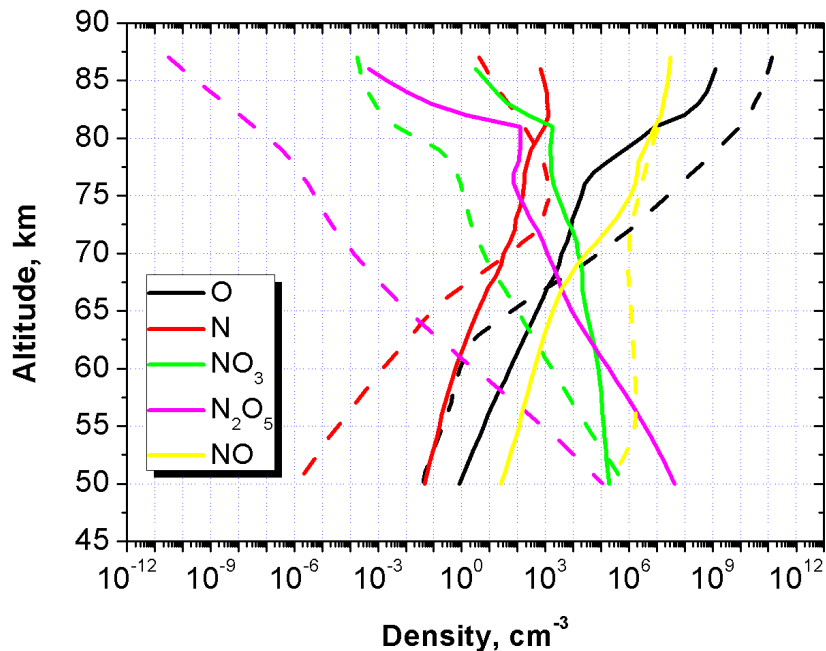


Figure 2.3: Altitude variation of the initial ambient densities where the dashed lines are the initial (before the relaxation stage) ambient densities extracted from WACCM, and the solid lines are the initial ambient densities obtained after the relaxation stage.

where σ is the local conductivity, and the Poisson equation

$$q = \epsilon_0 \nabla \cdot \mathbf{E}. \quad (2.8)$$

If we assume a planar geometry (1-D model) in equations (2.7) and (2.8), and we differentiate equation (2.8) with respect to time we obtain

$$\frac{\partial q}{\partial t} = \epsilon_0 \frac{\partial}{\partial t} \frac{\partial E}{\partial z}. \quad (2.9)$$

Combining equations (2.7) and (2.9), we obtain

$$\frac{\partial}{\partial z} \left[\epsilon_0 \frac{\partial E}{\partial t} + \sigma E \right] = \frac{\partial}{\partial z} J_T(t) = 0, \quad (2.10)$$

where the first term of the left hand side is the displacement current, and the second term of the sum is the conduction current. Note that equation (2.5) is coupled to the

2. SPRITE HALOS

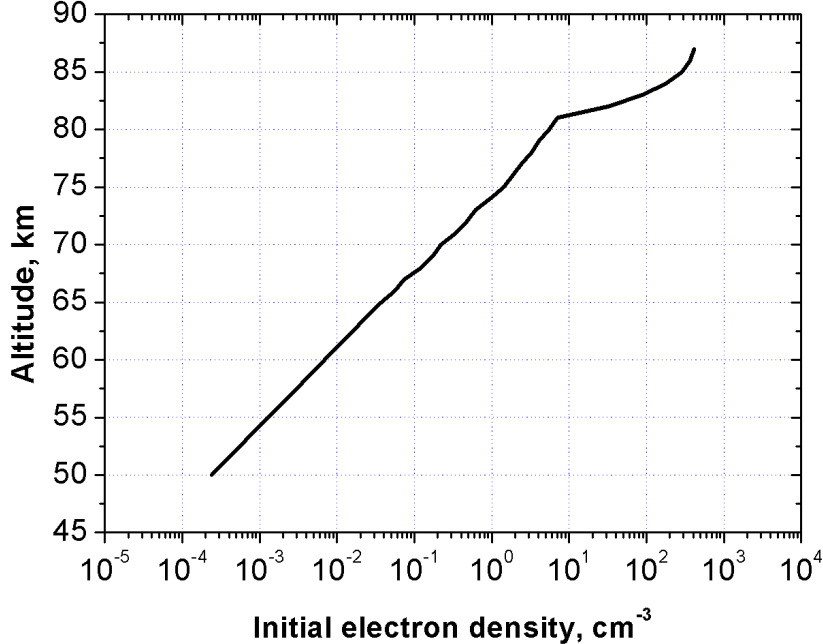


Figure 2.4: Variation of the initial ambient electron density with altitude taken from Hu et al. [2007].

set of chemical balance equations (2.1) through the ambient electric conductivity σ which is proportional to the electron density:

$$\sigma = en_e\mu(E/N), \quad (2.11)$$

where μ is the electron mobility extracted from the solution of equation (2.3). The electron mobility is calculated internally by ZDPlasKin in each timestep. It is also worth mentioning that equation (2.5) relies on the assumption of a perfectly planar geometry and hence remains valid only as long as the horizontal divergence of the electric field can be neglected. This assumption breaks down at the onset of filamentary structures such as sprite streamers; these have short characteristic horizontal length scales on the order of tens of meters and therefore electric fields with non-negligible horizontal components. Although our results are reliable only as long as sprites are not present, in order to avoid introducing a criterium for sprite inception, we have extended our calculations to low altitudes and high CMC, a situation where sprite emergence is

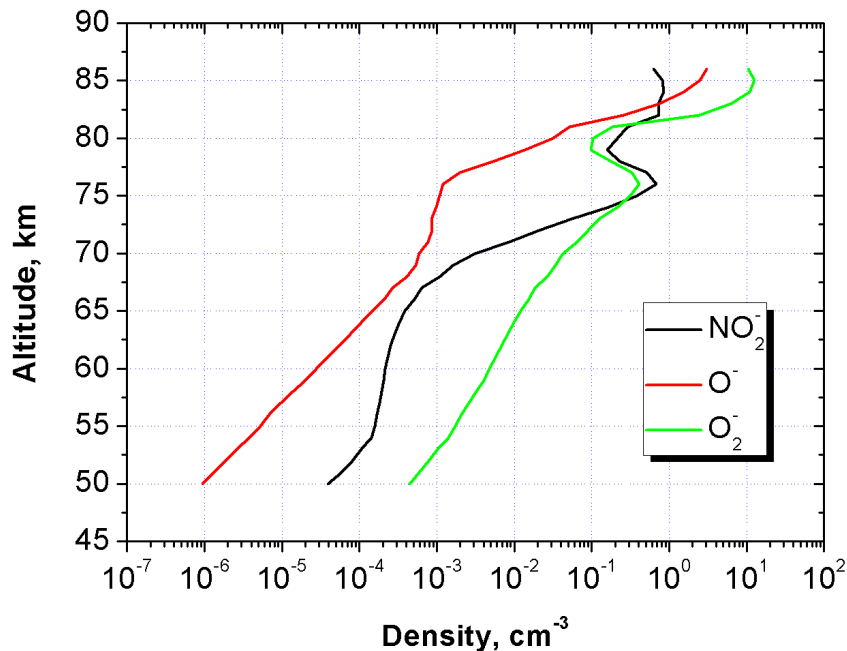


Figure 2.5: Altitude variation of the negatively charged species considered in our model, as obtained after the relaxation stage.

likely. For a discussion of sprite inception and its relation to our model, the reader is directed to the supplementary material of Luque and Gordillo-Vázquez [2012].

2.3 Results and discussion

We present and discuss here the chemical and electrical influence of lightning in the terrestrial mesosphere in the particular case that lightning produce halos, a type of TLE characterized by diffuse optical emissions. We have considered different peak values for the lightning current moments. In particular, we have distinguished between current moments with and without a continuing current signal. While -CG are usually associated with current moments without continuing current, +CG current moment almost always exhibit a continuous low value current (see Figure 2.8) connected to the occurrence of delayed sprites [Cummer and Füllekrug, 2001]. In the case of +CG we will also discuss the results of our kinetic simulations using measurements of lightning current moments published by Gamerota et al. [2011] (see Figure 2.10).

2. SPRITE HALOS

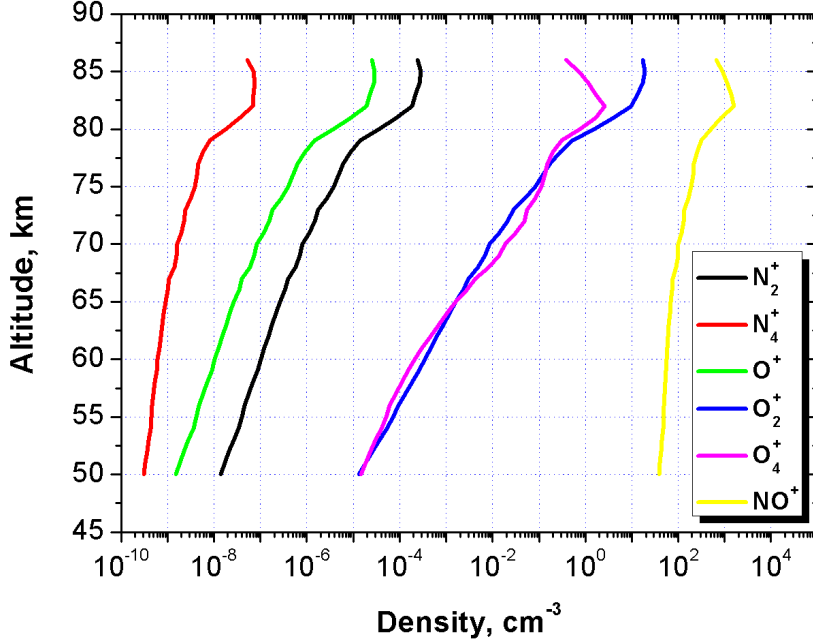


Figure 2.6: Altitude variation of the positively charged species considered in our model, as obtained after the relaxation stage.

The present simulations were performed by using triangular current moment signals of 2 ms duration, with the peak intensity occurring at $\tau = 1$ ms and parameterizing the maximum current moment peak with the values of 100 kAkm and 200 kAkm and by disregarding the impact of low value continuous current for -CGs (see Figure 2.8). In a similar way, two signals are considered for the case of a +CG with the peak intensity occurring at $\tau = 1$ ms with a constant continuous current of 20 kAkm that lasts up to 100 ms, and parameterizing the +CG maximum current moment peak with the values of 100 kAkm and 200 kAkm. We have assumed that the +CG low value continuous current is negligible after 100 ms (see Figure 2.8). The maximum current moment peak values of 100 kAkm and 200 kAkm are selected following Williams et al. [2012] showing statistics on the maximum lightning peak currents of -CG and +CG producing sprite halos (see Figures 5, 7 and 8 in Williams et al. [2012]).

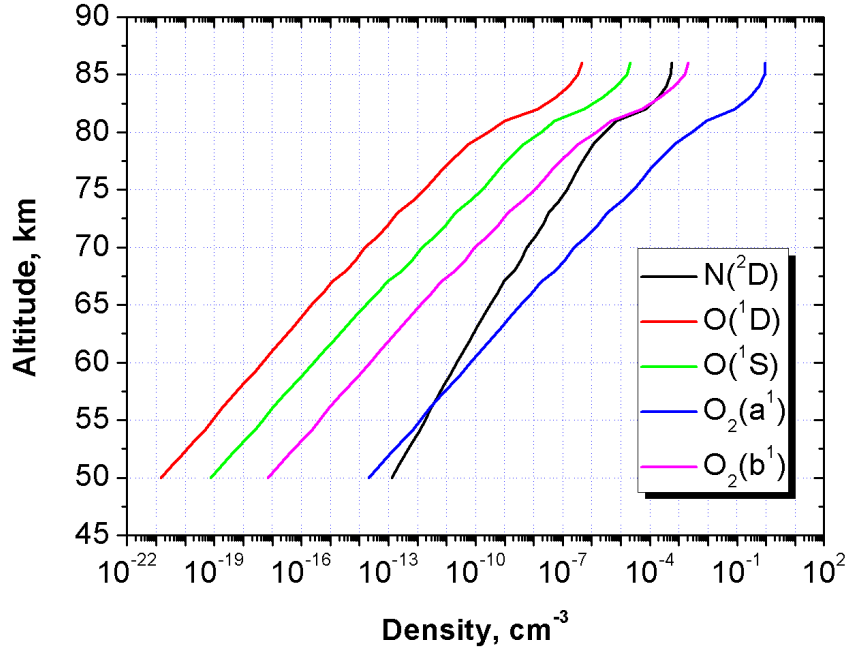


Figure 2.7: Altitude variation of the neutral excited species considered in our model, as obtained after the relaxation stage.

2.3.1 Reduced electric field

When we introduce the current intensity signals (hI) in equation (2.6) and solve equations (2.1)-(2.5) in a self-consistent way, we obtain the reduced electric field for the cases considered. We can see in Figure 3.3 that the largest increase of reduced electric field coincides with the peak current moment. Moreover, the duration of the electric field closely follows that of the current moment. As it is shown in Figures 3.3a, 3.3b and 3.3d for the realistic and 100 kAkm +CG and -CG cases, the field at the time (1 ms) of the current peak is just above 40 Td between 75 km and 82 km. For the cases of 200 kAkm (+CG and -CG) (Figures 3.3c and 3.3e) the reduced electric field reaches 100 Td between 80 km and 81 km at the time of the peak current. In the cases of +CG (Figures 3.3b and 3.3c) we can see that the 20 kAkm continuous current plays an important role in the extension of the reduced electric field up to 200 ms with values ranging from 100 Td (~ 80 km) to 60 Td (~ 55 km). It is important to note that, in all the cases studied, the E/N values remain under sub-breakdown (< 120 Td) levels

2. SPRITE HALOS

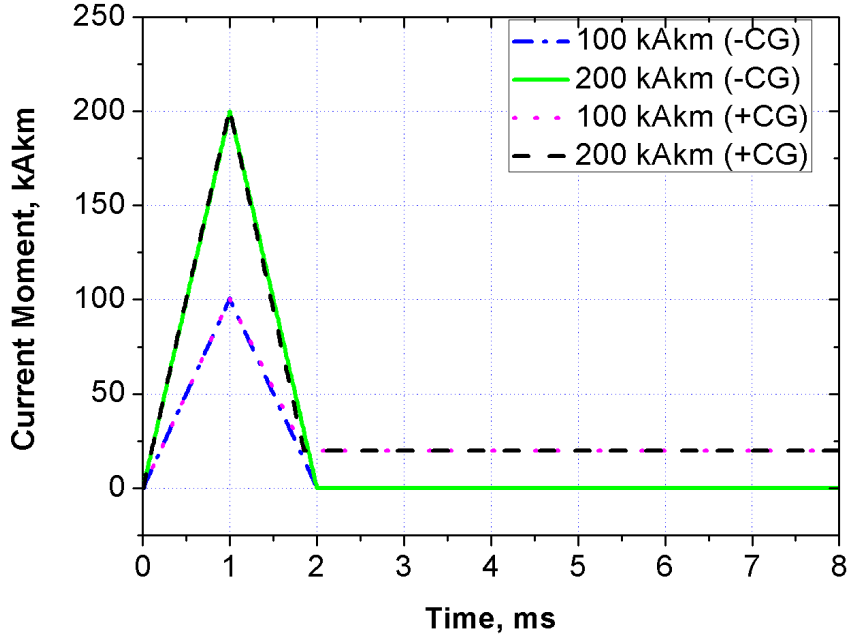


Figure 2.8: Time dependence of the various lightning electrical signals implemented in the model. All signals are triangular with 2 ms width. -CG lightnings (solid green line for 200 kAkm of current peak and dashed dotted blue line for 100 kAkm of current peak) have a negligible current moment beyond 2 ms. +CG lightnings (dashed black line for 200 kAkm of current peak and dotted violet line for 100 kAkm of current peak) have a continuous current moment of 20 kAkm from 2 ms to 100 ms. Beyond 100 ms the current moment is considered negligible.

(Luque and Gordillo-Vázquez [2012] and Liu [2012]).

Regarding the lightning intensity waveform measured by Gamerota et al. [2011], we can see in Figure 3.3a that the E/N altitude-time variation is similar to that of the case of 100 kAkm of the +CG (see Figure 3.3b). This might be due to the fact that, although the current signals are not identical, they are very close in their peak and continuous current values as well as in their duration.

The behaviour of the reduced electric field is strongly coupled to the evolution of the electron density through equation (2.5) and can be understood qualitatively in simple terms as the counteraction of field increases due to the ground current and decreases due to Maxwell relaxation. Above about 80 km, at the ionosphere's lower edge, the

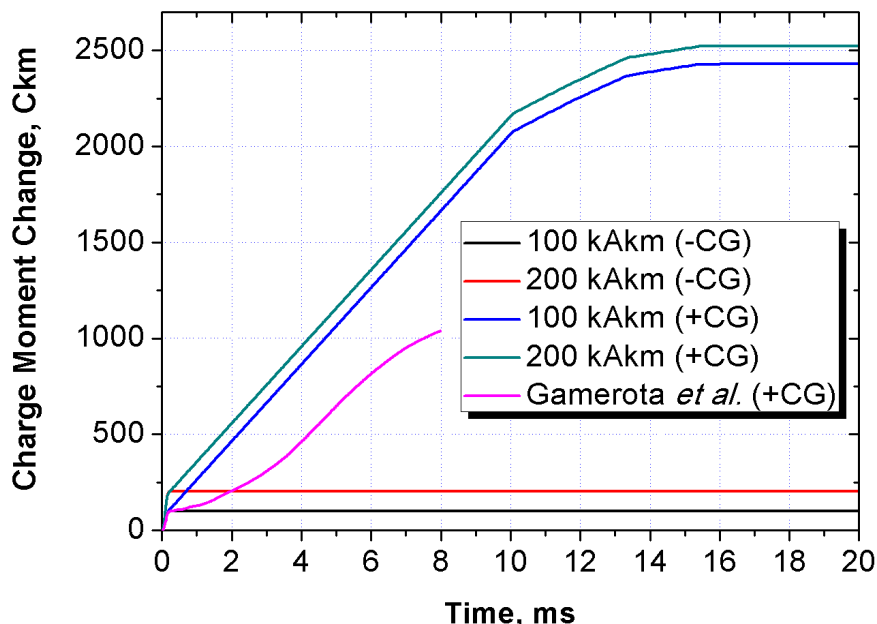


Figure 2.9: Time dependence of the charge moment change (CMC) for the different lightning electrical signals implemented in the model. -CG lightnings (solid red line for 200 kAkm of current peak and solid black line for 100 kAkm of current peak) have a negligible current moment beyond 2 ms (see Figure 2.8). +CG lightnings (solid green line for 200 kAkm of current peak and solid blue line for 100 kAkm of current peak) have a continuous current moment of 20 kAkm from 2 ms to 100 ms (see Figure 2.8). Beyond 100 ms the current moment is considered negligible. Finally, the solid pink line shows the charge moment change of a realistic +CG lightning measured by Gamerota et al. [2011].

relaxation is so fast that the electric field barely increases. At lower altitudes, the electrons are fewer and not so mobile so the electric field is allowed to increase. If the electron density remains low the electric field then simply decays after the ground-current pulse with the relaxation time of the unperturbed atmosphere, as seen in the tails of Figures 3.3b and 3.3c; their durations increase exponentially as the altitude decreases. On the other hand, if the electric field reaches the conventional breakdown threshold ($\simeq 120$ Td) or if it remains significant long enough for associative detachment to act, as in Figures 3.3a-3.3c, the electron density increases significantly. Then the relaxation time decreases correspondingly and produces the sharp decays shown in the figures. Below about 55 km the reduced field is lower due to a higher air density and

2. SPRITE HALOS

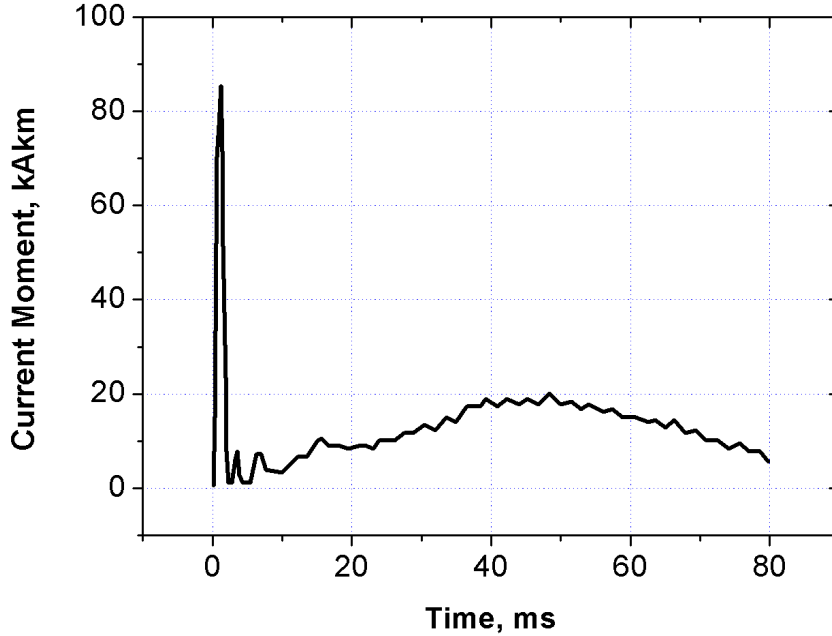


Figure 2.10: Time dependence of the measured (empirical) electrical signal used in the model, extracted from Gameraota et al. [2011], corresponding to a real +CG lightning discharge. The lightning discharge signal was obtained from ELF data recorded in Yucca Ridge Field Station (40.702N-105.031E) on July 3, 2008. The frequency range of the station covers from a few Hz up to 25 kHz. The authors do not specify the particular signal resolution used for these measurements.

hence does not significantly alter the electron density, keeping the decay time on the order of hundreds of seconds.

2.3.2 Negatively charged species

We discuss in this section the result shown in Figure 2.12-2.16 showing the behaviour of the electron density and negative ion concentrations. In the results presented in Figure 2.12b and Figure 2.12c, we can see similar profiles for the electron concentration as a function of the altitude both at 100 kAkm and 200 kAkm of peak current moments for the case of +CG lightnings. In addition, we see a small drop in the density of electrons at the time of the current peak followed by an abrupt increase which lasts up to 100 s at high altitudes (~ 78 km). As we descend in altitude, the increase in electron density

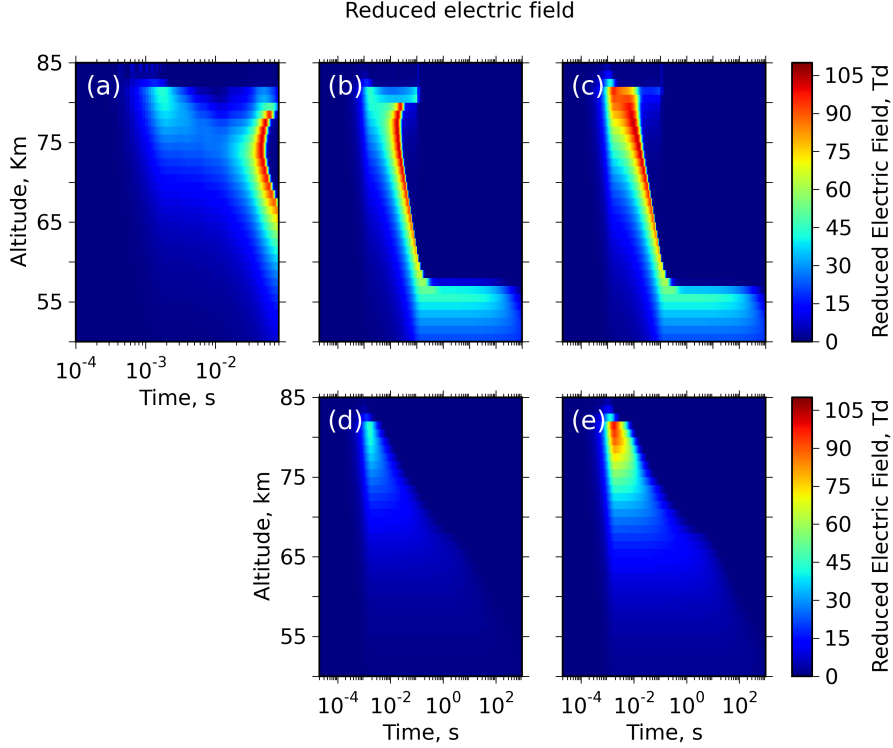
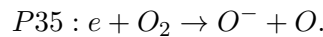


Figure 2.11: Altitude-time evolution of the reduced electric field due to cloud-to-ground lightnings with (a) realistic current moment, (b) 100 kAkm peak current moment and 20 kAkm continuous current moment, (c) 200 kAkm peak current moment and 20 kAkm continuous current moment, (d) 100 kAkm peak current moment and (e) 200 kAkm peak current moment.

occurs later in time and it lasts less. Below 53 km there is no noticeable variation in the electron density. The same (no variation) happens above 80 km due to the high ambient electron concentration (see Figure 2.4).

The small initial decrease in the electron concentration at the time of the current peak is due to dissociative attachment of O_2 by direct electron impact



The increase in the electron density just after the peak current is steeper as we descend in altitude. That is, at 75 km, the electron density increases by one order of magnitude while at 55 km the increase of the electron concentration is more than four orders of magnitude. For intermediate altitudes of 65 km, our model predicts

2. SPRITE HALOS

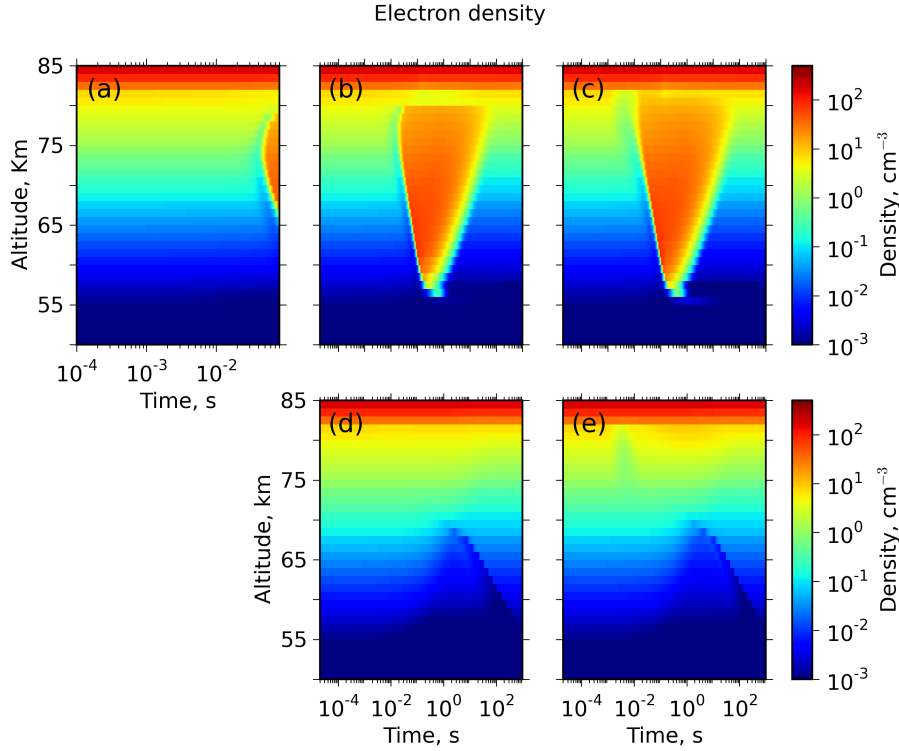
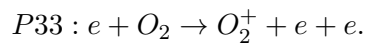
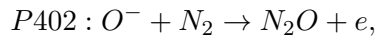


Figure 2.12: Altitude-time evolution of the electron density due to cloud-to-ground lightnings with (a) realistic current moment, (b) 100 kAkm peak current moment and 20 kAkm continuous current moment, (c) 200 kAkm peak current moment and 20 kAkm continuous current moment, (d) 100 kAkm peak current moment and (e) 200 kAkm peak current moment.

n_e enhancements of more than three orders of magnitude. Regarding the mechanisms responsible for the growth of the electron density, we have found that the dominant processes are associative detachment of O^- by N_2 producing N_2O and electron impact ionization of O_2

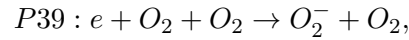
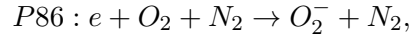


Note that the electron density is maintained at high values during the simulation mainly due to associative detachment of O^- by CO (P415) as long as the O^- concen-

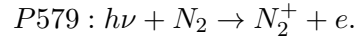
tration remains high (see Figures 2.13b and 2.13c).



The electron concentration begins to decrease between 1 second and 12 seconds after the parent lightning due to three-body electron attachment

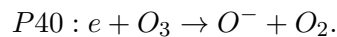


returning to its baseline ambient values controlled by the cosmic ray ionization of N_2 ,



The influence of associative detachment of O^- by N_2 producing N_2O and free electrons can be visualized in Figures 2.12b and 2.12c, where an increase of one order of magnitude can be seen in the electron concentration between 10 s and 100 s after the current peak of the parent lightning discharge. This late enhancement of the electron density has been proposed as the key responsible of delayed sprites (Luque and Gordillo-Vázquez [2012]).

Regarding -CG lightning, we can see in Figures 2.12d and 2.12e that the electron density does not exhibit substantial changes at the time of the peak current. However, when we use a peak current of 200 kAkm the model shows a factor 2 decrease in the electron density between 77 km and 81 km altitude and between 10^2 s and 10^3 s simulation time which is mainly due to dissociative attachment of O_2 by direct electron impact (P35) as reported very recently by Shao et al. [2013]. Moreover, 100 ms after the peak current, and between 67 km and 57 km, our model predicts a hole-like structure consisting in one order of magnitude decrease and subsequent increase in the density of electrons caused by electron impact O_3 dissociative attachment (see below). As we descend in altitude, the hole lasts longer (we have a reduction of one order of magnitude at 65 km). This reduction in the electron density is mainly caused by the dissociative attachment by ozone,

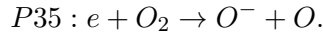


In the realistic case (see Figure 2.12a), we find the same behaviour for the electron density as the one already described for the case of +CG lightning (Figures 2.12b and

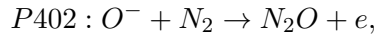
2. SPRITE HALOS

2.12c). The electron density decreases a factor 3 between 20 ms and 40 ms due to electron impact dissociative attachment of O_2 (P35) followed by an increase of more than one order of magnitude produced by the associative detachment of O^- by N_2 (P402) and electron impact ionization of O_2 (P33) and N_2 (P22). The electron density above 80 km and below 65 km does not exhibit noticeable changes.

The behaviour of the O^- concentration in the case of +CG lightnings (see Figures 2.13b and 2.13c) follows that of the electrons. At the time of the current peak (see Figure 2.13c), the density of O^- exhibits an abrupt increase (more than five orders of magnitude at its maximum located at 67 km) that gently descends to ambient values towards longer times or lower altitudes down to 53 km approximately. At mid altitudes (76 km), the increase in the concentration of O^- can be of up to four orders of magnitude during approximately 10 ms after the peak current and the mechanism responsible for this mid altitude O^- increase is



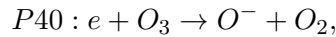
The processes responsible of returning the O^- density to its natural (ambient) values are associative detachment of O^- by N_2 producing N_2O as long as the reduced electric field is non zero (up to 100 ms)



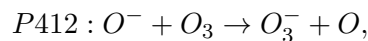
due to the detachment rate (P402) dependence with the electric field. When the reduced electric field goes back to zero (beyond 100 ms), associative detachment of O^- by CO producing CO_2 dominates



In addition, an increase of the O^- concentration is predicted at ionospheric altitudes (85 km) due to electron impact dissociative attachment by O_3



while the mechanisms that recover the ambient concentration of O^- are the ozone charge transfer (P412) and the associative detachment of O^- by O_3 (P407)



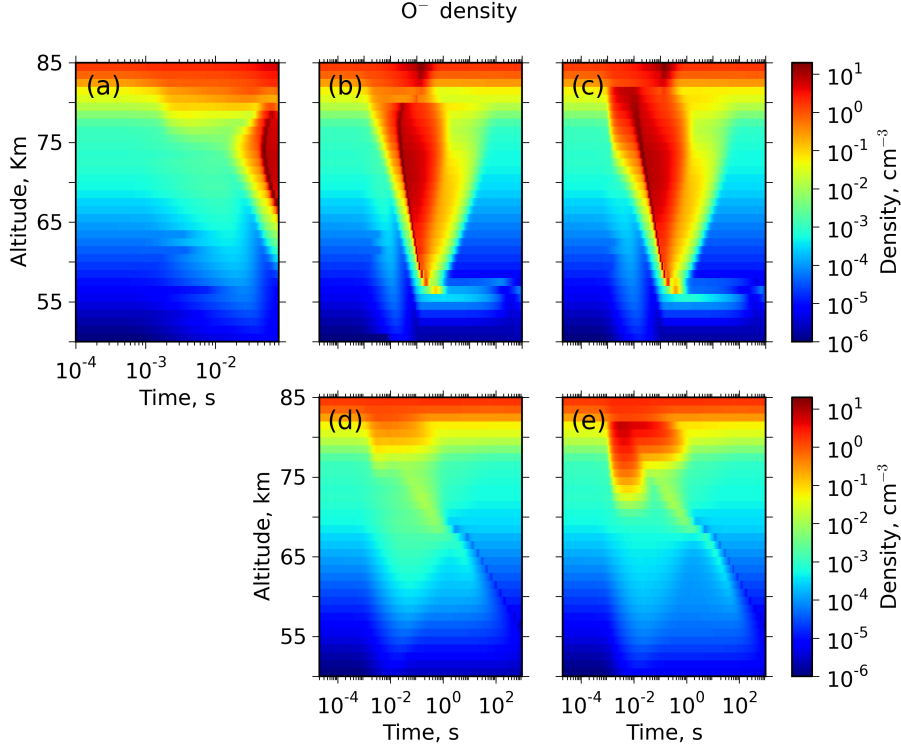
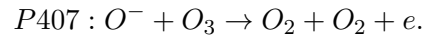


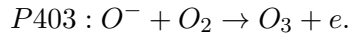
Figure 2.13: Altitude-time evolution of the O^- density due to cloud-to-ground lightnings with (a) realistic current moment, (b) 100 kAkm peak current moment and 20 kAkm continuous current moment, (c) 200 kAkm peak current moment and 20 kAkm continuous current moment, (d) 100 kAkm peak current moment and (e) 200 kAkm peak current moment.



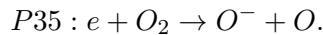
Unlike the cases of +CG lightning, where the evolution of the concentration of O^- does not depend on the peak current intensity but on the 20 kAkm continuous current, in the case of -CG lightning we have found a remarkable dependency with the peak current intensity (see Figures 2.13d and 2.13e). The O^- density shows an increase of almost an order of magnitude between 78 km and 81 km for the case of a -CG lightning with 100 kAkm of current peak (see Figure 2.13d). For the case of 200 kAkm current peak -CG lightnings, our model predicts a large increase of up to two orders of magnitude at 81 km (Figure 2.13e). For the latter case (e) of negative lightning, the behaviour of the O^- density exhibits the form of two lobes, one located between 77 km and 81 km that extends in time up to 100 ms after the current peak (see Figure 2.13e) and another one

2. SPRITE HALOS

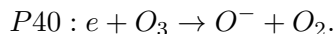
between 72 km and 81 km where the density of O^- increases in up to three orders of magnitude and whose duration does not exceed 40 ms after the current peak. The main mechanism underlying the production of O^- at the moment of the current peak in both -CG cases (100 kAkm and 200 kAkm) is the electron impact dissociative attachment of O_2 (P35) whereas the mechanism responsible for the O^- density relaxation after the current pulse are associative detachment by O_3 (P407) and O^- - O_3 charge transfer (P412) processes, together with associative detachment (P402) of O^- by N_2 for the 200 kAkm case. For intermediate altitudes (~ 76 km) and 200 kAkm of peak current (see Figure 2.13e), the production processes of O^- are the same as for higher altitudes. However, the O^- loss mechanisms are different, the most important being associative detachment of O^- by N_2 (P402) and by CO (P415). For low altitudes (between 53 km and 67 km) the density of O^- exhibits an increase that can be of about one order of magnitude at the moment of the peak current and that lasts for approximately 100 seconds (see Figure 2.14) mainly due to the action of electron impact O_3 dissociative attachment (P40). After 100 seconds, the concentration of O^- tends to its ambient values due to associative detachment of O^- by O_2 (P403),



For the realistic case (see Figure 2.13a) we found an O^- increase of more than four orders of magnitude located between 65 km and 79 km of altitude starting 30 ms after the current peak. This important increase of O^- is mainly due to electron impact dissociative attachment of O_2 (P35).



For lower altitudes, one can observe in Figure 2.13a a small increase of up to one order of magnitude in the density of O^- starting at approximately 4 ms after the current peak and caused by electron impact dissociative attachment of O_3 (P40)



We can see in Figures 2.15b and 2.15c, corresponding to the evolution of the concentration of the ion O_2^- under the action of +CG lightning, that there is a substantial

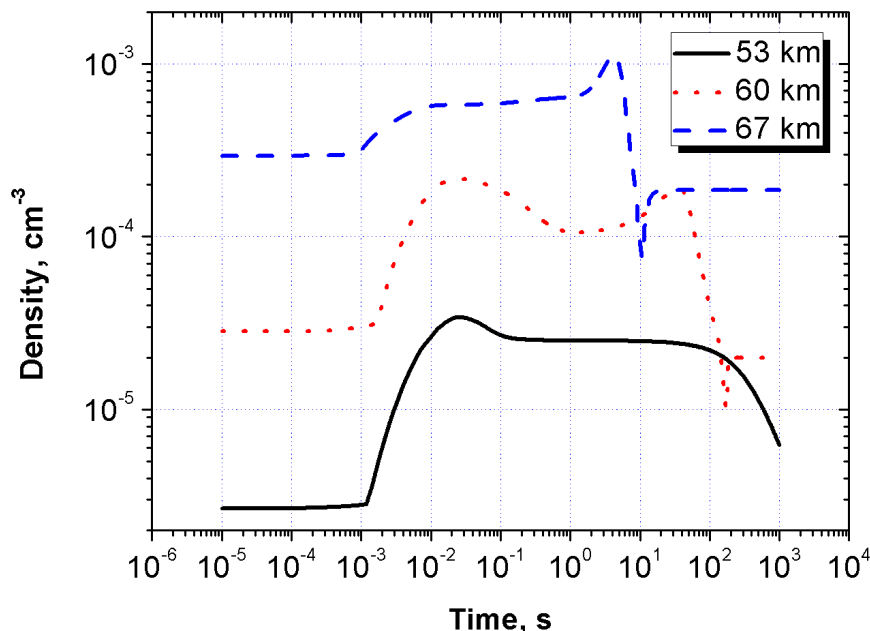
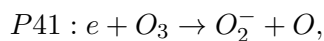


Figure 2.14: Altitude-dependent behaviour of the concentration of O^- under the conditions of a single sprite halo event generated by a -CG lightning with 200 kAkm peak current moment for three different altitudes. The dashed blue line is for an altitude of 67 km, the dotted red line indicates O^- density at 60 km and the solid black line corresponds to the case of an altitude of 53 km.

increase in the density of O_2^- about 100 ms after current peak. The one order of magnitude increase of O_2^- , shown between 83 km and 85 km, is due to electron impact dissociative attachment of O_3 (P41)



In addition, the transition region between 73 km and 78 km in Figures 2.15b and 2.15c where the increase of the concentration of O_2^- may be more than one order of magnitude is mainly caused by the aforementioned mechanism (P41). Below 78 km (down to almost 50 km altitude) higher increases in the density of O_2^- are predicted but during shorter times (see Figures 2.15b and 2.15c) as the altitude is lower. For example, at 63 km and for the case of 200 kAkm current peak (Figure 2.15c) we can see an increase of more than three orders of magnitude for more than one second.

2. SPRITE HALOS

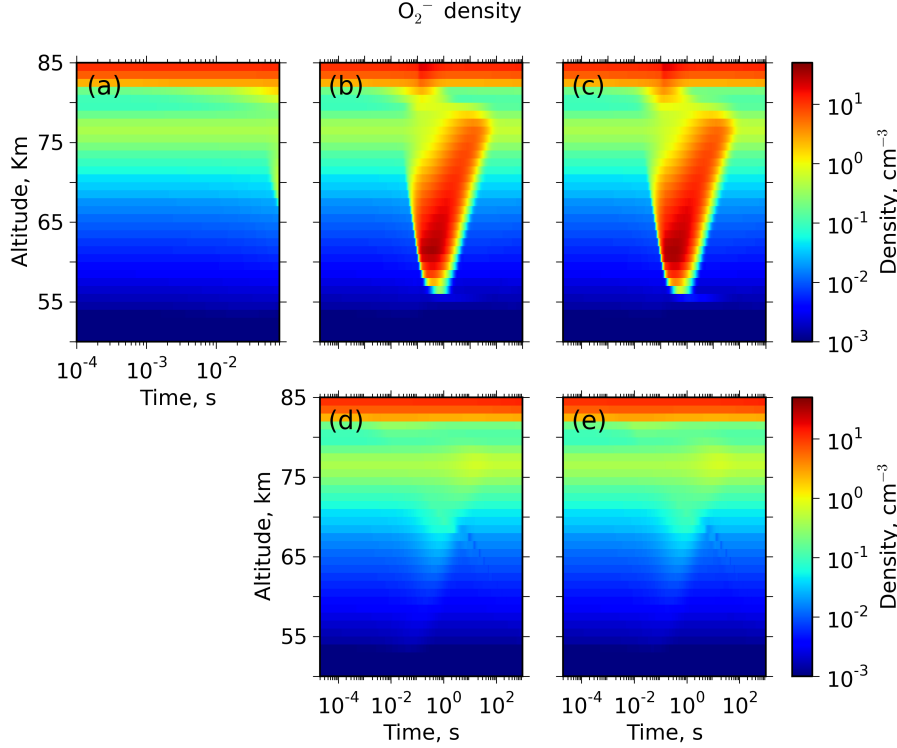
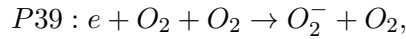
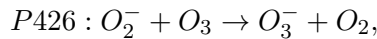


Figure 2.15: Altitude-time evolution of the O_2^- density due to cloud-to-ground lightnings with (a) realistic current moment, (b) 100 kAkm peak current moment and 20 kAkm continuous current moment, (c) 200 kAkm peak current moment and 20 kAkm continuous current moment, (d) 100 kAkm peak current moment and (e) 200 kAkm peak current moment.

However, at 53 km, the increase in the density of O_2^- is slightly larger than at 63 km while at 53 km the O_2^- enhancement lasts only 350 ms. The process responsible for this sudden increase in the O_2^- concentration is the electron impact dissociative attachment of O_3 (P41) and the O_2 three-body attachment



while

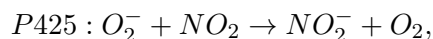


drives the O_2^- density back to its ambient values. For the cases of -CG lightning (see Figures 2.15d and 2.15e) there barely exists a variation in the density of O_2^- ions by a

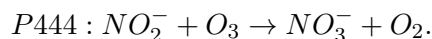
factor of 3 between 67 km and 70 km due to electron impact dissociative attachment of O_3 (P41).

For the realistic case (see Figure 2.15a) no significant changes in O_2^- density are noticeable since the time profile of the current moment used in the simulation (Gamerota et al. [2011]) only provides values up to 0.08 s.

Finally, for the NO_2^- ion, our model predicts an enhancement of the NO_2^- density above two orders of magnitude that remains for about 20 s only in the case of +CG lightning (see Figures 2.16b and 2.16c), and 100 ms after the current peak between 73 km and 51 km. This enhancement in the NO_2^- density is caused by



and the loss of NO_2^- is due to



In the realistic case (see Figure 2.16a) no changes are predicted as in the case of the O_2^- ion.

2.3.3 Positively charged species

We now present and discuss the results for the most representative positive ions. Out of the 14 positive ions included in the model we have chosen to show those with the greatest variability. We begin by analyzing the dependence on time and altitude of O_2^+ ions. We see in Figures 2.17b and 2.17c an abrupt increase in the concentration of O_2^+ ions during the 20 kAkm continuous current moment signal of +CG lightnings. This increase appears later in time and more intensely as we descend in altitude. The delay between the parent stroke and the peak of the O_2^+ density increases as we descend in altitude. The O_2^+ density enhancements for the 200 kAkm current peak case (see Figure 2.17c) can change from almost two orders of magnitude at 77 km to five orders of magnitude at 57 km. In the case of 100 kAkm current peak (see Figure 2.17b), the variations of the O_2^+ density are identical to those taking place for the case of 200 kAkm current peak (see Figure 2.17c), which suggests that they are only due to the 20 kAkm continuous current. Above 80 km there are no changes in the concentration of

2. SPRITE HALOS

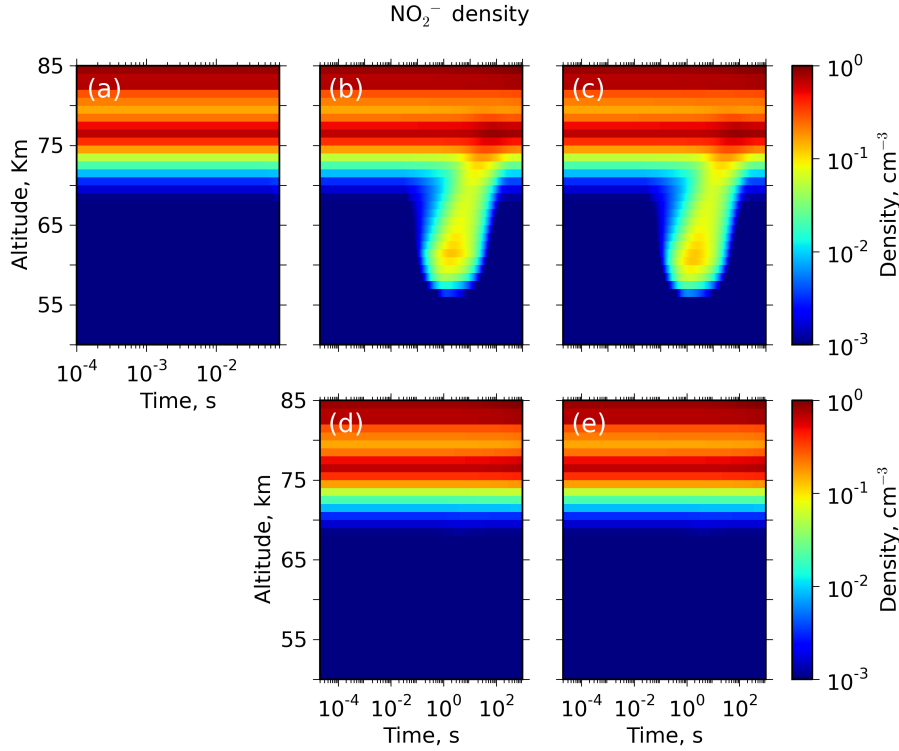
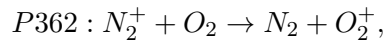
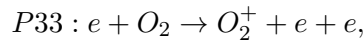
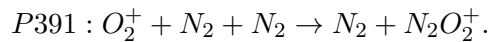


Figure 2.16: Altitude-time evolution of the NO_2^- density due to cloud-to-ground lightnings with (a) realistic current moment, (b) 100 kAkm peak current moment and 20 kAkm continuous current moment, (c) 200 kAkm peak current moment and 20 kAkm continuous current moment, (d) 100 kAkm peak current moment and (e) 200 kAkm peak current moment.

O_2^+ . The mechanisms responsible for the predicted O_2^+ increases are O_2 ionization by direct electron impact (P33) and charge transfer between N_2^+ and O_2 (P362)



while the main relaxation process of the enhanced O_2^+ densities towards ambient values is



In the realistic case (see Figure 2.17a), the behaviour of O_2^+ densities is almost identical to the one already described for the case of +CG strokes. In the case of

-CG strokes (see Figures 2.17d and 2.17e) the variation of the O_2^+ density is barely noticeable. Only in the case of 200 kAkm current peak and between 78 km and 82 km we see a slight increase in the O_2^+ concentration of a factor two that persists for a few seconds. This few seconds increase in the O_2^+ concentration is also seen in the 200 kAkm case of +CG lightning (see Figure 2.17c). The mechanisms of O_2^+ ion production and loss for -CG lightnings are the same as those presented above for the +CG cases.

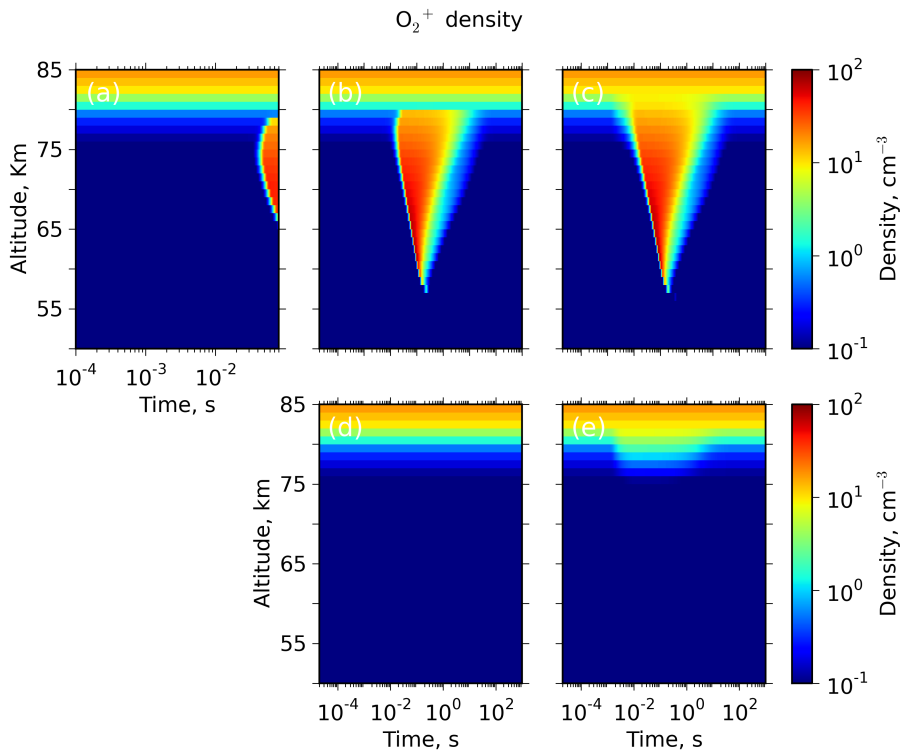
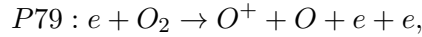


Figure 2.17: Altitude-time evolution of the O_2^+ density due to cloud-to-ground lightnings with (a) realistic current moment, (b) 100 kAkm peak current moment and 20 kAkm continuous current moment, (c) 200 kAkm peak current moment and 20 kAkm continuous current moment, (d) 100 kAkm peak current moment and (e) 200 kAkm peak current moment.

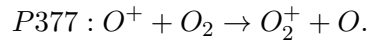
The concentration of O^+ ions in the case of +CG strokes shows a sharp increase between 10 ms and 100 ms after the peak current and a very fast relaxation (see Figures 2.18b and 2.18c). The time instant when the sharp O^+ increase occurs depends on the altitude considered so that as we descend in altitude the sudden increase takes place later and with less duration. This increase of the O^+ concentration exceeds three

2. SPRITE HALOS

orders of magnitude at 77 km. However, below 60 km, the model does not predict any significant change in the density of O^+ . In the case of 200 kAkm current peak (see Figure 2.18c) and for altitudes between 79 km and 82 km, a first increase in the O^+ density is predicted due to the initial pulse of the current moment. The mechanism underlying the increase in the concentration of O^+ is dissociative ionization of O_2 by direct electron impact



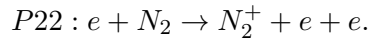
and the process that brings the O^+ concentration back to its ambient value is



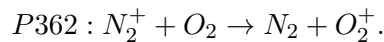
In the case of -CG lightning we see in Figure 2.18e an increase of O^+ slightly over two orders of magnitude at the time of the current peak for the 200 kAkm case. This enhancement in the concentration of O^+ is located between 79 km and 82 km of altitude. The mechanisms of O^+ production and loss are the same as for the +CG lightning cases, that is, electron-impact O_2 dissociative ionization (P79) and the O^+ - O_2 charge transfer process (P377). When the signal with 100 kAkm current peak is used no changes are observed (see Figure 2.18d).

The results obtained for the realistic case are similar to those obtained for the +CG lightning cases (2.18b and 2.18c) but restricted to 80 ms (see Figure 2.18a).

In Figure 2.19 we can see the altitude-time dependence of the concentration of N_2^+ ions. The trend followed is the same of the O^+ ions. In the +CG lightning case (see Figure 2.19c), the highest values are reached between 74 km and 81 km and in the 10-100 ms range after the 200 kAkm electric pulse going through the air plasma. The main kinetic mechanism controlling the production of N_2^+ , which increases in more than four orders of magnitude before the end of the current peak, is



On the other hand, the losses of N_2^+ before the end of the current peak are mainly due to the charge transfer between N_2^+ and oxygen molecules



At 60 km, the increase of N_2^+ can be of more than five orders of magnitude, although it is concentrated in a short time interval of about 20 ms. For the case of -CG lightning

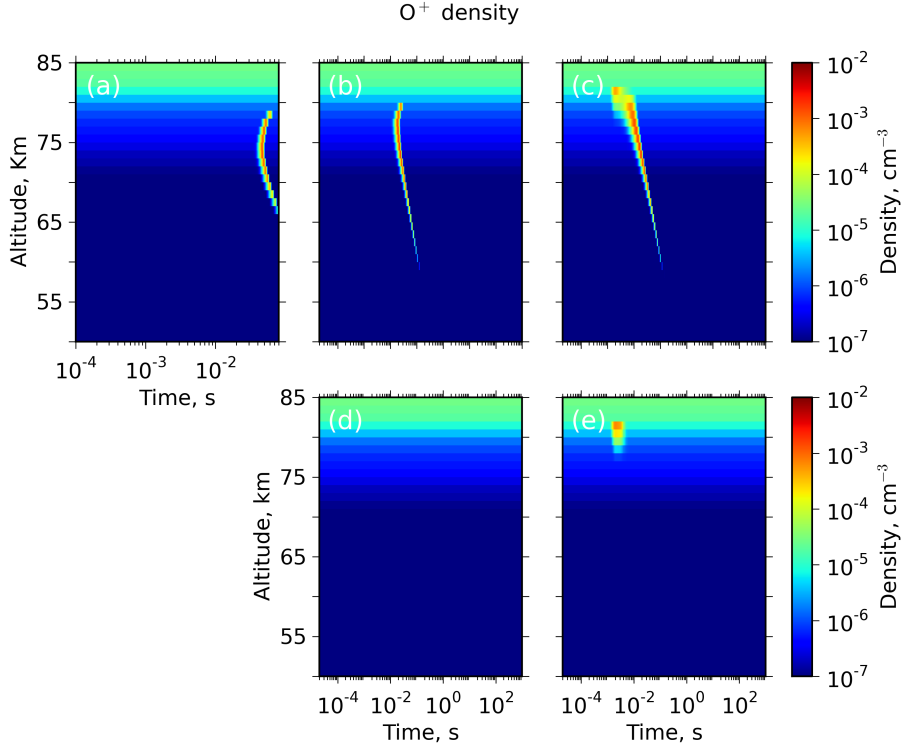
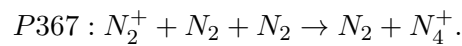


Figure 2.18: Altitude-time evolution of the O^+ density due to cloud-to-ground lightnings with (a) realistic current moment, (b) 100 kAkm peak current moment and 20 kAkm continuous current moment, (c) 200 kAkm peak current moment and 20 kAkm continuous current moment, (d) 100 kAkm peak current moment and (e) 200 kAkm peak current moment.

with 200 kAkm of current peak (see Figure 2.19e) the N_2^+ density increases in three orders of magnitude but confined within the 75-82 km altitude range and due to the same mechanisms of production and loss as already commented above for the +CG lightning cases. When the peak current is 100 kAkm, no significant changes in the concentration of N_2^+ ion are visible (see Figure 2.19d).

The time evolution of the concentration of N_4^+ ions is shown in Figure 2.20. The trend followed is the same of the O^+ and N_2^+ ions. For +CG lightning with 200 kAkm of current peak (see Figure 2.20c), the N_4^+ density increases in more than four and five orders of magnitude at 75 km and 60 km, respectively. The main production process of N_4^+ ions is



2. SPRITE HALOS

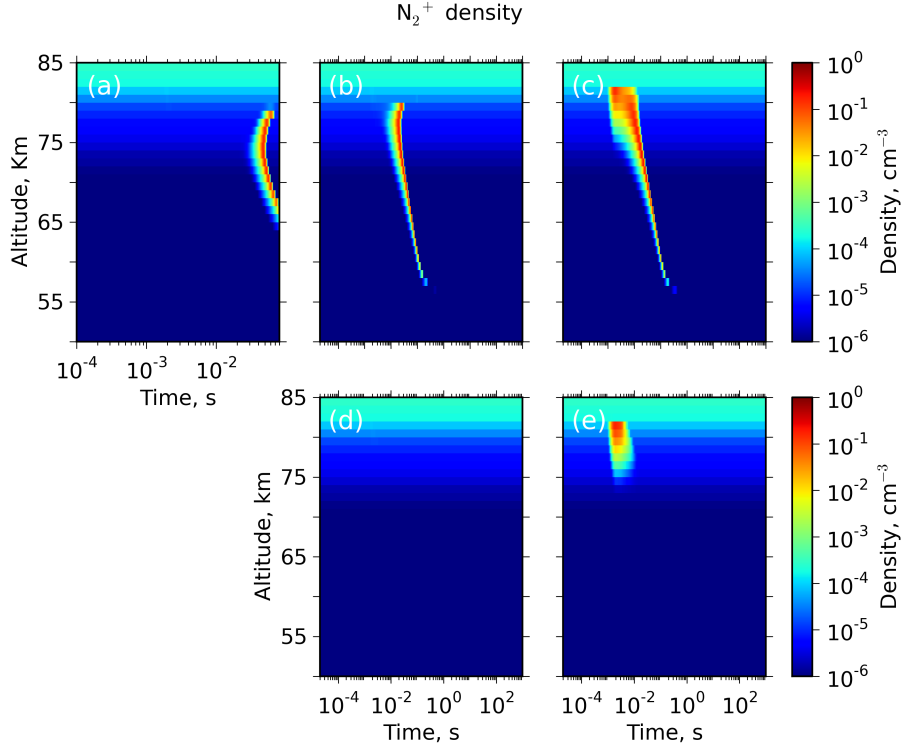
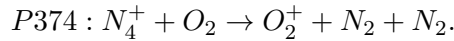


Figure 2.19: Altitude-time evolution of the N_2^+ density due to cloud-to-ground lightnings with (a) realistic current moment, (b) 100 kAkm peak current moment and 20 kAkm continuous current moment, (c) 200 kAkm peak current moment and 20 kAkm continuous current moment, (d) 100 kAkm peak current moment and (e) 200 kAkm peak current moment.

On the other hand, the losses of N_4^+ before the end of the current peak are dominated by



As with N_2^+ , already discussed, in the case of -CG lightning with 200 kAkm of current peak (see Figure 2.20e), the increase in the N_4^+ concentration by more than two orders of magnitude is located within the 75-81 km altitude region and is controlled by the same mechanisms discussed above for the +CG lightning case. When the peak current is 100 kAkm no significant changes in the concentration of N_4^+ ion are predicted (see Figure 2.20d).

Figure 2.21 shows the altitude and time-dependent behaviour of the concentration of the ion O_4^+ . The evolution of the concentration of the O_4^+ ion in the terrestrial

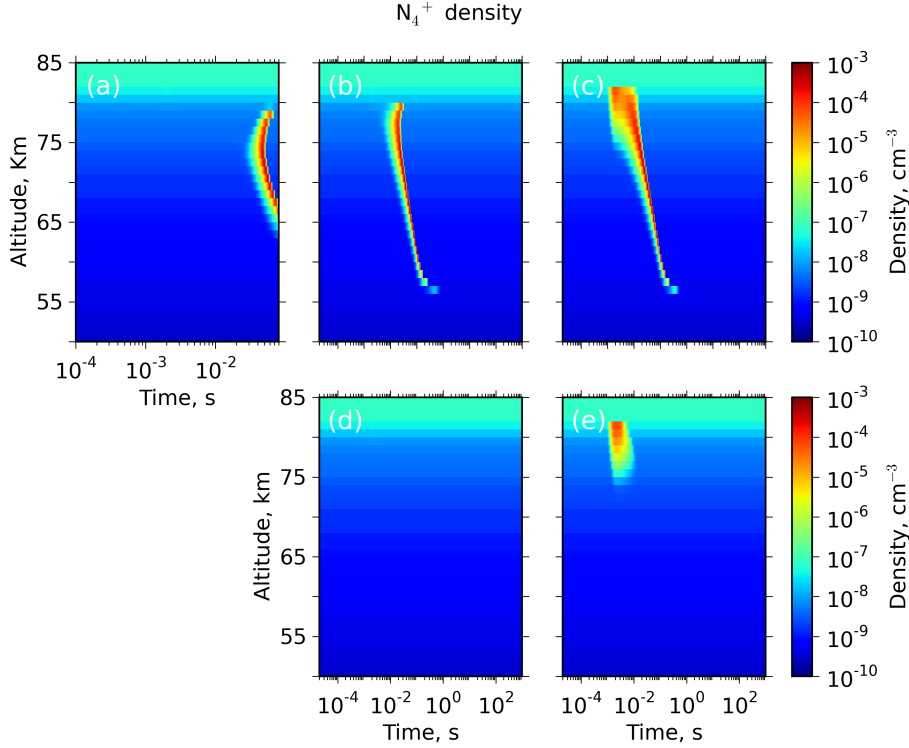
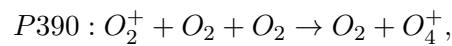


Figure 2.20: Altitude-time evolution of the N_4^+ density due to cloud-to-ground lightnings with (a) realistic current moment, (b) 100 kAkm peak current moment and 20 kAkm continuous current moment, (c) 200 kAkm peak current moment and 20 kAkm continuous current moment, (d) 100 kAkm peak current moment and (e) 200 kAkm peak current moment.

mesosphere is controlled by the reduced electrical field created by a cloud-to-ground lightning as in the case of the O_2^+ ion. We see in Figure 2.21c and Figure 2.21e that the behaviour of the O_4^+ density does not exhibit any current peak dependence but only a dependence on the continuous current and, consequently, there is no variation of the O_4^+ density in the case of -CG lightning (see Figure 2.21d and Figure 2.21e). By contrast, in the cases of +CG lightnings, we notice a sharp variation in the density of O_4^+ (of more than four orders of magnitude at 60 km) extending downwards from 80 km to 50 km and remaining at high values for over 10 s. The main mechanism of O_4^+ production is



2. SPRITE HALOS

while the losses of O_4^+ are controlled by

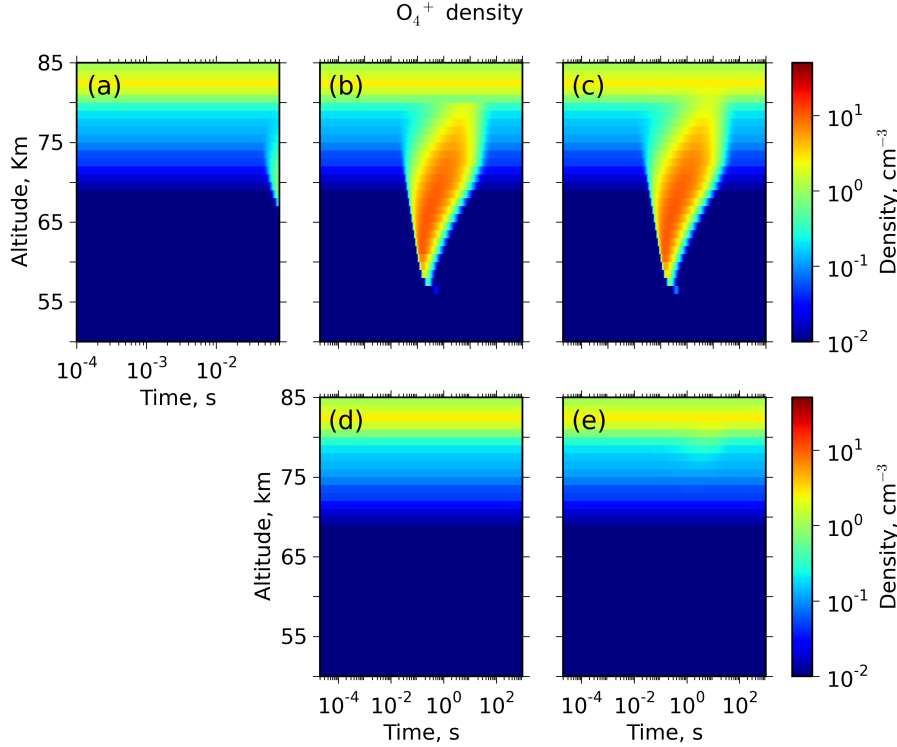
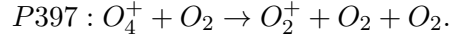


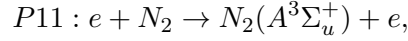
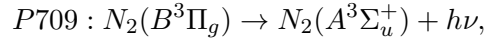
Figure 2.21: Altitude-time evolution of the O_4^+ density due to cloud-to-ground lightnings with (a) realistic current moment, (b) 100 kAkm peak current moment and 20 kAkm continuous current moment, (c) 200 kAkm peak current moment and 20 kAkm continuous current moment, (d) 100 kAkm peak current moment and (e) 200 kAkm peak current moment.

2.3.4 Excited species

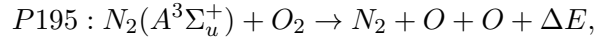
In this section we discuss the evolution and values exhibited by some of the excited species included in our model. We start by analyzing the behaviour of electronically excited neutral species of molecular nitrogen ($N_2(A^3\Sigma_u^+)$, $N_2(B^3\Pi_g)$ and $N_2(C^3\Pi_u)$).

The time-evolution of the metastable $N_2(A^3\Sigma_u^+)$ density at different altitudes and in the -CG lightning case is shown in Figures 2.22d and 2.22e. We can see that there is a sharp increase (of more than 12 orders of magnitude) in the concentration of $N_2(A^3\Sigma_u^+)$

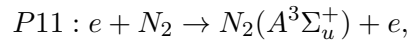
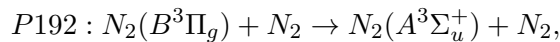
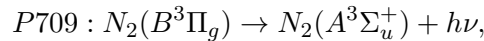
at the time (1 ms) of the current peak extending to 100 ms when it decays to its ambient values. These $N_2(A^3\Sigma_u^+)$ enhancements can occur from 83 km to 70 km for the case of a maximum current of 100 kAkm (see Figure 2.22d) and from 84 km to 65 km for 200 kAkm current peak (see Figure 2.22e). The mechanisms responsible for the increase in the density of $N_2(A^3\Sigma_u^+)$ are, in order of importance, the radiative decay of $N_2(B^3\Pi_g) \rightarrow N_2(A^3\Sigma_u^+)$ and the collisional excitation from ground electronic state N_2 by electron impact



while the quenching of $N_2(A^3\Sigma_u^+)$ by O_2 reduces its concentration to ambient values



where ΔE is the energy released in this reaction that can contribute to heat up (through fast heating) the surrounding atmosphere. The behaviour of $N_2(A^3\Sigma_u^+)$ in the +CG lightning case is shown in Figures 2.22b and 2.22c where we can see that, at 1 ms, it exhibits identical trends as found for the -CG lightning case. The difference is that for +CG lightnings there is a large increase in the concentration of $N_2(A^3\Sigma_u^+)$ even at low altitudes (50-65 km) accompanying the maximum values of the reduced electric field (see Figures 3.3b and 3.3c) that occur at lower altitudes. When the reduced electric field becomes zero, the density of $N_2(A^3\Sigma_u^+)$ returns to its ambient values. Between 100 ms and 100 s after the current peak, as occurs with the reduced electric field (see Figures 3.3b and 3.3c), there is a further increase in the density of $N_2(A^3\Sigma_u^+)$ (up to 10^{-3} cm^{-3} ambient values) below 56 km that is maintained in time. The metastable $N_2(A^3\Sigma_u^+)$, with a lifetime $\simeq 2$ s, is an energy reservoir that can play an important role in the possible fast heating of the local atmosphere. The mechanisms that produce this second sharp increase in the concentration of $N_2(A^3\Sigma_u^+)$ are, in order of importance:



and the main $N_2(A^3\Sigma_u^+)$ loss process that contributes to the recovering of its ambient value is the same as for the -CG lightning case, that is, quenching by O_2 (P195). The

2. SPRITE HALOS

results of the behaviour of $N_2(A^3\Sigma_u^+)$ for the realistic case (see Figure 2.22a) are very similar to the 100 kAkm -CG lightning case but restricted to 80 ms.

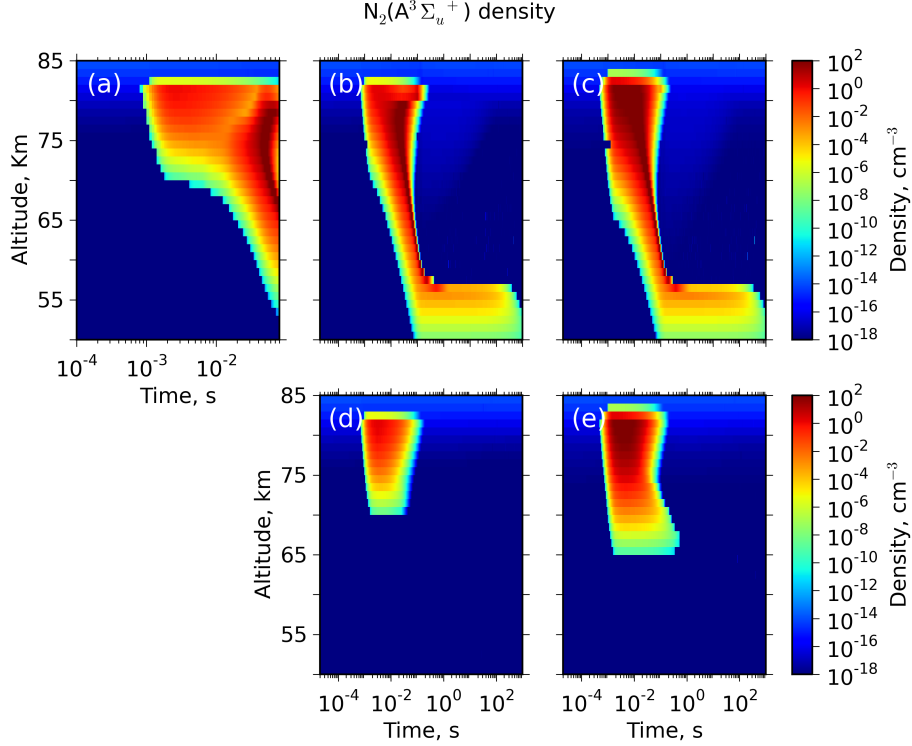
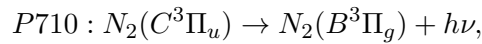
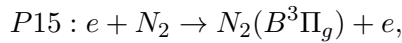


Figure 2.22: Altitude-time evolution of the $N_2(A^3\Sigma_u^+)$ density due to cloud-to-ground lightnings with (a) realistic current moment, (b) 100 kAkm peak current moment and 20 kAkm continuous current moment, (c) 200 kAkm peak current moment and 20 kAkm continuous current moment, (d) 100 kAkm peak current moment and (e) 200 kAkm peak current moment.

Figure 2.23 shows altitude- and time-dependence of the $N_2(B^3\Pi_g)$ density. Our model predicts a behaviour similar to that of the reduced electric field (see Figure 3.3), that is, the $N_2(B^3\Pi_g)$ density increases to values of 10 cm^{-3} at the instant of maximum reduced electric field and decays to ambient values when the electric field becomes negligible. The mechanisms responsible for the increase of the $N_2(B^3\Pi_g)$ density are, in order of importance, the electronic excitation of N_2 by electron impact and the radiative decay $N_2(C^3\Pi_u) \rightarrow N_2(B^3\Pi_g)$,



while the radiative decay of $N_2(B^3\Pi_g)$ to $N_2(A^3\Sigma_u^+)$ reduces the concentration of $N_2(B^3\Pi_g)$ to its ambient values.

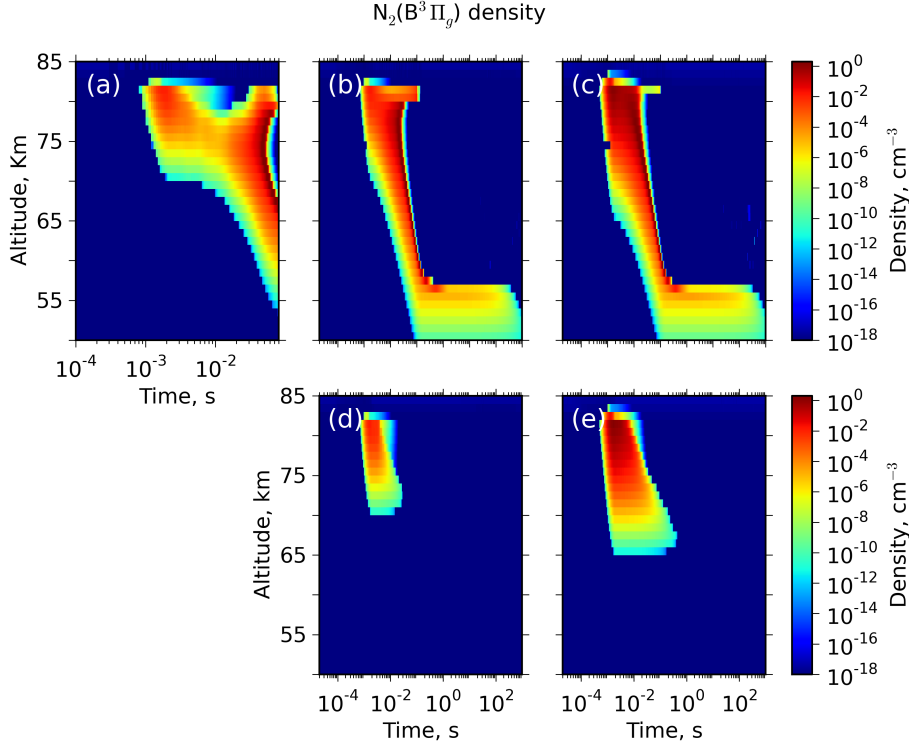


Figure 2.23: Altitude-time evolution of the $N_2(B^3\Pi_g)$ density due to cloud-to-ground lightnings with (a) realistic current moment, (b) 100 kAkm peak current moment and 20 kAkm continuous current moment, (c) 200 kAkm peak current moment and 20 kAkm continuous current moment, (d) 100 kAkm peak current moment and (e) 200 kAkm peak current moment.

The emission brightness (EB) measured in Rayleighs (R, $1 \text{ R} = 10^6 \text{ photons cm}^{-2} \text{ s}^{-1}$, [Hunten et al., 1956]) of the N_2 first positive band system ($1PN_2$) associated with its radiative decay ($B^3\Pi_g \rightarrow A^3\Sigma_u^+$), which is the most important spectral band in the sprite halo visible optical emission spectrum from 450 nm to 800 nm, is shown in Figures 2.24. The calculation of the EB is done through the expression

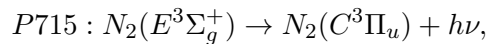
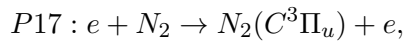
$$EB(R) = 10^{-6} \int_L V(l) dl, \quad (2.12)$$

valid for an optically thin atmosphere and where $V(l)$ is the volume emission rate (in photons $\text{cm}^{-3} \text{ s}^{-1}$) and the integral is taken along the line of sight through the emission

2. SPRITE HALOS

volume over an effective column length L . The magnitude L refers to the diameter of the halo, where in all cases we have chosen a value of 100 km. The volume emission rate $V(l)$ is equal to the product $A_k^{eff} \text{ (s}^{-1}\text{)} \times N_k \text{ (cm}^{-3}\text{)}$, that is, the product of the effective Einstein coefficients (A_k^{eff}) for spontaneous emission and the concentration of the k emitting excited state (N_k). We can see in Figure 2.24 that the maximum brightness occurs at the time of maximum electric field, exceeding 1 MR in all +CG lightning cases (see Figures 2.24a, 2.24b and 2.24c) and in the -CG lightning case with 200 kAkm peak current (see Figure 2.24e). This suggests the possibility of detecting the emission due to 1PN2 for +CG and -CG lightning produced halos above a certain value (200 kAkm) of current moment peak. For +CG lightning, the emission brightness can exceed 10 MR at certain altitudes while the 20 kAkm continuous current is on. Due to the continuous current stage associated to +CG lightning we can see a relatively strong increase in the electron concentration that is maintained in time due to the associative detachment of O^- by N_2 (with a reaction rate that depends on the reduced electric field) and of O^- by CO. The electrons released in the associative detachment process excite the nitrogen molecules and produce an increase in the $N_2(B^3\Pi_g)$ and $N_2(C^3\Pi_u)$ densities whose subsequent radiative decays could produce an instantaneous emission brightness that exceeds 1 MR for the 1PN₂ and 2PN₂. Regarding these results, we must be careful because, at low altitudes, sprite streamers are likely to emerge and our model assumptions might not be completely valid.

Figure 2.25 shows the behaviour of the density of $N_2(C^3\Pi_u)$ under the action of various types of lightning (-CG and +CG). We can see, for the +CG lightning cases (see Figures 2.25a, 2.25b, and 2.25c), that the $N_2(C^3\Pi_u)$ density reaches values of 10^{-2} cm^{-3} at the time of the maximum electric field while for -CG lightnings the concentration of $N_2(C^3\Pi_u)$ only changes when the current peak is 200 kAkm. The main mechanisms that produce this increase in the concentration of $N_2(C^3\Pi_u)$ are, in order of importance, direct electronic excitation of N_2 by electron impact and radiative decay $N_2(E^3\Sigma_g^+) \rightarrow N_2(C^3\Pi_u)$



while the process that reduces the concentration of $N_2(C^3\Pi_u)$ to its ambient value is the radiative decay responsible for the emission of the second positive band system of

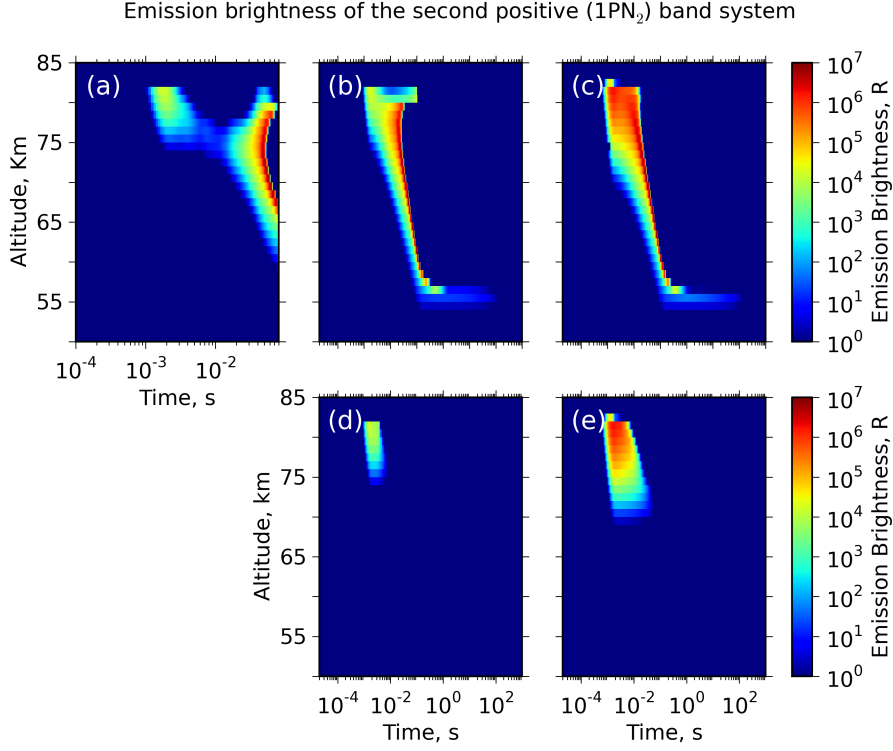
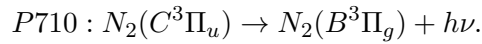


Figure 2.24: Altitude-time evolution of the first positive band system ($1PN_2$) emission brightness due to cloud-to-ground lightnings with (a) realistic current moment, (b) 100 kAkm peak current moment and 20 kAkm continuous current moment, (c) 200 kAkm peak current moment and 20 kAkm continuous current moment, (d) 100 kAkm peak current moment and (e) 200 kAkm peak current moment.

N_2 , that is,



Out of the three radiative mechanisms that deexcite $N_2(E^3\Sigma_g^+)$, the process P715 contributes more than 54 % to the total decrease of the $N_2(E^3\Sigma_g^+)$ concentration. The other two reactions, i.e. P714 and P713, contribute in about 34 % and 10 %, respectively.

2. SPRITE HALOS

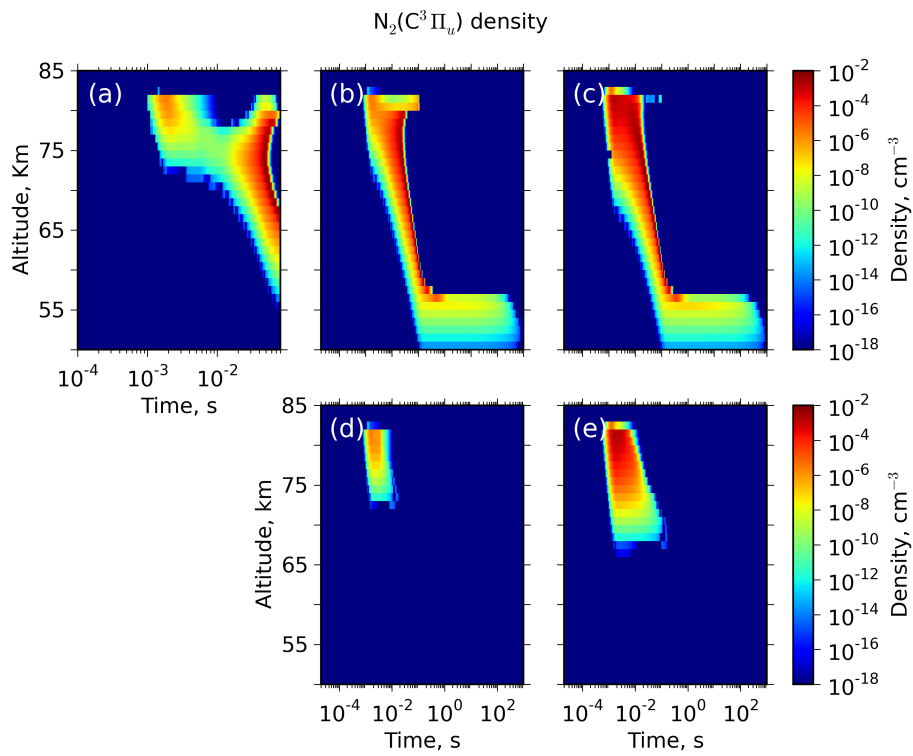


Figure 2.25: Altitude-time evolution of the $N_2(C^3\Pi_u)$ density due to cloud-to-ground lightnings with (a) realistic current moment, (b) 100 kAkm peak current moment and 20 kAkm continuous current moment, (c) 200 kAkm peak current moment and 20 kAkm continuous current moment, (d) 100 kAkm peak current moment and (e) 200 kAkm peak current moment.

The time-dependent emission brightness due to the second positive band system of N_2 ($2PN_2$) (responsible for the emission spectrum in the spectral region between 250 nm and 450 nm) is shown in Figure 2.26. The calculation is done using expression (2.12) and we can see how, as in the case of the emission brightness of $1PN_2$, the maximum brightness occurs at the time of maximum electric field due to the short radiative decay lifetime of $N_2(C^3\Pi_u)$. For the +CG lightning cases (see Figures 2.26a, 2.26b and 2.26c), the $N_2(C^3\Pi_u)$ EB maximum can reach 1MR while in the -CG lightning cases (see Figures 2.26d and 2.26e) barely reaches 1 MR in the case of 200 kAkm current peak.

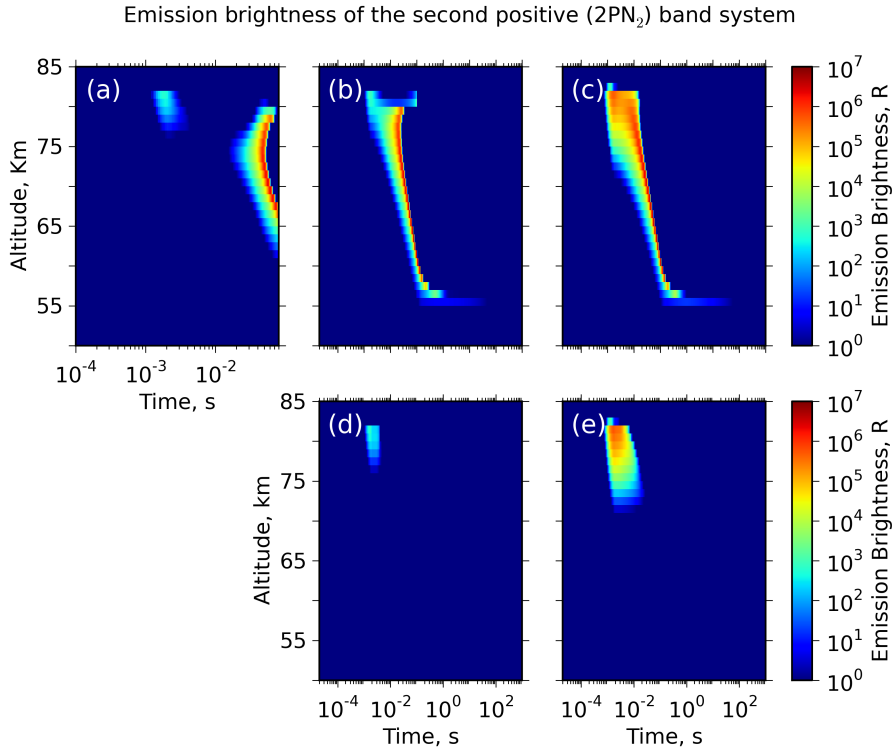


Figure 2.26: Altitude-time evolution of the second positive band system ($2PN_2$) emission brightness due to cloud-to-ground lightnings with (a) realistic current moment, (b) 100 kAkm peak current moment and 20 kAkm continuous current moment, (c) 200 kAkm peak current moment and 20 kAkm continuous current moment, (d) 100 kAkm peak current moment and (e) 200 kAkm peak current moment.

We can compare the previously reported instantaneous emission brightness (Figures 2.24 and 2.26) with the possible emission brightness captured by 30 fps and 1000 fps

2. SPRITE HALOS

cameras during TLE ground campaigns. Figure 2.27 shows the altitude evolution of the possible emission brightness captured by a 30 fps camera (standard camera) due to +CG lightning discharges where emission brightness of the 1PN_2 can exceed 1 MR in the 100 kAkm and 200 kAkm cases between 60 km and 70 km of altitude. However, in the case of a camera recording at 1000 fps (see Figure 2.28) the emission brightness can exceed 1 MR in the 1PN_2 and 2PN_2 cases for all the +CG lightning discharges considered. According to our model, the 2PN_2 emission brightness from relatively low layers, between 60 km and 75 km, could be observed. In the case of 1PN_2 , we could see emission brightness from up to 80 km of altitude. However, the reader must be careful with these results because at low altitudes the emergence of sprites is likely.

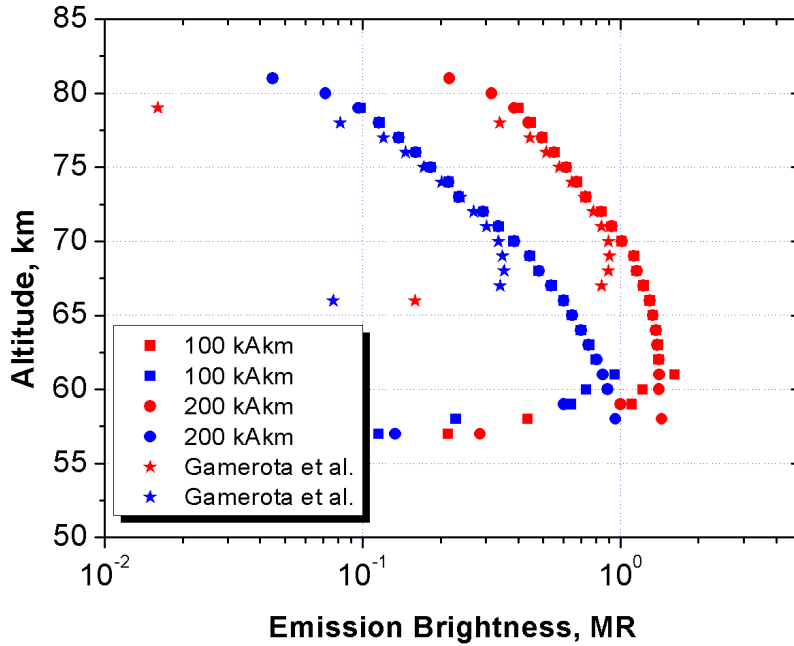


Figure 2.27: Altitude evolution of the emission brightness due to a positive cloud-to-ground lightning discharge with different current peaks as would be measured by a 30 fps camera. The red symbols correspond to the first positive band system and the blue symbols correspond to the second positive band system.

The altitude and time-evolution of the concentration of $\text{N}_2^+(\text{A}^2\Pi_u)$ ions (responsible for the Meinel band emission in the red and near infrared spectral region) is shown in Figure 2.29. As with the previous electronically excited N_2 species, the behaviour of

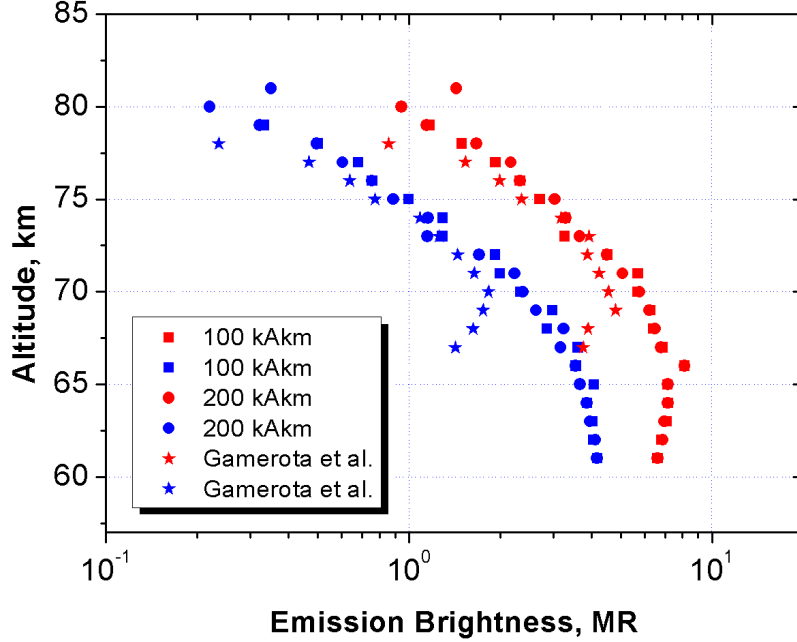
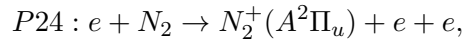
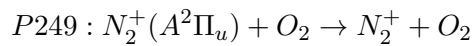
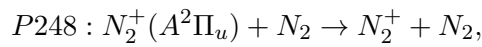


Figure 2.28: Altitude evolution of the emission brightness due to a positive cloud-to-ground lightning discharge with different current peaks as would be measured by a 1000 fps camera. The red symbols correspond to the first positive band system and the blue symbols correspond to the second positive band system.

the $N_2^+(A^2\Pi_u)$ density follows the reduced electric field (see Figure 3.3). Our model predicts an enhancement to 10^{-3} cm^{-3} above ambient values between 75 km and 60 km of altitude in the +CG lightning cases (see Figures 2.29a, 2.29b and 2.29c). For the cases of -CG strokes (see Figures 2.29d and 2.29e), we see similar values as in the previous cases around 76 km but only when the lightning reaches 200 kAkm of current peak. The increase of the $N_2^+(A^2\Pi_u)$ density is due to

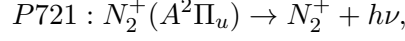


while the mechanisms that recover the ambient concentration of $N_2^+(A^2\Pi_u)$ are, in order of importance,



2. SPRITE HALOS

and



the latter (P721) with a $N_2^+(A^2\Pi_u)$ lifetime of 0.1 ms.

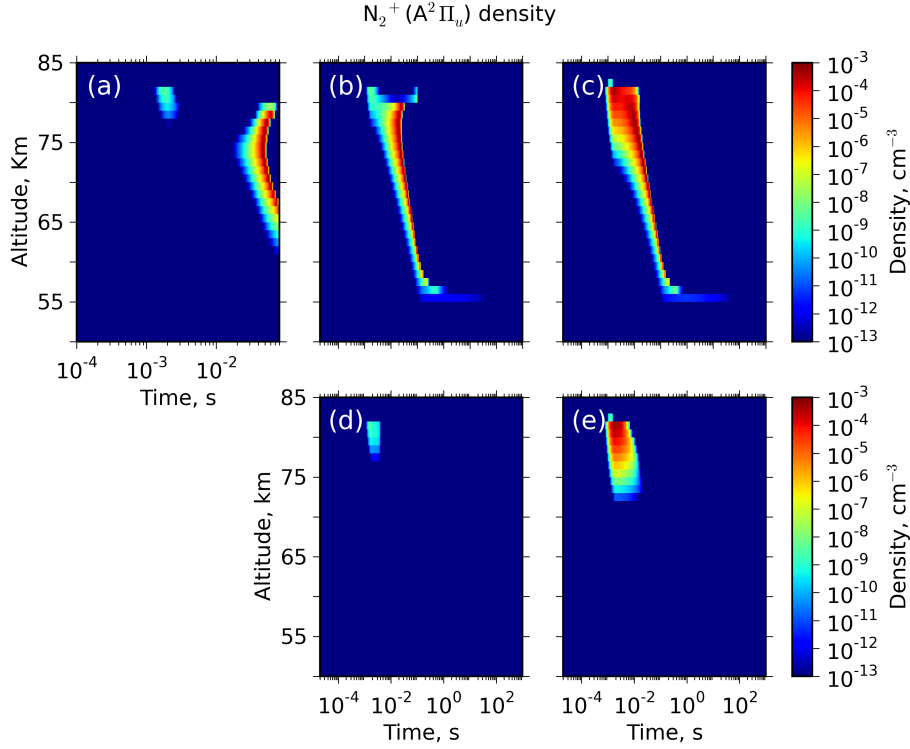
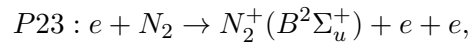
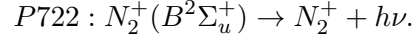


Figure 2.29: Altitude-time evolution of the $N_2^+(A^2\Pi_u)$ density due to cloud-to-ground lightnings with (a) realistic current moment, (b) 100 kAkm peak current moment and 20 kAkm continuous current moment, (c) 200 kAkm peak current moment and 20 kAkm continuous current moment, (d) 100 kAkm peak current moment and (e) 200 kAkm peak current moment.

The behaviour of the $N_2^+(B^2\Sigma_u^+)$ concentration (responsible for the first negative band emission in the ultraviolet spectral region) is the same as the previous excited ion $N_2^+(A^2\Pi_u)$ both in time and in altitude. In this case (see Figure 2.30), our model predicts an increase to 10^{-5} cm^{-3} above ambient (background) values. The main production process of $N_2^+(B^2\Sigma_u^+)$ ions is the direct electron impact ionization of ground state N_2



while the losses of $N_2^+(B^2\Sigma_u^+)$ are controlled by the radiative decay



It is worth mentioning that the calculated maximum emission brightness (not shown) of the first negative band of N_2 is 10 times greater than that of the Meinel emission which could explain the reported difficulties in the detection of Meinel optical emission in halos and sprites (Morrill et al. [1998] and Bucselá et al. [2003]).

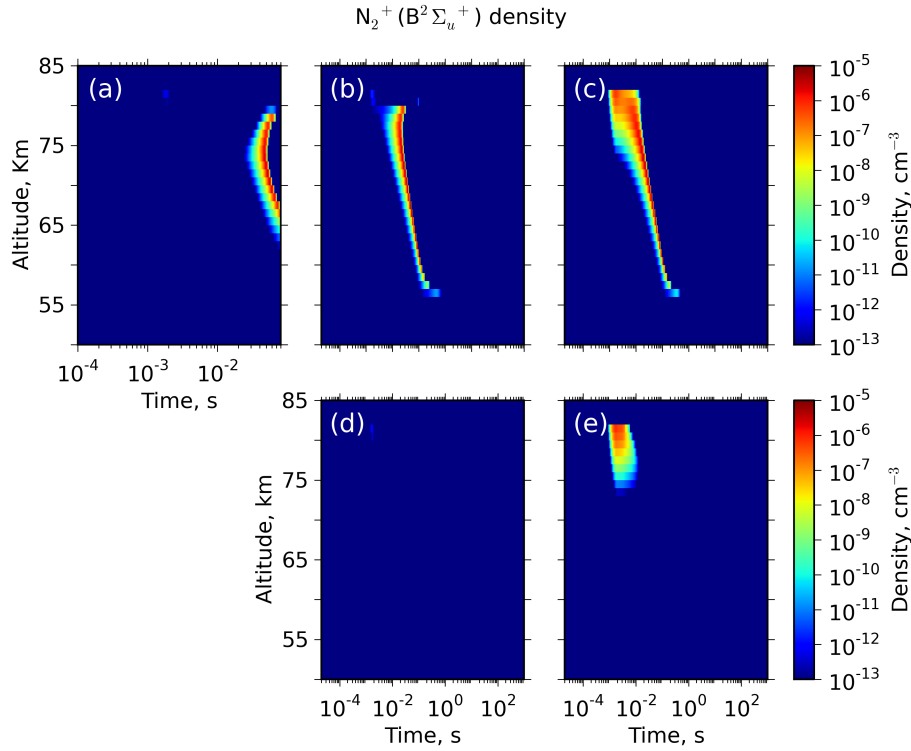
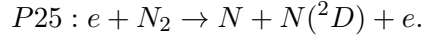


Figure 2.30: Altitude-time evolution of the $N_2^+(B^2\Sigma_u^+)$ density due to cloud-to-ground lightnings with (a) realistic current moment, (b) 100 kAkm peak current moment and 20 kAkm continuous current moment, (c) 200 kAkm peak current moment and 20 kAkm continuous current moment, (d) 100 kAkm peak current moment and (e) 200 kAkm peak current moment.

The altitude-time dependence of the density of $N(^2D)$ due to cloud-to-ground strokes are shown in Figure 2.31. The behaviour of the $N(^2D)$ density is associated with the reduced electric field (see Figure 3.3) so that when E/N is maximum, the concentration of $N(^2D)$ may exceed 10 cm^{-3} above ambient values in the case of +CG lightnings (see

2. SPRITE HALOS

Figures 2.31a, 2.31b and 2.31c) and 10^{-1} cm^{-3} in the case of -CG lightning with 200 kAkm of current peak (see Figure 2.31e). The main production process of $N(^2D)$ is the electron impact N_2 dissociative excitation



On the other hand, the loss of the previously produced $N(^2D)$ density is dominated by

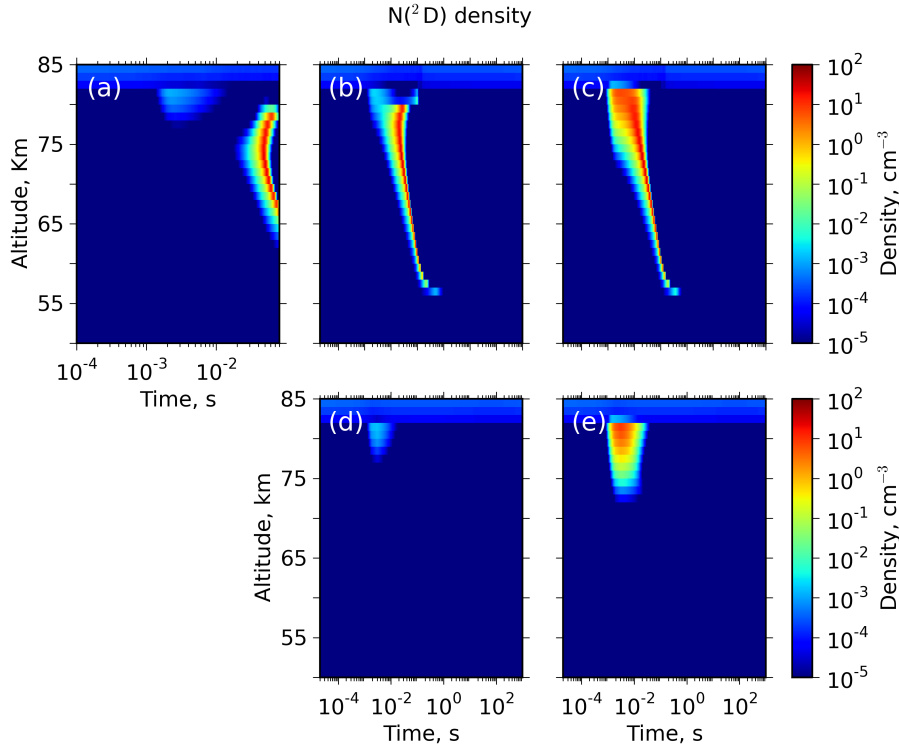
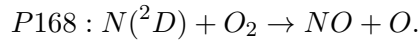
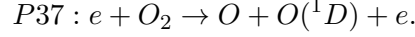


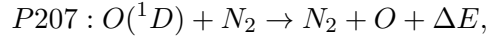
Figure 2.31: Altitude-time evolution of the $N(^2D)$ density due to cloud-to-ground lightnings with (a) realistic current moment, (b) 100 kAkm peak current moment and 20 kAkm continuous current moment, (c) 200 kAkm peak current moment and 20 kAkm continuous current moment, (d) 100 kAkm peak current moment and (e) 200 kAkm peak current moment.

Figure 2.32 shows the altitude and time-dependent behaviour of the concentration of the metastable oxygen atom $O(^1D)$ (110 s lifetime). Its evolution is also similar to

that of the reduced electric field shown in Figure 3.3. The main production mechanism of O(¹D) is the electron impact dissociative excitation of O₂

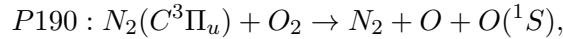
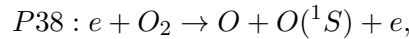


The instantaneous density of O(¹D) can overtake 10 cm⁻³ in +CG lightnings (see Figures 2.32a, 2.32b and 2.32c) as well as in -CG lightning (see Figure 2.32e) with significant charge moment change in time and locations where the maximum reduced electric field takes place. When the reduced electric field goes back to zero, the O(¹D) is lost through quenching by N₂ molecules

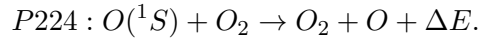


where ΔE is the energy released in this exothermic reaction. Hiraki et al. [2004] obtained a maximum nighttime production of accumulated O(¹D) density above 10⁴ cm⁻³ located at 73 km considering lightning charge moment change values (1000 C km) much higher than the ones used in our model. These authors used a simplified kinetic model with initial densities and cross sections different than ours.

As shown in Figure 2.33a, 2.33b and 2.33c, the increase of the O(¹S) metastable (0.7 s lifetime) density in more than ten orders of magnitude with respect to ambient values occurs while the reduced electric field reaches its maximum in the +CG stroke cases. The main source of O(¹S) production is dissociative excitation of O₂ by collisions with electrons energized by the electric field followed by dissociative quenching of N₂(C³Π_u) by O₂



while the O(¹S) loss process is exothermic quenching through collisions with O₂ molecules



Between 75 km and 82 km the O(¹S) density remains at relatively high values (over 1 cm⁻³) about 1 second after the current peak. For the -CG lightning cases, the O(¹S) concentration exhibits a sharp increase (of more than five orders of magnitude) in the current peak time when the maximum current moment is 100 kAkm (see Figure 2.33d) and of more than eight orders of magnitude when the current moment peak is

2. SPRITE HALOS

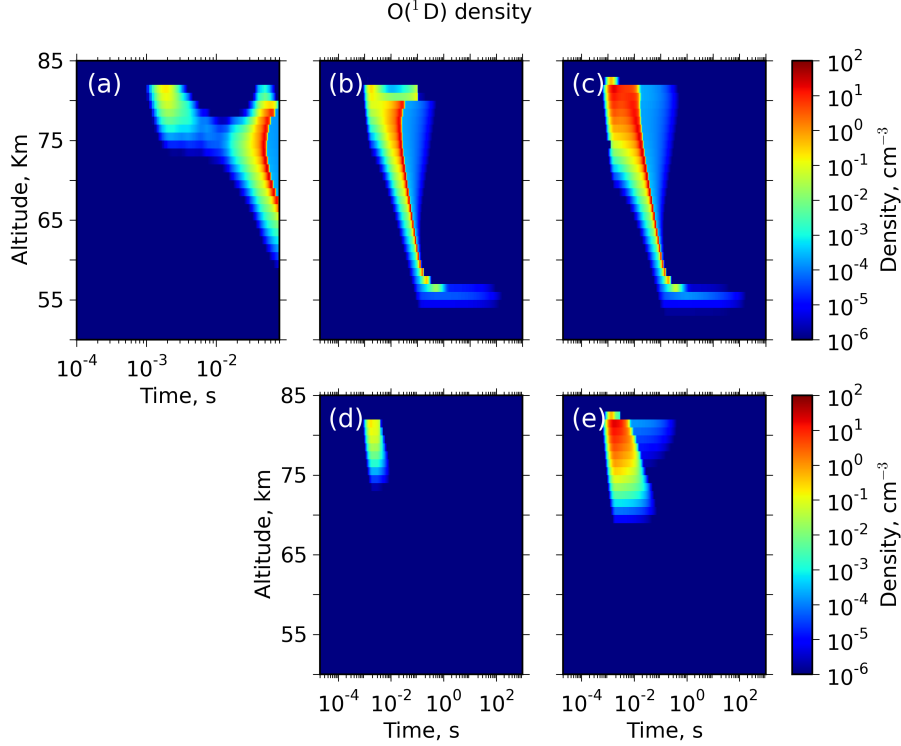


Figure 2.32: Altitude-time evolution of the $O(^1D)$ density due to cloud-to-ground lightnings with (a) realistic current moment, (b) 100 kAkm peak current moment and 20 kAkm continuous current moment, (c) 200 kAkm peak current moment and 20 kAkm continuous current moment, (d) 100 kAkm peak current moment and (e) 200 kAkm peak current moment.

200 kAkm (see Figure 2.33e). In addition, it remains at relatively high values during almost 1 second in the altitude range between 75 km and 82 km. The main $O(^1S)$ production processes are the same as in the +CG lightning case (P38 and P188) while the key loss mechanism is quenching by O_2 (P224).

The metastable $O_2(a^1\Delta_g)$ (45 min lifetime) and $O_2(b^1\Sigma_g^+)$ (12 s lifetime) densities have also been studied. Due to their long lifetimes, they can store energy for a long time that, later on, can be released to heat up the local atmosphere. Regarding the case of +CG lightning strokes, the metastable $O_2(a^1\Delta_g)$ density (see Figures 2.34a, 2.34b and 2.34c) shows a similar behaviour in the three cases studied independently of the current peak. Our model predicts an important increase in the $O_2(a^1\Delta_g)$ concentration which is higher as we descend in altitude so that, at 76 km, the $O_2(a^1\Delta_g)$ density reaches a

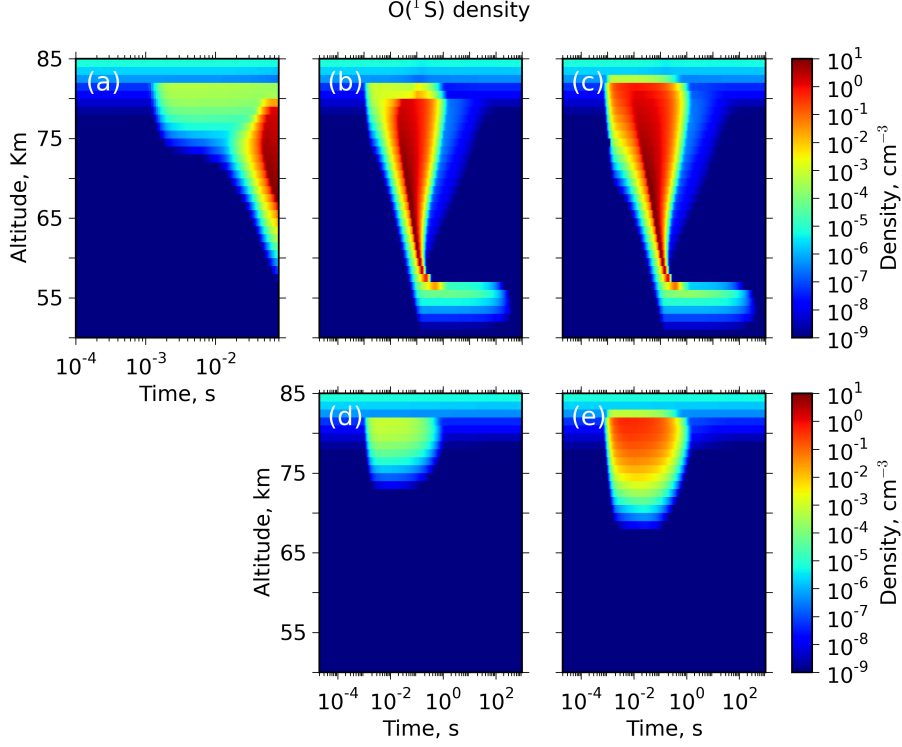
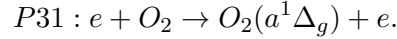
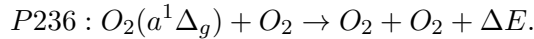


Figure 2.33: Altitude-time evolution of the $O(^1S)$ density due to cloud-to-ground lightnings with (a) realistic current moment, (b) 100 kAkm peak current moment and 20 kAkm continuous current moment, (c) 200 kAkm peak current moment and 20 kAkm continuous current moment, (d) 100 kAkm peak current moment and (e) 200 kAkm peak current moment.

value of about $5 \times 10^3 \text{ cm}^{-3}$ and, at 57 km, the $O_2(a^1\Delta_g)$ concentration exceeds $5 \times 10^4 \text{ cm}^{-3}$. The main source of $O_2(a^1\Delta_g)$ production is the excitation of O_2 by collisions with electrons previously energized by the electric field



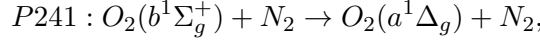
while the $O(a^1\Delta_g)$ loss process is exothermic quenching through collisions with O_2 molecules



Regarding -CG lightning strokes, we can see in Figures 2.34d and 2.34e a sharp increase (but lower than in the case of +CG lightning strokes) in the $O_2(a^1\Delta_g)$ concentration, this being higher at lower altitudes. The mechanisms responsible for this increase at

2. SPRITE HALOS

high altitudes (~ 76 km) are the excitation of O_2 by collisions with electrons (P31), only active during 40 ms after the current peak, and the quenching of $O_2(b^1\Sigma_g^+)$ by N_2 molecules



while, at lower altitudes (~ 57 km), the $O_2(a^1\Delta_g)$ production is only due to the excitation of O_2 by collisions with electrons (P31). The main $O_2(a^1\Delta_g)$ loss mechanism during -CG lightning strokes is the same of the previous cases (P236).

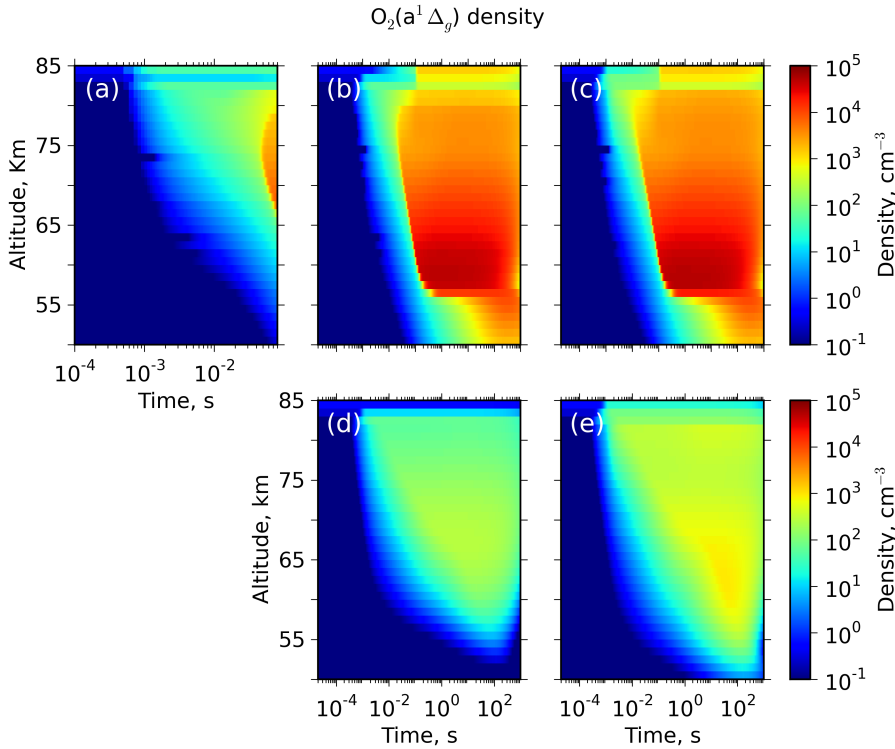
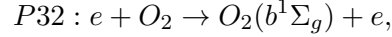


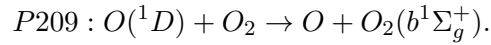
Figure 2.34: Altitude-time evolution of the $O_2(a^1\Delta_g)$ density due to cloud-to-ground lightnings with (a) realistic current moment, (b) 100 kAkm peak current moment and 20 kAkm continuous current moment, (c) 200 kAkm peak current moment and 20 kAkm continuous current moment, (d) 100 kAkm peak current moment and (e) 200 kAkm peak current moment.

The behaviour of the metastable $O_2(b^1\Sigma_g^+)$ concentration (see Figure 2.35) is similar to the trend of the $O(^1S)$ density (see Figure 2.33). Our model predicts a strong increase, in the cases of +CG lightning strokes (see Figures 2.35a, 2.35b and 2.35c), in the time period coinciding with the reduced electric field activation from background

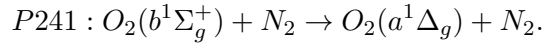
values. This enhancement of $O_2(b^1\Sigma_g^+)$ density is higher as we descend in altitude. At high altitudes (~ 76 km), the main $O_2(b^1\Sigma_g^+)$ concentration production is the excitation of O_2 by collisions with electrons



only active during 3 milliseconds after the current peak, and the quenching of $O(^1D)$ by O_2 molecules



The $O_2(b^1\Sigma_g^+)$ loss process is, like in the previous excited species, quenching of $O_2(b^1\Sigma_g^+)$ by N_2 molecules



At lower altitudes (~ 57 km), the main $O_2(b^1\Sigma_g^+)$ production mechanism is the excitation of O_2 by collisions with electrons (P32). On the other hand, in the cases of -CG lightning strokes, we can see in Figures 2.35d and 2.35e an enhancement in the $O_2(b^1\Sigma_g^+)$ density localized at high altitudes (between 65 km and 82 km) that remains high (40 cm^{-3}) during 1 second. The $O_2(b^1\Sigma_g^+)$ production and loss processes are the excitation of O_2 by collisions with electrons (P32), and the quenching of $O_2(b^1\Sigma_g^+)$ by N_2 molecules (P241), respectively.

2.3.5 Neutral species

Finally, we study the variations of ground state neutral species under the action of a sprite halo. Only atomic oxygen and nitrogen out of the 13 ground state neutral species considered in our model exhibit substantial variation. Neither nitrogen oxides (NO_x and N_2O) nor CO_2 modify their ambient densities. The evolution of the densities of ground state N and O is very similar, as shown in Figures 2.36 and 2.37, respectively. We only see a significant variation in the density of these species (N and O atoms) in the case of +CG lightnings, which suggest that their behaviour significantly depends on the intensity of the continuous current. The concentrations of both N and O begin their increment at the time when the electric field begins to grow (see Figure 3.3), remaining with high values for most of the simulation time. In the case of atomic nitrogen (see Figures 2.36b and 2.36c) we can see that, from 80 km to 61 km, there is an increase of the N density of up to 300 cm^{-3} over its ambient values. Between 55 km and 61

2. SPRITE HALOS

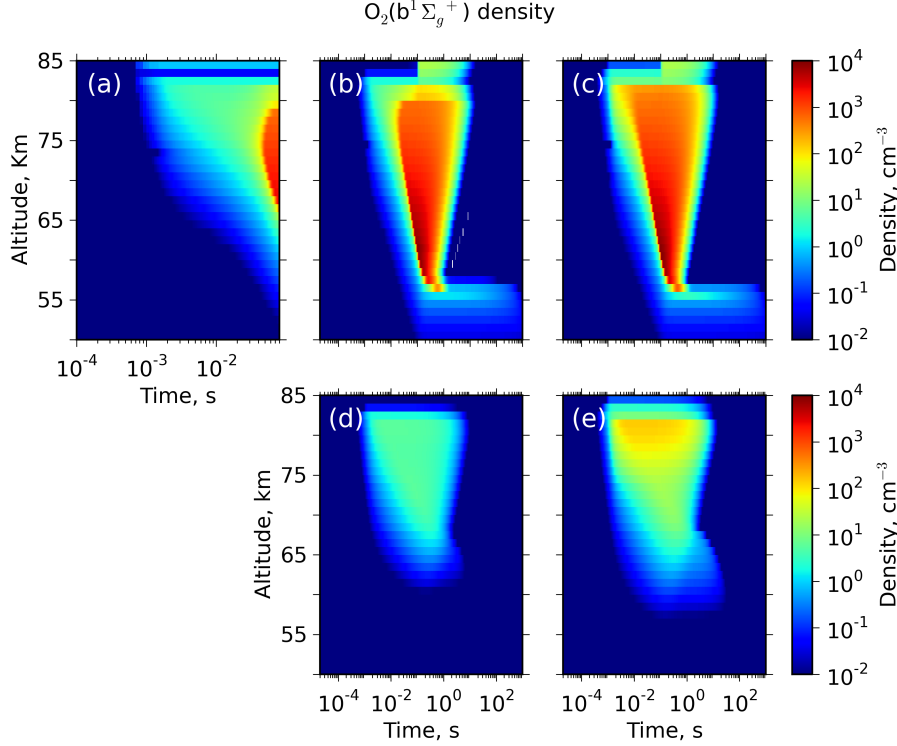
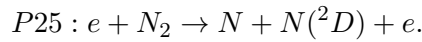
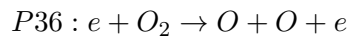


Figure 2.35: Altitude-time evolution of the $O_2(b^1\Sigma_g^+)$ density due to cloud-to-ground lightnings with (a) realistic current moment, (b) 100 kAkm peak current moment and 20 kAkm continuous current moment, (c) 200 kAkm peak current moment and 20 kAkm continuous current moment, (d) 100 kAkm peak current moment and (e) 200 kAkm peak current moment.

km, the density of atomic nitrogen reaches values of 160 cm^{-3} while below 55 km, it exhibits values close to 50 cm^{-3} . The mechanism responsible for the production of atomic nitrogen is



Similarly, atomic oxygen shows an increase in its mesospheric concentration at the time when the electric field is highest (see Figures 2.37b and 2.37c). The density of atomic oxygen reaches values of $5 \times 10^4 \text{ cm}^{-3}$ for practically all the altitudes analyzed and maintains these high values over time. The mechanisms responsible for the O density increase are, in order of importance,



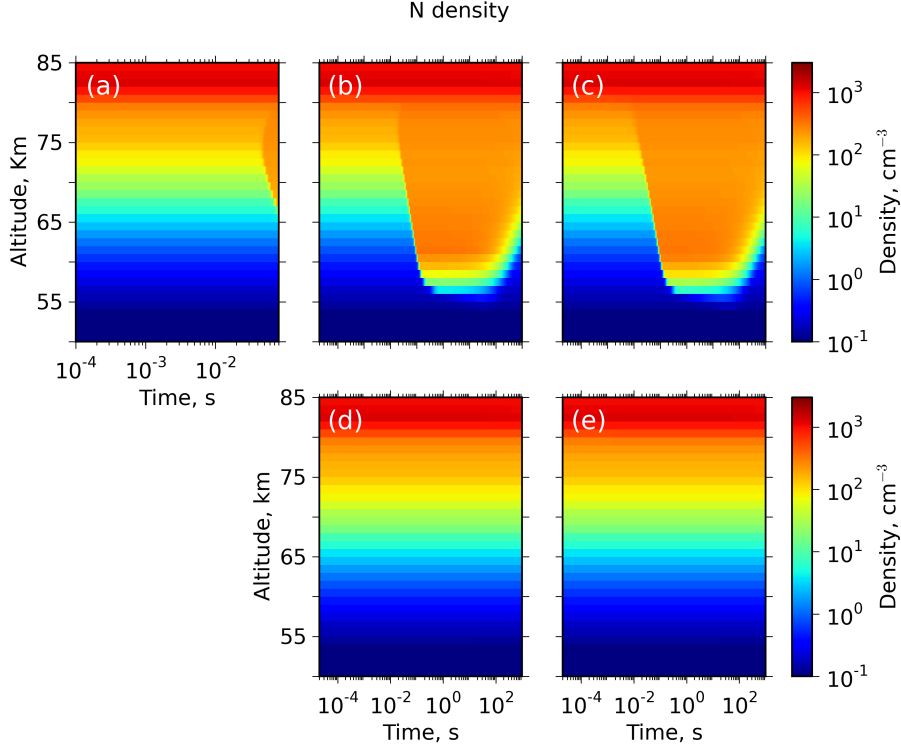
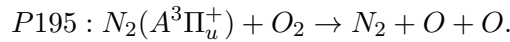


Figure 2.36: Altitude-time evolution of the N density due to cloud-to-ground lightnings with (a) realistic current moment, (b) 100 kAkm peak current moment and 20 kAkm continuous current moment, (c) 200 kAkm peak current moment and 20 kAkm continuous current moment, (d) 100 kAkm peak current moment and (e) 200 kAkm peak current moment.

and



2.3.6 High current moment (500 kAkm) case

We now discuss an extreme case corresponding to a parent lightning with a peak current moment of 500 kAkm. This case represents an extreme scenario within the lightning CMC's causing halos as reported by Williams et al. [2012]. Now, the parent lightning has a peak current moment of 500 kAkm so that the reduced electric field, whose behaviour is similar to the cases of 100 kAkm and 200 kAkm (both -CG and +CG) reaches values close to 200 Td between 75 km and 81 km of altitude (see Figure 2.38a and 2.38b). As it is shown in Figure 2.38b, the reduced electric field reaches values close

2. SPRITE HALOS

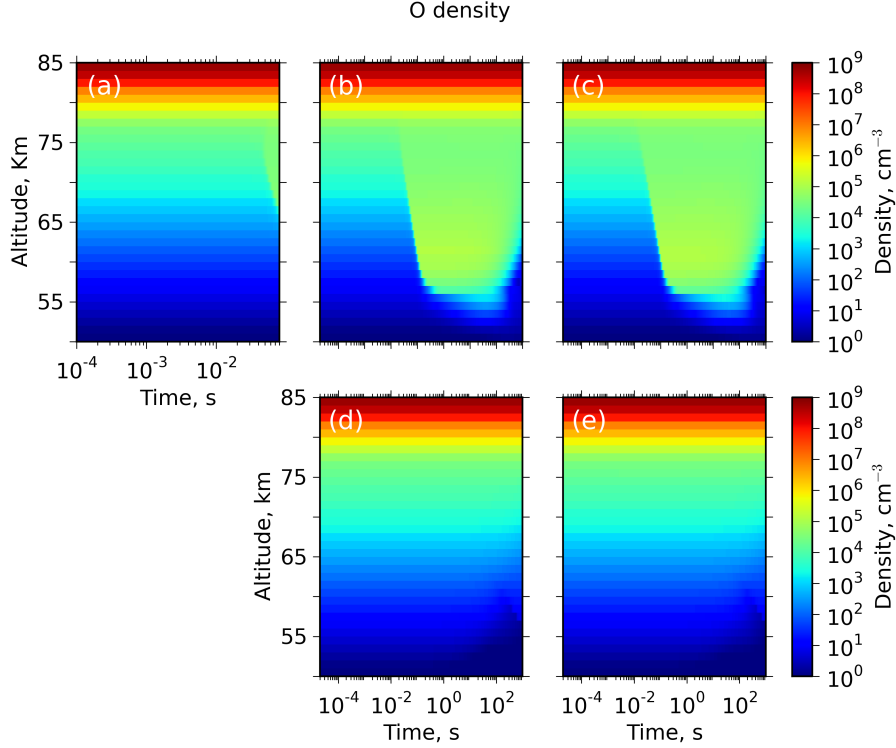
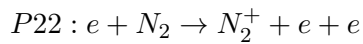
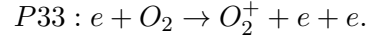


Figure 2.37: Altitude-time evolution of the O density due to cloud-to-ground lightnings with (a) realistic current moment, (b) 100 kAkm peak current moment and 20 kAkm continuous current moment, (c) 200 kAkm peak current moment and 20 kAkm continuous current moment, (d) 100 kAkm peak current moment and (e) 200 kAkm peak current moment.

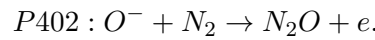
to breakdown below to 75 km of altitude due to the continuous current stage. The large electric field produced at high altitudes has important consequences in the electron density. In Figures 2.38c and 2.38d we show the temporal evolution of the electron density under the action of -CG and +CG lightning respectively. At the time of the electric field peak and between 75 km and 81 km of altitude, the electron density grows to $5 \times 10^2 \text{ cm}^{-3}$. In these cases the reduced electric field exceeds the breakdown limit (120 Td) and, consequently, the dominant processes are the electron-impact ionization of N_2 and O_2



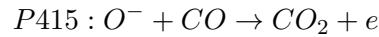
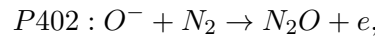
and



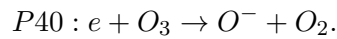
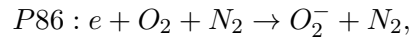
Between 75 km and 70 km and for both -CG and +CG lightning, the electron density increases almost one order of magnitude from its background value due to associative detachment (AD) of O^- by N_2 which has a strong dependence with the reduced electric field



These quantities persist in time (between 70 km with 2.8 cm^{-3} of electron density and 81 km with 280 cm^{-3} of electron density) for more than 10 s due to the balance between production electron processes



and loss electron processes



For low altitudes (below 70 km) and for the case of +CG lightning, a reduced electric field close to breakdown produces an increase in electron density of more than 5 orders of magnitude from background values mainly due to the AD process (P402). This rise in electron density occurs later in time and lasts less. The electron concentration begins to decrease to ambient values between 1 and 30 s after the parent lightning due to dissociative attachment of ozone (P40) and three-body electron attachment of N_2 and O_2 (P86).

We can see in Figure 2.39 the altitude-time dependence of the concentration of N_2^+ and O_2^+ ions. As we have shown previously, the main mechanisms of electron production under overvoltage conditions ($E_k/N > 120 \text{ Td}$) are electron-impact ionization of molecular nitrogen and molecular oxygen. For this reason, the concentration of N_2^+ increases to 10^2 cm^{-3} between 74 km and 81 km at the moment of the maximum electric field in the two cases studied (see Figure 2.39a and 2.39b). When the reduced

2. SPRITE HALOS

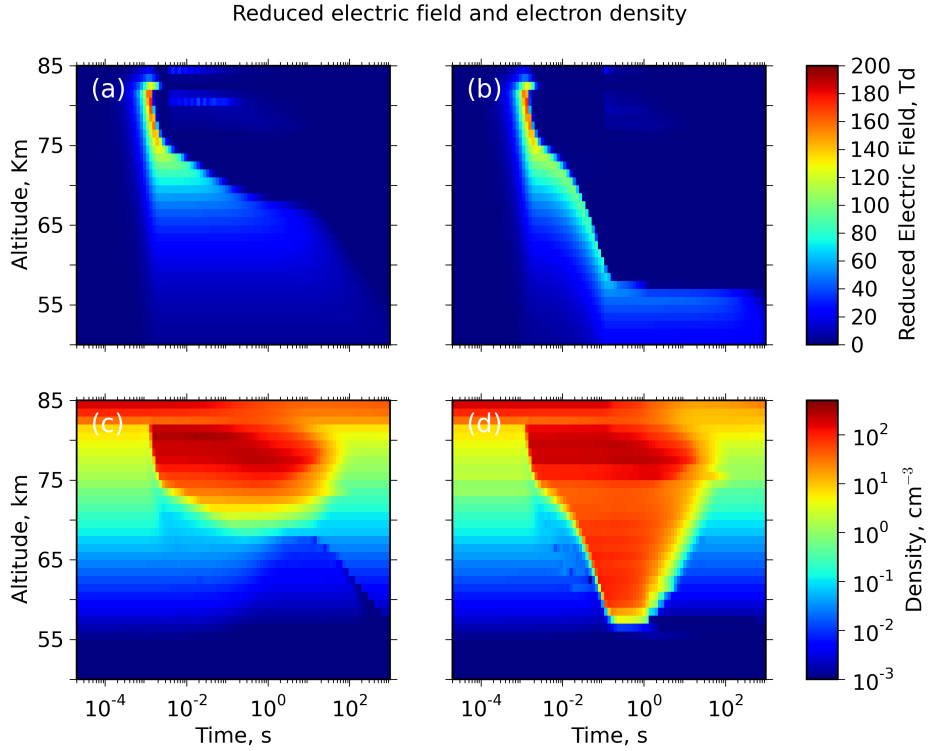
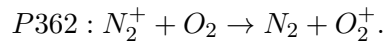


Figure 2.38: Altitude-time evolution of the reduced electric field ((a)-(b)) and electron density ((c)-(d)) due to cloud-to-ground lightnings. The plots in the left correspond to -CG lightnings and the plots in the right correspond to +CG lightnings both with 500 kAkm peak current moment.

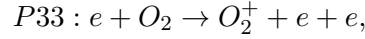
electric field falls below breakdown threshold ($\simeq 120$ Td), the density of N_2^+ returns to background values due to the charge transfer between N_2^+ and O_2



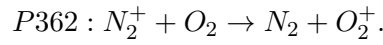
Below 68 km the chemical impact of a -CG lightning stroke in the concentration of N_2^+ is negligible (see Figure 2.39a). However, for the case of a +CG stroke, the N_2^+ density increases in more than 6 orders of magnitude above background values between approximately 85 km and 57 km (see Figure 2.39b). The significant N_2^+ growth is mainly due to the electron-impact ionization of N_2 .

The altitude and time-dependent behaviour of the concentration of O_2^+ positive ion in the cases of -CG and +CG lightnings is shown in Figures 2.39c and 2.39d, respectively. In both cases, the density of O_2^+ increases in more than 3 orders of

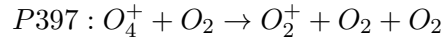
magnitude at the time of the maximum electric field between 80 km and 70 km of altitude. The main kinetic mechanism controlling the production of O_2^+ is electron-impact ionization of O_2



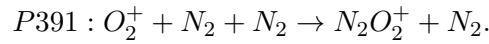
and the charge transfer process



After the current moment peak, the concentration of O_2^+ remains high for almost 10 s due to the balance between the chemical processes

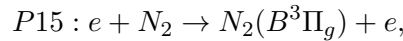


and

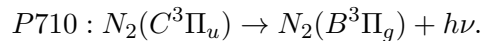


At altitudes below 70 km the continuous current of the +CG lightning produces a later increase in the O_2^+ density close to 5 orders of magnitude (see Figure 2.39d) that last less than at higher (> 70 km) altitudes.

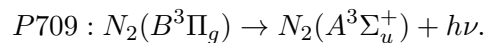
Figure 2.40 shows the behaviour of the density of $N_2(B^3\Pi_g)$ and the emission brightness of the first positive band system of N_2 , the main optical emission source of halos. The concentration of $N_2(B^3\Pi_g)$ evolves along the reduced electric field (see Figure 2.40a and 2.40b), reaching values of up to $2 \times 10^2 \text{ cm}^{-3}$ between 75 km and 81 km for the two kinds of lightning studied. Due to the high electron production the main mechanisms of $N_2(B^3\Pi_g)$ production are, in order of importance, electron-impact electronic excitation



and radiative decay $N_2(C^3\Pi_u) \rightarrow N_2(B^3\Pi_g)$



On the other hand, the process that reduces the concentration of $N_2(B^3\Pi_g)$ to its ambient values is the radiative decay responsible for the optical emission of the first positive band system of N_2



2. SPRITE HALOS

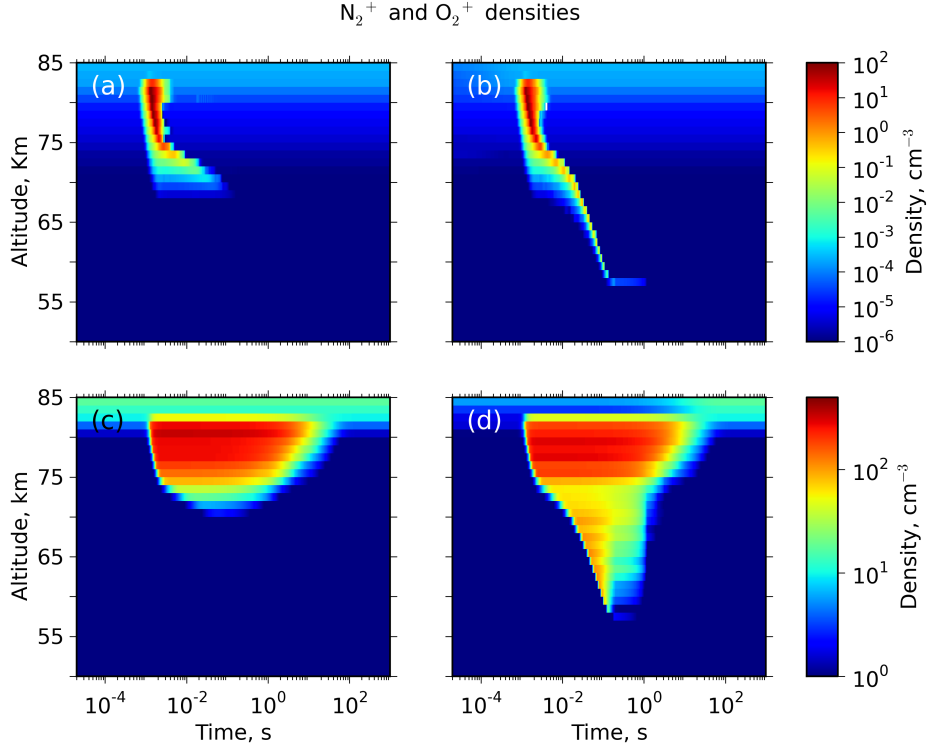
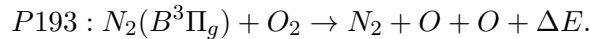


Figure 2.39: Altitude-time evolution of the N_2^+ density ((a)-(b)) and the O_2^+ density ((c)-(d)) due to cloud-to-ground lightnings. The plots in the left correspond to -CG lightning and the plots in the right correspond to +CG lightning both with 500 kAkm peak current moment.

For -CG lightnings and below to 75-74 km, the production of $N_2(B^3\Pi_g)$ is negligible (see Figure 2.40a). However for +CG lightnings, from approximately 80 km to 73 km the density of $N_2(B^3\Pi_g)$ increases to 10 cm^{-3} at the time of the maximum electric field (see Figure 2.40b). In this case, the main mechanism which recovers the ambient concentration of $N_2(B^3\Pi_g)$ is exothermic quenching through collisions with O_2 molecules



The significant increase in the $N_2(B^3\Pi_g)$ density results in a strong emission of $1PN_2$ which, between 80-75 km of altitude, can exceed 100 MR in the cases of -CG and +CG lightnings (see Figure 2.40c and 2.40d). For +CG lightning (see Figure 2.40d), the emission brightness of the $1PN_2$ reaches 10 MR between 75 km and 72 km while the 20 kAkm continuous current is on. Once again, we must be careful with these results

because at low altitudes the model assumptions might not be completely valid since sprite streamers emergence is likely.

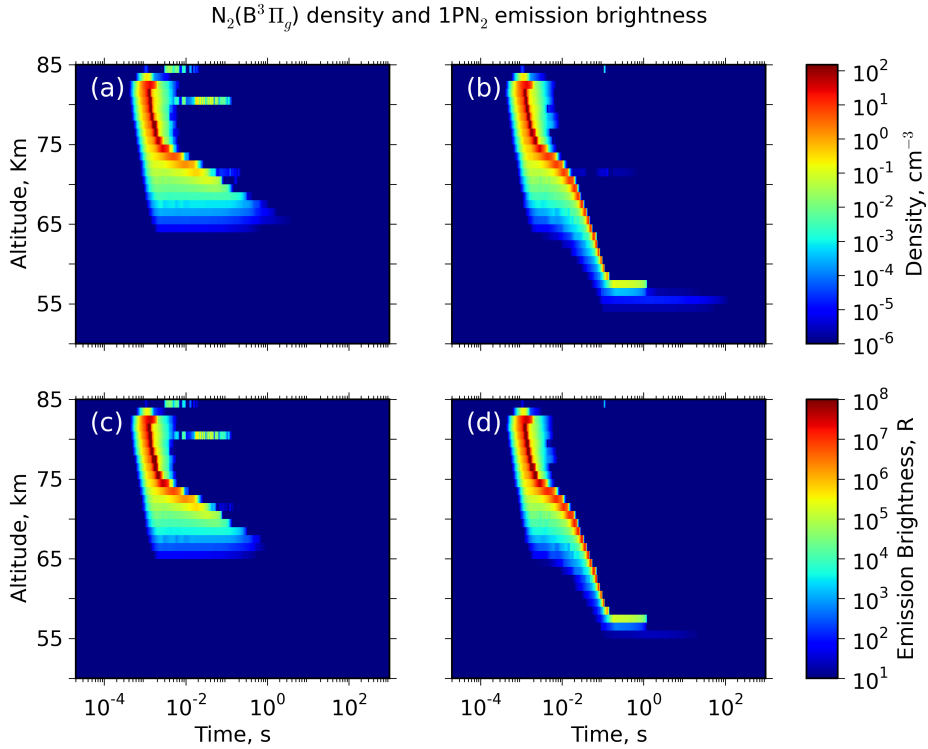
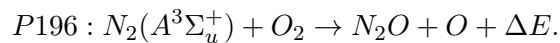


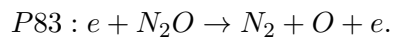
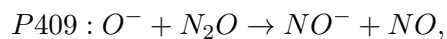
Figure 2.40: Altitude-time evolution of the $N_2(B^3\Pi_g)$ density ((a)-(b)) and the first positive band system ($1PN_2$) emission brightness ((c)-(d)) due to cloud-to-ground lightnings. The plots in the left correspond to -CG lightning and the plots in the right correspond to +CG lightning both with 500 kAkm peak current moment. The mistake at 80 km of altitude in the case of -CG discharges (Plots (a) and (c)) is due to numerical fluctuations.

Finally, we show the variation of the neutral species in the ground state N_2O (see Figure 2.41), which is a greenhouse gas and a very important species in the ozone cycle. The strong reduced electric field (see Figure 2.38) generated due to the presence of -CG and +CG lightning produces important variations in the N_2O concentration of up to 200 cm^{-3} above its ambient density in the 70-82 km range (see Figures 2.41a and 2.41b). The main mechanism responsible of the N_2O small variation is exothermic quenching of metastable $N_2(A^3\Sigma_u^+)$ (lifetime $\simeq 2\text{ s}$) with molecular oxygen

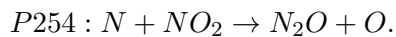


2. SPRITE HALOS

The enhancement, above its initial ambient value, of the N₂O density is maintained during all the time of simulation by the balance between the processes P196 and P402, and



From 65 km to approximately 55 km of altitude, we show in Figure 2.41b (+CG case) a variation in the N₂O density of up to $2 \times 10^3 \text{ cm}^{-3}$ over its initial ambient density. The mechanism responsible of this N₂O increase is AD of O⁻ by N₂ since, at low altitudes, the reduced electric field is too low to produce N₂(A³Σ_u⁺) but high enough to activate the mechanism of associative detachment. The enhanced N₂O density persists due to the balance between the process P409 and



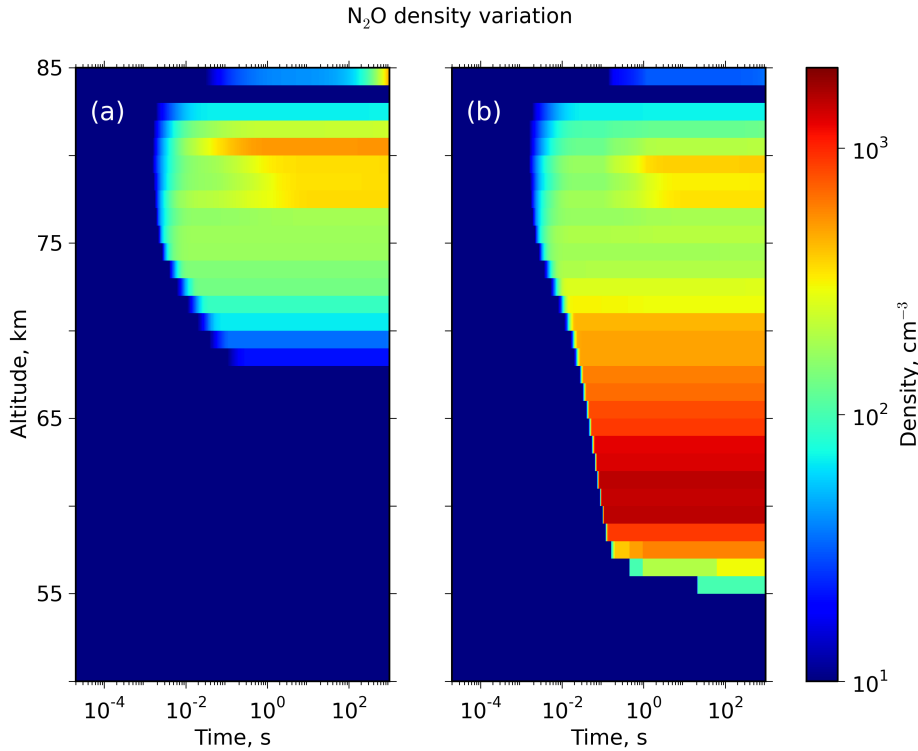


Figure 2.41: Altitude-time evolution of the N₂O density ((a)-(b)) variation due to cloud-to-ground lightnings. The plot in the left correspond to -CG lightning and the plot in the right correspond to +CG lightning both with 500 kAkm peak current moment.

2.4 Laboratory experiments

2.4.1 Experimental set-up for hollow cathode discharges in air

Non-thermal low temperature air plasmas were produced by means of a low pressure, hollow cathode discharge reactor, which has been previously used to study plasmas of air [Castillo et al., 2004b] and nitrogen oxides [de los Arcos et al., 1998, Castillo et al., 2002, 2004a]. Hollow cathode discharges provide a uniform, stable, and relatively intense light emission in the negative glow, as well as gas temperatures close to room temperature, which render clear advantages for spectroscopic purposes related with atmospheric research.

The detailed description of the reactor is given elsewhere [Castillo et al., 2004b, de los Arcos et al., 1998]. It has a modular configuration, suitable for emission [Castillo et al., 2004b] and absorption spectroscopy [de los Arcos et al., 1998], as well as for mass

2. SPRITE HALOS

spectrometry and the use of electrical probes [Castillo et al., 2004b, de los Arcos et al., 1998], with the proper selection of the different adaptors or windows to be employed at its two ends.

We can see in Figure 2.42 the experimental set up of the hollow cathode discharge used and an image of the air plasma produced. In brief, it has a cylindrical electrode geometry and consists of a grounded stainless steel hollow cathode, 16 mm inner diameter, 90 mm long, and two circular copper anodes, placed symmetrically at the ends of the cathode to ensure the uniformity and extension of the negative glow along the whole cathode length. The total volume of the cell is 130 cm^3 . The electrodes are refrigerated by circulating water. The discharge is fed by a DC source, able to supply up to 2 kV and 200 mA. Plasma currents $\simeq 20 - 100 \text{ mA}$ and voltages $\simeq 350 - 450 \text{ V}$ were applied during the present experiments. The discharge was sustained in a continuous flow of natural air ($\simeq 5 - 20 \text{ sccm}$), at pressures of 0.1 - 2 mbar. Pressure and gas flow were regulated by a needle valve at the input, and a rotary pump with a regulating valve at the exit. Diffusion of excited species to the cathode walls, where they might collide and experiment de-excitation, is described by Fick's Law [Levine, 1978, McDaniel, 1989]. We have assumed a model of rigid spheres and employed the effective diameters of N_2 and O_2 from Hirschfelder et al. [1954] to estimate the typical diffusion times along the cathode radius, as it was done in Castillo et al. [2004a,b] and de los Arcos et al. [1998]. Under the present air pressures ranging from 0.1 to 2 mbar these diffusion times result to be within the interval 0.1 - 1 ms, considerably longer than the radiative lifetimes of the excited N_2 and N_2^+ levels in this work, whereas the average time between successive collisions at these pressures (equivalent to some 68 - 50 altitudes) are of some $10^{-6} - 10^{-7} \text{ s}$, respectively [McDaniel, 1989].

Complete emission spectra of the plasmas were recorded in the 300 - 1060 nm wavelength range through a BK7 optical window. A red filter (cut off at 600 nm) was used to avoid second order lines in spectra taken at wavelengths above this value. The light from the discharge was transmitted by an optical fibre imaged on the entrance slit of a Jobin Yvon-HORIBA FHR1000 spectrometer, 1 m focal length, in Czerny-Turner configuration, with two concave mirrors and two interchangeable planar gratings of 1200 and 1800 grooves/mm, and was detected by a front exit SYNAPSETM CCD camera, or a side exit photomultiplier Hamamatsu R928P. The spectral resolution of the FHR1000 spectrometer spans from 0.006 nm to 0.13 nm, depending on the

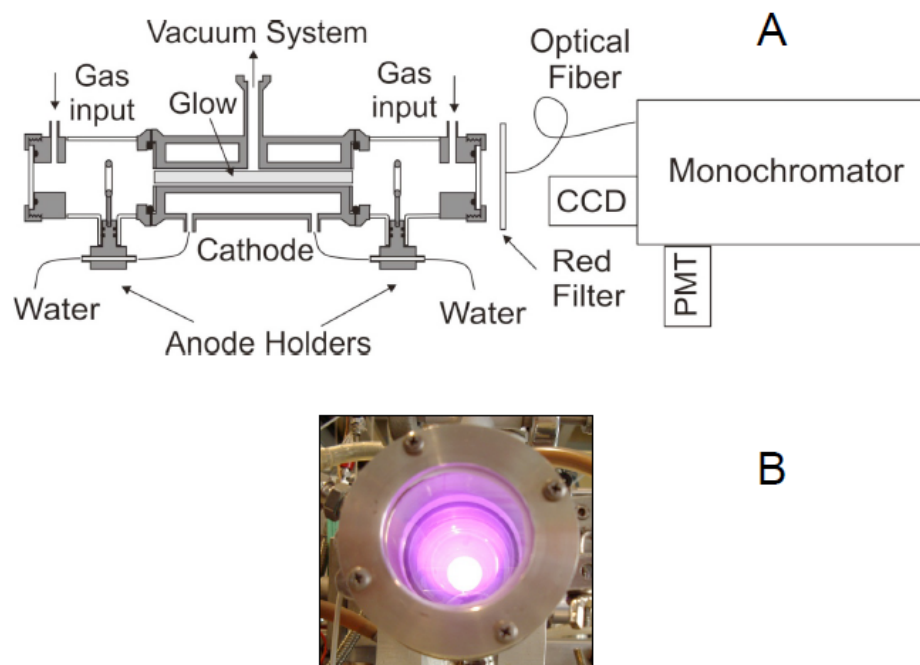


Figure 2.42: Experimental set up (panel A) of the DC hollow cathode discharge used for spectroscopic diagnostics and an image (panel B) of the generated air plasma where a more intense pink light emission can be seen in the center of the discharge

2. SPRITE HALOS

slit widths, grating and detector used. This resolution can be numerically lowered by convolution of the acquired spectra with a Gaussian profile of the desired width to simulate broader line profiles. With this method, one can easily apply some of the analytical procedures for gas temperature estimations proposed here (see below), or can compare the originally high resolution spectra with the spectra obtained with lower resolution field spectrometers. Alternatively, an Ocean QE65000 spectrograph with 300 grooves/mm grating, 25 μm slit width and CCD was employed, supplying 2 nm spectral resolution spectra. The spectral efficiency calibrations of these instruments were obtained from their spectral responses to the emission of a previously calibrated 500 W tungsten lamp. The spectra acquisition times were selected, depending on the spectrometer, detector and spectral resolution used in each case, in order to obtain signal to noise ratios in the spectra of the HC discharges good enough for not being a limiting factor in the temperature estimation methods proposed here. These signal to noise ratios increased even more with the convolution process employed to decrease the spectral resolution of the spectra originally taken with the FHR1000. It should be mentioned that the improvement of signal to noise ratios is of vital interest in measurements of very short emission features like those produced by TLEs.

2.4.2 Brief description of GRASSP

The instrument GRASSP (GRanada Sprite Spectrograph and Polarimeter) is formed by a spectrograph and a polarimeter, being each of them located in the two arms of a mobile mount. So far, only the spectrograph is used and it consists of a f/3.4 and 170 mm focal length lens telescope which can gather an optical beam at its focal plane, where an entrance slit of about 100 μm is placed before a F/3.8 and 190 mm focal length field lens, in order to define the observed field of view of 4 degrees and prevent vignetting. The slit is oriented parallel to the horizon to optimize the likelihood of TLE detection. After the field lens, a F/2.8 and 135 mm focal length collimator is placed to narrow the beam that will reach the dispersive element. After the 1440 grooves/mm and 70 \times 70 mm aperture diffraction grating, a commercial intensified (60 dB + 30 dB) CCD camera of 1360 x 1024 pixels, 0.01 mm/px, F/1.7 and 50 mm in focal length provides the spectral pattern on the detector. The described spectrograph provides a free spectral range of 110 nm (650 nm to 760 nm), with a mean spectral resolution of $R = \lambda/\Delta\lambda = 1500$; $\Delta\lambda = 0.45$ nm. A calibrated halogen tungsten spectral lamp was

used in order to obtain the spectroscopic system response and to make further spectral efficiency corrections. In order to test it, the spectra of three different commercial cylindrical lamps of N₂, air and Ne at 0.2 mbar, with the electrodes separated by a distance of 26 cm (0.5 cm width) and fed by a 5 kV, 10 mA DC source, were used. The spectra obtained from these commercial lamps were corrected by the instrument spectral sensitivity response function and compared to the spectra of air plasmas produced in DC hollow cathode reactors under similar gas pressure (0.23 mbar) to check the instrument performance.

2.4.3 Gas temperature determination by spectral analysis of low pressure air and N₂ plasmas

In this section we will describe the three spectroscopic methods used, together with their range of applicability, to determine the rotational (gas) temperature of laboratory air plasmas produced at pressures (0.1 mbar ($\simeq 70$ km) $\leq p \leq 2$ mbar ($\simeq 45$ km)), similar to the ones under which TLE air plasmas are produced in the Earth atmosphere.

2.4.3.1 Rotational structure of N₂⁺(B²Σ_u⁺, v' = 0 → X²Σ_g⁺, v'' = 0)

When the resolution of the spectrograph employed is high enough (between 0.005 nm and 0.05 nm), we can use different bands of the first negative system of N₂⁺, that is N₂⁺-1NG, to determine the rotational (gas) temperature by optical emission spectroscopy. In order to use this method, we first need to choose a particular (v', v'') band and determine the conditions under which the emitting rotational levels are in thermal (Boltzmann) equilibrium. Then, the intensity of the emission lines in a rovibronic band, being J' and J'' the rotational quantum numbers of the upper and lower rotational levels, is given by the thermal distribution of the emitting rotational levels as

$$I_{em}(T_R) = \frac{C_{em} \times \nu^4}{Q_R} \times (J' + J'' + 1) \times e^{-B_{v'} J'(J'+1)hc/kT_R}, \quad (2.13)$$

where T_R is the rotational temperature, C_{em} is a constant depending on the change of the dipole moment and the total number of molecules in the initial vibrational level (v') [Herzberg, 1950] and ν, Q_R and B_{v'} are, respectively, the frequency, the rotational partition function and the first order rotational constant of the upper vibrational level (v') of the excited state N₂⁺(B²Σ_u⁺). The symbols c, h and k stand for the speed of light

2. SPRITE HALOS

and the Planck and Boltzmann constants, respectively. Since the second order rotational constant $D_{v'}$ is usually $10^{-5}B_{v'}$, equation (2.13) remains a good approximation for low $J' \leq 25$ (as in our case). From equation (2.13) we have

$$\ln F = A - \frac{B_{v'} J'(J' + 1)hc}{kT_R} \quad (2.14)$$

where $F = I_{em}/(J' + J'' + 1)$ and $A = \ln(C_{em}\nu^4/Q_R)$ is almost constant for a given rotation-vibration band at a given temperature. We can see from equation (2.14) that by plotting $\ln(I_{em}/(J' + J'' + 1))$ against $J'(J' + 1)$ a straight line is obtained whose slope is $B_{v'}hc/kT_R$. Thus, if the relative line emission intensities (I_{em}) have been measured and the rotational constant $B_{v'}$ of the excited state $N_2^+(B^2\Sigma_u^+)$ is known, the rotational temperature (T_R) of the emitting source can be obtained [Herzberg, 1950]. The above procedure of obtaining T_R remains valid as long as the excitation of the emitting levels is purely thermal or if they are excited in electron-impact collisions. If other excitation channels (such as collisions with other neutrals, dissociation of molecules and/or recombination of molecular ions in electric discharges) come into play, the population distribution of the emitting levels can considerably deviate from the thermal (Boltzmann) distribution. We see in Figure 2.43 an example of a Boltzmann plot corresponding to the case of 1.5 mbar ($\simeq 48$ km) obtained with the hollow cathode discharge and the Jobin-Yvon spectrometer using the CCD and the 1800 grooves/mm grating, with a spectral resolution of 0.023 nm. The two lines correspond to the fits of the even (blue line) and odd (red line) J'' values resulting in gas temperatures of 474 K and 426 K, respectively. The difference in temperatures is within 10 % discrepancy, attributable to the experimental uncertainty in line intensity measurements. The rotational (gas) temperature that we consider is the mean value (450 K) of the even and odd J'' fits.

2.4.3.2 Subband head peaks of $N_2(B^3\Pi_g, v' \rightarrow A^3\Sigma_u^+, v'')$ vibrational transitions

Given a certain (v', v'') band of the first positive group of N_2 , that is, $N_2(B^3\Pi_g, v' \rightarrow A^3\Sigma_u^+, v'')$ (or simply $N_2 - 1PG$), Simek and DeBenedictis [1995] proposed a method to estimate the gas temperature. It is based on the use of the ratios of the intensities of three selected peaks (I_1, I_2 and I_3) formed by the three sub-band heads of the (3,0) transition. The upper $N_2(B^3\Pi_g)$ state, with spin and orbital quantum numbers $S = 1$ and $\Lambda = 1$, consists of $(2 - \delta_{0,\Lambda})(2S + 1) = 6$ electronic substates ${}^3\Pi_{\Omega g}^{e,f}$, where (e, f)

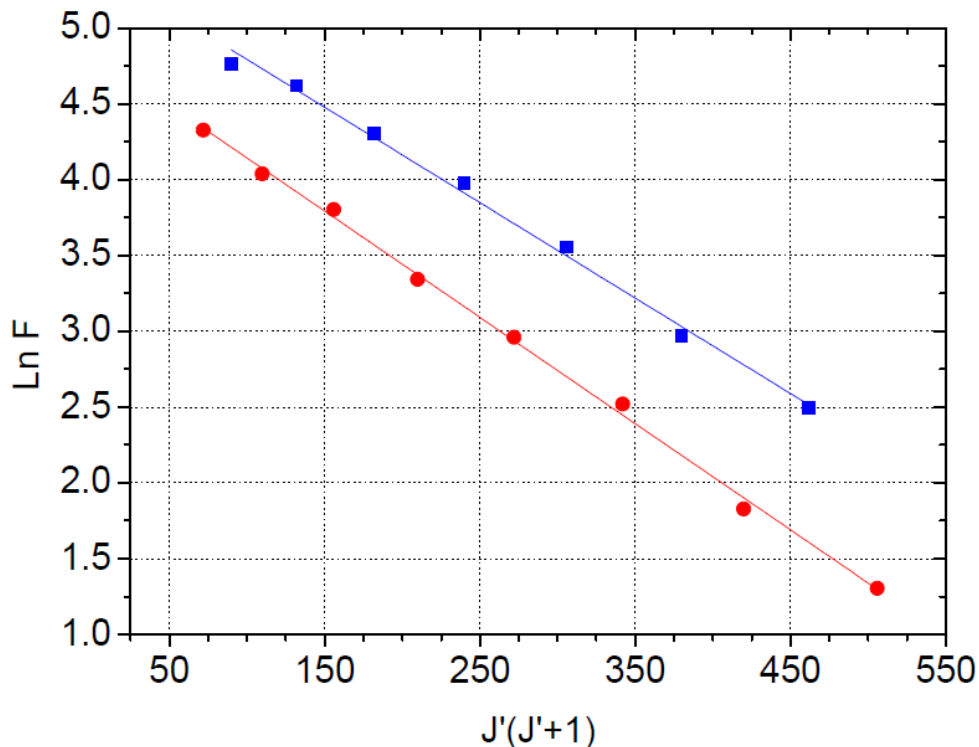


Figure 2.43: Boltzmann plots ($\ln F$ vs $J'(J'+1) = (J'' + 1)(J'' + 2)$, see equation (2.13)) of the rotational R - branch ($\Delta J = +1$) transitions involving even (square symbols and blue line) and odd (circles and red line) J'' of $N_2^+(B^2\Sigma_u^+, v' = 0, J' \rightarrow X^2\Sigma_g^+, v'' = 0, J'')$ in a 1.5 mbar ($\simeq 48$ km) DC hollow cathode discharge in air. The rotational (gas) temperatures resulting from the even and odd J'' are 474 K and 426 K, respectively. The $N_2^+(B^2\Sigma_u^+, v' = 0, J' \rightarrow X^2\Sigma_g^+, v'' = 0, J'')$ spectrum was recorded with the Jobin-Yvon spectrometer using the CCD and the 1800 grooves/mm grating providing a spectral resolution of 0.023 nm

denotes the parity of the state and $\Omega = |\Lambda + \Sigma|$ with Σ taking $(2S + 1)$ values from $-S$ to $+S$. The $\delta_{0,\Lambda}$ is a Kronecker delta (equal to 1 if $\Lambda = 0$ and 0 for all other values). The method proposed by Simek and DeBenedictis [1995] makes use of two main facts: (i) the relative populations of the ${}^3\Pi_{\Omega_g}^{e,f}$ substates in the $N_2(B^3\Pi_g)$ electronic state are temperature dependent, and (ii) the subband heads formed by individual branches are well separated in wavelengths [Simek, 1994].

The method was extended for other 1PG bands [Simek, 1994] and, actually, allows using three (v', v'') bands of the N_2 - 1PG corresponding to (2,0), (1,0) and (0,0)

2. SPRITE HALOS

transitions, which usually show stronger intensities in the 1PG spectrum, compared to the (3,0) band. The wavelength intervals for each of the selected (v' , v'') bands are (678 nm - 690 nm) for (3,0), (760 nm - 780 nm) for (2,0), (870 nm - 900 nm) for (1,0) and (1020 nm - 1060 nm) for (0,0).

When applying the method using the (3,0) or (2,0) bands, one needs to take the ratios of the intensities of the second (I_2) and third (I_3) peaks to the intensity of the first sub-band head (I_1) of a given band, that is, one need to experimentally estimate $R_{21} = I_2/I_1 = f_1(\Delta\lambda, T_R)$ and $R_{31} = I_3/I_1 = f_2(\Delta\lambda, T_R)$ in each case. If, instead, one wants to use the (1,0) or (0,0) bands then, in addition to R_{21} and R_{31} , one can also determine $R_{41} = I_4/I_1 = f_3(\Delta\lambda, T_R)$, that is, the ratio of the fourth peak intensity (I_4) to the intensity of the first sub-band head (I_1) of the (1,0) or (0,0) band, respectively. Once R_{21} , R_{31} and R_{41} are known for any of these two bands, Simek [1994] provided a procedure to calculate $T_{21} = T_{21}(R_{21}, \Delta\lambda)$, $T_{31} = T_{31}(R_{31}, \Delta\lambda)$ and $T_{41} = T_{41}(R_{41}, \Delta\lambda)$ in a way that, for a given spectral resolution ($\Delta\lambda$), the mean value of T_{21} , T_{31} and T_{41} provides the rotational (gas) temperature. All the data and coefficients needed to implement this fast T_R estimation method can be found in Simek and DeBenedictis [1995] for the (3,0) band and in [Simek, 1994] for the (2,0), (1,0) and (0,0) bands. The position of the I_1 , I_2 , I_3 and I_4 peaks were given by Simek [1994] and are now reproduced in Table 2.1.

Band	I_1	I_2	I_3	I_4
(0,0)	1050.0 - 1051.2	1047.5 - 1048.5	1045.6 - 1046.4	1053.0 - 1054.5
(1,0)	890.5 - 891.5	888.8 - 889.4	887.5 - 888.1	893.4 - 894.0
(2,0)	774.8 - 775.4	773.5 - 774.1	771.0 - 771.6	-
(3,0)	687.0 - 687.6	686.0 - 686.6	685.2 - 685.8	-

Table 2.1: I_1 , I_2 , I_3 and I_4 sub-band peak positions (nm) of the (0,0), (1,0), (2,0) and (3,0) bands of the N_2 - 1PG

The method proposed by Simek and DeBenedictis [1995] can be of wide use since the N_2 - 1PG is one of the most accesible band systems of N_2 extending from the red to the near infrared. In addition, since the method deals with optical emissions from the N_2 - 1PG, it can be applied to determine the rotational (gas) temperature in a

variety of air plasmas produced in a wide range of pressures from 0.03 mbar (\simeq 75 km altitude) to high pressures (even atmospheric pressure) as long as the rotational-translation relaxation time at the considered pressure remains much smaller than the characteristic time (τ_q) of the collisional (quenching) deexcitation. Moreover, it allows the calculation of the rotational (gas) temperatures in the range 200 - 1500 K (with a step of $dT = 25$ K) using medium spectral resolutions that depend on the N_2 - 1PG (v' , v'') band selected. In particular, the best sensitivity of the method is achieved when using spectral resolutions in the ranges 0.1 - 0.2 nm for the (3,0) band and 0.2 - 0.3 nm for the (2,0), (1,0) and (0,0) bands. Lower spectral resolutions can be employed, though the sensitivity of the method decreases. The lowest recommended spectral resolutions are, respectively, 0.5 nm, 0.6 nm, 0.68 nm and 0.76 nm for the (3,0), (2,0), (1,0) and (0,0) bands [Simek, 1994].

Since 1995, TLE spectroscopy campaigns have provided different spectra of the N_2 - 1PG visible and near infrared optical emissions covering the spectral range between 540 nm and 900 nm. These spectroscopic recordings were done with spectral resolutions of 13 nm (at 900 nm) and 9 nm (at 620 nm) Morrill et al. [1998] for 57 km altitude sprite spectrum and 7 nm (across the entire analyzed range of 619 - 897 nm) for 53 km altitude sprite spectrum, 9 nm (540 - 800 nm) [Mende et al., 1995], 10 nm and 6 nm (540 nm - 840 nm) [Hampton et al., 1996] and 3 nm (640 nm - 820 nm) that is the best resolution so far achieved [Kanmae et al., 2007]. The papers by Morrill et al. [1998] and Bucselo et al. [2003] dealt with sprite tendrils (53 km and 57 km) spectroscopic observations and provided preliminary spectral data of the N_2 - 1PG (1,0) band up to \simeq 900 nm. However, as acknowledged by the authors, their results regarding 57 km altitude spectra were affected by sensitivity calibration errors, while those of the 53 km altitude spectrum were more certain in the same spectral range [Bucselo et al., 2003]. These results suggest that the (3,0) and (2,0) bands of the N_2 - 1PG are the most accessible bands to derive the rotational (gas) temperature using the method proposed by Simek and DeBenedictis [1995]. However, spectral resolutions one order of magnitude higher than the ones used so far in TLE spectroscopy campaigns are needed in order to partially resolve the rotational structure of the different N_2 - 1PG (v' , v'') bands selected.

2. SPRITE HALOS

2.4.3.3 Spectral fitting of $N_2(B^3\Pi_g, v' \rightarrow A^3\Sigma_u^+, v'')$ rovibronic bands

We have developed a program written in python programming language to calculate the synthetic spectrum of the rovibronic bands for the N_2 - 1PG that involves transitions between the upper electronic state $N_2(B^3\Pi_g)$ (with $\Lambda' = 1$) and the lower electronic state $N_2(A^3\Sigma_u^+)$ (with $\Lambda'' = 0$). The $N_2(A^3\Sigma_u^+)$ state (with spin-orbit constant $A_{v''} = 0$) belongs to the Hund's case (b). However, the coupling of the $N_2(B^3\Pi_g)$ electronic state is Hund's case (a) for the lower rotational quantum number J' values and Hund's case (b) for J' values higher than 15 [Herzberg, 1950]. Therefore, we have considered the intermediate Hund case coupling for the $N_2(B^3\Pi_g)$ state. In calculating the N_2 - 1PG rovibronic band spectrum, we have taken into account the parity (Λ -type doubling) of the 3 substates ${}^3\Pi_{\Omega_g}^{e,f}$ of the upper electronic state $N_2(B^3\Pi_g)$. Thus, the triplet fine structure of the $N_2(B^3\Pi_g \rightarrow A^3\Sigma_u^+)$ rovibronic band spectrum consists of a total of 27 branches divided into the 3 sub-bands ${}^3\Pi_{0g}^{e,f} \rightarrow {}^3\Sigma_u^+$, ${}^3\Pi_{1g}^{e,f} \rightarrow {}^3\Sigma_u^+$ and ${}^3\Pi_{2g}^{e,f} \rightarrow {}^3\Sigma_u^+$ with 9 branches, each denoted P , Q and R that correspond to $\Delta J = J' - J'' = -1, 0, +1$, respectively. At medium spectral resolutions (0.1 - 0.5 nm) the small spin splitting causes the overlap of the three subbands producing the appearance of, depending on the (v', v'') considered, 3 or 4 subband head peaks whose positions are listed in Table 2.1 [Simek and DeBenedictis, 1995], [Simek, 1994]. Given a set of (v', v'') vibrational bands within the N_2 - 1PG, the emission intensity of each of the rovibronic transitions considered between (v', J') and (v'', J'') is given by [Whiting et al., 1980]

$$I_{v'', J''}^{v', J'}(T_R) = N_{v', J'}(T_R) A_{v'', J''}^{v', J'} \frac{hc}{\lambda_j} = C_1 \times N_{v', J'}(T_R) B_{v''}^{v'} \frac{\nu_j^A S_{J', J''}}{2J + 1}, \quad (2.15)$$

where C_1 is a constant and ν_j , $S_{J', J''}$, v' , J'_j and N_{v', J'_j} are, respectively, the frequency, the Hönl-London (or line strength) factor, the vibrational ($0 \leq v' \leq 12$) and rotational ($2 \leq J'_j \leq 39$) quantum numbers, and the population of the corresponding upper rovibronic level, each for the j -th rotational line. T_R stands for the rotational temperature and $A_{v'', J''}^{v', J'}$ is the Einstein spontaneous emission probability. In equation (2.15), we have assumed that

$$A_{v'', J''}^{v', J'} = \frac{A_{v'', J''}^{v', J'} S_{J', J''}}{(2 - \delta_{0, \Lambda})(2S + 1)(2J + 1)} = \frac{B_{v''}^{v'} S_{J', J''}}{\lambda_j^3 (2 - \delta_{0, \Lambda})(2S + 1)(2J + 1)} \quad (2.16)$$

where $B_{v''}^{v'}$ are the (v', v'') Einstein spontaneous emission probabilities tabulated by Gilmore et al. [1992]. The $S_{J', J''}$ rotational line intensity strength factors, that is, the

Hönl-London factors, are normalized as $\sum S_{J'_j, J''_j} = (2 - \delta_{0, \Lambda'}, \delta_{0, \Lambda''})(2S + 1)(2J + 1)$ [Whiting et al., 1980] where $\delta_{0, \Lambda'}$ and $\delta_{0, \Lambda''}$ are Kronecker deltas (equal to 1 if $\Lambda' = 0$ or $\Lambda'' = 0$ and 0 for all other values) and $(2S + 1)$ is the spin multiplicity. The summation in $\sum S_{J'_j, J''_j}$ is over all allowed transitions from (or to) the group of $(2 - \delta_{0, \Lambda})(2S + 1)J$ levels with the same value of J' or J'' and, since the $\sum S_{J'_j, J''_j}$ sum rule is symmetrical in J' and J'' , explicit use of the primes is omitted. In addition, the factor of 2, which appears in the sum rule for all spin-allowed transitions, except $\Sigma^\pm \leftrightarrow \Sigma^\pm$, is present because the summation is over both Λ (parity) substates of non Σ states. Following Whiting et al. [1980], in $\Sigma \leftrightarrow \Pi$ and $\Pi \leftrightarrow \Sigma$ transitions, even though only the Π state contains two Λ substates, the factor 2 is present in the sum rule of $S_{J'_j, J''_j}$ regardless of which state is the initial one.

Assuming equilibrium (Boltzmann) distribution within the rotational levels, the concentration of a single rotational level (J'_j) in each of the electronic substates ${}^3\Pi_{\Omega g}^{e, f}$ can be written as [Simek and DeBenedictis, 1995]

$$N_{v', J'_j}(T_R) = N_{v'} \frac{\exp(\frac{-hc}{kT_R} A_{v'} \Lambda \Sigma)}{1 + 2 \cosh(\frac{hc}{kT_R} A_{v'})} \frac{(2J'_j + 1) \exp(\frac{-hc}{kT_R} F(J'_j))}{Q_R(T_R)} \Phi_{J'_j} \quad (2.17)$$

where v' is the upper vibrational quantum number, $N_{v'}$ is the concentration of the v' th vibrational level, $Q_R = kT_R/hcB_{v'}$, $F(J'_j)$ is the rotational energy of a given upper J'_j rotational level, and $\Phi_{J'_j}$ is an alternation factor which is a function of the nuclear spin I and takes into account the parity (e, f) of the considered rotational level. For homonuclear molecules (like N_2) their values are $(I + 1)/(2I + 1)$ for symmetric levels and $I/(2I + 1)$ for asymmetric levels. For N_2 , $I = 1$ and thus $\Phi_{J'_j} = 2/3$ or $1/3$ for symmetric levels (e) and asymmetric levels (f), respectively.

Considering equations (2.15)-(2.17) and, given a set of (v', v'') vibrational bands within the $N_2 - 1PG$, the emission intensity of each of the rovibronic transitions considered between (v', J') and (v'', J'') is given by

$$I_{v'', J''_j}^{v', J'_j}(T_R) = C_2 \times N_{v'} \frac{S_{J'_j, J''_j}}{\lambda_j^4} \frac{1}{T_R} \Phi_{J'_j} \exp(\frac{-hc}{kT_R} F(J'_j)), \quad (2.18)$$

where C_2 is a constant and the $1/T_R$ dependency comes from the expression of $Q_R(T_R)$. In calculating the line intensities, we computed the Hönl-London factors using the formulae given by Kovacs [1969] for triplet transitions in the intermediate regime between Hund's case (a) and case (b).

2. SPRITE HALOS

For the electronic states $N_2(B^3\Pi_g)$ and $N_2(A^3\Sigma_u^+)$, every rotational level N is subdivided in three sub-levels with quantum numbers J corresponding to $J = N - 1$, $J = N$ and $J = N + 1$ corresponding, respectively, to the rotational energies $F_3(J'_j)$, $F_2(J'_j)$ and $F_1(J'_j)$. For the rotational energies of each of the three sub-states of $^3\Pi$ states, we have used the expressions given by Budo [1935], valid for any degree of spin uncoupling [Herzberg, 1950]. For the three sub-states of the lower $^3\Sigma$ electronic state, we have used the formulae for the rotational energy terms from Mulliken [1930], Roux et al. [1990]. In order to calculate $F_3(J'_j)$, $F_2(J'_j)$ and $F_1(J'_j)$ we have considered the spin-orbit ($A_v = 0$ for $N_2(A^3\Sigma_u^+)$) rotational and centrifugal spectroscopic constants of the $N_2(B^3\Pi_g)$ and $N_2(A^3\Sigma_u^+)$ states given by Roux et al. [1983]. The electronic energies T'_e and T''_e of, respectively, the $N_2(B^3\Pi_g)$ and $N_2(A^3\Sigma_u^+)$ electronic states, together with the spectroscopic constants (ω_e , $\omega_e x_e$, $\omega_e y_e$ and $\omega_e z_e$), needed to evaluate the vibrational energy terms of the $N_2(B^3\Pi_u)$ and $N_2(A^3\Sigma_u^+)$ electronic states, were taken from Naghizadeh-Kashani et al. [2002]. For a given (v', v'') transition within the N_2 - 1PG, the wavelengths of each of the 27 rotational lines involved in a (J', J'') rotational band are $\lambda_{kl}^{J', J''} (cm) = 1/(\nu_{ev}(cm^{-1}) + F'_k(J') - F'_l(J''))$, where $\nu_{ev}(cm^{-1}) = (T'_e - T''_e) + G'(v') - G''(v'')$ with $1 \leq k, l \leq 3$ and $\Delta J = J' - J''$. Given the rotational levels J' and J'' , the three possible transitions between the subrotational levels (k, l) of, respectively, (J', J'') , correspond to those fulfilling $\Delta J = -1$ (branch P), 0 (branch Q) and $+1$ (branch R) selection rules. So, we end up having 3 allowed rotational transitions in each of the 9 pairs (k, l) .

In order to compare the synthetic spectra with the observed (measured) spectra, each line of the synthetic spectrum needs to be convolved with an instrument function taking into account the finite spectral resolution of the spectrograph used. To model the instrument spectral broadening, we have used a combination of a Gaussian and a Lorentzian function, that is, a Voigt function as [Biloiu et al., 2007]

$$S_{p,w}(\lambda) = p \frac{\sqrt{4 \ln 2}}{\sqrt{\pi} w} \exp\left(-\frac{4 \ln 2}{w^2}(\lambda - \lambda_{kl}^{J', J''})^2\right) + \frac{2}{\pi} \frac{(1-p)w}{w^2 + 4(\lambda - \lambda_{kl}^{J', J''})^2} \quad (2.19)$$

where p and $1-p$ are the relative magnitudes of the Gaussian and Lorentzian functions contributions, respectively, w is a parameter measuring the spectral resolution as the full width at half maximum (FWHM) of the line considered, and $\lambda_{kl}^{J', J''}$ is the central wavelength or the wavelength corresponding to the calculated (synthetic) rotational

lines. We have used Gaussian lines shapes ($p = 1$) in spectral fitting of laboratory measured spectra of particular (v', v'') rovibronic transitions of $N_2(B^3\Pi_g \rightarrow A^3\Sigma_u^+)$ recorded with 0.43 nm spectral resolution to obtain the rotational (gas) temperature (see Figures 2.45, 2.46 and 2.47b, 2.47c). However, Voigt line shapes ($p = 0.5$) were used in spectral fitting of partial N_2 1PG spectra recorded with 2 nm spectral resolution to derive the VDF of $N_2(B^3\Pi_g)$ (see Figures 2.49b, 2.49c).

2.4.4 Experimental quantification of vibrational distribution functions

In order to experimentally obtain the VDF of $N_2(B^3\Pi_g)$ from laboratory data, we have fitted synthetic spectra of N_2 1PG to experimental spectra recorded using different pressures (0.1 mbar - 2 mbar) at low resolution (2 nm). For such fits, we have used the rotational (gas) temperature resulting from previous fitting of certain rovibronic bands, like (3,0) and (2,0), at medium (0.45 nm) spectral resolution of laboratory HC discharges spectra.

The resulting VDFs were compared with those recorded for sprites by, respectively, Bucselá et al. [2003] at 53 km and Kanmae et al. [2007] at 53 km and 74 km. In addition, we will compare present VDF laboratory results with available sprite and halo VDF model predictions [Gordillo-Vázquez, 2010, Luque and Gordillo-Vázquez, 2011, Gordillo-Vázquez et al., 2011, 2012] where a gas temperature of 220 K is assumed.

2.4.5 Results and discussion

As mentioned in the introduction, the employment of the so-called Boltzmann plot method using different bands of the first negative system of $N_2^+(B^2\Sigma_u^+ \rightarrow X^2\Sigma_g^+)$ is justified for altitudes between $\simeq 60$ km and $\simeq 48$ km (quenching altitude), that is, for pressures between $\simeq 0.23$ mbar and $\simeq 1.5$ mbar. This altitude (pressure) region corresponds to the one where giant blue jets, blue jets and sprite tendrils take place.

We have implemented the Boltzmann plot method measuring the relative intensities of the rotational R - branch ($\Delta J = +1$) of the vibrational transition (0,0) of the first negative system of N_2^+ , that is, $N_2^+(B^2\Sigma_u^+, v' = 0, J' \rightarrow X^2\Sigma_g^+, v'' = 0, J'')$, with the band head wavelength at 391.4 nm. Since $B_{v'} = B_e + \alpha_e (v' + 0.5)$ and the rotational spectroscopic constants for $N_2^+(B^2\Sigma_u^+, v' = 0, J')$ are $B_e = 2.085 \text{ cm}^{-1}$ and $\alpha_e = 0.0212 \text{ cm}^{-1}$, we find that $B_{v'=0} = 2.074 \text{ cm}^{-1}$ and, since $hc/k = 1.438 \text{ cm K}$, the slope $-B_{v'=0}hc/kT_R$ of equation (2.14) becomes $-2.984/T_R$.

2. SPRITE HALOS

The Boltzmann plot method has been applied to air plasmas produced in DC hollow cathode discharges at 2.0 mbar ($\simeq 45$ km), 1.5 mbar ($\simeq 48$ km), 1.0 mbar ($\simeq 50$ km), 0.23 mbar ($\simeq 60$ km) and 0.11 mbar ($\simeq 70$ km) using the Jobin Yvon spectrometer with the photomultiplier (FM) and the CCD, with the 1800 grooves/mm grating, with spectral resolutions of $\Delta\lambda = 0.010$ nm (FM), 0.020 nm (CCD) and 0.034 nm (CCD), able to resolve nearly completely the rotational structure of the (0,0) vibrational transition of $\text{N}_2^+ - 1\text{NG}$. The standard deviation in the slopes of the Boltzmann plot is less than 10 %, which produces an uncertainty in the obtained T_R of about 3 %. Note that due to the even-odd alternation in the rotational quantum numbers [Herzberg, 1950], relative line intensities with odd J'' must be multiplied by 2. The wavelengths and $J'(J'+1) = (J''+1)(J''+2)$ values for the R branch ($\Delta J = +1$) rotational transitions of the (0,0) vibrational band of the first negative system of $\text{N}_2^+(\text{B}^2\Sigma_u^+)$ are shown in Table 2.2. As commented on formerly, an example of the method is given in Figure 2.43.

The sub-band head peak and spectral fitting methods to determine the gas temperature have been also applied to air plasmas produced in DC hollow cathode discharges for pressures between 0.11 mbar ($\simeq 70$ km) and 2 mbar ($\simeq 45$ km) using the (3,0) and (2,0) bands with spectral resolutions of 0.25 nm and 0.43 nm (subband head peak method) and 0.43 nm (spectral fitting method).

The rotational (gas) temperatures derived with the three methods commented above are shown in Figure 2.44. The temperatures obtained with the Boltzmann plot and subband head peak methods are shown in Figure 2.44a while Figure 2.44b shows a comparison between the gas temperatures obtained with the subband head peak and spectral fitting methods. As shown in Figure 2.44a, the temperature obtained (using the excited state rotational constant $B_{v'}$) with the ion N_2^+ is higher than that derived using vibrational transitions within $\text{N}_2(\text{B}^3\Pi_g \rightarrow \text{A}^3\Sigma_u^+)$. The reason of this behaviour can be due to the different spatial distribution of the excited neutrals $\text{N}_2(\text{B}^3\Pi_g)$ and excited ions $\text{N}_2^+(\text{B}^2\Sigma_u^+)$ in the hollow cathode discharges under investigation. Ions (like electrons) are concentrated (both radially and longitudinally) in the center of the hollow cathode discharge [de los Arcos et al., 1998, Castillo et al., 2005, Méndez et al., 2006] while the excited neutrals $\text{N}_2(\text{B}^3\Pi_g)$ could also reach a maximum in the center (due to the highest value of the electron density there) but with a less steep gradient than excited ions. Consequently, more excited neutrals $\text{N}_2(\text{B}^3\Pi_g)$ could be located towards the water refrigerated cathode/anode walls where the gas temperature

J''	λ (nm)	$(J'' + 1)(J'' + 2)$
6	390.49	56
7	390.40	72
8	390.29	90
9	390.19	110
10	390.08	132
11	389.97	156
12	389.85	182
13	389.73	210
14	389.59	240
15	389.43	272
16	389.33	306
17	389.20	342
18	389.04	380
19	388.90	420
20	388.74	462
21	388.58	506

Table 2.2: Wavelengths and $J'(J' + 1) = (J'' + 1)(J'' + 2)$ values for the R branch ($\Delta J = +1$) rotational transitions of the (0,0) vibrational band of the first negative system of $N_2^+(B^2\Sigma_u^+)$

should be smaller than in the center of the discharge, where most ions $N_2^+(B^2\Sigma_u^+)$ are concentrated. In this regard, Figure 2.44b shows a comparison of the gas temperatures derived when applying the subband head peak and the spectral fitting methods to the (3,0) and (2,0) vibrational transitions of $N_2(B^3\Pi_g \rightarrow A^3\Sigma_u^+)$ using spectral resolutions of 0.43 nm and 0.25 nm. We can see in Figure 2.44b that both methods based on the excited neutral $N_2(B^3\Pi_g)$ show a good agreement.

The spectral fitting of the (3,0) and (2,0) vibrational transitions of $N_2(B^3\Pi_g \rightarrow A^3\Sigma_u^+)$ at different pressures are shown in Figure 2.45 and Figure 2.46 for a spectral resolution of 0.43 nm.

2. SPRITE HALOS

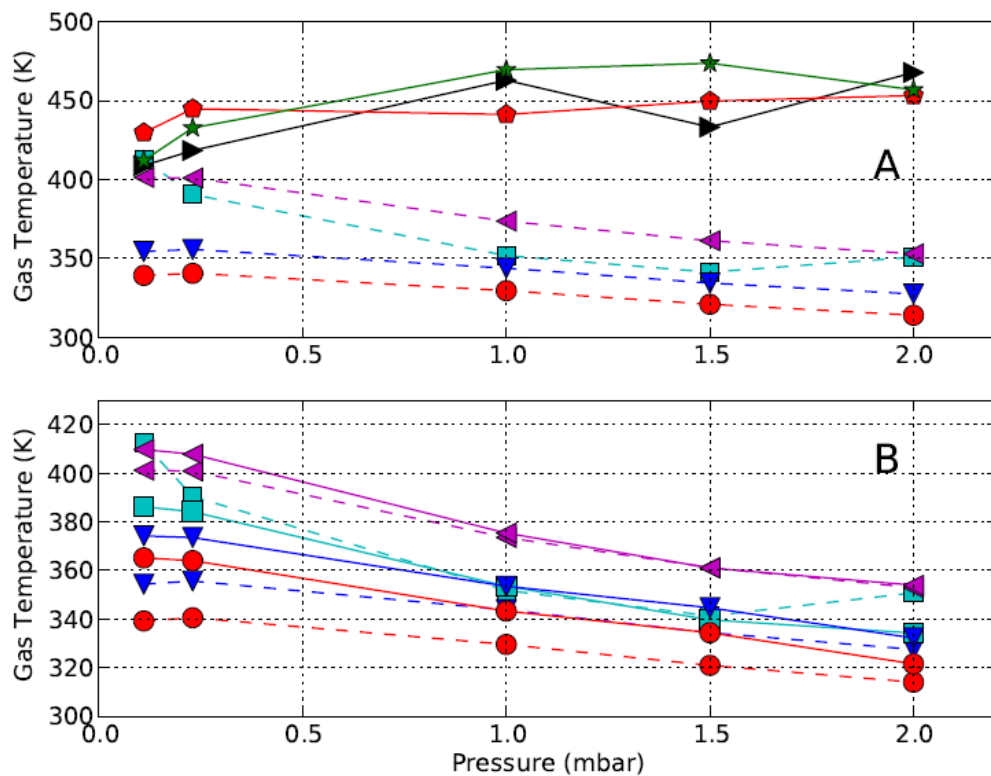


Figure 2.44: Rotational (gas) temperatures measured in the hollow cathode discharge: (Panel A) derived with the Boltzmann plot of the $N_2^+(B^2\Sigma_u^+)$ (solid line, right triangle FM-0.010 nm; pentagon CCD-0.02 nm; star CCD-0.034 nm) and the sub-band head peak methods applied to the $N_2 - 1PG$ band (dashed line, left triangle (3,0)-0.25 nm; square (3,0)-0.43 nm; down-triangle (2,0)-0.25 nm; circle (2,0)-0.43 nm). (Panel B) derived from the analysis of sub-band head peaks (3,0) and (2,0) recorded (each of them) with two spectral resolutions (0.25 nm and 0.43 nm) (dashed line and symbols correspond to the same data that in panel A) and from spectral fitting methods (solid line, left triangle (3,0)-0.25 nm; square (3,0)-0.43 nm; down-triangle (2,0)-0.25 nm; circle (2,0)-0.43 nm) for different pressures.

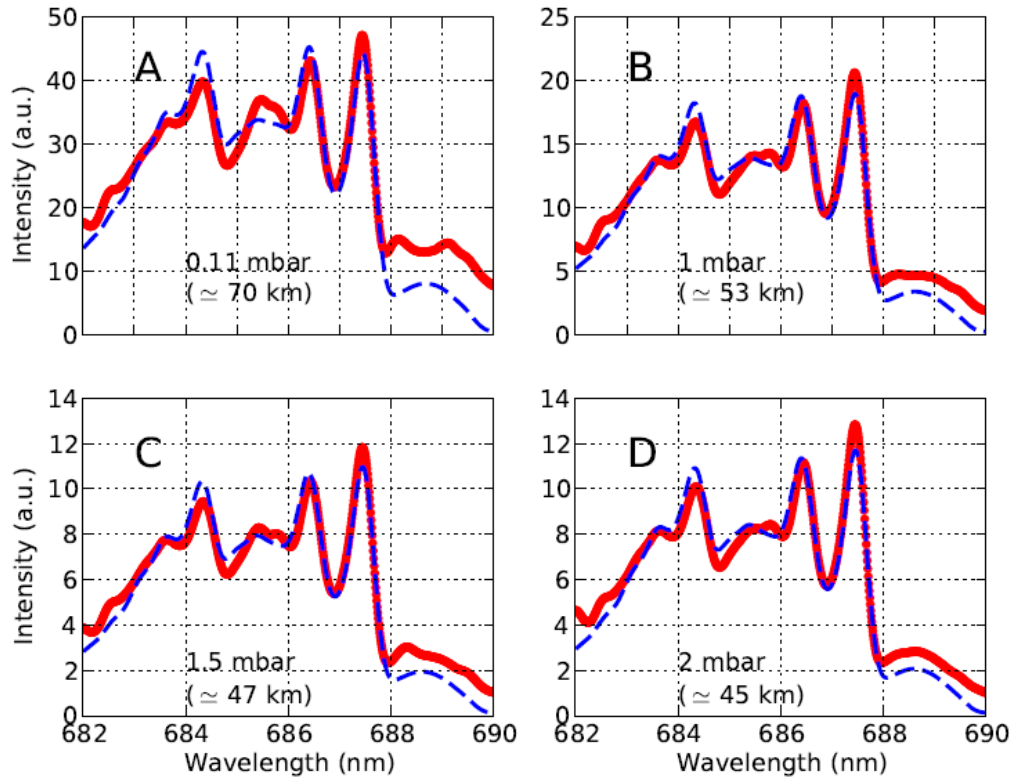


Figure 2.45: Spectral fitting (dashed blue line) of laboratory measured (solid red line) spectra of the (3,0) rovibronic transitions of $\text{N}_2(\text{B}^3\Pi_g \rightarrow \text{A}^3\Sigma_u^+)$ using 0.43 nm spectral resolution for 0.11 mbar (panel A resulting in $T_{gas} = 386$ K), 1 mbar (panel B resulting in $T_{gas} = 353$ K), 1.5 mbar (panel C resulting in $T_{gas} = 340$ K) and 2 mbar (panel D resulting in $T_{gas} = 334$ K). The spectra shown in panels A - D were recorded in the laboratory hollow cathode air discharge.

2. SPRITE HALOS

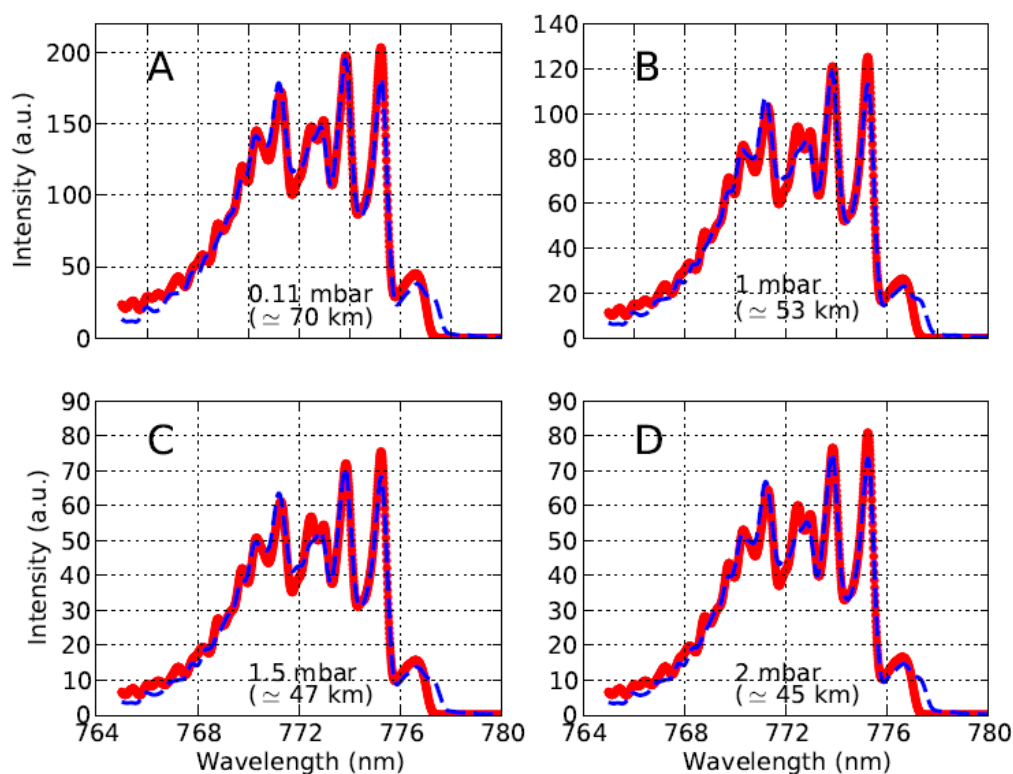


Figure 2.46: Spectral fitting (dashed blue line) of laboratory measured (solid red line) spectra of the (2,0) rovibronic transitions of $\text{N}_2(\text{B}^3\Pi_g \rightarrow \text{A}^3\Sigma_u^+)$ using 0.43 nm spectral resolution for 0.11 mbar (panel A resulting in $T_{gas} = 365$ K), 1 mbar (panel B resulting in $T_{gas} = 343$ K), 1.5 mbar (panel C resulting in $T_{gas} = 334$ K) and 2 mbar (panel D resulting in $T_{gas} = 321$ K). The spectra shown in panels A - D were recorded in the laboratory hollow cathode air discharge.

A comparison between the $\text{N}_2(\text{B}^3\Pi_g)$ 1PG spectrum recorded by a commercial spectrometer (Jobin Yvon-HORIBA FHR 1000) in the hollow cathode air discharge at 0.23 mbar and the spectrum taken by GRASSP from an air commercial lamp at 0.20 mbar is shown in panel A of Figure 2.47. Both spectra are represented at the same spectral resolution (0.45 nm). We see in Figure 2.47 (panel A) that the spectrum recorded by GRASSP reproduces well all the spectral features visible in the hollow cathode air discharge spectrum recorded with the commercial spectrograph. The main significant difference between the spectra shown in panel A of Figure 2.47 is due to the fact that the hollow cathode air discharge produces relatively cold plasmas with gas temperature of $\simeq 400$ K (see Figure 2.44) while the commercial discharge lamps that we use generate a plasma with higher gas temperature that promotes the excitation of higher rotational levels (than in the hollow cathode discharge). The excitation of higher rotational levels within each vibrational level (v') changes the shape of the (v' , v'') bands of the commercial lamp spectrum recorded by GRASSP with respect to those of the HC spectrum, producing more intense rotational emissions to the left of each band head that are responsible for the higher intensity of the (v' , v'') band envelope valleys (see the 660 nm - 690 nm spectral region in panel A of Figure 2.47). Panels B and C of Figure 2.47 show the spectral fitting of the (5,3) and (5,2) rovibronic transitions in the air commercial lamp $\text{N}_2(\text{B}^3\Pi_g)$ 1PG spectrum resulting in gas temperatures of 524 K and 656 K, respectively. The different (higher) gas temperatures obtained in the air commercial lamp discharge (at 0.2 mbar or 60 km altitude) and in the hollow cathode glow discharges might be due to the different power densities in the commercial lamp ($\simeq 10$ W/cm³) and in the air hollow cathode discharges (0.05 - 0.35 W/cm³).

2. SPRITE HALOS

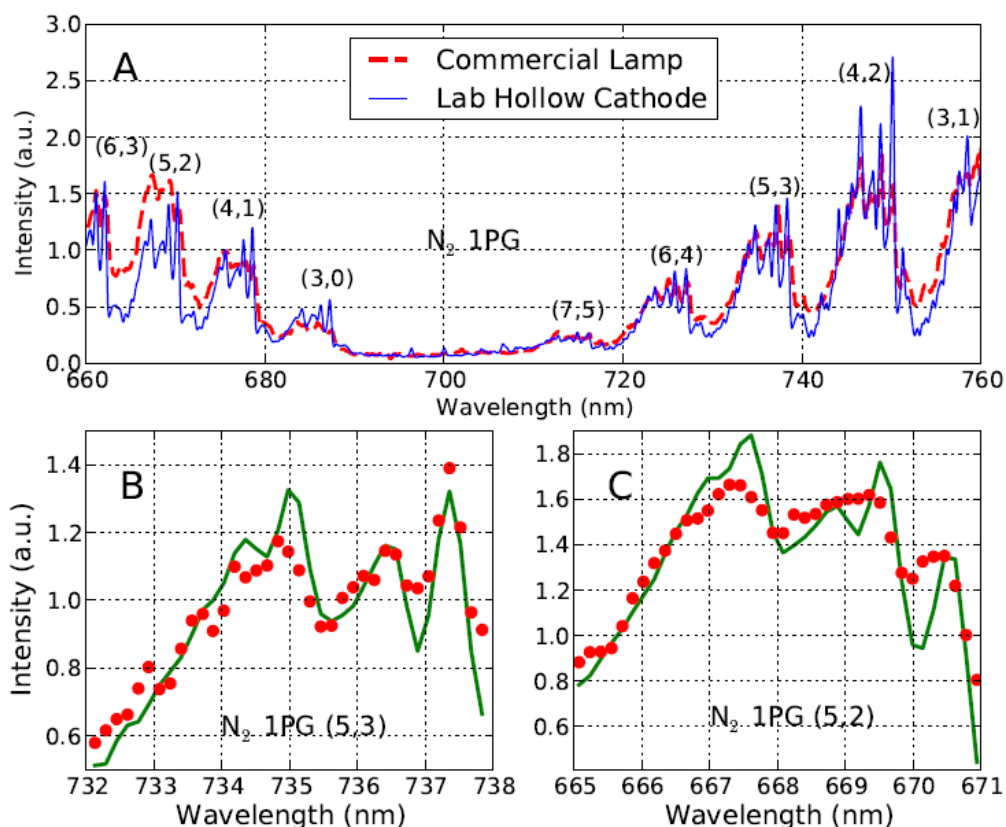


Figure 2.47: Panel A shows instrument efficiency corrected partial spectra of N_2 1PG band in a hollow cathode air discharge (solid line) at 0.23 mbar recorded by a commercial spectrograph (Jobin Yvon-HORIBA FHR 1000) and of a commercial air discharge lamp (dashed line) at 0.2 mbar taken with GRASSP. Panels B and C show the spectral fitting (solid line) of, respectively, the experimentally recorded (circles) (5,3) and (5,2) rovibronic band transition spectra of N_2 1PG in the commercial air lamp as recorded by GRASSP. The gas temperatures obtained by the (5,3) (panel B) and (5,2) (panel C) fits of the commercial air lamp N_2 1PG experimental spectrum taken by GRASSP are 524 K and 656 K, respectively. The gas temperature obtained in the hollow cathode discharge at 0.23 mbar is $\simeq 380$ K (see Figure 3). The spectral resolution used in both cases (hollow cathode and commercial lamp) is 0.43 nm.

2.4 Laboratory experiments

We have represented in Figure 2.48 the VDF of $N_2(B^3\Pi_g)$ experimentally derived from the N_2 1PG 53 km sprite emission spectra [Bucsela et al., 2003, Kanmae et al., 2007], and 74 km emission spectra [Kanmae et al., 2007], from model calculations for halos and sprites [Gordillo-Vázquez, 2010, Luque and Gordillo-Vázquez, 2011, Gordillo-Vázquez et al., 2011, 2012] and from the present hollow cathode discharges in air.

Panel A of Figure 2.48 shows the VDF of $N_2(B^3\Pi_g)$ obtained from N_2 1PG sprite emission spectra recorded at low altitude (53 km) or relatively high pressure ($\simeq 1$ mbar). We can see that the available sprite VDFs of $N_2(B^3\Pi_g)$ measured by Bucsela et al. [2003] and Kanmae et al. [2007] coincide between $v' = 2$ and $v' = 7$ with the VDFs of $N_2(B^3\Pi_g)$ derived from emission spectra of 1 mbar hollow cathode discharge in air and from model predictions. The results for $v' = 1$ by Bucsela et al. [2003] at 53 km follows the trend predicted by available sprite kinetic models (assuming $T_R = 220$ K) at higher (74 km) altitudes [Gordillo-Vázquez, 2010, Luque and Gordillo-Vázquez, 2011, Gordillo-Vázquez et al., 2011, 2012] though differ from the VDF ($v' = 1$) obtained from emission spectra recorded in hollow cathode discharges at 1 mbar. The latter can be due to the more effective excitation of $N_2(B^3\Pi_g)$ ($v' = 1$) in sprites than in hollow cathode air discharges, as can be seen by looking at the ratio of the (1,0) to (2,1) bands of, respectively, the laboratory hollow cathode (lab HC) discharge (solid line) and of the 53 km altitude sprite spectrum (dashed line) recorded by Bucsela et al. [2003], shown in panel A of Figure 2.49. The intensity of the (1,0) band is almost a factor of two higher than the (2,1) band intensity in the 53 km sprite spectrum (dashed line), while it is 40 % lower in the lab HC spectrum (solid line).

In panel B of Figure 2.48 we see a comparison between the VDF of $N_2(B^3\Pi_g)$ derived from a sprite instrument corrected N_2 1PG emission spectra at 74 km using $\Delta\lambda = 3$ nm [Kanmae et al., 2007], from a kinetic model (assuming $T_R = 220$ K) to predict the VDF of $N_2(B^3\Pi_g)$ in sprites and halos at, respectively, 74 km and 80 km [Luque and Gordillo-Vázquez, 2011, Gordillo-Vázquez et al., 2011, 2012] and from the $N_2(B^3\Pi_g)$ 1 PG spectrum of a hollow cathode air discharge generated at 0.11 mbar ($\simeq 70$ km) recorded with $\Delta\lambda = 2$ nm. The agreement between the experimentally recorded VDF of sprites at 74 km [Kanmae et al., 2007] and the model predicted VDF of sprites and halos is now more evident while at 0.11 mbar the discrepancy with the VDF ($v' = 1$) obtained from emission spectra recorded in hollow cathode discharges persists. It is worth mentioning that, in order to derive the VDF of $N_2(B^3\Pi_g)$ from experimentally

2. SPRITE HALOS

recorded N₂ 1PG sprite spectra, both Bucselá et al. [2003] at 53 km and Kanmae et al. [2007] at 53 km and 74 km fitted their observed sprite spectra assuming a rotational (gas) temperature of $T_R = 220$ K.

Finally, we represent in Figure 2.49 (panel A) a comparison of the partial N₂ 1PG instrument corrected spectra recorded from a sprite at 53 km altitude taken by Bucselá et al. [2003] (dashed line) and by Kanmae et al. [2007] (circles), from a hollow cathode discharge in air produced at 1 mbar ($\simeq 53$ km) (solid line) and transmission corrected spectrum of sprites at 74 km obtained from models (dotted lines) incorporating the plasma vibrational kinetics of TLEs [Gordillo-Vázquez, 2010, Luque and Gordillo-Vázquez, 2011, Gordillo-Vázquez et al., 2011, 2012]. All spectra shown in panel A of Figure 2.49 were normalized to the (2,0) transition at 773.2 nm and were recorded or calculated at spectral resolutions of $\Delta\lambda = 7$ nm (sprite at 53 km, [Bucselá et al., 2003]), $\Delta\lambda = 3$ nm (sprite at 53 km, [Kanmae et al., 2007]), $\Delta\lambda = 2$ nm (laboratory hollow cathode discharge) and $\Delta\lambda = 3$ nm (synthetic spectrum produced by a kinetic model of sprites and halos [Gordillo-Vázquez et al., 2012]). The spectra shown in panels B and C of Figure 2.49 were normalized to the atomic oxygen multiplet line at 777 nm.

The shape of the different (v' , v'') bands in the four spectra shown in Figure 2.49 (panel A) are not completely the same. For example, a sharp line around 777 nm is clearly visible very close to the right of the (2,0) transition of the laboratory HC spectrum (solid line) but is not present in the field recorded spectra nor in the synthetic sprite spectra. The 777 nm feature and the one at $\simeq 844$ nm between transitions (4,3) and (3,2) are both associated to strong radiative transitions of atomic oxygen. Moreover, the peaks at $\simeq 868$ nm and $\simeq 878$ nm to the left and to the right of, respectively, the (2,1) and (1,0) transitions of the N₂ 1 PG, might be also due to atomic nitrogen and oxygen emissions, respectively. Finally, the small peaks at $\simeq 811$ nm and $\simeq 823$ nm just before and after the (5,4) transition could also be associated to atomic oxygen emissions.

We see in Figure 2.49 (panel A) that, in general, the laboratory HC air spectrum, the two sprite spectra recorded at 53 km and the synthetic spectrum of sprites at 74 km agree well between 640 nm and 820 nm. However, beyond 820 nm and up to $\simeq 900$ nm, we see that while the (2,1) and (1,0) transitions in the 53 km sprite spectrum by Bucselá et al. [2003] (dashed line) and the synthetic sprite spectrum at 74 km (dotted

line) exhibit similar trends (the (1,0) peak higher than the (2,1) one), though with different quantitative values, they behave differently with respect to the trend of the (2,1) and (1,0) transitions in laboratory HC air spectrum, where both transitions reach more or less the same amplitude. The latter explains why the relative population of $v' = 1$ takes a greater value in the $N_2(B^3\Pi_g)$ VDF of sprites than in those of laboratory HC.

Finally, panels B and C of Figure 2.49 show the spectral fitting of the emission spectra (normalized to the 777 nm oxygen line) from the hollow cathode discharges in air at 0.11 mbar and 1 mbar, respectively. The VDF of $N_2(B^3\Pi_g)$ derived from the N_2 1PG spectrum observed in hollow cathode discharges, shown in Figure 2.48, were derived from the fits shown in panels B and C of Figure 2.49 using the previously obtained gas temperature values of 385 K (0.11 mbar) and 356 K (1 mbar). It should be noted that, because of the not yet well understood streamer branching dynamics of sprite streamers moving downward, there are no kinetic models available able to predict sprite streamer optical emissions close to the mesopause ($\simeq 53$ km).

2. SPRITE HALOS

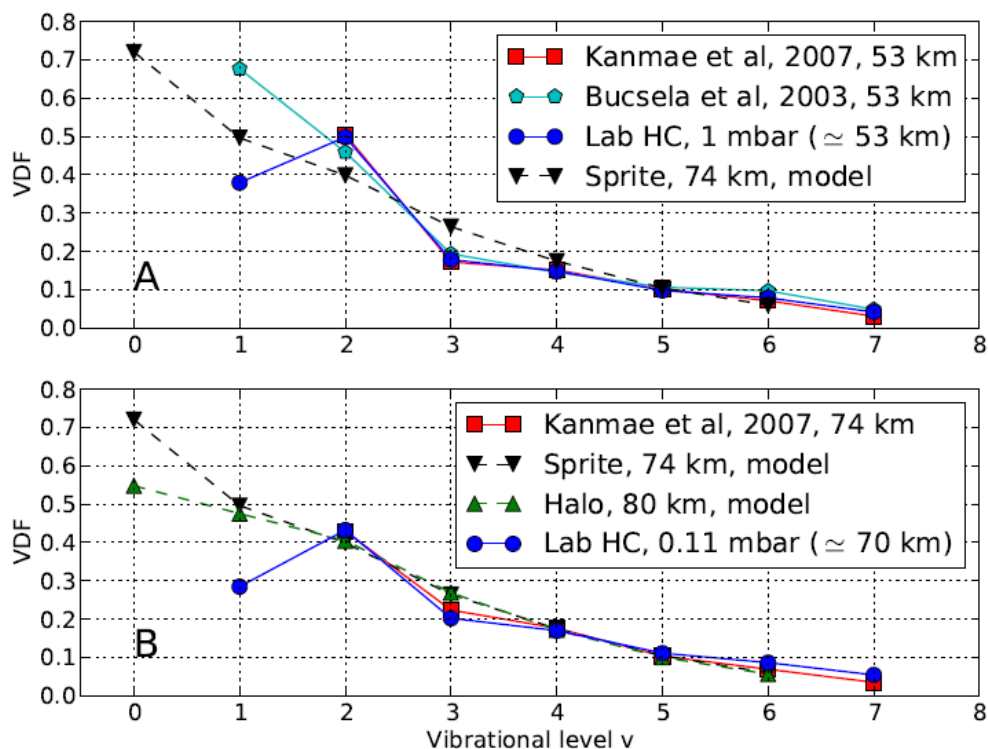


Figure 2.48: Panel A shows a comparison of the VDF of $N_2(B^3\Pi_g)$ derived from the N_2 1PG instrument corrected sprite emission spectrum at 53 km (≈ 1 mbar) using $\Delta\lambda = 7$ nm [Bucselá et al., 2003] and $\Delta\lambda = 3$ nm [Kanmae et al., 2007], from the N_2 1PG spectrum of a hollow cathode air discharge generated at 1 mbar (≈ 53 km) recorded with $\Delta\lambda = 2$ nm and from a kinetic model to predict the VDF of $N_2(B^3\Pi_g)$ in sprites at 74 km [Luque and Gordillo-Vázquez, 2011, Gordillo-Vázquez et al., 2011, 2012]. In panel B we see a comparison between the VDF of $N_2(B^3\Pi_g)$ recorded from the instrument corrected N_2 1PG sprite emission spectra at 74 km using $\Delta\lambda = 3$ nm [Kanmae et al., 2007], from a kinetic model to predict the VDF of $N_2(B^3\Pi_g)$ in sprites and halos at, respectively, 74 km and 80 km [Luque and Gordillo-Vázquez, 2011, Gordillo-Vázquez et al., 2011, 2012] and from the N_2 1PG spectrum of a hollow cathode air discharge generated at 0.11 mbar (≈ 70 km) recorded with $\Delta\lambda = 2$ nm. The VDF is normalized to the sum of the populations from $v' = 2$ to $v' = 6$.

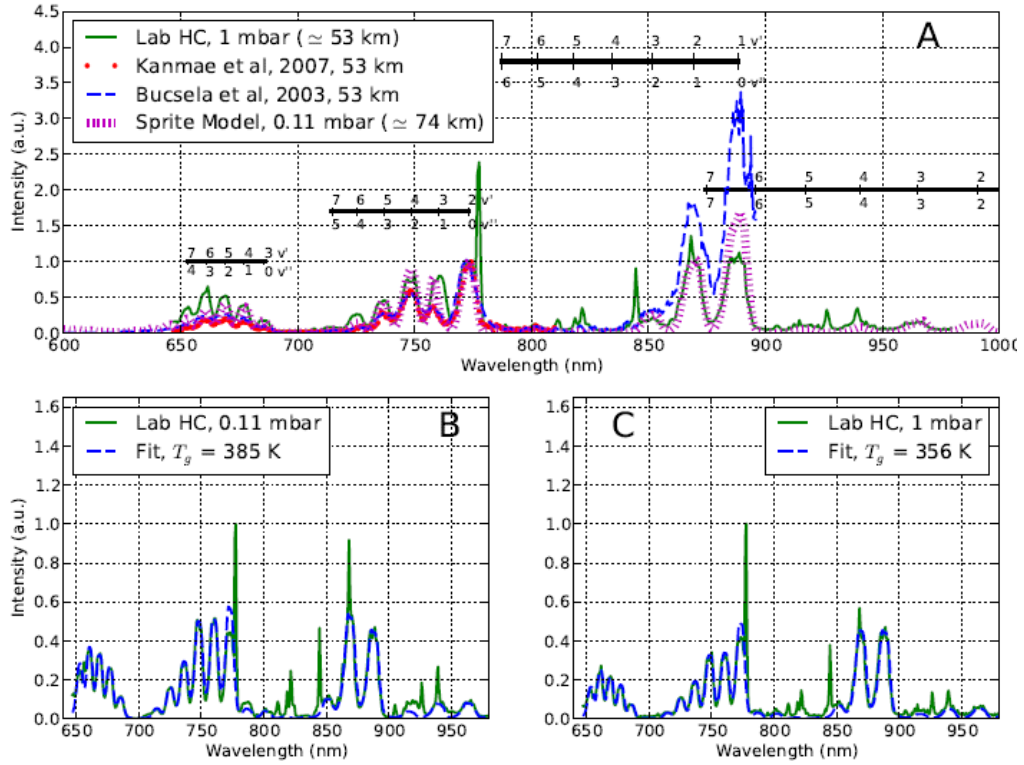


Figure 2.49: Panel A shows a comparison of the instrument corrected N₂ 1PG spectra recorded from sprites at 53 km using $\Delta\lambda = 3$ nm (circles) [Kanmae et al., 2007] and $\Delta\lambda = 7$ nm (blue dashed line [Bucsela et al., 2003], from a laboratory hollow cathode air discharge (green solid line) generated at 1 mbar ($\simeq 53$ km) recorded with $\Delta\lambda = 2$ nm and a transmission corrected synthetic sprite spectrum (dotted line) for a sprite at 74 km calculated with a kinetic model of sprites and halos assuming $\Delta\lambda = 3$ nm [Gordillo-Vázquez et al., 2012]. All spectra in panel A are normalized to the (2,0) transition at 773.2 nm while experimental spectra (green solid line) in panels B and C are normalized to the oxygen 777 nm line. Panel B shows the spectral fit (blue dashed line), using $T_{gas} = 385$ K, to the N₂ 1PG spectrum recorded in a hollow cathode air discharge generated at 0.11 mbar ($\simeq 70$ km) recorded with $\Delta\lambda = 2$ nm. Panel C shows the spectral fit (blue dashed line), using $T_{gas} = 356$ K, to the N₂ 1PG spectrum recorded in a hollow cathode air discharge generated at 1 mbar ($\simeq 53$ km) recorded with $\Delta\lambda = 2$ nm.

2. SPRITE HALOS

3

Sprites

“That is strength, boy! That is power! What is steel compared to the hand that wields it? Look at the strength in your body, the desire in your heart, I gave you this! Such a waste. Contemplate this on the tree of woe”

– Thulsa Doom, *Conan the Barbarian*

3.1 State of the art

Sprites, as we commented in Section 1.3, are huge weakly ionized plasma structures [Neubert, 2003, Pasko, 2003] which extend from the lower ionosphere (80-85 km) through the mesosphere down to 40 km of altitude approximately. Sprites are produced by air breakdown caused by mesospheric electrons accelerated by the quasi-electrostatic (QE) fields induced by lightning discharges [Pasko et al., 1995, Cho and Rycroft, 1998]. The QE field is mainly generated by positive cloud-to-ground (+CG) lightning strokes [Boccippio et al., 1995] although it can also be produced by negative cloud-to-ground (-CG) lightnings with a large charge moment change [Barrington-Leigh et al., 1999, Taylor et al., 2008]. The runaway electron avalanche process can also be considered as a sprite initiation mechanism. Some previous studies have associated sprite emissions at low altitude with high energetic runaway electrons [Bell et al., 1995]. Füllekrug et al. [2010], through low-frequency radio observations, detected electromagnetic pulses associated with an electron avalanche a few milliseconds after the causative lightning discharge coinciding with the sprite luminosity. These researchers concluded that relativistic runaway breakdown could emit broadband electromagnetic pulses and possibly

3. SPRITES

generates sprites.

The first sprite images taken from a plane were published by Sentman et al. [1995]. These first sprite color pictures showed that reddish optical emission predominates at the top of sprites while bluish emissions are the most visible at the bottom of sprites. Since then, there have been many observations from ground [Rairden and Mende, 1995, Lyons, 1996, Winckler et al., 1996, Stanley et al., 1999, Gerken et al., 2000, Barrington-Leigh et al., 2001, Stenbaek-Nielsen et al., 2013], from balloons [Bering et al., 2004, Bhusal et al., 2004], from the Space Shuttle [Vaughan et al., 1992, Boeck et al., 1995, 1998, Yair et al., 2004] and from the International Space Station [Blanc et al., 2004, Jehl et al., 2013]. There are also observations from other space platforms such as FORMOSAT-2, using the instrument ISUAL (Imager of Sprites and Upper Atmospheric Lightnings) in operation since 2004. ISUAL has recorded photometric data in the visible and ultraviolet optical range [Kuo et al., 2005, Mende et al., 2005, Liu et al., 2006, Adachi et al., 2006, 2008, Liu et al., 2009], as well as images [Chen et al., 2008].

It is now well established that sprites exhibit a common structure with three distinct regions [Pasko et al., 1998, Pasko and Stenbaek-Nielsen, 2002]: an upper diffuse region (90-80 km), a middle transition region (80-75 km) and a lower region where streamers are visible (< 75 km). The values of the above mentioned altitudes are average and depend on, among others factor, the characteristics of the lightning precursor. Subsequent ground-based observations with better resolution [Gerken et al., 2000, Gerken and Inan, 2003, 2005] and with high-speed cameras [Marshall and Inan, 2005, 2006, Cummer et al., 2006, McHarg et al., 2007, Stenbaek-Nielsen et al., 2007] have shown a complex set of streamers in the lower part of sprites as well as various types of sprites [Bór, 2013]. In addition, high-speed sprite imaging have also shown a great similarity with streamer discharges at atmospheric pressure [Raizer, 1991, Raizer et al., 1998]. Sprite streamers generally develop downwards [Moudry et al., 2003, Cummer et al., 2006, McHarg et al., 2007]. However, some upward streamer propagation have also been reported [Cummer et al., 2006, Stenbaek-Nielsen and McHarg, 2008].

The first spectroscopic sprite observations [Mende et al., 1995, Hampton et al., 1996, Morrill et al., 1998] with low spectral (between 10 nm and 6 nm) and temporal resolution (at standard video rate) identified the $1PN_2$ transition ($N_2(B^3\Pi_g) \rightarrow N_2(A^3\Sigma_u^+)$) as the most important optical emissions from sprites in the 550-840 nm spectral range.

Subsequent modeling studies [Pasko et al., 1997] confirmed that both $1PN_2$ and $2PN_2$ ($N_2(C^3\Pi_u) \rightarrow N_2(B^3\Pi_g)$) were the molecular transitions responsible for the red and blue optical emission features apparent in sprite spectra, as previously suggested by Sentman et al. [1995]. Later on, Heavner [2000] and Heavner et al. [2010] also confirmed the presence of ultraviolet (UV) emission in sprite spectra. The blue optical emission has also been associated with $N_2^+(B^2\Sigma_u^+)$ [Armstrong et al., 1998, 2000, Morrill et al., 2002], although it is not usually detected in sprite spectra [Armstrong et al., 2000]. Some studies have reported the possible presence of Meinel ($N_2^+(A^2\Pi_u) \rightarrow N_2^+(X^2\Sigma_g^+)$) emission in sprite spectra [Morrill et al., 1998]. Possible Meinel emission features in sprite spectra tend to be more apparent at lower layers of the atmosphere [Bucsele et al., 2003]. On the other hand, the confirmation of the presence of $1NN_2$ ($N_2^+(B^2\Sigma_u^+) \rightarrow N_2^+(X^2\Sigma_g^+)$) in sprite spectra is important since it indicates that sprites can also excite electronic levels of ionized species.

Sprites (and other TLEs) can also emit in the IR and UV [Liu et al., 2006] due to the excitation of species such as CO_2 , N_2 , NO and/or N_2^+ . However the IR and UV emissions are mainly reabsorbed by H_2O and O_2 and O_3 , respectively. Therefore, the detection of IR and UV features in sprite spectra need to be done from space, from balloons or from high altitude planes. There are some models of the NUV and NIR TLE optical emission and detection from space [Picard et al., 1997, Milikh et al., 1998, Luque and Gordillo-Vázquez, 2011, Gordillo-Vázquez et al., 2011, 2012]. Other modeling work on $NO-\gamma$ ($(NO(A^2\Sigma^+) \rightarrow NO(X^2\Pi_r))$) emissions in ultraviolet and Lyman-Birge-Hopfield (LBH, $N_2(a^1\Pi_g) \rightarrow N_2(X^1\Sigma_g^+)$) optical emission in the Far-UV show that, at 70 km, UV emission from NO are less intense than those due to LBH emission from N_2 [Liu and Pasko, 2005, 2007]. The LBH emission has been detected by ISUAL [Mende et al., 2004] and compared with streamer models [Liu et al., 2006]. On the other hand, the emission of $NO-\gamma$ from sprites has not yet been detected not even from space.

Regarding precise determination of the gas temperature in the TLE surrounding atmosphere, it is worth mentioning that the recording of TLE spectra with the instrument GRASSP (GRAnada Sprite Spectrograph and Polarimeter) between 700 nm and 800 nm and with a spectral resolution of 0.06 nm/px or 0.26 nm will allow to better resolve TLE spectra and to be able to quantify a possible local heating due to TLE activity in the lower mesosphere [Passas et al., 2014, Parra-Rojas et al., 2013b].

3. SPRITES

Although spectroscopic data provide valuable information about the excited species, the full impact of sprites in the chemical composition of the mesosphere is not well determined by spectroscopic means. Measurements by ISUAL between 40 and 60 km indicate that the mean energy of the electrons and the reduced electric field underlying the optical spectra of sprites are, respectively, between 6.2-9.2 eV and 243-443 Td [Kuo et al., 2005]. It is thus possible that these intense electric fields create highly reactive chemical species (such as energetic electrons, ions and NO_x) that can induce local changes in the chemical [Sentman and Wescott, 1995, Stenbaek-Nielsen et al., 2000] and electrical [Gordillo-Vázquez and Luque, 2010] properties of the mesosphere. The dipolar electric field and the electromagnetic pulse (EMP) generated by CG lightning strokes also affect to the electron concentration in the mesosphere and lower ionosphere [Taranenko et al., 1993, Shao et al., 2012]. Recent kinetic simulations of halos carried out by Parra-Rojas et al. [2013a] predicted an increase of up to 70 cm^{-3} in the mesospheric electron density due to the action of tropospheric +CG lightning. The enhanced electron concentration can stay high between 10 and 100 s after the current peak of the parent positive lightning discharge. In this regard, Luque and Gordillo-Vázquez [2012] showed that the electron production due to associative detachment (AD) of O^- by N_2 could be the underlying kinetic mechanism responsible of delayed sprites [Bell et al., 1998, Cummer and Füllekrug, 2001], that occur more than 10 ms after the parent lightning stroke.

A present line of active research is focussed on understanding how sprites and their post-discharge phase affect the atmospheric chemistry of NO_x and N_2O . Variations of NO and O_3 concentrations due to Blue Jets exhibit enhancements between, respectively, 10 % and 0.5 % at 30 km altitude [Mishin, 1997]. However, according to [Parra-Rojas et al., 2013a], the concentrations of NO and O_3 exhibit a negligible variation due to halos. Moreover, the simulations by Hiraki et al. [2004] predict a substantial increase in the concentration of $\text{O}(^1\text{D})$ and the measurements made by UARS (Upper Atmosphere Research Satellite) indicate a substantially enhanced $\text{O}(^1\text{S})$ emission rate [Lee and Shepherd, 2010] probably due to the presence of sprites. Concerning kinetic modeling of sprites, Sentman et al. [2008b] developed a kinetic model with more than 800 chemical reactions to study the impact of a streamer pulse with $E_{max} = 5E_k$ (where E_k is the breakdown electric field, $E_k/N = 120 \text{ Td}$) and $\Delta t = 6 \mu\text{s}$ at 70 km of altitude in the mesosphere. With this model, Sentman et al. [2008b] estimated an increase of the

streamer head electron density of up to 10^6 cm^{-3} persisting about 1 s. These authors also estimated an increase in the concentration of NO by 50 % while Hiraki et al. [2008] estimated an increase of four orders of magnitude in the density of NO at the same altitude. Enell et al. [2008], however, predicted an increase of 50 % in the concentration of NO_x at 73 km. Gordillo-Vázquez [2008, 2010] employing a reduced electric field of 400 Td, found increases of an order of magnitude in the concentration of NO and NO_2 while for the density of NO_3 predicted an increase of more than three orders of magnitude at 68 km. Moreover, Gordillo-Vázquez [2008] was also able to calculate the brightness of the sprite-related CO_2 $4.3 \mu\text{m}$ IR emission predicting a value as high as 100 MR at 68 km of altitude that pointed to its possible detection from space. The substantial differences found between the different sprite kinetic model predictions may be due to different initial conditions employed and to the use of different rates for some of the processes.

Regarding data analysis from instruments aboard different satellites, the results by Arnone et al. [2008], through analysis of the data recorded by MIPAS (Michelson Interferometer for Passive Atmospheric Sounding) aboard ENVISAT (ENVironmental SATellite) showed a possible sprite induced NO_2 enhancement of about 10 % at 52 km of altitude in correspondence with active thunderstorm and with a tendency to grow up with height. Also aboard ENVISAT but using the GOMOS (Global Ozone Monitoring by Occultation of Stars) instrument, Rodger et al. [2008] showed that there is no significant global impact of sprites and other TLEs in the concentration of NO_x at altitudes between 20 and 70 km.

The possible chemical impact of the sprite streamer tails in the mesosphere was also investigated by Sentman and Stenbaek-Nielsen [2009] at 70 km of altitude. In this case, assuming undervoltage conditions ($E=0.5E_k$), the derived electron concentration decreases smoothly due to dissociative attachment of electrons to molecular oxygen O_2 . More recently, Evtushenko et al. [2013] developed a self-consistent model to study the influence of sprites on the mesosphere as a function of the altitude. They obtained the maximum of the electron density variation at 75 km together with an important increase in the concentration of the metastable $\text{N}_2(\text{A}^3\Pi_u^+)$ between 72 and 76 km.

As reported by Stanley et al. [2000], sprites can also occur during daytime triggered by exceptionally large lightnings. Later on, Farges et al. [2005] and Kumar et al. [2008] also detected daytime sprites through infrasound and VLF perturbations, respectively.

3. SPRITES

The chemical fingerprint of daytime sprites on the mesosphere is presently not well known. In this regard, the recent simulations by Winkler and Nothold [2014] suggest a depletion in the ozone concentration ($\sim 15\%$) under the action of diurnal sprites.

In this thesis we aim to contribute to the fundamental understanding of the chemistry of non-equilibrium plasmas produced by nighttime sprite streamers in the mesosphere and their influence on the mesosphere chemical composition and thermal evolution. This chapter describes the kinetic model used, the time evolution of the concentration of many important species for the sprite and its afterglow through an upgrade of the self-consistent model by Parra-Rojas et al. [2013a]. We study the processes involved in the chemistry of the atmosphere between 50 km and 80 km under the action of sprite streamers with three different driving currents. Although the model is less reliable as we descend in altitude because below 70 km sprite streamers often branch, we think that the model is quite realistic between 80 and 70 km. It is nevertheless interesting to show the approximate chemical and thermal evolution of the atmosphere at lower (< 70 km) altitudes under the action of sprite streamers. We also discuss in this chapter the main instantaneous optical emission of sprites in the visible (1PN_2 and 2PN_2) and infrared ($4.26\ \mu\text{m}$ and $14.9\ \mu\text{m}$) together with the optical emission as seen by cameras recording at 33 fps and 1000 fps. Finally, we present a detailed study of the local thermal impact of sprite streamers in the Earth's mesosphere describing the most important mechanisms responsible for the local energy exchange between sprite streamers and the surrounding atmosphere.

3.2 Model

3.2.1 Model description

Although sprites have a downward development, this kinetic model does not aim to study the vertical evolution of the sprite streamer but to understand how a single sprite streamer can chemically and thermally activate each layer of the mesosphere. It is known that a single streamer tends to branch as it propagates downwards. For the sake of simplicity we are neglecting here this branching dynamics and, consequently, our model can only be considered as a pseudo 1-D model.

The kinetic model used here is an upgrade of the one by Parra-Rojas et al. [2013a] with 97 chemical species and more than 900 kinetic processes (see Appendix E), which

integrates a set of differential equations to model the chemical and thermal behaviour of the air plasma generated by sprite streamers. The temporal evolution of the density of each species i , is obtained through equation (2.1). The Electron Energy Distribution Function (EEDF) is also obtained to calculate the reaction rates of the electron-impact processes. To do this, equation (2.1) is solved self-consistently with the steady state Boltzmann transport equation (2.2). Coulomb interactions between electrons are negligible due to their low density in the upper atmosphere.

Finally, we studied the thermal impact of sprite streamers in the surrounding atmosphere by considering the balance between the processes which inject energy into the gas and the mechanisms which extract energy from it. The processes that contribute to increase the gas temperature obtain energy from an external power source and they can also absorb radiated energy by the surrounding atmosphere. The corresponding powers of each of these two mechanisms are P_{ext} and P_{abs} for the external power source and for the energy absorbed from the surrounding atmosphere, respectively. The reabsorption power per molecule is expressed by

$$P_{abs} = k_{corr} \sum_j n_j \frac{A_{ij} h\nu_{ji} g_i}{4\pi N g_j \exp(\frac{h\nu_{ji}}{k_B T_{gas}^{bg}}) - 1}, \quad (3.1)$$

where k_{corr} is a correction factor of the gas temperature (we will explain it below), n_j is the population of the lower absorbing level in each considered transition. A_{ij} is the Einstein spontaneous emission probability, $h\nu_{ji}$ is the energy needed to excite a molecule from a lower level j to an upper level i , N is the total gas number density, g_i and g_j are the statistical weights of the upper and lower excited levels respectively, k_B is the Boltzmann constant and T_{gas}^{bg} is the ambient gas temperature. The process represented by P_{abs} stands for the radiative power absorbed by air from the surrounding atmosphere at a constant ambient temperature T_{gas}^{bg} . The power per molecule dissipated by the streamer electric field is what we have called external power, P_{ext} , that is given by

$$P_{ext} = en_e v_e \frac{E}{N}, \quad (3.2)$$

where e is the elementary charge, n_e and v_e are the electron density and drift velocity respectively, and E/N is the reduced electric field. The powers deposited into the gas (P_{abs} and P_{ext}) are redistributed among different channels. The term P_{elec} is the power

3. SPRITES

which goes to the translational degrees of freedom of electrons in the plasma and is obtained through

$$P_{elec} = \frac{3}{2} \frac{k_B}{N} \frac{d(n_e T_e)}{dt}, \quad (3.3)$$

where T_e is the electron temperature. A large percentage of the deposited power goes to the translational degree of freedom of the gas, P_{gas} , represented by

$$P_{gas} = \frac{\gamma}{\gamma - 1} k_B \frac{dT_{gas}}{dt}, \quad (3.4)$$

where γ is the specific heat ratio of dry air ($\gamma = 1.4$) and T_{gas} is the gas temperature. Another important channel in which the powers P_{abs} and P_{ext} are redistributed to the internal degrees of freedom of the gas is the chemical power, P_{chem} , given by

$$P_{chem} = \frac{1}{N} \sum_i Q_i \frac{dn_i}{dt}, \quad (3.5)$$

where Q_i is the potential energy or the standard enthalpy of formation of species i . We note that P_{chem} can be positive or negative depending of the sign of Q_i or dn_i/dt . In the case of negative chemical power, this released power can go to the gas heating. Finally, the power released during spontaneous radiative emission, P_{rad} , reads

$$P_{rad} = \frac{\kappa^*}{N} \sum_i h\nu_{ij} A_{ij} n_i, \quad (3.6)$$

where $h\nu_{ij}$ is the energy released during the radiative decay from an upper level i to a lower level j . The assumed factor κ^* (equal to 0.5) accounts for the reabsorption coefficient calculated through the mean free path of the CO₂ IR photons [López-Puertas, 1982] in a sprite streamer of 50 m of average diameter. All these terms are included in the power balance equation

$$P_{abs} + P_{ext} = P_{elec} + P_{gas} + P_{chem} + P_{rad}. \quad (3.7)$$

The 0-dimensional simulations were performed for a pressure range equivalent to altitudes between 50 km and 80 km using ZDPlasKin, a tool developed by Pancheshnyi et al. [2008] that incorporates the BOLSIG+ solver to calculate the EEDF [Hagelaar and Pitchford, 2005].

The simulation process basically consists of three stages. The first step is what we have called electronic relaxation of our kinetic scheme. In this stage (based in the relaxation

stage of Sentman et al. [2008a] and Parra-Rojas et al. [2013a]) we use a reduced electric field $E/N \sim 0$ Td during a simulation time $t \sim 10^6$ s. With this preliminary simulation we obtain a chemical equilibrium consistent with the background electron density estimated by Hu et al. [2007]. In doing this we calculated the equilibrium concentrations of the ionized and excited species considered together with consistent rates of ionization and dissociative ionization of N_2 , O_2 due to the flux of cosmic rays [Yelinov et al., 2009]. The initial ambient densities of the neutral species used at each altitude were taken from the Whole Atmosphere Community Climate Model (WACCM) [Marsh et al., 2013] for midlatitudes and nighttime conditions.

The second step is the thermal relaxation of our system of equations and it is very similar to the previous stage. Using the concentrations obtained through the previous electronic relaxation stage we get, for each altitude, a parameter (k_{corr} in P_{abs}) to keep constant the gas temperature at long times ($t \sim 3 \times 10^4$). In the nighttime atmosphere (without solar photochemistry) with no external perturbations ($E=0$), the gas temperature tends to decrease by emitting thermal radiation (cooling). The introduction of the k_{corr} factor (added *ad hoc*) in the expression of P_{abs} contributes to partially compensate this effect, and allow us to obtain a more accurate thermal impact of sprites on the surrounding atmosphere.

Finally, the third stage is the main simulation in which we calculate the thermal and chemical impact of sprites in the mesosphere. For this we need to estimate first the local electric field as a function of time at each of the altitudes of interest. However, externally imposing this electric field as derived from independent microscopic simulations leads to unrealistic predictions since small differences in the rates of ionization between two models grow exponentially and often result in wildly overestimated electron densities. Following da Silva and Pasko [2014], we have found it more convenient to impose an electric current as input, instead of the electric field. As we will see now, this provides a certain degree of self-consistency in the sense that an overshoot in the electron density is quickly damped by the consequent decrease in the electric field.

We have calculated the electric field associated with a sprite streamer through the microscopic Ohm law

$$J = \sigma E, \quad (3.8)$$

where J is the current density, σ is the electron conductivity and E is the electric field. The electron conductivity has a strong dependence with the electron density and

3. SPRITES

mobility, that in turn depends on the electric field as

$$\sigma = en_e\mu_e(E/N), \quad (3.9)$$

where μ_e is the electron mobility. We used BOLSIG+ to obtain the dependence of $\mu_e N$ on the reduced electric field in an air plasma with the same composition as ours. Once calculated, we fitted $\mu_e N$ to a power law (see Figure 3.1).

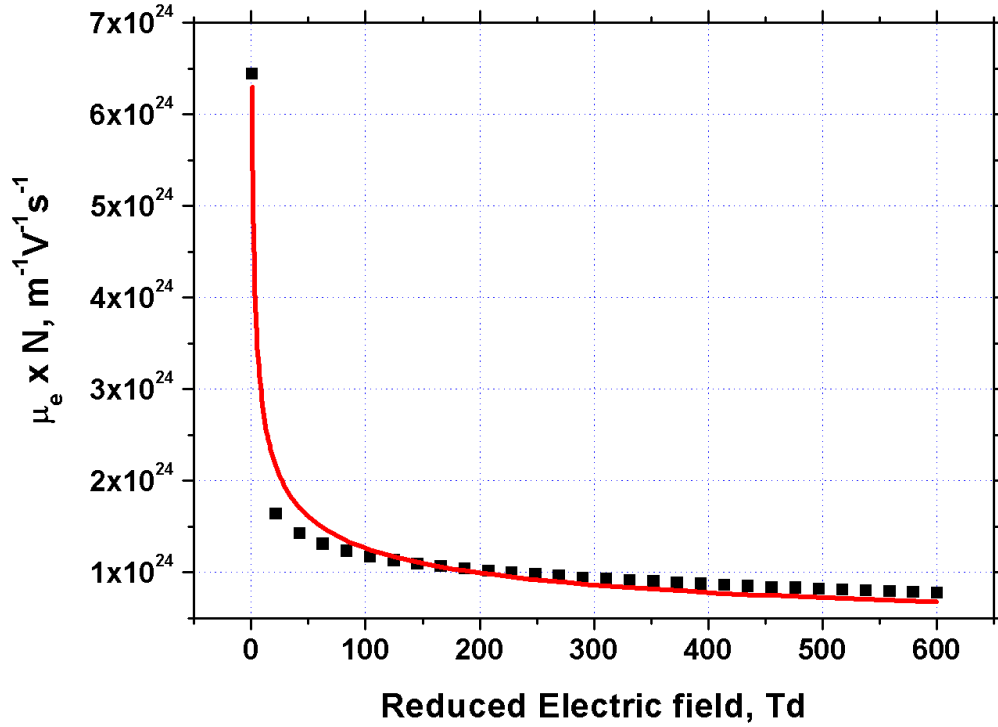


Figure 3.1: Dependence of $\mu_e N$, where μ_e is the electron mobility and N is the gas density, with the reduced electric field in dry air. The solid red line is the power fit with a correlation coefficient of 0.9808.

$$\mu_e N = a \left(\frac{E/N}{1Td} \right)^b, \quad (3.10)$$

where we found $a = 6.3 \times 10^{24} m^{-1}V^{-1}s^{-1}$ and $b = -0.35$. Using equations (3.8) and (3.9), we derived an approximate expression for the reduced electric field in a sprite

streamer channel as

$$\frac{E}{N} = \left(\frac{J}{en_e a} \right)^{\frac{1}{b+1}} \times 1Td. \quad (3.11)$$

In our simulations, the externally imposed current consists of three phases (see Figure 3.2): (a) a peak corresponding to the passage of the streamer head, (b) a constant plateau and (c) an exponential decay with a time constant of 4 ms. For the streamer

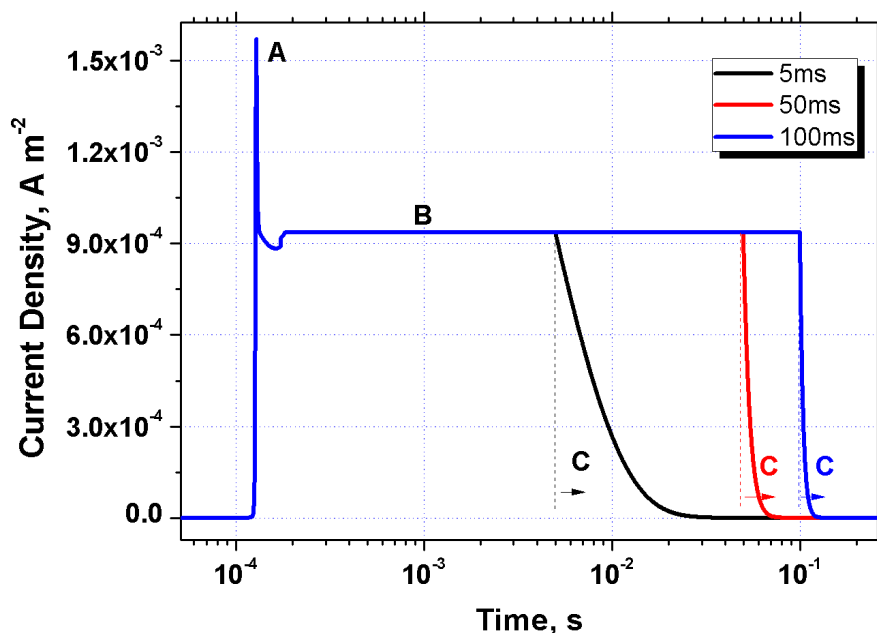


Figure 3.2: Time evolution of the current density of a sprite streamer at 75 km of altitude. The black, red and blue lines are for driving currents of 5 ms, 50 ms and 100 ms, respectively. Label A corresponds to the streamer head, B corresponds to the driving current and C (black, red and blue) is associated to the post-afterglow stage.

head (a) we run microscopic streamer simulations similar to those described by Luque et al. [2008] and Luque and Ebert [2010]. For each altitude h we run a simulation with the electron density resulting from the electronic relaxation stage and a gaussian ionization seed a few kilometers above h . The resulting electric current at h was later on used as an input in the kinetic model.

In Figure 14 of the work by Stenbaek-Nielsen et al. [2013], we can see an image of a single sprite streamer which width, at 76 km of altitude, is approximately 500

3. SPRITES

m. According to Pancheshnyi et al. [2005], the streamer electrodynamic radius can be a factor 2 greater than the optical radius. Thus, we have rescaled the streamer diameter with the inverse of the density (for each altitude) establishing a reference sprite streamer diameter of 1 km at 76 km. With this sprite streamer rescaling of its radius, the current flowing through the streamer channel is $\simeq 190$ A and $\simeq 1120$ A at 80 km and 50 km, respectively. In this way, our current density becomes consistent with the sprite core currents estimated by da Silva and Pasko [2014].

The currents resulting from these simulations contain first a strong peak due to the field enhancement at the streamer head and then a re-enhancement of the field that, as argued by Liu [2010] and Luque and Ebert [2010] corresponds to the streamer afterglow. Microscopic simulations are limited to only a few milliseconds but Stenbaek-Nielsen and McHarg [2008] report observations of sprite afterglows lasting up to 100 ms. It is to simulate these long-lasting afterglows that we extended the current input with a constant plateau (b) as mentioned above. We have used current durations of 5 ms, 50 ms and 100 ms and, as we can see in Figure 3.2. They are all terminated by an exponential decay (c) lasting 4 ms. To summarize, our model solves self-consistently the equations (2.1), (2.2), (3.7), and (3.11) for each altitude in the mesosphere (between 50 km and 80 km) for a complete set of chemical species under the action of a single sprite streamer.

3.3 Results and discussion

In this section, we show and discuss the effects of sprite streamers in the electric, chemical and thermal properties of the mesosphere. Therefore, we have performed simulations with different driving current durations (after the streamer head) since we can have relatively high electric fields (> 50 Td) during a long time (~ 100 ms).

3.3.1 Reduced Electric Field

We start our analysis with the reduced electric field, which drives many of the chemical processes in our model. Figure 3.5 shows the evolution of the field at 50 km when the driving current lasts 50 ms. There the evolution is characterized by three features: (1) a strong peak, reaching 700 Td, produced by the passage of the streamer head and approximately coinciding with the peak of the driving current, (2) a re-enhancement of

the field to values close to the breakdown field 120 Td that lasts about 0.1 ms and (3) a train of periodic oscillations starting around 6 ms that persists up to the end of the driving current. With the exception of feature (3), which appears only at low altitudes (< 60 km), the overall behavior of the reduced field is similar at all altitudes. This is shown in Figures 3.3a-3.3c and 3.3d-3.3f, which extend the plots of reduced electric field and driving current to the complete range of altitudes considered in our model and to the three durations of the driving current used: 5 ms ((a)-(d)), 50 ms ((b)-(e)) and 100 ms ((c)-(f)).

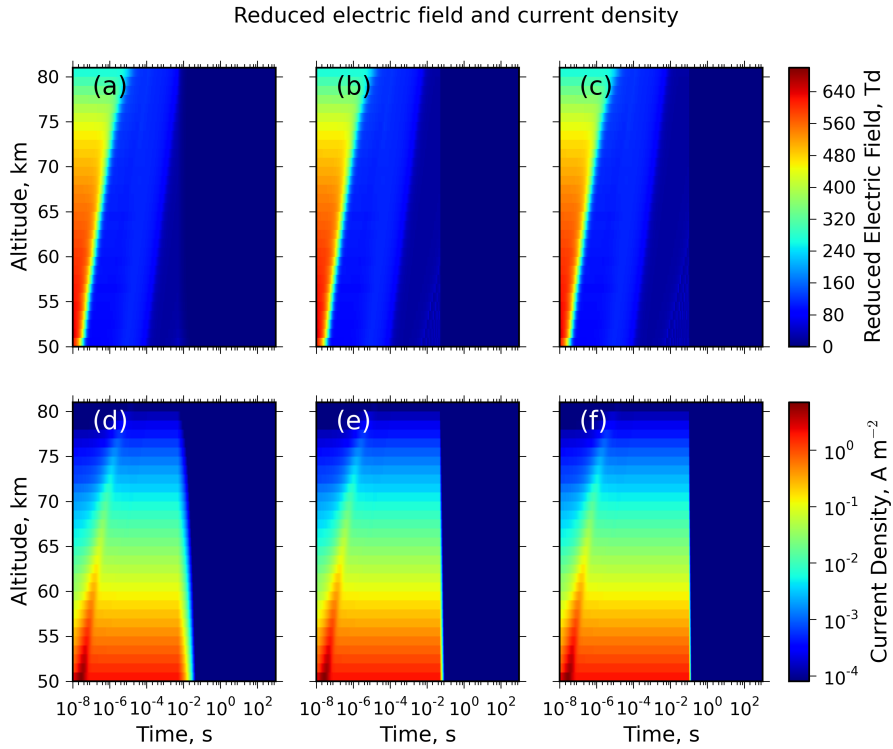


Figure 3.3: Altitude-time evolution of the reduced electric field (top panel) and current density (bottom panel) due to a single sprite streamer with a driving current of 5 ms ((a)-(d)), 50 ms ((b)-(e)) and 100 ms ((c)-(f)).

In Figure 3.4 we plot the dependence with altitude of the maximum values of the reduced electric field and of the streamer current density corresponding to the streamer head. Since the reduced electric field (E/N) is driven by the imposed current density J , the highest value of the reduced electric field and the highest value of the streamer current density are approximately simultaneous for any given altitude. Both peak

3. SPRITES

values decrease with increasing altitude, so the absolute maxima are at the lowest considered altitude, 50 km (650 Td with 6.53 Am^{-2}).

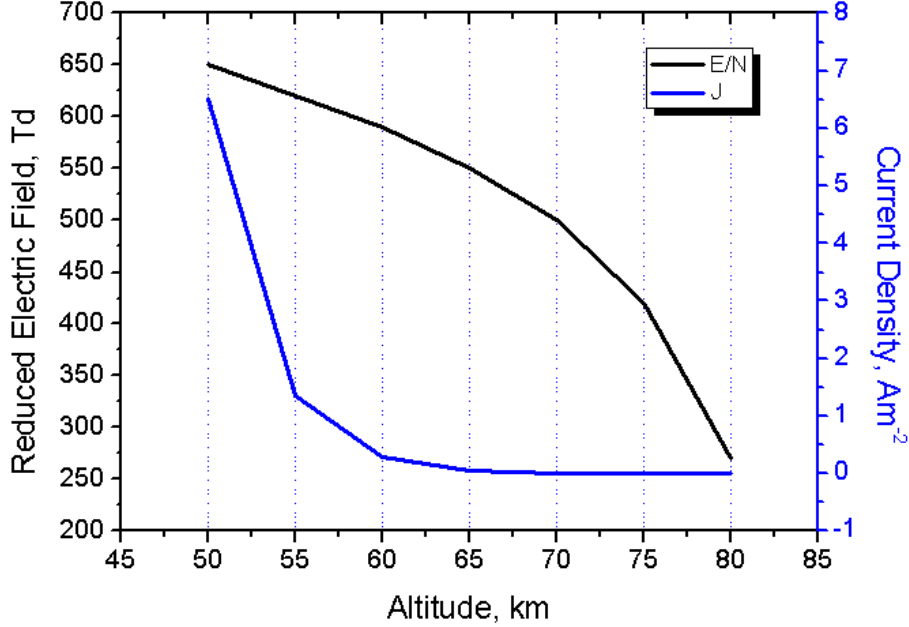


Figure 3.4: Altitude evolution of the maximum reduced electric field (black line) and maximum streamer current density (blue line).

The second phase of the electric field evolution is the re-enhancement to values close to the breakdown threshold. As we will see later, this re-enhancement will play a relevant role in activating many chemical pathways; we will refer to it as the *high-field phase* of the simulation. Figure 3.3a, 3.3b and 3.3c shows that the duration of this high-field phase depends on the altitude, scaling as $1/N$, and ranges from 10^{-4} s at 50 km to 10^{-2} s at 80 km of altitude. As we mentioned above, the third stage of the evolution of the electric field consists in a set of periodic oscillations and, as we appreciate in Figures 3.3b and 3.3c, it is present only below 60 km and when the driving current lasts 50 or 100 ms. This is a consequence of typical times scaling as $1/N$ combined with a duration of the driving current that does not depend on altitude.

The high-field phase and the oscillations appear during the driving current. Therefore, as shown in equations (3.8)-(3.9), the evolution of the electric field is partly determined by the electron concentration (the reduced electric field decreases with the

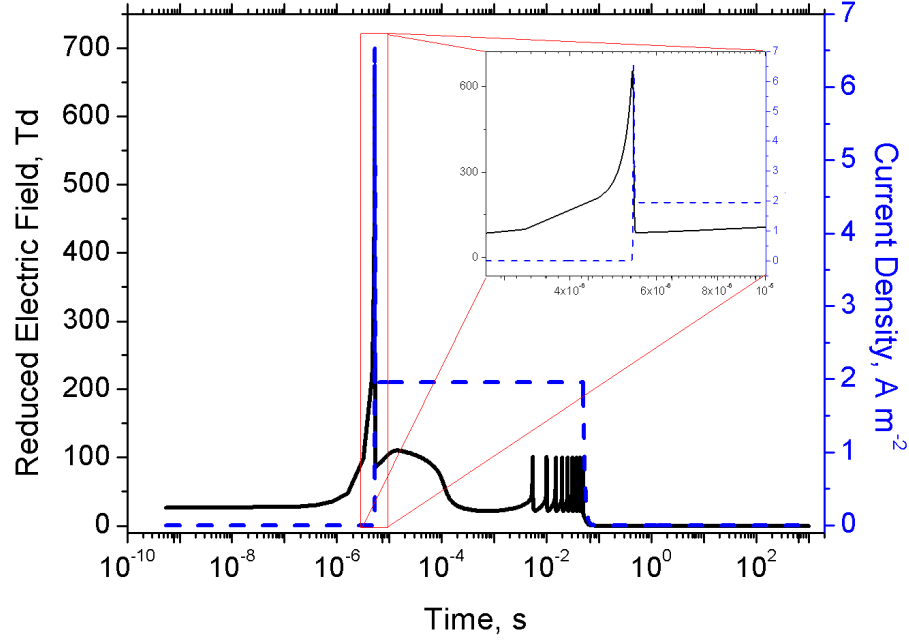
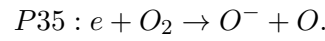
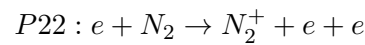
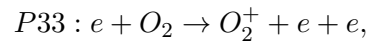


Figure 3.5: Reduced electric field (black solid line) and current density (blue dotted line) temporal behaviour of a single sprite streamer at 50 km of altitude with a driving current duration of 50 ms.

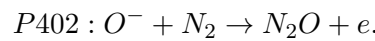
electron density n_e and increases with the current density). The high-field phase is produced by a small decrease in the electron concentration, just after the streamer head, caused by dissociative attachment of O_2



This process pushes upward the electric field until it is high enough to cause significant electron-impact ionization of O_2 and N_2 :

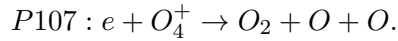


and associative detachment of O^- by N_2 :



3. SPRITES

The strong ionization produced by the streamer head (see times between 10^{-6} s and 10^{-4} s in Figure 3.7) screens the electric field so that after 10^{-4} s (at 50 km) and 10^{-2} s (at 80 km), it drops to around 20 Td. Consequently, the reaction constant of the associative detachment (that depends on E/N) decreases to 2×10^{-13} cm³ s⁻¹ (see supplementary documentation of Luque and Gordillo-Vázquez [2012]) and electrons are removed by

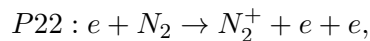


With this decrease of the electron density (due to electron recombination with O_4^+) the reduced electric field increases strongly during the constant driving current and activates the dissociative attachment of O_2 . Thus, in summary, the strong decrease of the reduced electric field from the pulse peak is due to the contribution of the three processes explained previously (P33, P22 and P402). Finally, when the driving current drops to zero, the reduced electric field vanishes.

We note that the oscillations in the electric field are, to some degree, a consequence of the imposition in our model of a constant electric current. They would probably disappear or be modified in models with a fully self-consistent calculation of the electric field. However, they may also indicate a physical tendency of the electric field to rise due to the removal of electrons at time scales of some tens of milliseconds. This higher electric field would be seen as a re-brightening of the lower portions of decayed sprite tendrils. In Figure 3.6 we show the electric field at the lowest altitudes of our simulations; there we see that the oscillations appear as upward-moving spots of increased luminosity. We speculate that these spots may be related with the so-called *crawlers*, described by Moudry [2003] as bright segments that move upward with a velocity of 10^4 - 10^5 m/s. As seen in Figure 3.6, we obtain a velocity of about 10^5 m/s at 60 km.

3.3.2 Electron density and O^-

We see in Figure 3.7a, 3.7b and 3.7c the altitude and time dependence of the electron density for the three driving current durations that we considered. In the three cases, above 65 km, the electron concentration increases between 4 and 5 orders of magnitude in the streamer head due to N_2 and O_2 electron-impact ionization:



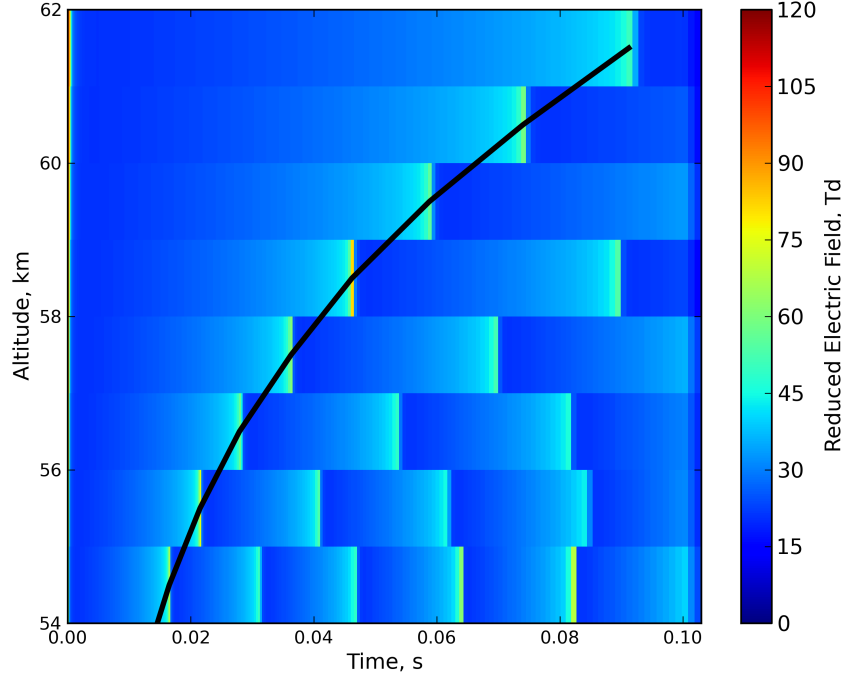
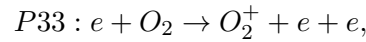
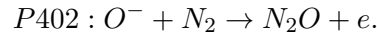


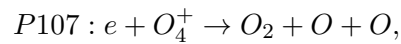
Figure 3.6: Altitude-time evolution of the reduced electric field oscillations during the driving current (50 ms duration) and between 54 and 62 km of altitude. The black line shows the upward movement of the possible crawlers [Moudry, 2003].



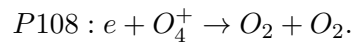
electron-impact ionization is the main mechanism producing electrons above breakdown ($E/N > 120$ Td) scenarios. When the reduced electric field falls down to sub-breakdown values (after the streamer head), the electron concentration grows again by a factor 6 due to the associative detachment (AD) of O^- by N_2 :



The electron density remains high for a few seconds due to AD and it decreases later to background values due to the recombination processes

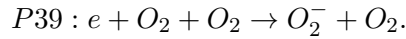


and

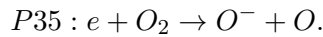


3. SPRITES

Below 65 km and at the time of the streamer head, the electron density increases between 8 and 11 orders of magnitude due to ionization of N_2 and O_2 . Between 10^{-4} s and 10^{-3} s after the passage of the streamer head, an increase of a factor of 6 occurs due to associative detachment (AD) of O^- by N_2 . In the cases of 50 ms and 100 ms driving current durations (Figures 3.7b and 3.7c), and following the oscillations of the reduced electric fields, the electron concentration changes due to the mechanisms P22, P33, P35, P107 and P402 commented in the previous section. After the electric field oscillations, the electron concentration remains elevated, around 10^5 cm^{-3} , up to nearly 100 s. After about 100 s, the electron density returns to ambient values due to three-body electron attachment:



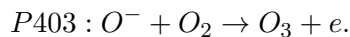
The concentration of the O^- anion is closely related to the temporal evolution of the electron density. The largest increase in the concentration of O^- is produced by the streamer head field, increasing between 14 and 5 orders of magnitude above its ambient value at, respectively, 50 km and 80 km of altitude (see Figures 3.7d, 3.7e and 3.7f). The main chemical mechanism responsible of this strong increase is dissociative attachment (DA) of O_2



When the reduced electric field goes below ~ 60 Td, the O^- density decreases by associative detachment of O^- by N_2 , producing N_2O and free electrons. This drop in the O^- ion concentration is directly related to the increase of the electron density through associative detachment. In the final stage of the simulation, when the electric field has dropped to zero, the O^- density returns to its ambient value due to AD with CO and O_2 :

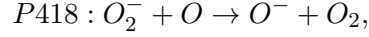


and

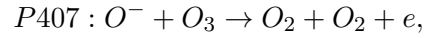
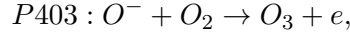


For current durations of 50 ms and 100 ms, we observe in Figures 3.7e and 3.7f that the density of O^- decreases faster than in the case of 5 ms duration (see Figure 3.7d). This is due to the stronger influence of the AD of O^- . In these cases, and at middle

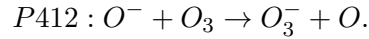
altitudes, we see a small increase during the final stage (when the reduced electric field is negligible) due to charge transfer:



The O^- density returns smoothly to background values by associative detachment (AD) processes



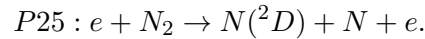
and charge transfer



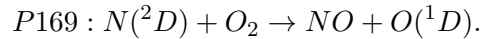
At low altitudes (below 60 km) we obtain variations in the concentration of O^- associated with the oscillations of the reduced electric field described above. The density of O^- remains at values between 10^3 - 10^5 cm^{-3} up to 100 s after the passage of the streamer head.

3.3.3 $N(^2D)$ and NO

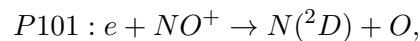
Figures 3.8a, 3.8b and 3.8c show the density of excited atomic nitrogen $N(^2D)$. The evolution of these species is closely related with that of the reduced electric field. Consequently, when the reduced electric field reaches a maximum, the $N(^2D)$ density reaches values of up to 10^7 cm^{-3} and 10^5 cm^{-3} at, respectively, 50 km and 80 km. The main production process of $N(^2D)$ is direct electron-impact N_2 dissociative excitation:



These maximum values of the $N(^2D)$ density persist during the high-field phase due to the balance between the electron-impact dissociative excitation of N_2 (P25) and quenching by O_2 :



At the end of the high-field phase, the concentration of $N(^2D)$ decreases slightly since P25 is less effective than quenching by O_2 . When the reduced electric field vanishes, the density of $N(^2D)$ still increases up to 2 orders of magnitude due to dissociative recombination of electrons with NO^+ :



3. SPRITES

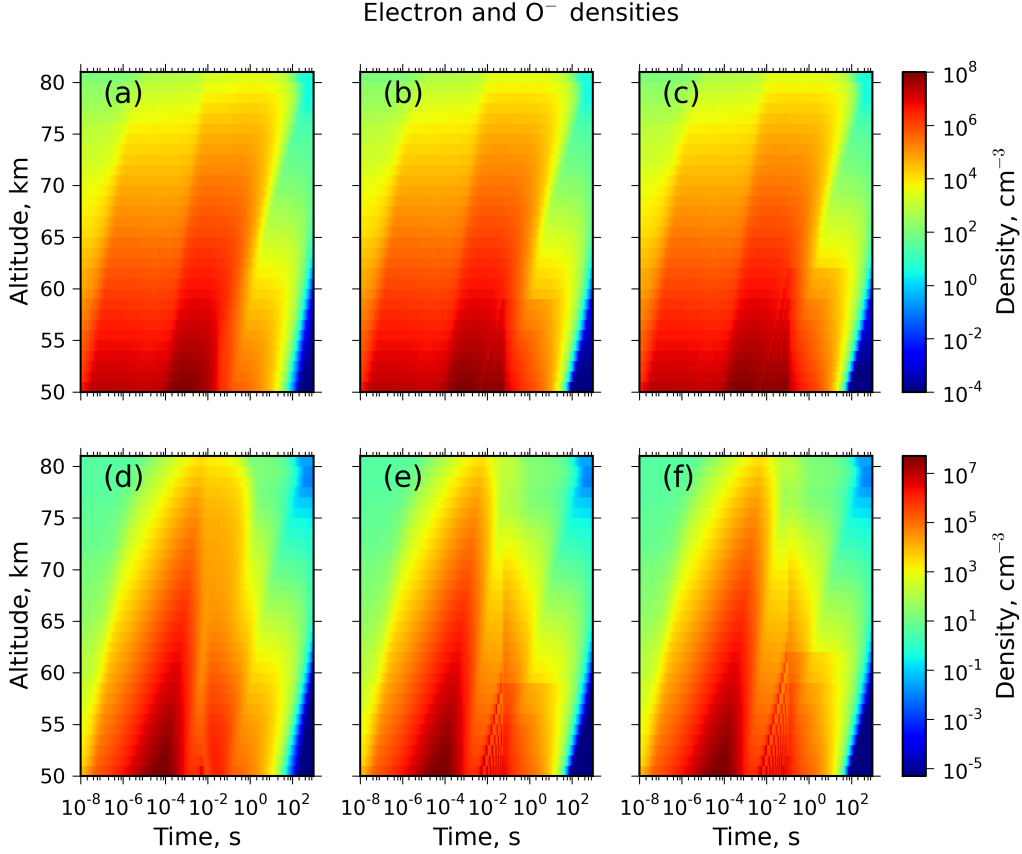
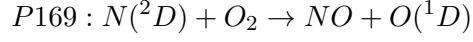


Figure 3.7: Altitude-time evolution of the electron density (upper plots) and O^- density (lower plots) due to a single sprite streamer with a driving current of 5 ms ((a)-(d)), 50 ms ((b)-(e)) and 100 ms ((c)-(f)).

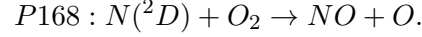
once this process (P101) stops, the density of $N(^2D)$ slowly returns to its background value due to quenching by O_2 (P169) at later times. Between 65-50 km and in the cases of 50 ms and 100 ms of current durations (see Figures 3.8b and 3.8c respectively), the density of $N(^2D)$ grows more than 7 orders of magnitude above its background value due to the action of the reduced electric field oscillations.

The altitude and time dependence of the ground state NO density is shown in Figures 3.8d, 3.8e and 3.8f. Note that, above 74 km, the impact of a sprite streamer in the NO concentration is almost negligible (factor 3). Below this altitude the density of NO increases up to 8 orders of magnitude during the passage of the streamer head. The

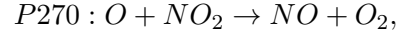
main mechanisms responsible for this strong variation are



and



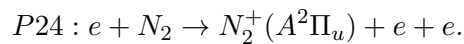
When the driving current lasts 5 ms the density of NO remains unchanged during the complete simulation due to the balance between the gain and loss reactions



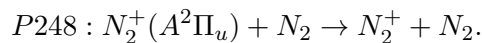
In the rest of the considered cases, we see a secondary increase of up to 10^9 cm^{-3} in the concentration of NO. The oscillations of the reduced electric field underlie this strong NO enhancement since they induce the production of $N(^2D)$ which, after quenching (P168 and P169), generates NO. These results disagree with Gordillo-Vázquez [2008], which shows an increase of one order of magnitude at 68 km of NO concentration, mainly because we employ a stronger and more realistic streamer electric field and different initial conditions. In the same way, Sentman et al. [2008b] estimated a growth of 75 % in NO density at 70 km, where we predict an increase of more than one order of magnitude for the 50 ms intermediate case.

3.3.4 $N_2^+(A^2\Pi_u)$ and $N_2^+(B^2\Sigma_u^+)$

Figures 3.9a, 3.9b and 3.9c show the altitude and time dependence of the density of the $N_2^+(A^2\Pi_u)$ ion, responsible for the Meinel band emission, in the red and near infrared spectral regions. Its behavior is similar to that of the reduced electric field shown in Figures 3.3a, 3.3b and 3.3c. Due to the streamer head field, the concentration of $N_2^+(A^2\Pi_u)$ increases up to 10^5 cm^{-3} and 10^1 cm^{-3} at, respectively, 50 km and 80 km of altitude due to direct electron-impact ionization of N_2 :



$N_2^+(A^2\Pi_u)$ remains constant during the high-field phase due to the chemical balance between P24 and the collisional deexcitation process



3. SPRITES

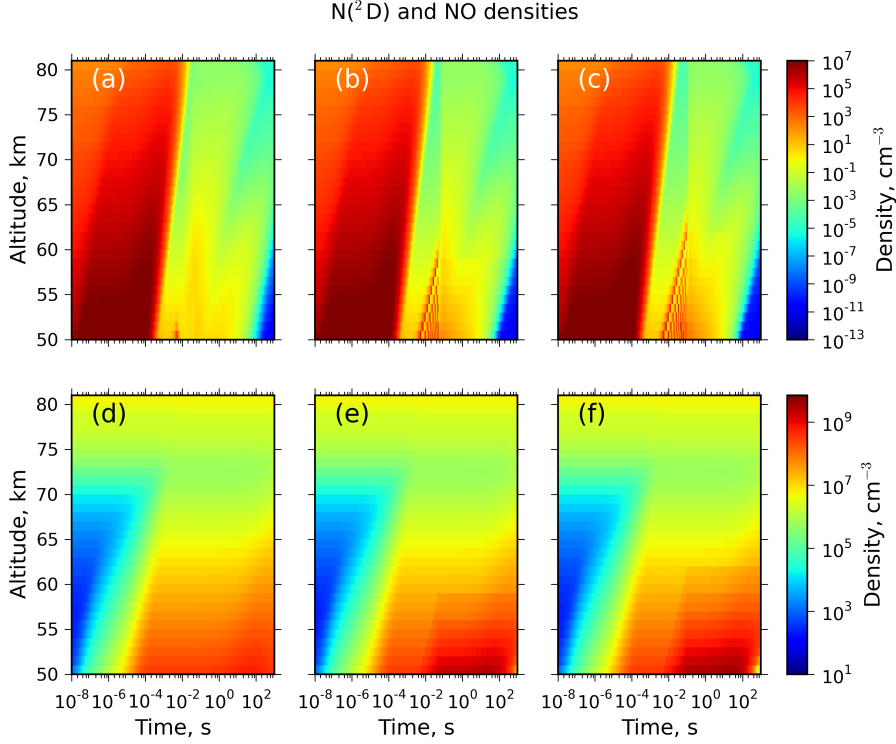
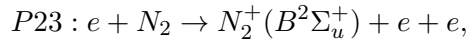
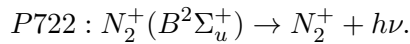


Figure 3.8: Altitude-time evolution of the N(²D) density (upper plots) and NO density (lower plots) due to a single sprite streamer with a driving current of 5 ms ((a)-(d)), 50 ms ((b)-(e)) and 100 ms ((c)-(f)).

Below 65 km, and in the cases of 50 ms and 100 ms of current duration (see Figures 3.9b and 3.9c), the concentration of N₂⁺(A²Π_u) reaches values close to 10³ cm⁻³ due to the reduced electric field oscillations. The evolution of the electronically excited N₂⁺(B²Σ_u⁺) ion is similar to that of the previously discussed species (see Figures 3.9d, 3.9e and 3.9f). At 50 km the concentration of N₂⁺(B²Σ_u⁺) reaches values close to 10⁴ cm⁻³ and, at 80 km, it reaches just 10⁻³ cm⁻³. At low altitudes this behavior is due to direct electron-impact ionization of N₂:



which is activated by a very high reduced electric field in the streamer head (see Figure 3.4). After the high-field phase, the N₂⁺(B²Σ_u⁺) density returns to ambient values by spontaneous radiative decay:



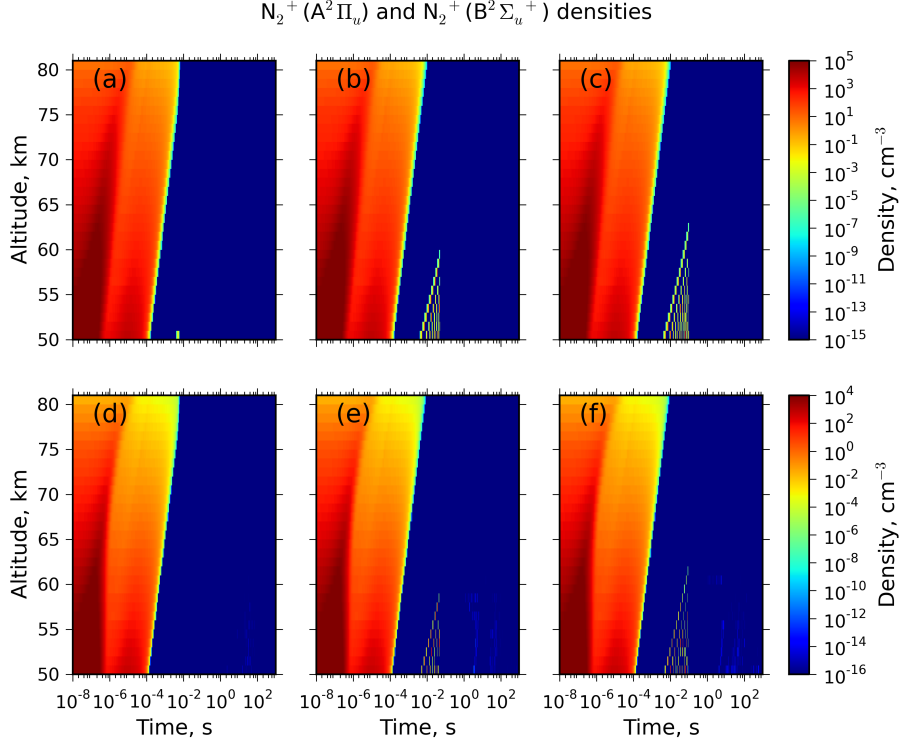
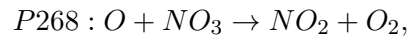


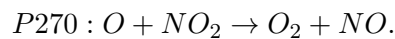
Figure 3.9: Altitude-time evolution of the $N_2^+(A^2\Pi_u)$ density (upper plots) and $N_2^+(B^2\Sigma_u^+)$ density (lower plots) due to a single sprite streamer with a driving current of 5 ms ((a)-(d)), 50 ms ((b)-(e)) and 100 ms ((c)-(f)).

3.3.5 NO_2 and NO_3

The temporal evolution of the density of NO_2 at different altitudes for the three different driving current durations investigated is shown in Figures 3.10a, 3.10b and 3.10c. The impact of the streamer head and the high-field phase between 58 km and 80 km is negligible due to the balance of

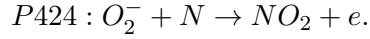


and



3. SPRITES

At low altitudes (< 59 km), we also see a constant NO_2 density due to the previous processes (P408 and P270), except P268, and

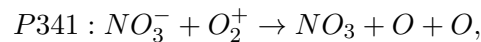


However, 0.1 s after the streamer head, the concentration of NO_2 decreases up to 1 order of magnitude because the detachment of O_2^- by N (P424) is less effective. Finally, at longer times (> 10 s), the density of NO_2 increases above its background value (up to one order of magnitude) due to an enhanced ozone concentration at these times and the process

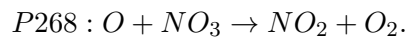


This NO_2 increase is proportional to the duration of the driving current. Arnone et al. [2008] show a possible enhancement of 10% in the concentration of NO_2 above thunderstorms through MIPAS/GMTR measurements at 52 km with a tendency to increase with height. This value is significantly below our estimate because we use a limited ozone kinetics. In this regard, we might be overestimating the production of O_3 by sprites since we did not consider H_2O , H or OH species and, consequently, did not evaluate the loss of O_3 in reactions with H atoms, that could be significant during nighttime conditions. This could be the reason why we don't get a significant variation in NO_x ($= \text{N} + \text{NO} + \text{NO}_2$) concentration in the extreme case of 100 ms of driving current at 70 km in contrast to measurements obtained by Enell et al. [2008] through ISUAL (FORMOSAT-2) that show a local enhancement of up to 5 times from the minimum value (in extraordinary cases).

The behavior of the NO_3 concentration (see Figures 3.10d, 3.10e and 3.10f) is very similar to the previous case of NO_2 . The NO_3 density is not affected by the streamer passage due to the balance between



and



For the case of the 5 ms driving current and below 60 km starting approximately 10 s after the streamer head, we have small increases (up to a factor 4) due to the process P341. For the driving currents of 50 ms and 100 ms duration, and similar to the

NO₂ case, the density of NO₃ decreases between 59 km and 62 km almost 2 orders of magnitude 1 s after the streamer head due to the process P268. The concentration of NO₃ reverts to background values due to the increase of ozone and NO₂ densities for long times, which activates the process

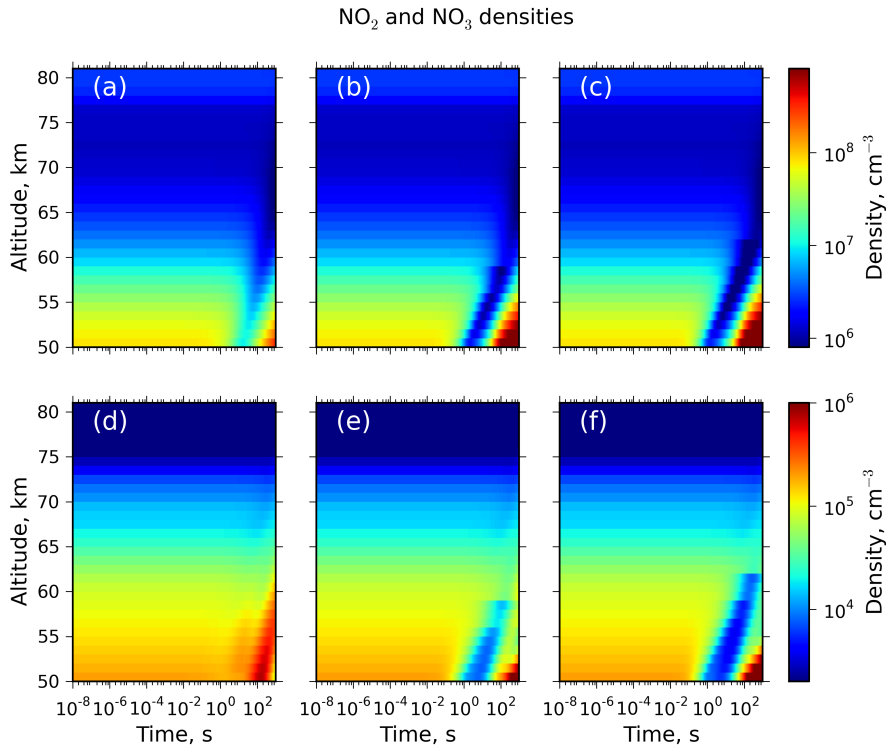
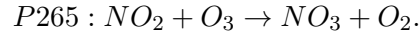


Figure 3.10: Altitude-time evolution of the NO₂ density (upper plots) and NO₃ density (lower plots) due to a single sprite streamer with a driving current of 5 ms ((a)-(d)), 50 ms ((b)-(e)) and 100 ms ((c)-(f)).

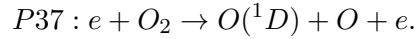
Due to the altitude at which sprites occur, we only have experimental data of their optical emissions that are proportional to the concentration of the excited emitting species. We can compare our results with previous models, i.e. [Sentman et al., 2008b] and [Gordillo-Vázquez, 2008]. In the case of the nitrogen oxides we obtain different results and behaviors. This is mainly due to the use of different initial conditions and different reduced electric field characteristics. However, as in previous models, we

3. SPRITES

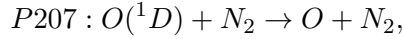
obtain a higher impact in these species (NO_x) at low altitudes although our values are somewhat higher than in those models.

3.3.6 Metastable excitations of atomic oxygen

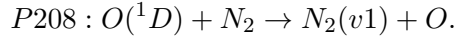
The altitude and time-dependence of the most important metastable excited species densities of atomic oxygen, i.e. $\text{O}({}^1\text{D})$ and $\text{O}({}^1\text{S})$, are shown in Figure 3.11. The concentration of the excited atomic oxygen $\text{O}({}^1\text{D})$, which has a lifetime of 110 s, is shown in Figure 3.11a, 3.11b and 3.11c. At high altitudes the behavior of the density of $\text{O}({}^1\text{D})$ is very similar in the three cases studied: the density of $\text{O}({}^1\text{D})$ increases strongly in the streamer head and remains elevated during the high-field phase. The $\text{O}({}^1\text{D})$ density reaches values between 10^8 cm^{-3} at 50 km of altitude and 10^4 cm^{-3} at 80 km of altitude. These increases are due to electron-impact dissociative excitation,



After the high-field phase, the $\text{O}({}^1\text{D})$ density returns slowly to its background value through the quenching reactions

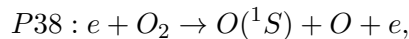


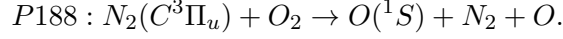
and



For the cases of 50 ms and 100 ms current duration and at altitudes below 65 km (see Figures 3.11b and 3.11c), there are fast variations in the $\text{O}({}^1\text{D})$ density between 10^{-3} s and 10^{-1} s associated with the reduced electric field oscillations acting during the afterglow. The reduced electric field oscillations increase the $\text{O}({}^1\text{D})$ concentration up to 10^8 cm^{-3} due to the direct electron-impact dissociative excitation process P37.

Similarly to $\text{O}({}^1\text{D})$, the $\text{O}({}^1\text{S})$ density, with a lifetime of 0.7 s, also increases strongly in the streamer head reaching about 10^7 cm^{-3} and 10^3 cm^{-3} at 50 km and 80 km of altitude, respectively (see Figures 3.11d, 3.11e and 3.11f). The main processes responsible of these increases are the direct electron-impact dissociative excitation during the passage of the streamer head and the quenching of $\text{N}_2(\text{C}^3\Pi_u)$ by O_2 during the afterglow





Above 75 km, the concentration of $O(^1S)$ maintains these values until 1 s due to process P188. Later, $O(^1S)$ slowly returns to its background density by collisional deexcitation with molecular oxygen:



For the cases of 50 ms and 100 ms driving current (see Figures 3.11e and 3.11f respectively) we see a number of variations in the $O(^1S)$ density between 10^{-3} s and 10^{-1} s due to direct electron-impact dissociative excitation of O_2 (P38).

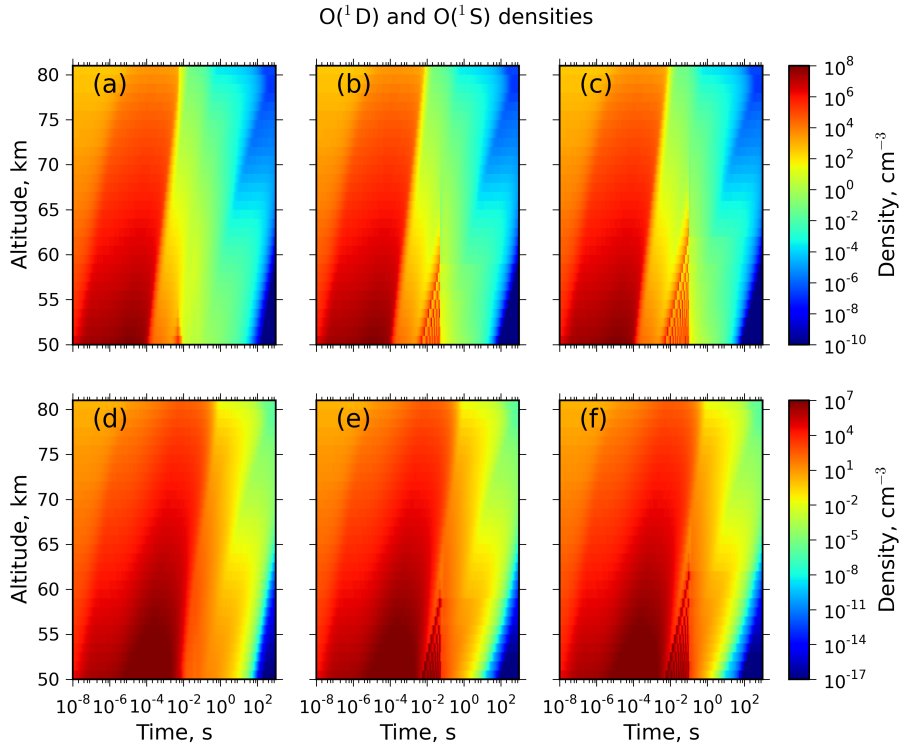


Figure 3.11: Altitude-time evolution of the $O(^1D)$ density (upper plots) and $O(^1S)$ density (lower plots) due to a single sprite streamer with a driving current of 5 ms ((a)-(d)), 50 ms ((b)-(e)) and 100 ms ((c)-(f)).

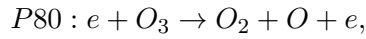
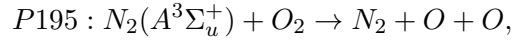
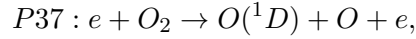
Recent measurements made by UARS (Upper Atmosphere Research Satellite) [Lee and Shepherd, 2010] indicate sudden and significant 557.7 nm optical outbursts from $O(^1S)$ between 73 km and 87 km in coincidence with lightning flashes (or some seconds after lightning) that could have produced sprites in the upper atmosphere. The

3. SPRITES

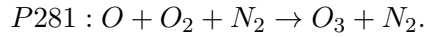
transient enhancement of the O(¹S) concentration (and subsequent sudden optical outbursts) can be produced by electron impact dissociative excitation ($e + O_2 \rightarrow O + O(^1S) + e$) due to the abundant presence of energetic free electrons released by sprite streamer ionization events.

3.3.7 Atomic oxygen and ozone

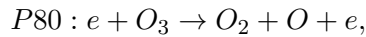
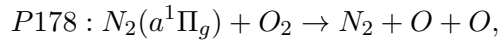
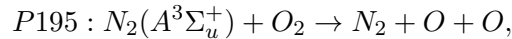
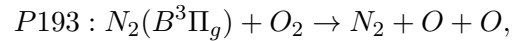
The behavior of the ground-state atomic oxygen concentration (see Figures 3.12a, 3.12b and 3.12c) is very similar to the evolution of the NO density (see Figures 3.8d, 3.8e and 3.8f). At the moment of the passage of the streamer head, the concentration of O increases between 10 orders of magnitude at 50 km of altitude and 1 order of magnitude at 80 km. This is produced by the direct electron-impact dissociative excitation process (P37) of molecular oxygen. For longer times, the O density remains high due to the balance between quenching and dissociation:



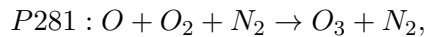
and



On the other hand, below 60 km the processes producing and removing ground state atomic oxygen are:



and



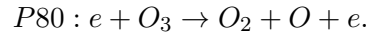
which decrease the density of O starting 10 s after the streamer head. For the cases of 50 ms and 100 ms driving current (see Figures 3.12b and 3.12c respectively), low altitudes and 10^{-2} s after the streamer head, the density of O increases up to 1 order

of magnitude by quenching of $N_2(B^3\Pi_g)$ by O_2 (P193) following the oscillations in the reduced electric field.

Looking now at ozone, Figures 3.12d, 3.12e and 3.12f, show that the O_3 density barely changes between 55 km and 80 km of altitude due to the balance between



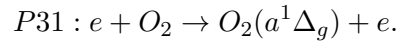
and



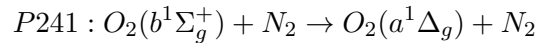
Below 56 km, there is an increase of O_3 by more than 1 order of magnitude for the case of 100 ms driving current (see Figure 3.12f) due to efficient three-body recombination of atomic oxygen (P281) at lower altitudes. This increase occurs 1 s after the streamer head because the electron density is too low and therefore the electron-impact dissociation of O_3 (P80) is not as effective as the three-body recombination of O (P281).

3.3.8 Molecular oxygen metastables

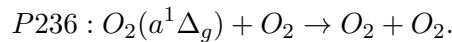
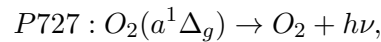
We have also studied the metastables $O_2(a^1\Delta_g)$, with a lifetime of about 45 minutes, and $O_2(b^1\Sigma_g^+)$, with a lifetime of 12 s (see Figure 3.13). Regarding the first one, the $O_2(a^1\Delta_g)$ density shows a strong increase coinciding with the streamer head and reaches values close to 10^9 cm^{-3} and 10^6 cm^{-3} at, respectively, 50 km and 80 km of altitude (see Figure 3.13a, 3.13b and 3.13c). The main mechanism controlling the variation of $O_2(a^1\Delta_g)$ is direct electron-impact excitation



After the production of $O_2(a^1\Delta_g)$ by P31, its high concentration remains constant due to the balance between



and



Below 55 km, there is a secondary increase of $O_2(a^1\Delta_g)$ up to 10^{12} cm^{-3} (in the 100 ms case) due to the electron production by the oscillations of the electric field. Electrons

3. SPRITES

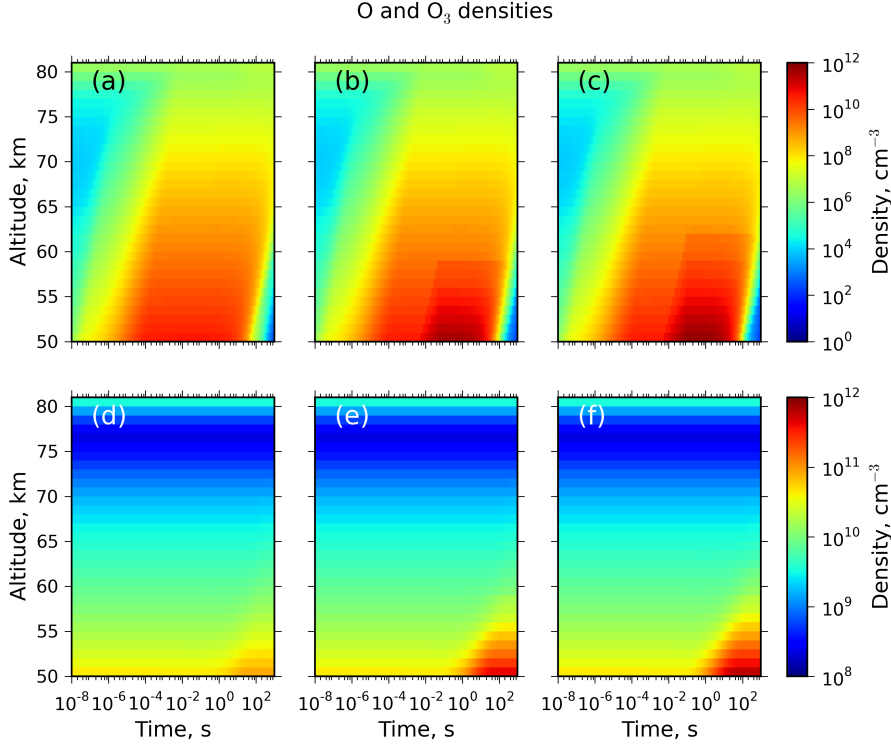
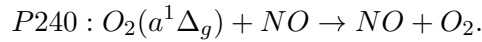
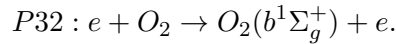


Figure 3.12: Altitude-time evolution of the O density (upper plots) and O₃ density (lower plots) due to a single sprite streamer with a driving current of 5 ms ((a)-(d)), 50 ms ((b)-(e)) and 100 ms ((c)-(f)).

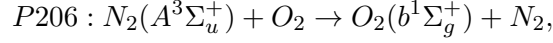
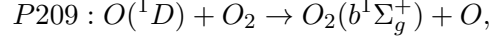
accelerated by a high E/N produce $O_2(a^1\Delta_g)$ by direct electron-impact excitation of O_2 (P31). After about 10^2 s, the density of $O_2(a^1\Delta_g)$ returns to its ambient value due to collisional deexcitation with NO:



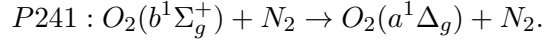
The behavior of the metastable $O_2(b^1\Sigma_g^+)$ is similar to that of $O_2(a^1\Delta_g)$. Figures 3.13d, 3.13e and 3.13f show values, immediately after the streamer head, of between 10^8 cm^{-3} and 10^6 cm^{-3} at 50 km and 80 km of altitude, respectively. As for $O_2(a^1\Delta_g)$, the main mechanism producing $O_2(b^1\Sigma_g^+)$ is direct electron-impact excitation of O_2 ,



Above 60 km, the concentration of $O_2(b^1\Sigma_g^+)$ remains constant up to 1 s after it is produced. This is due to the balance between the processes



and the reaction



The removal of $O_2(b^1\Sigma_g^+)$ is explained by the decay of the electron density and the subsequent decrease of the density of $O(^1D)$ and $N_2(A^3\Sigma_u^+)$. For this reason, the quenching of $O_2(b^1\Sigma_g^+)$ by N_2 becomes more effective. Below 60 km, we see another increase of $O_2(b^1\Sigma_g^+)$ up to 10^{11} cm^{-3} for the cases of 50 ms and 100 ms driving current (see Figures 3.13e and 3.13f) due to the quenching of $O(^1D)$ by O_2 (P236).

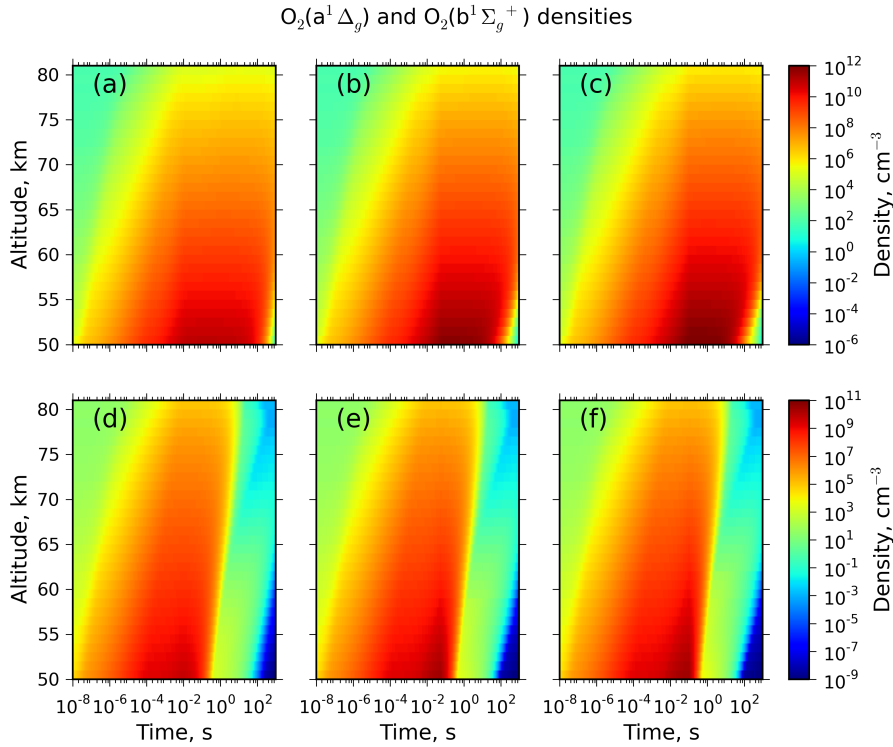
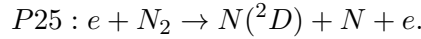


Figure 3.13: Altitude-time evolution of the $O_2(a^1\Delta_g)$ density (upper plots) and $O_2(b^1\Sigma_g^+)$ density (lower plots) due to a single sprite streamer with a driving current of 5 ms ((a)-(d)), 50 ms ((b)-(e)) and 100 ms ((c)-(f)).

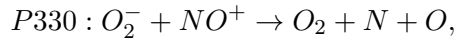
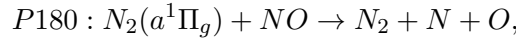
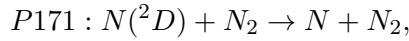
3. SPRITES

3.3.9 Atomic nitrogen

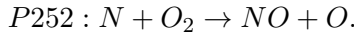
The evolution of the density of ground-state nitrogen atoms is shown in Figure 3.14. We can see how the N concentration increases by 7 orders of magnitude (up to 10^8 cm^{-3}) at 50 km at the moment of the streamer head and 2 orders of magnitude (up to 10^5 cm^{-3}) at 80 km. There is a further increase of 1 order of magnitude in the atomic nitrogen concentration during the high-field phase (between 10^{-5} - 10^{-4} s). The underlying mechanism of this later enhancement of N is direct electron-impact dissociative excitation of N_2 :



The density of N atoms remains high up to 10 s (at 50 km) due to the balance between



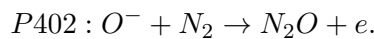
and



Above 67 km, a high concentration of N persists for more than 1000 s due to the balance between the processes P171, P100 and the process P252. For the cases of 50 ms and 100 ms driving current durations (see Figures 3.14b and 3.14c, respectively) and below about 62 km, the density of ground-state N increases up to a factor 5 driven by the oscillations of the reduced electric field. The cause of this secondary increase is direct electron-impact dissociative excitation of N_2 (P25).

3.3.10 N_2O

The altitude and time dependence of the density of N_2O (a greenhouse gas) is shown in Figure 3.15. We see that after the streamer head, the N_2O density increases up to 1 order of magnitude due to associative detachment (AD) of O^- by N_2 :



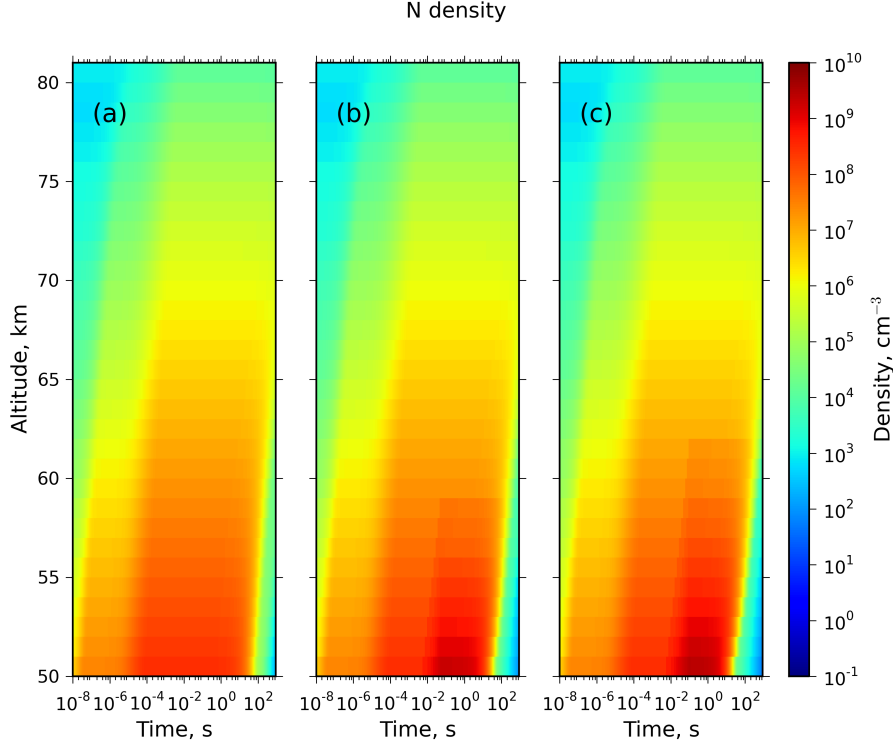
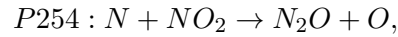
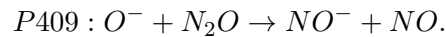
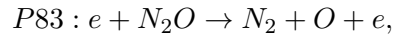


Figure 3.14: Altitude-time evolution of the atomic nitrogen density (N) due to a single sprite streamer with 5 ms (a), 50 ms (b) and 100 ms (c) driving current.

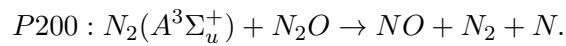
As we have previously discussed, this process (P402) strongly depends on the reduced electric field. The N_2O density remains at these enhanced values during all the simulation due to the AD process together with



and



In a similar way but at altitudes above 75 km, the concentration of N_2O increases by factor 6 due to AD and it remains high due to the balance between AD, P254, P409 and



3. SPRITES

We also see in Figures 3.15b and 3.15c (50 ms and 100 ms driving current, respectively) that the N_2O density grows one additional order of magnitude due to the influence of the reduced electric field oscillations on the AD process of O^- by N_2 at low altitudes (below 62 km in the case of 100 ms driving current).

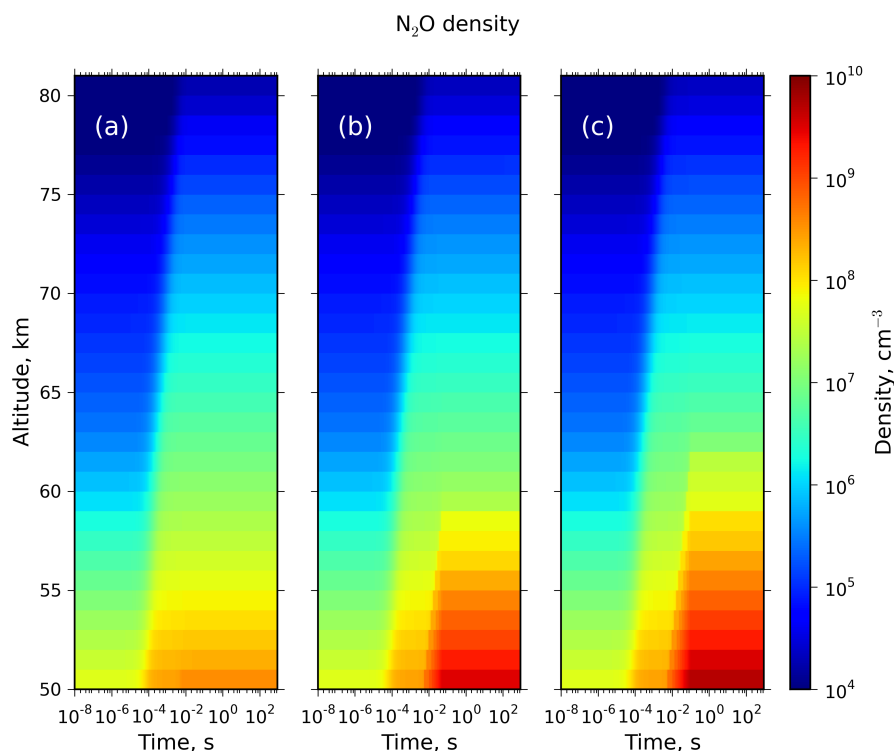
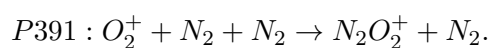


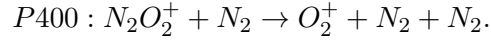
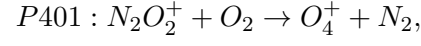
Figure 3.15: Altitude-time evolution of the N_2O density due to a single sprite streamer with 5 ms (a), 50 ms (b) and 100 ms (c) driving current.

3.3.11 $N_2O_2^+$

The concentration of $N_2O_2^+$ ions at the moment of the streamer head passage exhibits a sharp increase of 8 orders of magnitude at low altitudes (see Figure 3.16). The $N_2O_2^+$ density also shows a smooth increase of one additional order of magnitude following the high-field phase. Both increases of the concentration of $N_2O_2^+$ are produced by three-body associative recombination



Afterwards, it decays toward its ambient value due to dissociative recombination:



Above 75 km, the concentration of $N_2O_2^+$ increases up to 4 orders of magnitude by three-body associative recombination (P391) but then slowly returns to its initial ambient value due to dissociative recombination (P401). For the cases of 50 ms and 100 ms driving currents (see Figures 3.16b and 3.16c respectively) and below 60 km, the concentration of $N_2O_2^+$ barely changes during the oscillations of the reduced electric field.

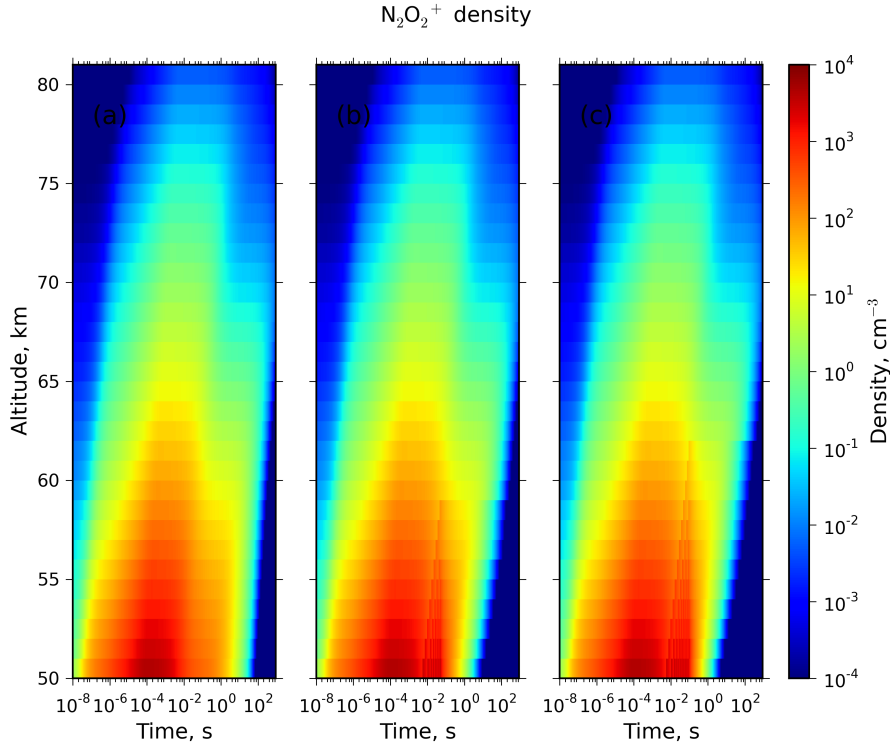


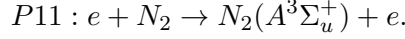
Figure 3.16: Altitude-time evolution of the $N_2O_2^+$ ion density due to a single sprite streamer with 5 ms (a), 50 ms (b) and 100 ms (c) driving current.

3.3.12 $N_2(A^3\Sigma_u^+)$

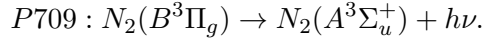
The time evolution of the metastable $N_2(A^3\Sigma_u^+)$ density is shown in Figure 3.17. The behavior of the $N_2(A^3\Sigma_u^+)$ concentration is very similar to that of the reduced electric

3. SPRITES

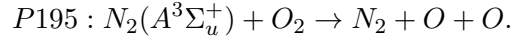
field (see Figures 3.3a, 3.3b and 3.3c). Below 60 km, it increases sharply to 10^8 cm^{-3} at the moment of the passage of the streamer head due to direct electron-impact excitation



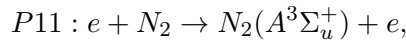
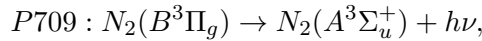
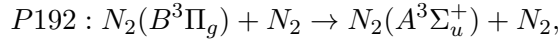
Later, the enhanced $N_2(A^3\Sigma_u^+)$ density persists due to the spontaneous decay of $N_2(B^3\Pi_g)$



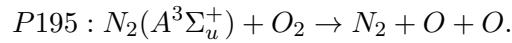
The density of $N_2(A^3\Sigma_u^+)$ finally returns to its ambient values due to quenching with O_2 when the reduced electric field vanishes:



Above 75 km, the density of $N_2(A^3\Sigma_u^+)$ increases smoothly to about 10^6 cm^{-3} due to the spontaneous radiative decay of $N_2(B^3\Pi_g)$ to $N_2(A^3\Sigma_u^+)$. For the cases of 50 ms and 100 ms durations of the current (see Figures 3.17b and 3.17c respectively) we see fast variations in the $N_2(A^3\Sigma_u^+)$ density associated to the reduced electric field oscillations. These fast variations are caused by



and



3.3.13 Optical emission brightness

In this section we will show and discuss the results of the optical emission brightness of the first and second positive band systems of N_2 as well as the near infrared (NIR) emission brightness of the Meinel band of N_2^+ and those of the $4.26 \mu\text{m}$ and $14.9 \mu\text{m}$ IR bands of CO_2 under the action of a single sprite streamer. As in the previous section, we have used three different driving current durations (5 ms, 50 ms and 100 ms) to study the possible detection scenarios at different altitudes using suitable instrumentation. The emission brightness measured in Rayleighs ($1 \text{ R} = 10^6 \text{ photons cm}^{-2} \text{ s}^{-1}$, [Hunten

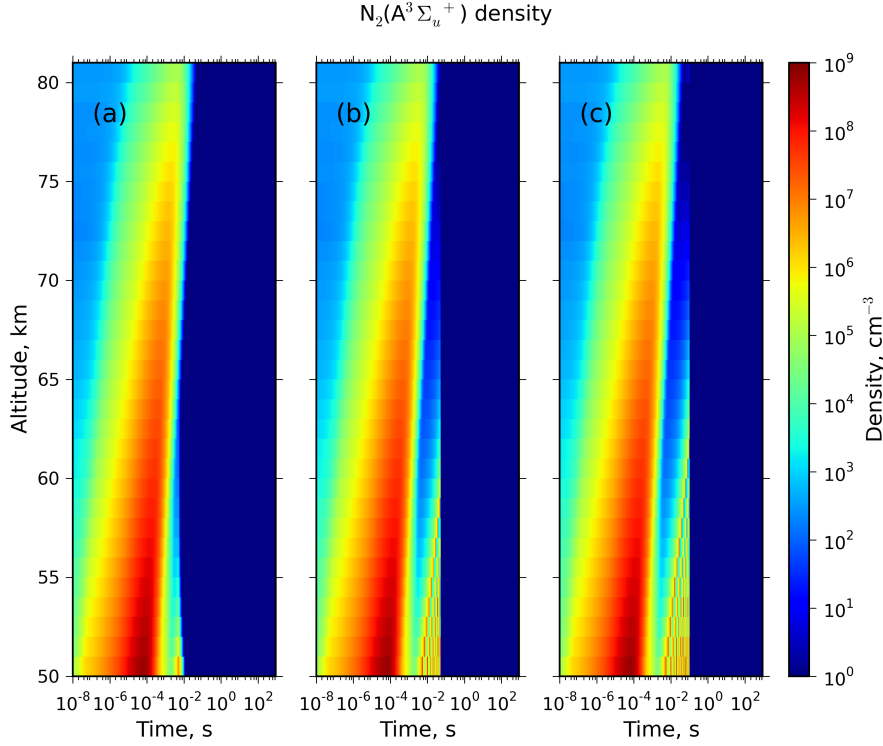
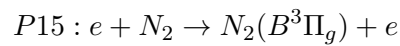


Figure 3.17: Altitude-time evolution of the metastable $N_2(A^3\Sigma_u^+)$ due to a single sprite streamer with 5 ms (a), 50 ms (b) and 100 ms (c) driving current.

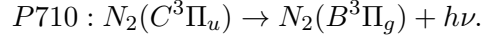
et al., 1956]) is calculated through the expression (2.12). In our case, the magnitude l is the diameter of a sprite streamer which we have rescaled with air density using the observations by [Stenbaek-Nielsen et al., 2013] where a diameter of 500 m at 76 km, is taken as a reference

In Figures 3.18a, 3.18b and 3.18c we can see the time evolution of the $N_2(B^3\Pi_g)$ density, which radiative decay to $N_2(A^3\Sigma_u^+)$ is responsible of the first positive band system (1PN₂) of N_2 . The emission brightness (EB) of the 1PN₂ is shown in Figures 3.18d, 3.18e and 3.18f. The EB of the 1PN₂ exceeds the value of 1 MR in almost all altitudes considered. This high brightness is produced by the strong $N_2(B^3\Pi_g)$ excitation in the streamer head and during the afterglow by, respectively, direct electron-impact excitation

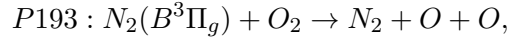


3. SPRITES

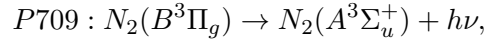
and radiative cascading from $N_2(C^3\Pi_u)$



The main deexcitation mechanism of $N_2(B^3\Pi_g)$ is, at high altitudes, quenching by O_2



and, at low altitudes, the radiative decay responsible of the $1PN_2$ emission



At very low altitudes (between 55 km and 50 km), the brightness of the reddish emission of $1PN_2$ can exceed 10 GR. The variations in the emission brightness (and therefore in the density of $N_2(B^3\Pi_g)$) are associated to the reduced electric field oscillations.

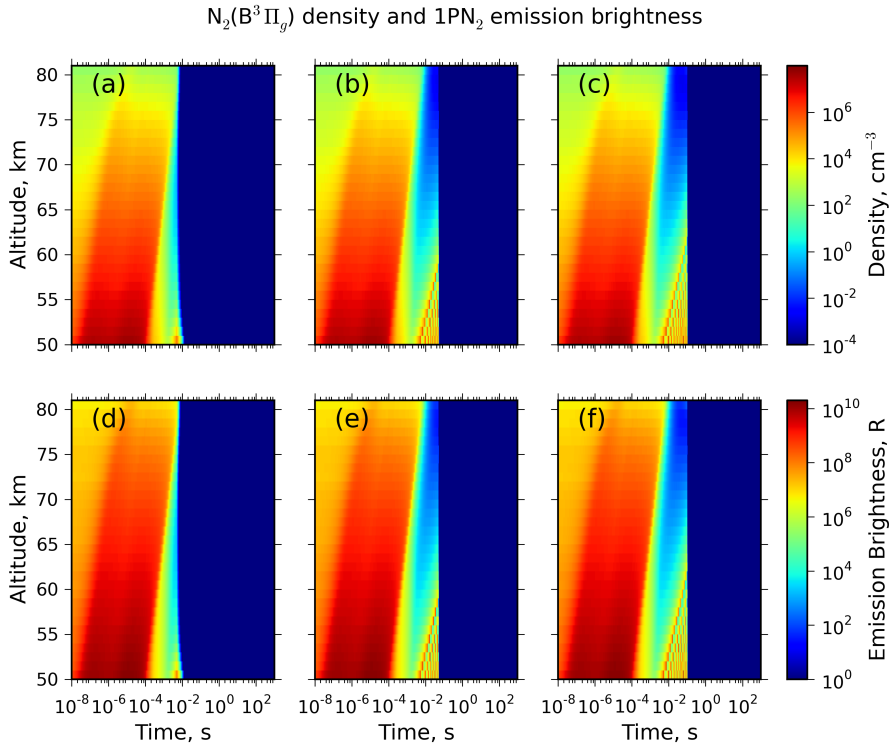
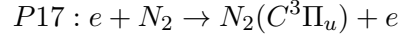
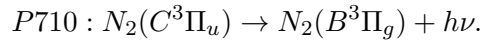


Figure 3.18: Altitude-time evolution of the $N_2(B^3\Pi_g)$ density (upper plots) and the first positive band system ($1PN_2$) emission brightness (lower plots) due to a single sprite streamer with a driving current of 5 ms ((a)-(d)), 50 ms ((b)-(e)) and 100 ms ((c)-(f)).

The behavior of the $2PN_2$ emission brightness (see Figure 3.19) is very similar to that of $1PN_1$. In this case, the EB also exceeds 1 MR at almost all altitudes for the three cases considered due to the strong increase of the $N_2(C^3\Pi_u)$ density by direct electron-impact excitation



and its subsequent radiative decay



Similarly to the previous case, at low altitudes, the EB of the $2PN_2$ can exceed 10 GR for the blue emission corresponding to $2PN_2$.

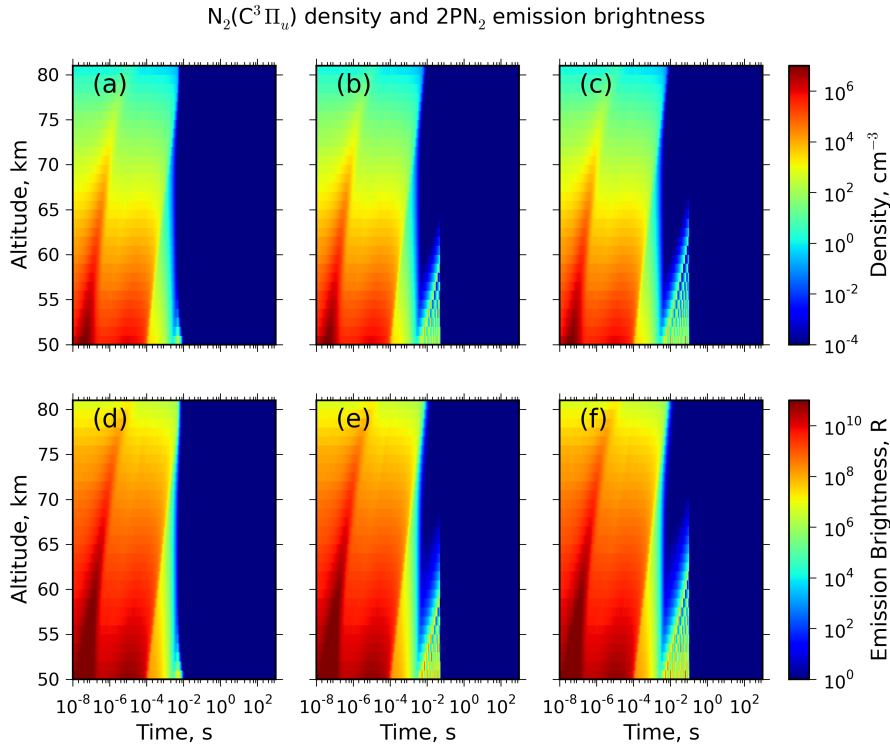
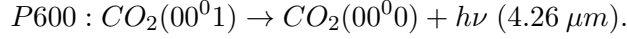


Figure 3.19: Altitude-time evolution of the $N_2(C^3\Pi_u)$ density (upper plots) and the second positive band system ($2PN_2$) emission brightness (lower plots) due to a single sprite streamer with a driving current of 5 ms ((a)-(d)), 50 ms ((b)-(e)) and 100 ms ((c)-(f)).

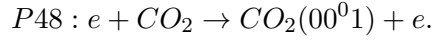
In Figure 3.20a, 3.20b and 3.20c, we can see that the predicted IR ($4.26 \mu\text{m}$) emission brightness can also exceed 1 MR below 75 km for the case of 100 ms driving current

3. SPRITES

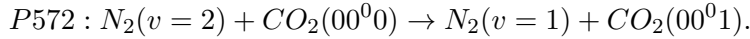
(reaching 100 GR at 50 km) and below 70 km for the case of 5 ms driving current (exceeding 1 GR at 50 km). Just before the end of the driving current, the IR (4.26 μm) emission begins to increase due to the radiative deexcitation from $\text{CO}_2(00^01)$ to the fundamental vibrational state $\text{CO}_2(00^00)$.



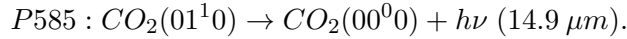
In order to achieve this strong IR emission, a high rate of $\text{CO}_2(00^01)$ production is necessary, with direct electron-impact vibrational excitation of CO_2 being the main production mechanism of $\text{CO}_2(00^01)$ during the first stages of the emission



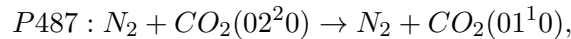
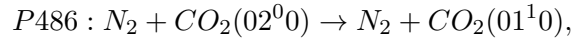
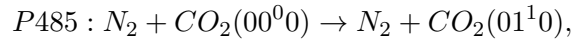
However, when the reduced electric field falls to negligible values, the production of $\text{CO}_2(00^01)$ is dominated by the vibrational-vibrational process



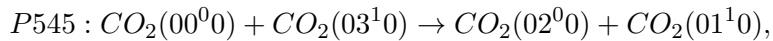
However, for the IR emission brightness at 14.9 μm , it can reach values above 1 GR for low altitudes (< 60 km) only for the cases of 50 ms and 100 ms driving currents (see Figures 3.20e and 3.20f). This 14.9 μm emission is produced by the radiative decay of the first vibrationally excited state of CO_2 to the ground state



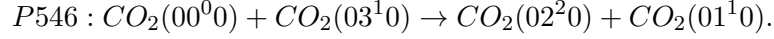
The production of $\text{CO}_2(01^10)$, necessary for the 14.9 μm IR emission, is dominated by vibrational-translational (VT) and vibrational-vibrational (VV) processes, the initial vibrationally excited states of which have been generated by electron-impact excitation. The sum of several VT processes explains the increase of the $\text{CO}_2(01^10)$ density:



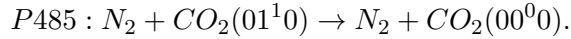
together with the VV processes



and



The main loss mechanisms of $CO_2(01^10)$ are radiative decay (P579) and quenching of $CO_2(01^10)$ by N_2



Considering now that the atmosphere, from the mesosphere to space, behaves as optically thin we believe that the IR emissions associated to sprites could be detected with suitable space instrumentation pointing to the limb as in the case of LBH emissions calculated by Gordillo-Vázquez et al. [2011, 2012] and recorded by ISUAL [Mende et al., 2004].

A successful detection, however, would require enough sensibility and time resolution to distinguish between the transient emissions from a sprite and the atmospheric background. Evaluating this possibility falls outside the scope of the present thesis.

Finally, we show in Figure 3.21 the Meinel emission brightness due to a single sprite streamer for different driving current durations. Our model predicts, for the three cases studied (5 ms, 50 ms and 100 ms), that the Meinel emission brightness doesn't reach 1 MR or barely reaches it at 50 km of altitude. Our predicted Meinel emission brightness grows with decreasing altitudes. Therefore, we speculate that the brightness due to Meinel emissions could reach and exceed 1 MR at tendrils altitudes and, consequently, the chances to detect it from ground or space platforms are small or none.

Figure 3.22 shows the altitude dependence of the emission brightness as would be recorded by a camera of 33 fps (standard video rate) due to a single sprite streamer with 50 ms driving current. We see in Figure 3.22 that the emission brightness of all the bands studied with our model are above 1 MR (except for the Meinel band) the highest altitude range (70-80 km). It is also interesting to note that the CO_2 IR emission brightness (4.26 μm and 14.9 μm) could even exceed values of 1 GR. Therefore, the possibility of detecting of sprite infrared emissions from the space depends basically on the characteristics of the instrumentation. Even so, if we consider an optically thin atmosphere above 50 km, the infrared absorption is negligible. The emission brightness of the 4.26 μm band with respect the atmospheric background could be estimated through the ratio between the population of the $CO_2(00^01)$ after the streamer passage and the background population of the $CO_2(00^01)$. In this instance, the post streamer

3. SPRITES

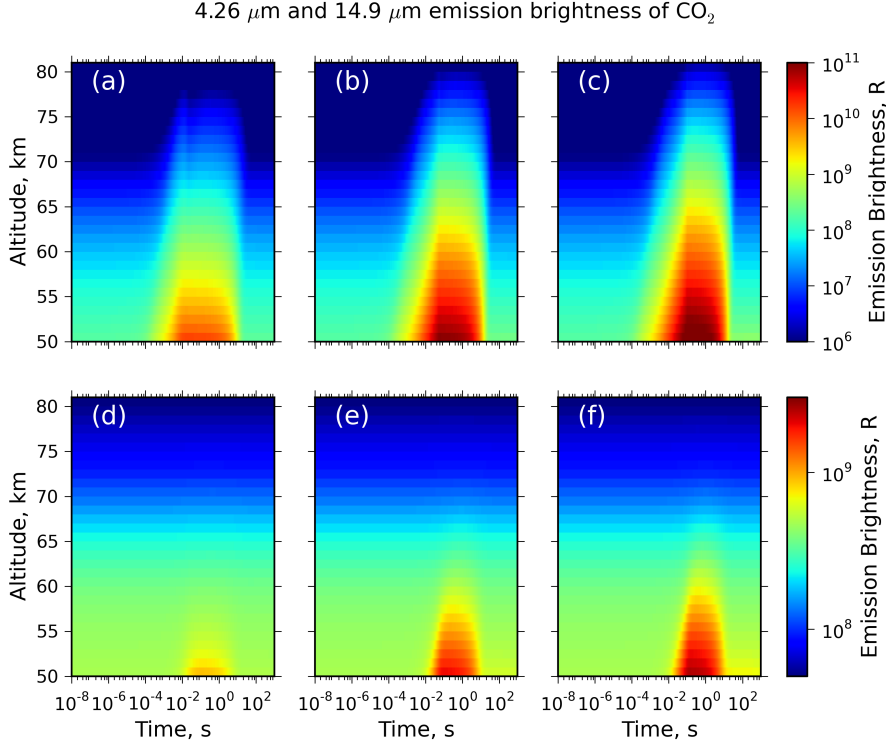


Figure 3.20: Altitude-time evolution of the 4.26 μm (upper plots) and 14.9 μm (lower plots) infrared emission brightness of CO_2 due to a single sprite streamer with a driving current of 5 ms ((a)-(d)), 50 ms ((b)-(e)) and 100 ms ((c)-(f)).

infrared emission brightness of the 4.26 μm band is more than two orders of magnitude higher than the IR emission of the atmospheric background at 50 km and one order of magnitude higher at 65 km (Figure 3.20).

In the same way, for the case of a camera recording at 1000 fps (see Figure 3.23) the emission brightness of all bands can exceed, according to our model, 1 MR in the 70-80 km altitude range. However, the brightest band in this case is that of 1PN_2 , reaching values close to 10 GR at 70 km for the 1000 fps camera. As stated before, we need to be careful about our model results below 70 km since at these altitudes sprite streamers tend to branch and our model does not follow streamer branching dynamics.

As in the case of the nitrogen oxides, our emission brightness results disagree with previous models. We obtain higher values for the optical emission brightness than those reported by Sentman et al. [2008b] and Gordillo-Vázquez [2008]. However, at altitudes between 68 km and 63 km, our calculations are in good agreement with the

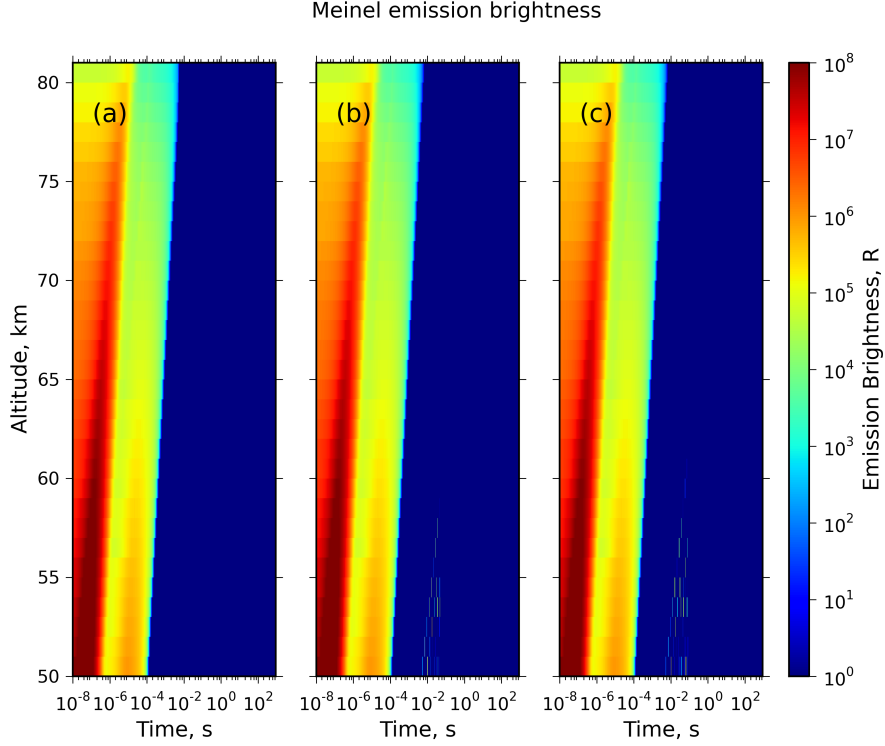


Figure 3.21: Altitude-time evolution of the Meinel ($N_2^+(A^2\Pi_u) \rightarrow N_2^+(X^2\Sigma_g^+)$) emission brightness due to a single sprite streamer with 5 ms (a), 50 ms (b) and 100 ms (c) driving current.

results by Gordillo-Vázquez [2008] for the N_2 second positive system band emission, which predict EB between 100 MR (68 km) and 10 GR (63 km). Finally, at 75 km, our model predicts sprite optical emissions between 10 MR and 1 GR for the first positive band system of N_2 . These results also agree, in the upper limit, with the observations reported by Stenbaek-Nielsen et al. [2007].

3. SPRITES

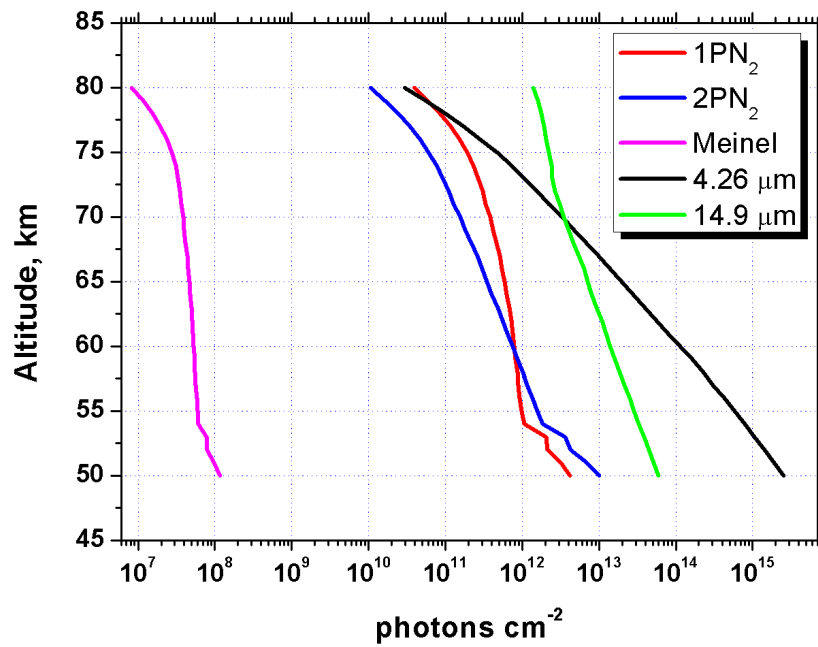


Figure 3.22: Altitude dependence of the emission brightness due to a single sprite streamer with 50 ms driving current as would be measured by a 33 fps camera. The red, blue and purple lines correspond, respectively, to the first and second positive band systems of N_2 and to the Meinel band of N_2^+ . The black and green lines correspond to the 4.26 μm IR and 14.9 μm IR bands of CO_2 .

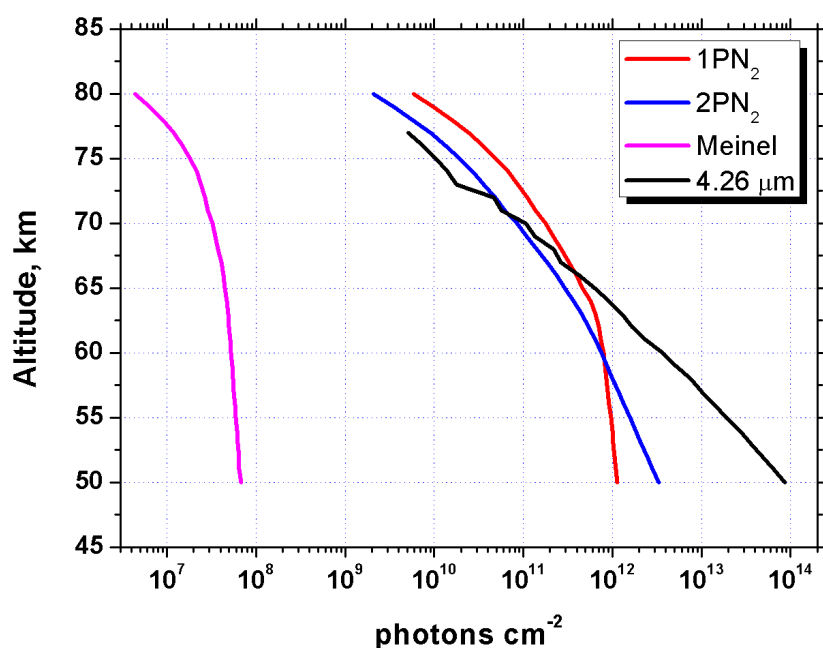


Figure 3.23: Altitude dependence of the emission brightness due to a single sprite streamer with 50 ms driving current as would be measured by a 1000 fps camera. The red, blue and purple lines correspond, respectively, to the first and second positive band systems of N_2 and to the Meinel band of N_2^+ . The black line corresponds to the $4.26 \mu\text{m}$ IR band of CO_2 . We have not included the integrated emission brightness of the $14.9 \mu\text{m}$ IR band because our model has not enough temporal resolution at these timescales.

3. SPRITES

3.3.14 Energy balance

Finally, we discuss in this section the result shown in Figure 3.24a, 3.24b and 3.24c in connection with the thermal impact of sprite streamers with 5 ms, 50 ms and 100 ms driving current in the Earth mesosphere. The most important increase in the gas temperature occurs at lower altitudes, between 60 km and 50 km, and it is proportional to the duration of the driving current. At higher altitudes the variation of the gas temperature is negligible compared to that produced at lower layers.

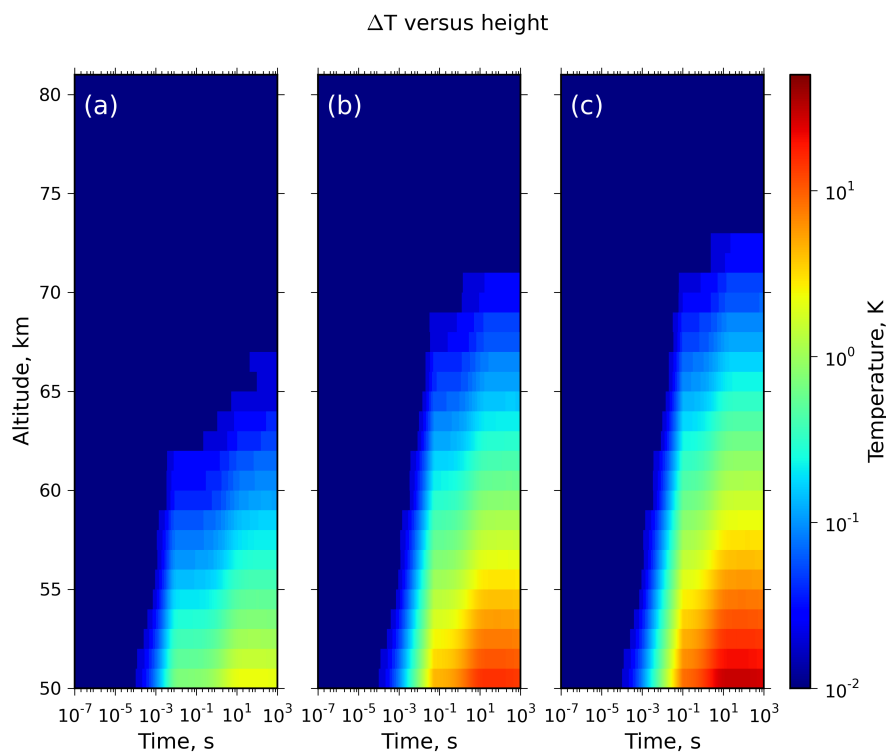


Figure 3.24: Altitude-time evolution of the gas temperature variation due to a single sprite streamer with (a) 5 ms, (b) 50 ms and (c) 100 ms of driving current.

We can see in Figure 3.25 the altitude-dependence of the maximum variation of the gas temperature under the action of a sprite streamer. As previously discussed, the maximum gas temperature is reached at 50 km and it is strongly related to the duration of the driving current so that the temperature variation is greater for longer driving currents. The gas temperature maxima are 2.26 K, 14.9 K and 29.2 K with 5 ms, 50 ms and 100 ms driving currents, respectively.

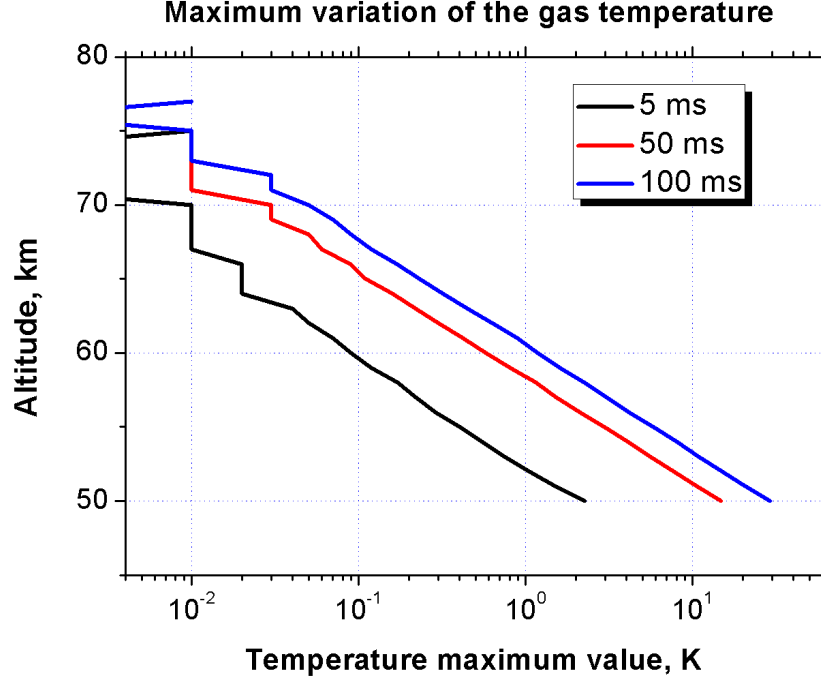


Figure 3.25: Altitude evolution of the maximum value of the gas temperature. The solid black, red and blue lines are for driving currents of, respectively, 5 ms, 50 ms and 100 ms.

The chemical mechanisms responsible for the gas heating are the same in the three cases studied and, consequently, we will only describe in detail the results for the intermediate case (50 ms of afterglow) at 50 km of altitude. In Figure 3.26 we show, for this case, the temporal evolution of the gas heating (blue line) and the reduced electric field (black line). We can see two different behaviors in the temporal evolution of the gas temperature related to the evolution of the reduced electric field. The first one is called “afterglow stage” and corresponds to the driving current while the second one is called “post-afterglow stage” and it is related to the regime of vanishing reduced electric field between 54 ms and 33.6 s.

Figure 3.27 shows the evolution of the energy contained in the gas under the action of a sprite streamer at 50 km of altitude. We can compare Figure 3.26 with Figure 3.27 for a better understanding of the energetic channels responsible for the gas heating. The red area in Figure 3.27 shows the total energy density imposed on the gas ($P_{ext} + P_{abs}$), the green area is the energy density of the chemical channel (P_{chem}) and the

3. SPRITES

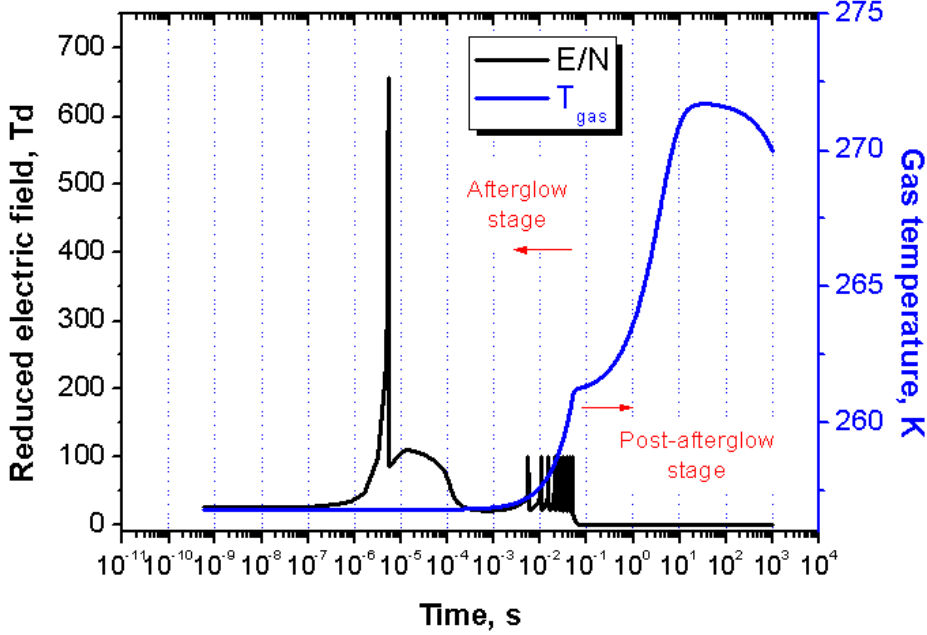


Figure 3.26: Temporal evolution of the gas temperature (blue line) and the reduced electric field (black line) at 50 km of altitude for the 50 ms driving current.

yellow area is the energy density corresponding with the radiative channel (P_{rad}). The electron energy channel P_{elec} is negligible. In the afterglow stage (up to 54 ms) the reduced electric field is the main mechanism injecting energy in the system, with a large fraction of this electric field energy being absorbed through the chemical channel. The difference between the energy density injected by the electric field and the energy density absorbed by the chemical processes is the net gas heating of the afterglow stage. When the reduced electric field goes to zero (post-afterglow stage), the energy densities of the chemical and radiative channels decrease and the gas temperature increases again (see post-afterglow stage in Figure 3.26).

From the thermal point of view, we can see in Figure 3.28 the time-integrated contribution of each channel to gas heating in the afterglow (red bars) and post-afterglow (yellow bars) stages. We represent in Figure 3.28 the gas temperature variations produced by absorption/emission of external, chemical and radiative power. We note that, in the afterglow stage (up to 54 ms), the reduced electric field, through P_{ext} , produces an increase in the gas temperature of more than 20 K. However 15 K of those 20 K

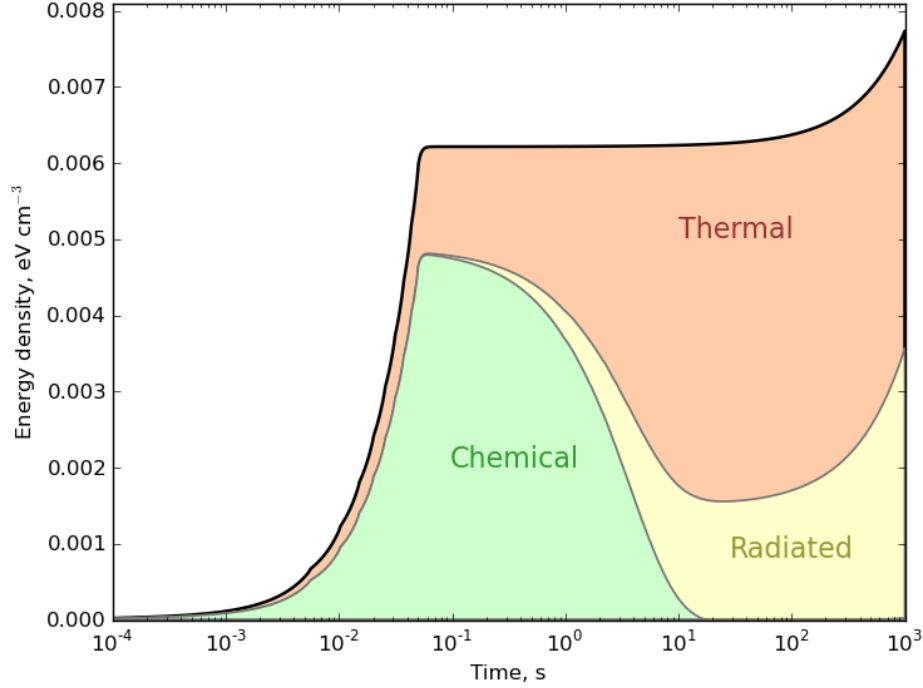


Figure 3.27: Time-dependent distribution of the energy density dissipated by a single sprite streamer with 50 ms driving current at an altitude of 50 km.

are deposited into the internal degrees of freedom of the gas, i.e. P_{chem} (note that a negative sign of the temperature contribution in Figure 3.28 corresponds to the temperature absorbed by the gas in non-thermal processes). The temperature losses due to radiative decay are negligible (0.04 K) during the afterglow. Therefore, the total (net) temperature increases in the afterglow stage is approximately of 4.5 K.

The energy loss fraction of electrons by electron-impact collisions in the afterglow stage is shown in Figure 3.29. Out of the 15.8 K deposited by the sprite streamer in P_{chem} , 92.7 % goes to vibrational excitation of molecular nitrogen $N_2(v)$, 2.63 % to rotational excitation of molecular nitrogen $N_2(rot)$ and 1.96 % to vibrational excitation of molecular oxygen $O_2(v)$. These results are consistent with what we see in Figure 3.30, where we show the different energy loss fractions as a function of E/N for direct electron-impact processes. The reduced electric field reached by the streamer head is approximately 650 Td (at 50 km of altitude) but for a very short time (of about several

3. SPRITES

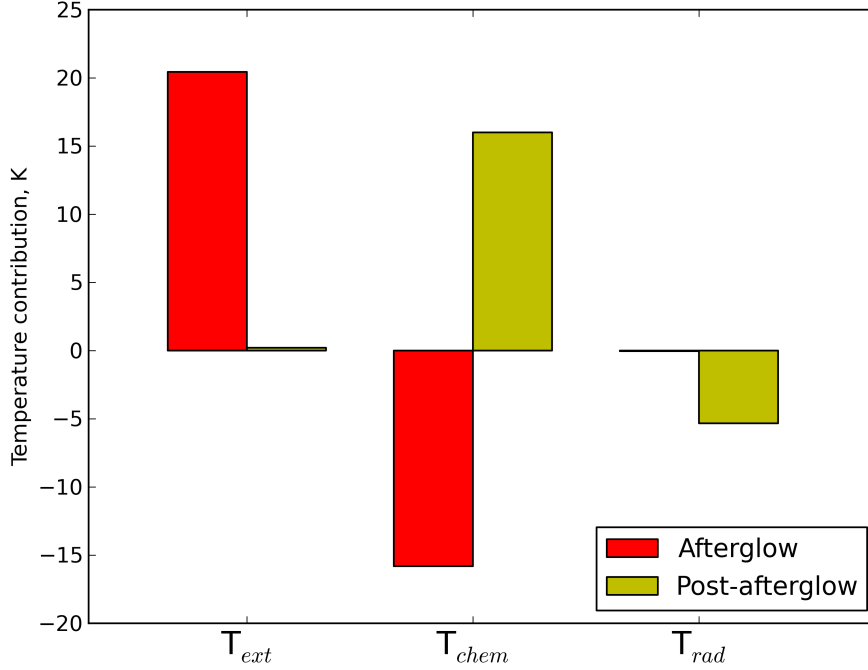


Figure 3.28: Time-integrated contribution to gas temperature of each energetic channel in the afterglow stage (red bars) and in the post-afterglow stage (green bars) after the streamer head at 50 km of altitude and for the 50 ms driving current. Note that a negative sign of the temperature contribution corresponds to the temperature absorbed by the gas in non-thermal processes.

micro seconds). However, the mean reduced electric field of all the sprite streamers E/N profile is below breakdown values and, consequently, direct electron-impact vibrational excitation of N_2 is the main kinetic mechanism where the P_{chem} energy is stored.

Once the reduced electric field has dropped to negligible values, the P_{ext} channel only provides 0.2 K to the gas (see Figure 3.28, green bars) in the post-afterglow stage. However, the external energy, mainly stored in the vibrational states of molecular nitrogen $N_2(v)$, is now transferred by vibrational-vibrational processes to $CO_2(v_1 v_2^l v_3)$. The vibrational quenching of $CO_2(v_1 v_2^l v_3)$ by N_2 and the radiative decay of vibrational excited CO_2 levels are the responsables of the ~ 11 K gas temperature increase during the post-afterglow stage. The main processes underlying gas heating in the post-afterglow stage are shown in Figure 3.31.

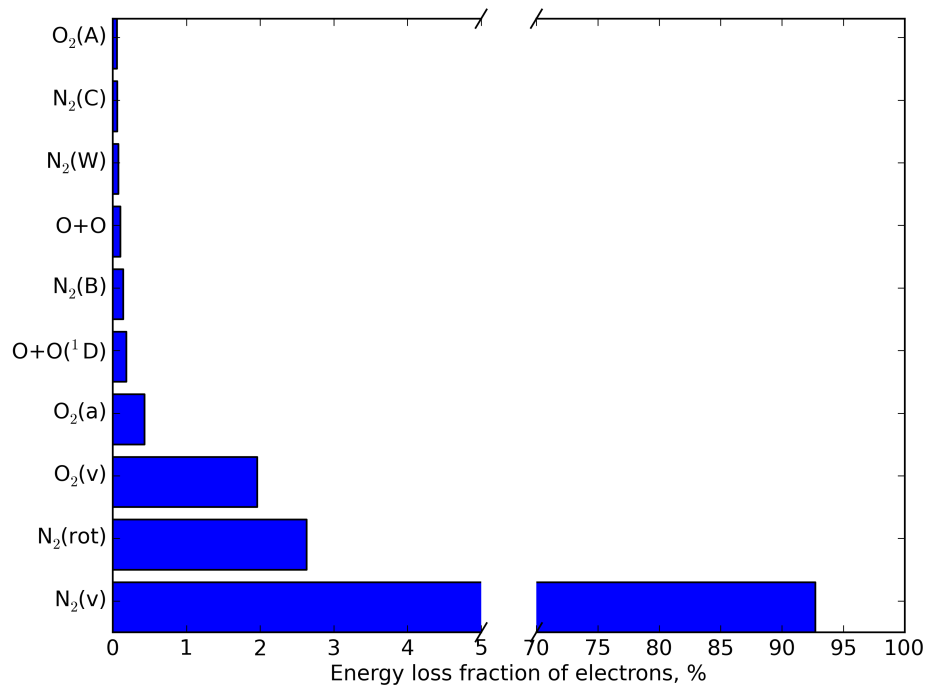


Figure 3.29: Electron energy loss fractions through electron-impact collision processes producing species above 50 km of altitude for a 50 ms driving current during the afterglow stage. Note that in O₂(v) and N₂(v) we have taken into account all the vibrational levels considered.

3. SPRITES

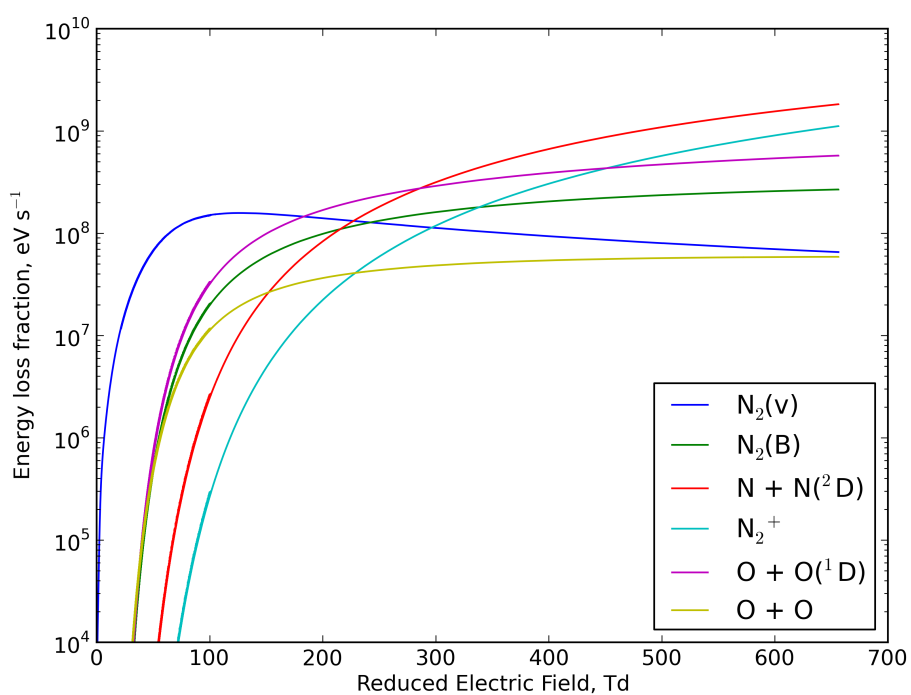


Figure 3.30: Fractions of electron energy partitioned into the excitation, ionization and dissociation of molecules. These values are calculated at 50 km of altitude for a 50 ms driving current considering the afterglow and post-afterglow stages. Note that in O₂(v) and N₂(v) we have taken into account all the vibrational levels considered.

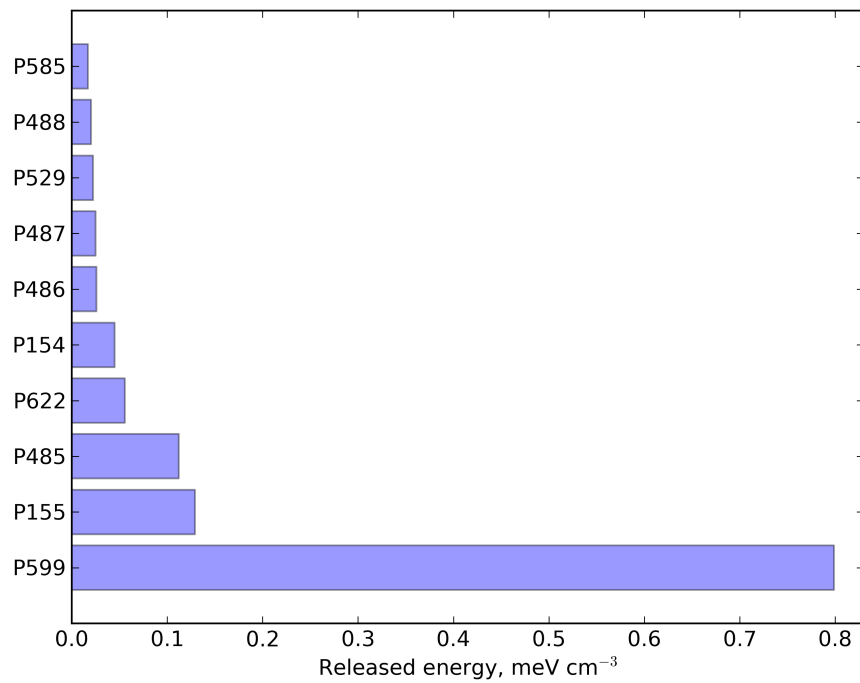


Figure 3.31: Time-integrated contribution of different kinetic processes to gas heating up to 33.6 s at 50 km of altitude for a 50 ms driving current during the post-afterglow stage.

3. SPRITES

4

Electrical discharges on Saturn

“Forth! Down fear of darkness! Arise, arise, Riders of Théoden! Fell deeds awake: fire and slaughter! spear shall be shaken, shield be splintered, a sword-day, a red day, ere the sun rises! Ride now, ride now! Ride! Ride for ruin and the world’s ending!!”

– King Théoden son of Thengel, *The Lord of the Rings*

4.1 State of the art

Atmospheric electrical activity is not confined to the Earth. Lightning flashes have been observed directly in some planets of the Solar System and detected in an indirect way in others [Yair, 2012]. The only terrestrial planet with signs of thunderstorm activity is Venus. From the 80’s, all the spacecrafts that have approached to Venus have searched for evidences of electrical activity with controversial results. The soviet lander Venera 12 in its descent through the venusian atmosphere detected the first indirect evidence of lightning discharges in clouds on Venus [Ksanfomaliti, 1980]. This discovery was based in set of quasi-periodic VLF pulses recorded on the planetary surface (see Figure 4.1).

Ten years later, in 1990 the NASA, spacecraft Galileo carried out a flyby over Venus in its journey to Jupiter. Galileo detected, with its plasma wave instrument, nine events of impulsive radio signals in the range of LF band [Gurnett et al., 1991] associated to lightning activity. However, the spacecraft Cassini/Huygens (NASA-ESA-ASI) carried out a flyby on Venus during its trip to Saturn but high-frequency radio

4. ELECTRICAL DISCHARGES ON SATURN

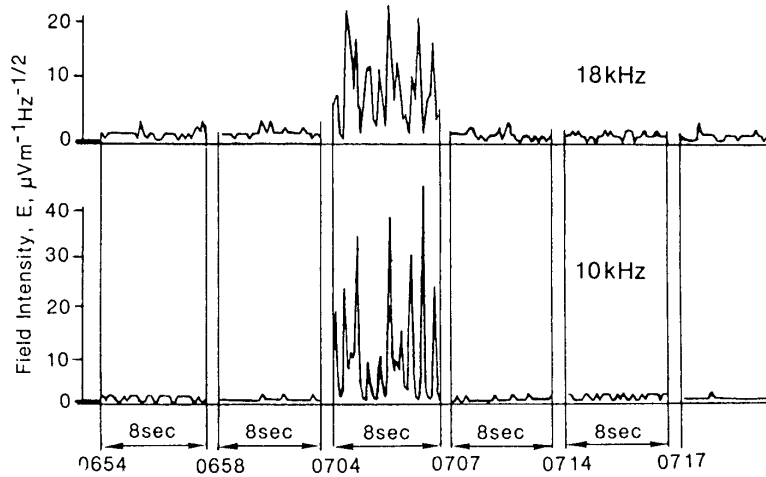


Figure 4.1: The set of VLF pulses recorded by Venera 12 on the Venus surface, 30 min after landing [Ksanfomaliti, 1980].

signals (characteristic of terrestrial lightnings) were not detected [Gurnett et al., 2001]. The Venus Express (ESA) mission reported observations of the venusian ionosphere that revealed strong, circularly polarized, electromagnetic waves with frequencies near 100 Hz which is a typical feature of whistler signals generated by lightning discharges in the atmosphere of Venus [Russell et al., 2007]. Anyway, if there are lightning discharges on Venus' atmosphere, these should occur at altitudes where the H_2SO_4 clouds are formed (50 km of altitude over the surface of Venus) and, due to the high pressure (90 times greater than the Earth's) on its surface, the discharges should be intra-cloud or inter-cloud. Electrical activity on Mars has also been detected by radio emissions [Renno et al., 2003], but in this case they are due to the triboelectricity generated into de dust devils.

Thunderstorm activity has been detected in the atmospheres of giant planets with in-situ spacecraft and observations from the Earth. The first direct lightning images out of the Earth were taken on Jupiter by the spacecraft Voyager 1 in 1979 (see Figure 4.2) [Smith et al., 1979, Cook et al., 1979, Magalhães and Borucki, 1991], by Voyager 2 in 1979 [Borucki and Magalhães, 1992], followed by observations by Galileo [Little et al., 1999], Cassini [Dyudina et al., 2004] and New Horizons [Baines et al., 2007].

Lightning discharges on Jupiter are estimated to discharge channels of 20 km length [Yair et al., 1995], located at pressures between 2 bar to 5 bar [Desch et al., 2002] and releasing an energy of about 10^{12} J [Desch et al., 2002, Yair et al., 2008], three orders of

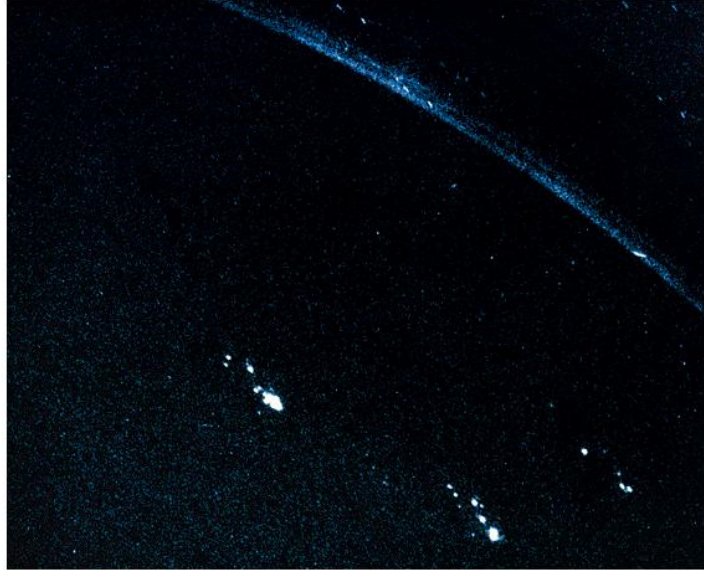


Figure 4.2: Dark-side multiple-image view of Jupiter captured by Voyager 1 in 1979 from a distance of 320000 km. The blue arc of the limb is an aurora in the north pole of Jupiter. The white spot clusters are lightning flashes in jovian thunderstorms [Smith et al., 1979]

magnitude stronger than the median terrestrial lightning energy. The Voyager mission also detected radio emissions attributed to lightning on Neptune [Gurnett et al., 1990, Kaiser et al., 1991]. More recently, through the near-infrared camera NIRC2 coupled to the adaptative optics system of the 10-m Keck telescope, de Pater et al. [2015] detected the brightest storm ever seen on Uranus at $2.2 \mu\text{m}$ (see Figure 4.3).

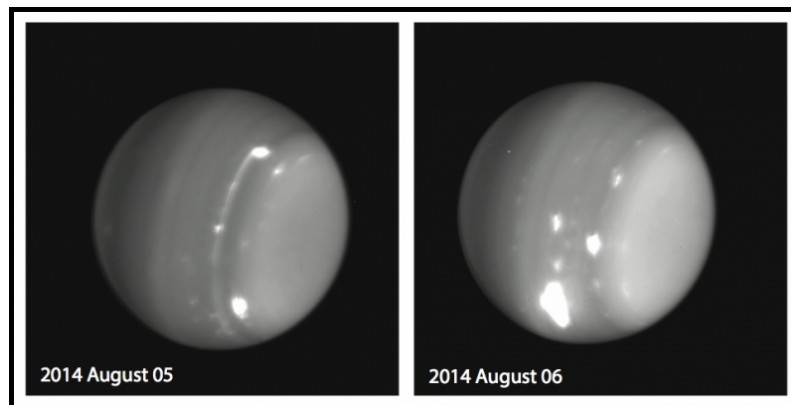


Figure 4.3: Images of Uranus at K' band ($2.2 \mu\text{m}$) obtained with the 10-m Keck telescope on UT 5 and 6 August 2014 [de Pater et al., 2015]

4. ELECTRICAL DISCHARGES ON SATURN

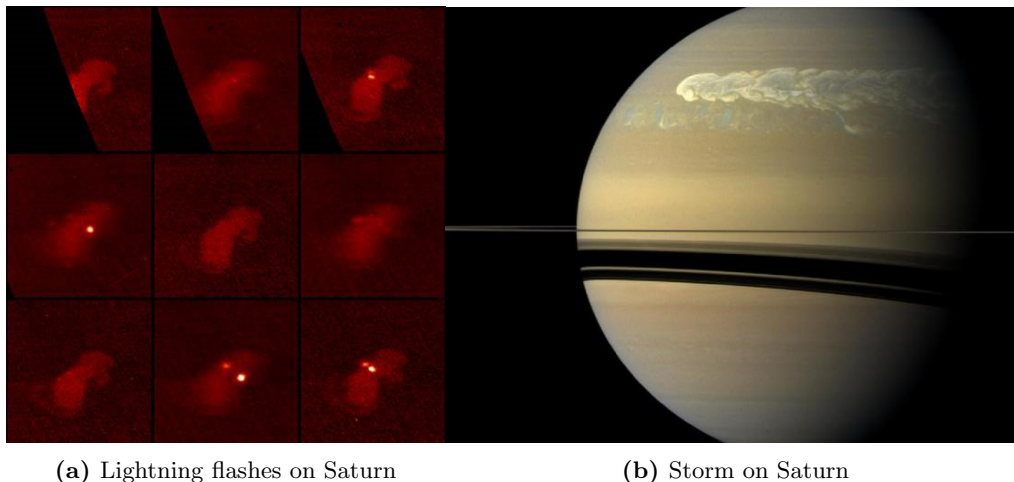


Figure 4.4: (a) NASA’s Cassini spacecraft captured the first lightning flashes on Saturn when it took these images on Nov. 30, 2009 [Dyudina et al., 2013]. (b) The huge storm churning through the atmosphere on Saturn’s northern hemisphere (Dic. 10, 2009) overtakes itself as it encircles the planet in this true-color view from NASA’s Cassini spacecraft [Fischer et al., 2011].

The electrical activity in giant planets like Jupiter and Saturn is concentrated in large dimension storms which exhibit huge convective system. Discharges on Saturn have been detected by a lot of high frequency radio measurements called SED (Saturn Electrostatic Discharges) by Voyager 1 [Warwick et al., 1981] and from Cassini [Fischer et al., 2008] as well as through optical observations with Cassini spacecraft [Dyudina et al., 2010, 2013, Fischer et al., 2011] (see Figure 4.5a) and whose electrical activity can persist up to 9 months [Sayanagi et al., 2013] (see Figure 4.5b).

Lightning flashes on Saturn are very rare and they are usually located around the latitude 35° in both hemispheres (in the respective hemisphere’s summer). The existence of powerful electrical thunderstorm in other planets [Yair et al., 2009] would allow us to study the formation of sprites and other TLEs in extraterrestrial atmospheres. Yair et al. [2009] compared the electric field induced by several charge configurations with the local conventional breakdown electric field E_k [Sentman, 2004] for each atmospheric composition. This approach neglected the finite conductivity in a weakly ionized atmosphere below the ionosphere.

It is reasonable to think that the above conclusion could be extended to the other giant cold planets, and brown dwarfs. Giant gaseous planets have been the first type of

planets detected out of the Solar System. They are defined as planets having between 0.3 and 10 Jupiter masses and an atmosphere dominated mainly by H_2 . These giant planets, together with brown dwarfs, form clouds of gas and dust with enough volume to be susceptible to discharge events [Helling et al., 2011]. Prominent continuous radio emissions and sporadic H_α and X-ray emissions observed in substellar objects may be the result of electrical activity on brown dwarfs [Mokler et al., 2009].

The presence of TLEs in the atmospheres of other planets has never been observed. However, many studies have tried to obtain the properties of these ephemeral phenomena through simulations and laboratory experiments using the atmospheric composition of each planet. Yair et al. [2009] carried out theoretical simulations about the possibility of sprite triggering above thundercloud in other planets of the Solar System. They calculated the Charge Moment Change (CMC) associated with lightning in the atmospheres of Venus ($\text{CO}_2\text{-N}_2$), Mars (CO_2), Titan (N_2) and Jupiter ($\text{H}_2\text{-He}$) and the altitudes where sprites could occur. The information collected by the numerous spacecrafts which have visited Venus, have revealed that the Venusian atmosphere is almost globally surrounded by a thin H_2SO_4 layer located around 50-70 km of altitude [Markiewicz et al., 2007] above the surface of the planet (with ~ 9 MPa of pressure). Due to the high ground pressure and the very high altitude of the clouds, the possibility of Cloud-to-Ground lightning in the Venusian atmosphere is very low. Therefore, if the only possible electrical activity is Intra/Inter-Cloud lightnings and considering that the ionosphere is located at 140 km of altitude [Pätzold et al., 2007], sprites generated by a lightning of 250 C of charge can occur around 84 km above the surface of Venus (see Figure 4.5a). These authors also estimated that electrical discharges with 1000 C between H_2O clouds could trigger sprites at 280 km above the 1-bar level in the atmosphere of Jupiter (see Figure 4.5b). This altitude is more than 100 km above the visible NH_3 crystal clouds, so sprites and halos in Jupiter could be observed with limb observations and suitable instrumentation.

Laboratory experiments on streamers in appropriate $\text{CO}_2\text{-N}_2$ and $\text{H}_2\text{-He}$ mixtures have also been performed to simulate the atmospheres of Venus and Jupiter-like planets, respectively. Dubrovin et al. [2010] demonstrated that the planetary sprites in the atmospheres of Venus and Jupiter-like planets can be expected with a morphology similar to Earth-like sprites but with significantly weaker optical brightness. Spectroscopic measurements carried out by Dubrovin et al. [2010] showed strong N_2 transitions from

4. ELECTRICAL DISCHARGES ON SATURN

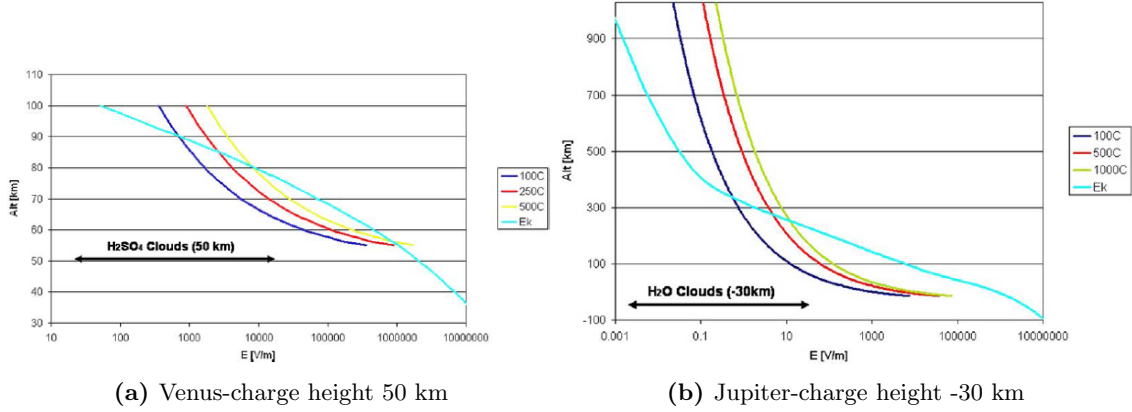


Figure 4.5: (a) The electrostatic field above a Venusian charge configuration placed at 50 km over the surface with different values of total charge. (b) The electrostatic field above a Jovian thundercloud possessing a negative charge located 30 km below the 1-bar pressure level for different values of total charge. When the conventional breakdown field (solid blue line) crosses the electric field, a sprite can potentially occur [Yair et al., 2009].

the second positive band and considerably weaker CO lines in the Venusian atmosphere as well as a continuum in the UV-Vis range with a relatively intense H_{α} line for Jupiter-like planets.

The effect of EMPs (Electromagnetic Pulses) emitted by lightning strokes in the upper layers of gaseous giant planets have been also studied by Luque et al. [2014]. These researchers estimated that the lightning electromagnetic pulses can transport between 10^7 and 10^{10} J of energy toward the ionosphere of giant planets and the emission of light could be up to 10^8 J creating a TLE analogous to the terrestrial elve but probably stronger.

This chapter examines the response of Saturn atmosphere to lightning flashes formed within the ice crystal clouds. We have developed a self-consistent one-dimensional model of the electric field and electron density to estimate the changes of the local electron density enhancement and photon emissions through the quasi-electrostatic field and the induction field.

4.2 A brief description of the model

To estimate all the parameters of a lightning (current intensity, rise time of the current wave, etc) we need to know the charge neutralized by the lightning flash and the duration of the stroke. The total energy dissipated by a lightning discharge in the atmosphere of Saturn atmosphere is estimated in 10^{12} - 10^{13} J based in direct optical observations and SEDs [Fischer et al., 2006, 2007, Dyudina et al., 2010, 2013]. According to Dyudina et al. [2010] the lightning flashes observed in Saturn are 3 orders of magnitude stronger than the average terrestrial lightning stroke (it is comparable with terrestrial super-bolts). According to Fischer et al. [2006] the duration of a saturnian lightning could be similar to a terrestrial Intra-Cloud discharge (tens of microseconds), however Farrell et al. [2007] suggested that a faster discharge ($\sim 1 \mu\text{s}$) could fit better to a SED frequency spectrum with energies (10^9 J) comparable with typical terrestrial lightnings. Recent optical observations reported by Dyudina et al. [2010, 2013] show an independent confirmation of the high energy super-bolt like scenario.

Here, we follow the scenario described by Farrell et al. [2007] which suggested that the current flows through the lightning channel following a biexponential function

$$I(t) = I_0[\exp(-t/\tau_1) - \exp(-t/\tau_2)], \quad (4.1)$$

where τ_2 is the rise time of the current wave which is typically 10 times faster than the overall duration τ_1 .

It is assumed that the lightning discharge is located almost 1000 km below the region of study (between 400-900 km over the 1-bar level). Due to the vertical orientation of the dipole-like discharge, the vertical component of the electric field E_p is dominated by the quasi-electrostatic and the induction fields [Bruce and Golde, 1941]

$$E_p(z, t) = \frac{1}{\pi\epsilon_0} \left(\frac{1}{(z - z_p)^3} M(t - (z - z_p)/c) + \frac{1}{c(z - z_p)^2} \frac{d}{dt} M(t - (z - z_p)/c) \right), \quad (4.2)$$

where $M(t)$ is the charge moment change (CMC), z is the altitude where we measure the field, z_p is the altitude of the center of the dipole, ϵ_0 is the permittivity of the vacuum and c is the speed of light. The left-hand term of equation (4.2) represents the quasi-electrostatic (QE) component of the field, which is dominant in the Earth (see Figure 4.6), while the right-hand term of equation (4.2) is the induction component that prevails in Saturn (see Figure 4.6). In Figure 4.6 we can see how the QE field is

4. ELECTRICAL DISCHARGES ON SATURN

the dominant component above lightning discharges on the Earth's atmosphere while on Saturn we find that the induction component dominates. The far field generated by EMP lightning signals is neglected because we have only studied the 1-dimensional case just over the lightning stroke (for small angles, the EMP field approaches to zero).

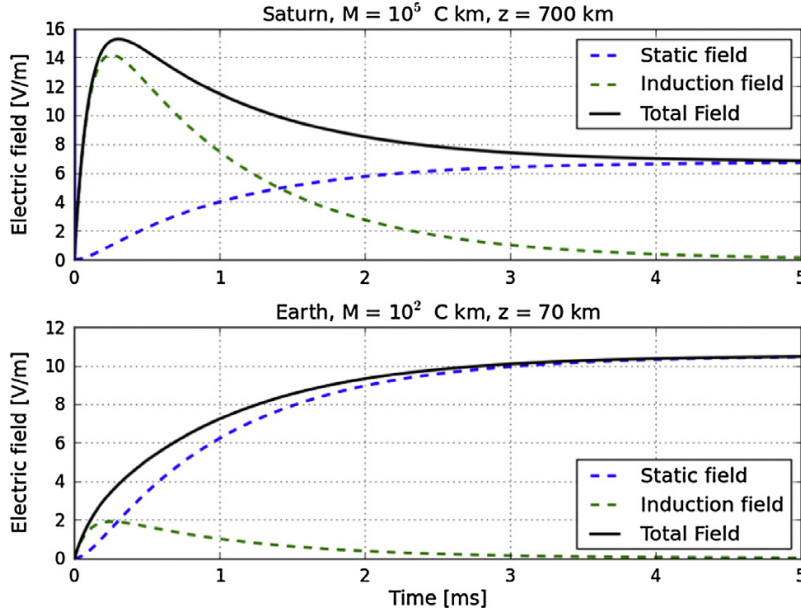


Figure 4.6: Top: Time evolution of the electric field at 700 km of altitude above the 1-bar pressure level due to a lightning discharge with a charge moment change of $M = 10^5$ C km located at -110 km below the 1-bar pressure level on the Saturn's atmosphere. Bottom: Time evolution of the electric field at 70 km of altitude over a thunderstorm due to a cloud-to-ground discharge located on Earth induced by a charge moment change of $M = 10^2$ C km. The center of the dipole is at 0 km. The dotted blue and green lines represent the static and induction components of the electric field and the solid black line represents the total electric field applied, all of them calculated through equation (4.2) [Dubrovin et al., 2014].

The induction component rises and decays with $I(t)$ on the Saturn's atmosphere (see Figure 4.6 Top), reaching its maximum value at timescales of τ_2 while the quasi-electrostatic component maintains the constant value $M/(z - z_p)^3$. After the current has decayed to negligible values at timescales of τ_1 and therefore decays in timescales of Maxwell relaxation time (τ_m). The induction component is stronger and faster than the quasi-electrostatic component and thereby it can produce a significant increase in the electron concentration, decreasing the Maxwell relaxation time and screening fastly

the quasi-electrostatic component.

We define the charge moment change (CMC) for cloud-to-ground lightnings as the product of the amount of charge stored in the cloud times the distance followed by the charge in its way to ground [Bruce and Golde, 1941]. On Saturn, we redefine the CMC as

$$M(t) = Q(t) \frac{a}{2}, \quad (4.3)$$

where a is the vertical separation of the charge centers and $Q(t)$ is the charge stored in the cloud

$$Q(t) = \int_0^t I(t') dt'. \quad (4.4)$$

Thunderclouds on Saturn are bigger than on the Earth (> 1000 km). Yair et al. [1995] modeled the charging process in the Jovian clouds and found that the charge separations correspond to a lightning channel of 20 km with upward flows of 50 m/s. The clouds on Saturn are larger than on Jupiter so according to Sánchez-Lavega et al. [2011], the vertical flows can reach up to 150 m/s. Thus we can assume that the lightning channel on Saturn is larger than Jupiter. The typical terrestrial return-stroke has a propagation speed, from ground to cloud, of 0.3 of the speed of light so for a lightning channel of 100 km it can't last shorter than 1 ms. For this reason, we choose $\tau_1 = 1$ ms and $\tau_2 = 0.1$ ms in the case of Saturn because if the lightning duration is larger than τ_m , the induced field component could be partially screened before it reaches its maximum value and the possibility of sprite/halo formation would be lower.

The CMC estimation on Saturn's atmosphere is carried out through the knowledge we have about the cloud characteristics, the lightning speed propagation and the lightning energy constraint. We know that the base of the clouds is located between 130-160 km below the 1-bar pressure level [Atreya, 1986, Atreya and Wong, 2005]. During the thunderstorm generation, the clouds develop vertically to the 0.1 bar level (90 km over the 1-bar reference level) [Sánchez-Lavega et al., 2011] at 150 m/s of speed. Optical observations carried out by Dyudina et al. [2010, 2013] showed a circular footprint of the lightning flash on the top of the clouds indicating that the light source could be between 125-250 km below the cloud-top. Dyudina et al. [2013] observed lightning discharges on the day-side estimating the cloud-top altitude deeper than about 1.2 bar.

We can assume that the lightning channel is located between the base of the ice water cloud, 130-160 km below 1-bar reference level and up to 100 km above this

4. ELECTRICAL DISCHARGES ON SATURN

altitude. With these cloud and lightning properties, we can derive the connection between the lightning CMC and the dissipated energy U_p . Dubrovin et al. [2014] showed that the dissipated energy by a lightning discharge can be approximated by the electrostatic energy stored by two oppositely charged spheres of radius R separated a distance h ($h > 2R$)

$$U_p = \frac{2Q^2}{4\pi\epsilon_0} \left(\frac{3}{5R} - \frac{1}{2h} \right), \quad (4.5)$$

where Q is the total charge within each sphere and ϵ_0 is the permittivity of vacuum. This equation gives a good estimation of the energy released by IC discharges. Taking into account the energy released by a Saturnian intracloud lightning, we can estimate its charge moment change in $M(t) \sim 10^5 - 10^6$ C km when the charge separation is of a few tens of kilometers, and it can reach 10^6 C km in an extreme scenario with 100 km of charge separation.

The knowledge of the ambient electron density in the atmosphere allows to estimate the Maxwell relaxation time and the triggering conditions for the electron avalanche. However, in the Saturnian atmosphere, the electron concentration below 1000 km layer is uncertain. Above this altitude, all measurements of the electron density have been obtained through radio occultations. Kliore et al. [2009] reported results of several radio occultation measurements of Saturn, of which the dawn electron density at 1000 km above the 1-bar reference level is between $10^2 - 10^3$ cm⁻³ and the dusk electron concentration is about one order of magnitude higher. Moore et al. [2004], through model simulations, proposed an electron density profile with a peak of 10^2 cm⁻³ at about 1000 km and a sharp decrease downward. On the other hand, Moses and Bass [2000] and Galand et al. [2009] assumed the photoionization of a CH_x layer between 600 km and 1000 km of altitude above the 1-bar pressure level and proposed a relatively uniform density of free electrons of 10^2 cm⁻³ along this layer. In this work, we have used both electron density profiles (see Figure 4.7): profile (a) proposed by Moore et al. [2004] where the ionosphere is situated above 1000 km and, profile (b) proposed by Galand et al. [2009] where the ionosphere is located above 600 km due to the presence of a hydrocarbon layer.

In our simulations, we have used a 90:10 volume mixture ratio of H₂:He as an intermediate value of the results by Conrath and Gautier [2000] and Gautier et al. [2006].

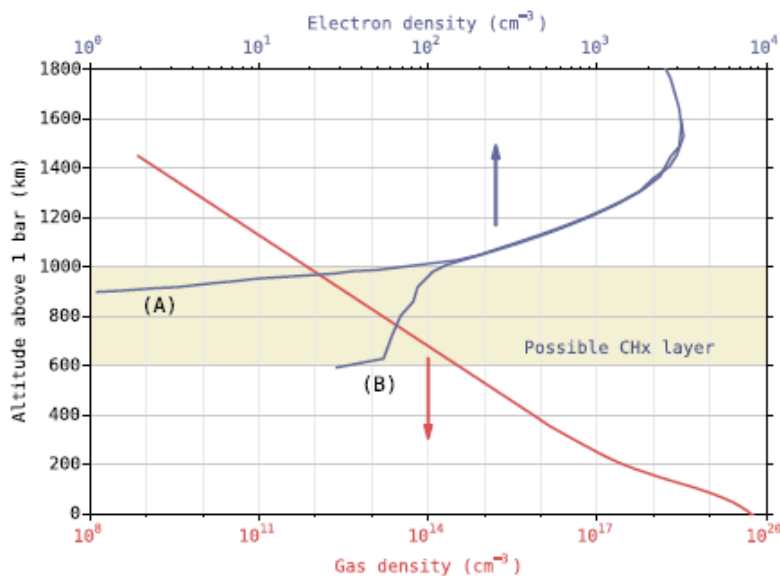


Figure 4.7: Density profiles of the neutral background gas (solid red line) and the ambient free electrons (solid blue lines) used in our simulations. The neutral gas density was obtained by Festou and Atreya [1982] by interpolating two sets of measurements. [Luque et al., 2014].

4.3 Results

The research of the possible triggering of TLEs (sprites, halos or elves) on Saturn atmosphere requires the understanding of two issues:

- the physical mechanisms that control the generation of TLEs
- the possible chemical influence of intracloud lightning discharges in the mesosphere and lower ionosphere of Saturn.

For doing that, we have developed a kinetic model to explore the chemical impact of H_2/He transient plasmas generated by TLEs on the atmosphere of Saturn. The model, which controls the chemical evolution of H_2/He non-equilibrium plasmas, solves in a self-consistent way a set of differential equations: the time-dependent spatially-uniform Boltzmann equation (equation (2.3)) controlling the EEDF of free electrons in the H_2/He plasma, the statistical balance equation (equation (2.1)) controlling the temporal evolution of the chemical species of the plasma, and the total current equation (equation (2.5)) that we use to calculate the electric field generated by a lightning

4. ELECTRICAL DISCHARGES ON SATURN

discharge above the thundercloud. This model is based on previous models developed by Gordillo-Vázquez [2008, 2010] and Parra-Rojas et al. [2013a, 2015] for the kinetics of TLEs on the Earth mesosphere.

For the Saturn kinetic model, like Earth’s model (Chapter 2), we need a set of kinetic and electric inputs. The electric inputs are the CMC values considered and the bi-exponential current function (equation (4.1)) traveling the lightning channel, assuming a stroke duration of $\tau_1 = 1$ ms ten times longer than the rise time of the current ($\tau_2 = 0.1$ ms). The kinetic inputs are the cross sections and the rate coefficients of the different chemical processes considered.

The chemical species considered in the H₂/He plasma model are listed in Appendix F.1. The 32 chemical species considered are classified into ground neutrals, electronically and vibrationally excited neutrals, electrons and negative ions and positive ions. The total number of the chemical processes considered is 160 including electron-driven processes, neutral-neutral reactions, Penning ionization mechanisms, ion-ion reactions, ion-neutral processes and spontaneous radiative deexcitation channels (see Appendix F.3 to F.7). There are 48 electron-impact reactions called “EEDF-dependent processes” (Appendix F.3) whose rates aren’t explicitly shown because they are calculated self-consistently using the available cross sections. This kinetic model doesn’t include photoionization processes because we are assuming nighttime conditions without diffusion.

In H₂/He plasma kinetic modeling, we have also considered the electron-impact dissociative attachment of H₂. Although its cross section is quite small for the lowest vibrational level of the ground electronic state H₂(X¹Σ_g⁺, v=0), it increases fastly with increasing vibrational levels [Bardsley and Wadehra, 1979]. Since the cross section for dissociative attachment of H₂ shows a peak ($\sigma_{peak}(v)$) in the threshold energies ($\epsilon_{th}(v)$) and a fast reduction in magnitude as the energy is increased above the threshold, Celiberto et al. [2001] proposed to fit the cross sections of the dissociative attachment of H₂(X¹Σ_g⁺, v) just above the threshold with the analytical expression

$$\sigma_{DA} = \sigma_{peak}(v) \exp\left(-\frac{\epsilon - \epsilon_{th}}{\epsilon_g}\right) \quad (4.6)$$

with $\epsilon_g = 0.45$ eV. We have considered dissociative attachment cross sections of H₂(X¹Σ_g⁺, v) up to v=9 using the values of $\sigma_{peak}(v)$ and $\epsilon_{th}(v)$ given by Bardsley and Wadehra [1979].

The kinetic model covers a range of altitudes from 450 km to 1000 km above the 1-bar pressure level on Saturn atmosphere. The species and the kinetic processes considered in the model are shown in Appendix F. We have also considered a constant gas temperature of 125 K for all altitudes studied [Nagy et al., 2009]. Finally we considered an optically thin plasma ($\kappa = 1$) and a simulation time of 5 ms.

The results for the electron density and the ion concentrations are shown in Figure 4.8 for the altitudes where the electron density reaches its maximum value.

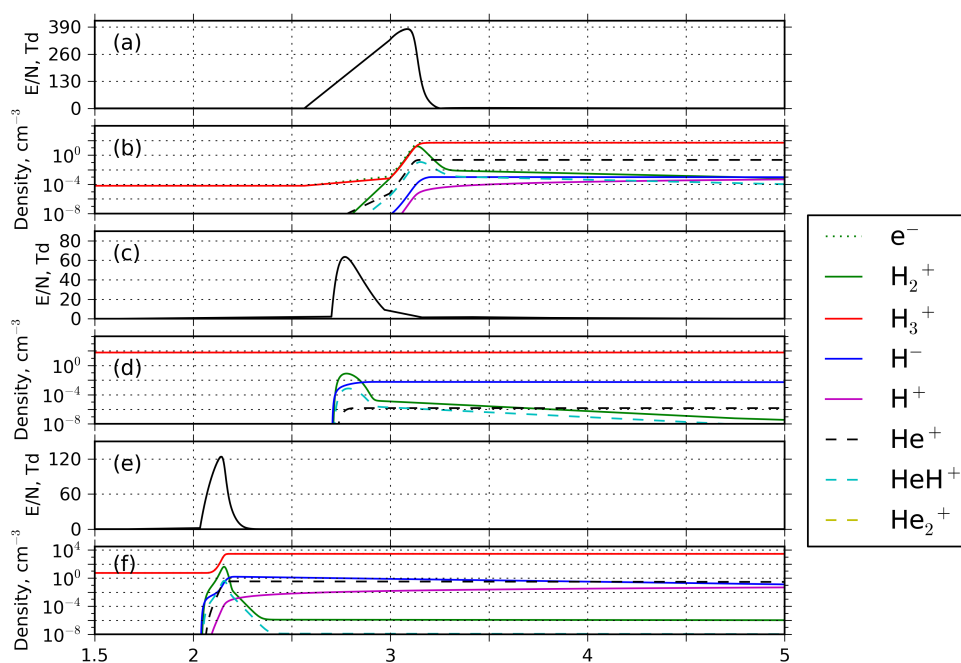
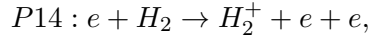


Figure 4.8: Temporal evolution of the reduced electric field (E/N), electron and ion concentration calculated with the kinetic model for $M = 10^5$ C km (profiles (a) and (b)) and with $M = 10^6$ C km (profile (b)). The plots have been calculated for altitudes where the electron density reaches its maximum value, that is, 750 km (panels (a) and (b)), 700 km (panels (c) and (d)) and 500 km (panels (e) and (f)). The panels (a) and (b) show results for the profile (a) and the panels (c), (d), (e) and (f) for the profile (b).

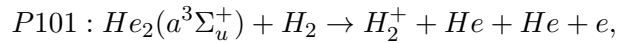
Panels (a) and (b), in Figure 4.8 show the reduced electric field and the ion densities respectively, for the profile (a) and $M = 10^5$ C km at 750 km of altitude over the 1-bar reference level. The rest of the panels correspond to the electron density profile (b), for

4. ELECTRICAL DISCHARGES ON SATURN

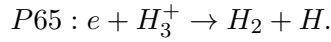
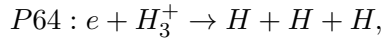
the case of $M = 10^5$ C km at 700 km of altitude (panels (c) and (d)) and for the case of $M = 10^6$ at 500 km (panels (e) and (f)). We can see in Figure 4.8b an increase in the electron concentration up to 50 cm^{-3} due to the electron-impact ionization of H_2



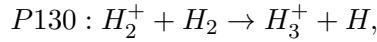
that persists in time due to the balance between



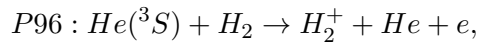
and

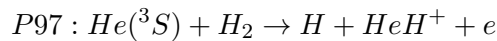


Moreover, we can also see a quick conversion of the ion H_2^+ into H_3^+ through the reaction

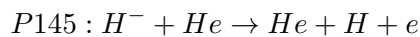


becoming dominant the H_3^+ ion. As we show in Figures 4.8a, 4.8c and 4.8e, the maximum electric field is reached later (and becomes wider) as we ascend in altitude due to the propagation and expansion of the lightning originated electromagnetic pulse from the thundercloud. We can also compare, for the same CMC (10^5 C km), the time evolution of positive He^+ ion through the Figures 4.8b, 4.8e and 4.8f. The concentration of this ion after $t = 3$ ms is the highest after the one of H_3^+ ion for the case of profile (a) while for the case of the electron density profile (b) the density of He^+ is negligible. However, if we increase the CMC from $M = 10^5$ C km (at 700 km) to $M = 10^6$ C km (at 500 km) for the same profile (b), we can see in Figures 4.8c and 4.8e how the reduced electric field increases from 65 Td to 125 Td, respectively. The consequence of this variation in the reduced electric field is a sharp growth of more than 2 orders of magnitude in the electron density up to nearly 3500 cm^{-3} (see Figure 4.8f). During the time in which the electric field is on, the electron-impact ionization of H_2 is the mechanism responsible of the important increase in the electron concentration. However, when the electric field falls down to zero, after $t = 3.2$ ms (see Figure 4.8a), after $t = 3.0$ ms (see Figure 4.8c) and after $t = 2.25$ ms (see Figure 4.8e), the electron gain is dominated by the Penning ionization



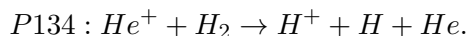


when $M = 10^5$ C km with electron density profile (a), and by detachment

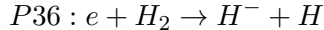


for $M = 10^5$ C km and $M = 10^6$ C km with electron density profile (b).

The increase of the density of H^+ right after the end of the reduced electric field pulse (Figures 4.8b and 4.8f) is due to

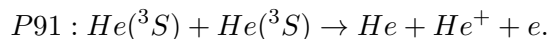


However, the behavior of the H^- ion after the end of the electric field pulse is different depending on the value of the CMC used and the electron density profile. In this connection, the density of H^- remains constant with $M = 10^5$ C km with profiles (a) and (b), and decreases for the $M = 10^6$ C km case. This is related to the detachment loss rate of H^- that was previously produced by



when the electric field is on: a small or high loss rate respect to the electric field-dependent production rate of H^- produces a constant H^- density (Figures 4.8b and 4.8d) or a decreasing concentration of H^- (Figure 4.8f), respectively.

The calculated concentrations of helium ions (He^+ , He_2^+ and HeH^+) are usually very small except for He^+ ion in the $M = 10^5$ C km and electron density profile (a) case, and $M = 10^6$ C km with ambient electron density profile (b). In these cases, He^+ becomes the second most important positive ion, after H_3^+ for $t > 3$ ms and $t > 4$ ms, respectively. This relative importance of He^+ is caused by Penning ionization



Figures 4.9 and 4.10 show the altitude-dependent instantaneous and cumulative number of H_2 continuum (UV) and Fulcher photons calculated with the kinetic model presented previously (Appendix F). The left and right panels of Figures 4.9 and 4.10 correspond, respectively, to the UV and Fulcher emissions associated with the same CMC and ambient electron density profiles as in Figure 4.8. Generally, both UV and Fulcher emissions are very fast, with the UV emission being slightly stronger than the

4. ELECTRICAL DISCHARGES ON SATURN

Fulcher band emission. We can see in Figure 4.9 that the instantaneous emissions at lower altitudes are longer. This effect is caused by a slower relaxation time at these altitudes.

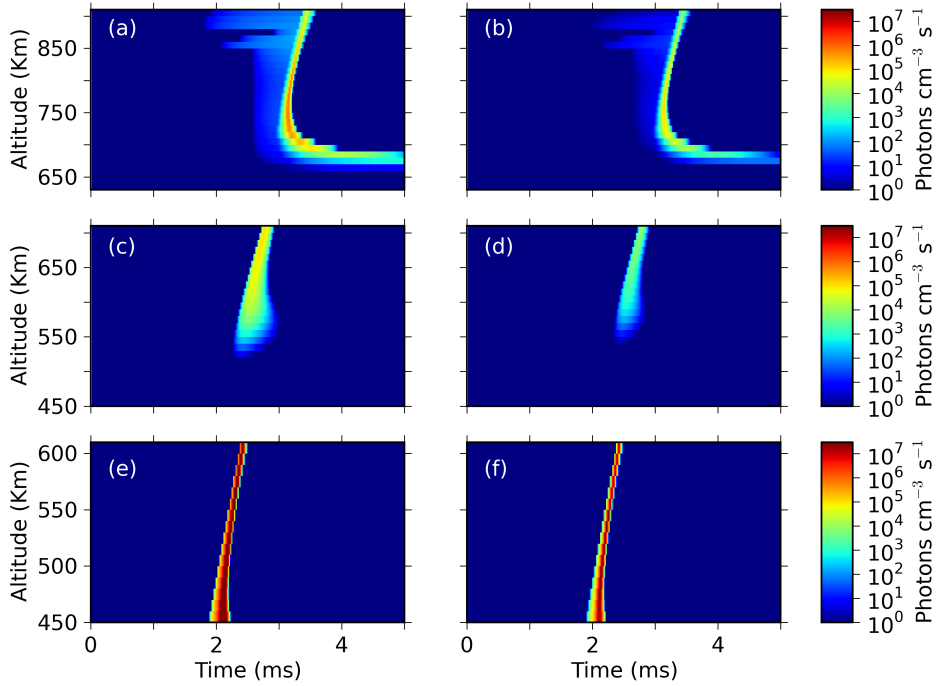


Figure 4.9: Altitude-dependent instantaneous number of UV continuum (left hand side panels) and Fulcher band (right hand side panels) photons $\text{cm}^{-3} \text{s}^{-1}$, calculated with the kinetic model for the same CMC and ambient electron density profiles as in Figure 4.8.

On the other hand, if the base of the ionosphere is at 1000 km (profile (a)) above 1-bar pressure level, the kinetic model predicts 40 and 6 photons cm^{-3} for UV continuum and Fulcher band respectively, at 700 km and $M = 10^5 \text{ C km}$ (Figures 4.10a and 4.10b). However, if the base of the ionosphere is at 600 km (profile (b)) over 1-bar pressure level, the model predicts $\simeq 9$ and $\simeq 0.6$ photons cm^{-3} for UV continuum and Fulcher band respectively, at 680 km with $M = 10^5 \text{ C km}$ (Figures 4.10c and 4.10d), and $\simeq 10000$ and $\simeq 1000$ UV and Fulcher photons cm^{-3} , respectively, at 450 km of altitude with $M = 10^6 \text{ C km}$ (Figures 4.10e and 4.10f).

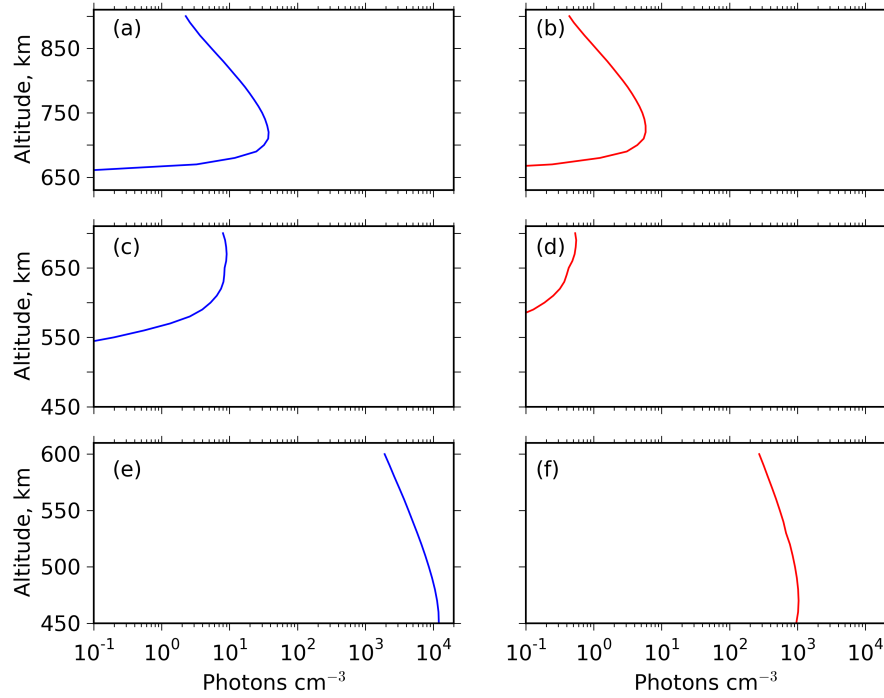


Figure 4.10: Altitude-dependent cumulative number of UV continuum (left hand side panels) and Fulcher band (right hand side panels) photons cm^{-3} , calculated with the kinetic model for the same CMC and ambient electron density profiles as in Figure 4.8.

Figure 4.11 shows the altitude-dependence concentration of $\text{H}(n=3)$ (right hand side panels) and cumulative number of Balmer band photons cm^{-3} (656.28 nm) which is approximately 2 orders of magnitude lower than the cumulative number density of H_2 UV continuum photons.

4. ELECTRICAL DISCHARGES ON SATURN

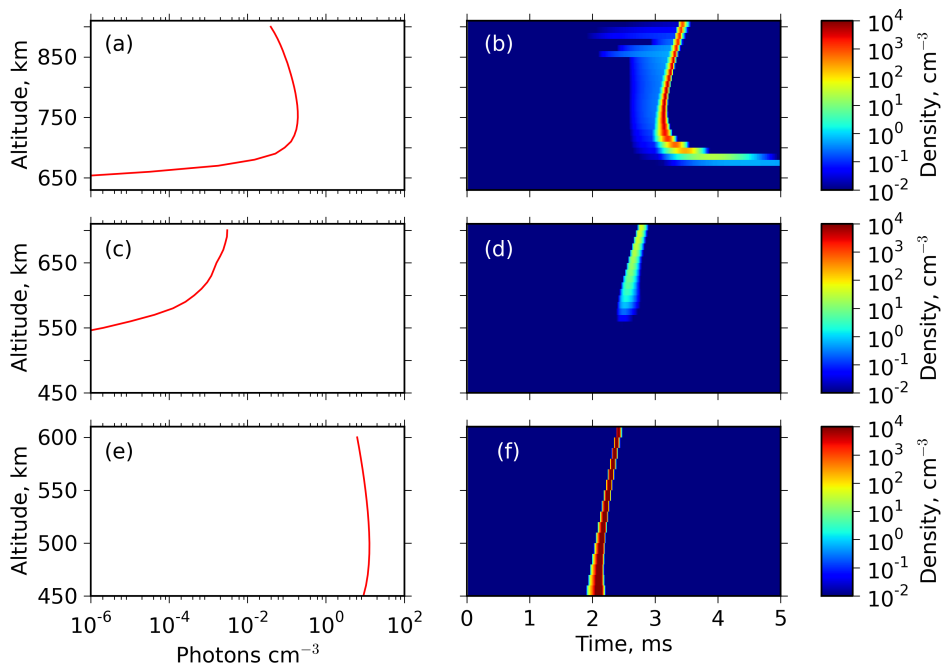


Figure 4.11: Altitude-dependent cumulative number of Balmer band (left hand side panels) photons cm^{-3} and H(n=3) density (right hand side panels) in cm^{-3} , calculated with the kinetic model for the same CMC and ambient electron density profile as in Figure 4.8.

5

Conclusions

“I love it when a plan comes together”

– Colonel John “Hannibal” Smith, *The A-team*

We have estimated the local electrochemical impact on the Earth’s mesosphere of tropospheric lightning with different polarities and different current moment peaks. The simulations have been performed using a sophisticated air kinetic scheme. We solve the statistical equilibrium equations of each species (2.1) coupled with the Boltzmann transport equation (2.3) and with the quasi-electrostatic electric field equation (2.5). This scheme is applied over a range of altitudes (50-87 km). Due to the low air pressures, the reduced electric field associated to -CG lightning discharges at high altitudes reaches values close to breakdown (120 Td) when the maximum of the current moment is greater than 200 kAkm. However, in the +CG lightning cases, we see a similar behavior as in the -CG lightning discharges at the time of the maximum of the current moment. We can also find electric field values close to breakdown at relatively low altitudes due to the high charge moment (more than 2000 Ckm) provided by the lightning continuous current stage (20 kAkm during the first 100 ms). In the last case (+CG), despite sub-breakdown conditions, we can see an enhancement in the electron density due to the electric field dependence of the associative detachment (AD) of N_2 by O^- . Moreover, the enhanced electron density remains high in time due to the AD of CO by O^- . This suggests that the ion O^- plays an important role in the electron density evolution. Therefore, a strong O^- production is needed at the time of the maximum current moment for a subsequent increase in electron concentration due to AD processes. The important enhancement in the O^- density is due to the strong dissociative attachment

5. CONCLUSIONS

of O_2 in coincidence with the maximum of the reduced electric field. The relatively high electron concentration (70 cm^{-3}) produced by +CG lightning discharges also provides a strong excitation of metastables $N_2(A^3\Sigma_u^+)$, $O_2(a^1\Delta_g)$, $O_2(b^1\Sigma_g^+)$, $O(^1D)$ and $O(^1S)$ due to electron impact collisions. These electronically excited species can be very important in the thermal behavior of the mesosphere because, due to their long lifetime, they are able to store energy, transferring it later to the surrounding gas through fast heating (Flitti and Pancheshnyi [2009]).

We have evaluated the emission brightness of the first (1PN₂) and the second (2PN₂) positive band systems of N_2 associated with the visible optical emission of sprite halo events. Our model predicts that the reddish instantaneous emission associated to the 1PN₂ can exceed 1 MR by one order of magnitude for the +CG lightning discharges considered. Using a 1000 fps camera, we could measure the red and blue emissions, associated with the 1PN₂ and the 2PN₂ over the threshold of visibility. Our model for sprite halos does not predict a significant variation in ground state neutral species such as CO_2 , NO_x and N_2O . However, we have found a strong increase in the atomic nitrogen and oxygen densities due to the electron-impact dissociation of N_2 and O_2 during +CG lightning discharges.

Spectroscopic diagnostics of low pressure (0.1 - 2 mbar) laboratory air glow discharges produced in, respectively, hollow cathode reactors and commercial lamps were used as benchmarks for rotational (gas) temperature determination in TLEs using three different methods requiring high (0.01 nm) and medium (0.1 - 0.5 nm) spectral resolutions. These methods have been implemented with commercial spectrographs (for the glow discharge) and with a recently developed inhouse instrument called GRANada Sprite Spectrograph and Polarimeter (GRASSP) (used with the commercial discharge lamp) designed for medium resolution (0.45 nm) spectroscopic surveys of TLEs. In particular, the high spectral resolution measurements used the so-called Boltzmann plot method to measure the relative intensities of the rotational R - branch ($\Delta J = +1$) of the vibrational band (0,0) of the first negative system of N_2^+ , that is, $N_2^+(B^2\Sigma_u^+, v' = 0, J' \rightarrow X^2\Sigma_g^+, v'' = 0, J'')$, with the wavelength band head at 391.4 nm. Because of the characteristic rotation-translation relaxation time of $N_2^+(B^2\Sigma_u^+)$ (compared to its radiative lifetime), the use of $N_2^+(B^2\Sigma_u^+ \rightarrow X^2\Sigma_g^+)$ as a “thermometer” should be restricted to TLE temperature probing at altitudes equal or lower than 60 km ($\simeq 0.23$ mbar) down to 48 km ($\simeq 1.5$ mbar). The other two methods require medium spectral

resolution and are based, on one side, on the analysis of several peaks appearing in low lying vibrational transitions, specifically (3,0), (2,0), (1,0) and (0,0), of the N₂ 1PG spectrum and on the numerical fitting of synthetic spectrum to the observed (measured) spectrum of the envelope of selected (v' , v'') bands of the N₂ 1PG spectrum. Since the rotational distribution of N₂(B³Π_g) is already thermalized at $\simeq 75$ km altitude, the use of N₂(B³Π_g) results in a good "thermometer" in a wide range of altitudes from $\simeq 75$ km down to $\simeq 53$ km where collisional (quenching) deactivation prevails over radiative decay. Therefore, the use of N₂(B³Π_g → A³Σ_u⁺) rovibronic transitions seems justified and very convenient to accurately determine the rotational (gas) temperature in TLE produced air plasmas.

The values of the rotational (gas) temperatures measured in glow discharges produced in DC hollow cathode reactors are almost the same (410 K - 320 K, depending on the pressure used) when the two methods employing N₂(B³Π_g) as the probing species are used, while higher temperatures (with a maximum difference of 100 K at 2 mbar or 45 km altitude) are found when N₂⁺(B²Σ_u⁺) is tracked. These differences can be principally caused by the spatial distribution of ionic (N₂⁺(B²Σ_u⁺)) and excited neutral (N₂(B³Π_g)) species in the hollow cathode discharge used to perform the spectroscopic diagnosis. On the other hand, the gas temperatures in the air commercial lamp discharges (at 0.2 mbar or 60 km altitude) obtained by GRASSP relies on the spectral fitting of certain (v' , v'') transitions of N₂(B³Π_g → A³Σ_u⁺). The temperatures measured were higher (up to 656 K) than in glow discharges since the power density in the commercial lamp was higher ($\simeq 10$ W/cm³) than in the air hollow cathode discharges (0.05 - 0.35 W/cm³). In addition, the partial N₂ 1PG spectrum recorded by GRASSP in air commercial discharge lamps exhibit the same features (though affected by the different gas temperatures) as the spectrum obtained with commercial spectrographs in air hollow cathode discharges, which supports the reliability of GRASSP for TLE field spectroscopic recordings. It is worth mentioning that the line-of-sight through TLEs (Sprites, Jets, Elves, Halos) is generally not so long as to cover a broad range of temperatures so the methods described in this work can be used to extract unique temperatures. This is not always the case with remote sensing of the atmosphere.

We found that the relative populations of the vibrational levels of N₂(B³Π_g) from $v' = 2$ to $v' = 7$ are similar in air plasmas produced in laboratory hollow cathode discharges and TLE (sprite) plasmas at different altitudes (53 km - 74 km). However, although

5. CONCLUSIONS

the results for $v' = 1$ by Bucselá et al. [2003] at 53 km follow the trend predicted by available sprite kinetic models at higher (74 km) altitudes [Gordillo-Vázquez, 2010, Luque and Gordillo-Vázquez, 2011, Gordillo-Vázquez et al., 2011, 2012], they differ from the VDF ($v' = 1$) obtained from emission spectra recorded in hollow cathode discharges at 1 mbar ($\simeq 53$ km). The latter can be due to the more effective excitation of $N_2(B^3\Pi_g)$ ($v' = 1$) in sprites than in hollow cathode air discharges. In fact, previous works in auroras [Cartwright, 1978, Morrill and Benesch, 1996] show that the $N_2(C^3\Pi_u)$ plays a significant role in populating the lower vibrational levels of $N_2(B^3\Pi_g)$. This can also explain the observed TLE (Sprite and Halos) enhancement (with respect to lab results) in the populations of $v' = 0$ and $v' = 1$ in $N_2(B^3\Pi_g)$ [Bucselá et al., 2003], [Kanmae et al., 2007]. The findings by Cartwright [1978], and Morrill and Benesch [1996] on the kinetics of $N_2(C^3\Pi_u)$ and its impact on the lower vibrational levels of $N_2(B^3\Pi_g)$ were incorporated into the TLE vibrational kinetic models used in this work [Gordillo-Vázquez, 2010, Luque and Gordillo-Vázquez, 2011, Gordillo-Vázquez et al., 2011, 2012].

We have found that hollow cathode DC discharges in air produced at low pressure (0.1 - 2 mbar), where wall effects on the plasma excited species are negligible, can be used as reasonable TLE analogs to explore and quantify some TLE spectroscopic features like key emitting species, N_2 1PG spectra, VDF of $N_2(B^3\Pi_g)$ and rotational (gas) temperature. In addition, the VDF of $N_2(B^3\Pi_g)$ found in hollow cathode DC discharges are quite similar, except the lowest ($v = 0, 1$) vibrational levels, to those derived from TLE N_2 1PG emission spectra.

To conclude, we have tested several spectroscopic techniques that can be applied to TLEs to quantify the gas temperature. According to our study, the best methods to determine the gas temperature in TLE produced air plasmas are those employing $N_2(B^3\Pi_g)$ as the probing species using medium (0.1 - 0.5 nm) spectral resolution spectrographs able to partially resolve the rovibronic band structure of different (v', v'') transitions of $N_2(B^3\Pi_g \rightarrow A^3\Sigma_u^+)$. Spectroscopic methods that use medium spectral resolution have the additional advantage, as compared with higher resolution ones, that they enable optical systems with larger apertures resulting in better signal to noise ratios at shorter acquisition times, of great interest in the study of very brief light emitting phenomena such as TLEs. Finally, we have successfully tested the capabili-

ties of a recently inhouse developed instrument called GRASSP, with 0.45 nm spectral resolution, that we plan to use for TLE spectroscopic surveys in Europe.

We have also studied in this thesis the electrical, chemical and thermal impacts of a single sprite streamer with different driving current durations in the terrestrial mesosphere (50-80 km). In order to quantify the temporal evolution of each chemical species, our model solves a set of differential continuity equations (2.1) for each of the chemical species considered coupled with the Boltzmann equation (2.3), the Ohm law (3.8) and the energy conservation equation (3.7). Using as initial conditions the current density profiles provided for a set of altitudes by the streamer model by Luque and Ebert [2010], we have extended them using different constant driving current durations (5 ms, 50 ms and 100 ms). For each of the driving currents we have obtained the reduced electric field of a single sprite streamer for each of the altitudes considered so that the maximum current density matches the maximum reduced electric field.

The constant driving current generates a high-field phase shorter than the driving current whose duration and value is, respectively, directly proportional to the altitude and close to breakdown ($\simeq 120$ Td). At low altitudes and for the cases of 50 ms and 100 ms driving currents, we found a set of oscillations at the final stage of the E/N afterglow. We think that these undervoltage E/N oscillations build arise from the opposite trends of electron production by associative detachment of O^- by N_2 and electron loss by dissociative recombination of electrons with O_4^+ during the driving current. At low altitudes, the electric field of the streamer head causes a huge growth in the electron concentration of up to 12 orders of magnitude (10^8 cm^{-3}) above ambient values. The tremendous increase in the electron concentration is driven by direct electron-impact ionization of N_2 and O_2 . In a similar way, the density of O^- exhibits a sharp enhancement past the streamer head due to dissociative attachment of O_2 .

Our model also predicts a quite significant enhancement in the concentration of metastable species ($N_2(A^3\Sigma_u^+)$, $O_2(a^1\Delta_g)$, $O_2(b^1\Sigma_g^+)$, $O(^1D)$ and $O(^1S)$) capable of storing energy for a relatively long time. The production of metastables is mainly caused by electron-impact processes fueled by the high electron concentration caused by the streamer head electric field.

We have also found an important (more than 2 orders of magnitude above ambient values at 50 km of altitude) and long lasting (more than 10^3 s) enhancement of the

5. CONCLUSIONS

N₂O density in the mesosphere. The presence of significant N₂O concentrations in the atmosphere for long times could substantially affect the ozone concentration.

We have also evaluated the emission brightness of the first (1PN₂) and second (2PN₂) positive band systems of N₂ associated with key visible optical emissions of sprites, the CO₂ infrared emission at 4.26 μm and 14.9 μm and the Meinel band of N₂⁺ associated with red and near infrared emissions. As expected, at low altitudes (< 57 km) the reddish and bluish emission brightness of 1PN₂ and 2PN₂ reach 10 GR both at the streamer head and during the afterglow.

In the same range of altitudes but at the final stages of the E/N afterglow, the 4.26 μm IR emission brightness can exceed 100 GR due to the high CO₂(00⁰1) density production by electron-impact collision and by VV processes involving N₂(v). We think that this IR emission could be recorded from space detectors pointing towards the limb. Moreover, we found that the Meinel band emission brightness under the action of a single sprite streamer does not reach 1 MR at any altitude considered. However, we can conclude from our simulations that it could exceed 1 MR at tendrill altitudes (< 50 km).

Our model predicts a relatively important increase in the temperature of the low altitude (< 65 km) atmosphere surrounding a single sprite streamer. This gas temperature enhancement increases at lower altitudes and depends directly on the duration of the driving current. A gas temperature increase ($\Delta T/T$) of up to ~ 6.1 % could be reached at 50 km for the intermediate case considered (50 ms of driving current). This gas temperature enhancement is mainly caused by the collisional quenching of the vibrationally excited CO₂(v₁ v₂^l v₃) (previously excited through VV collisions with N₂(v)) with ground N₂ and, also, by the radiative decays of CO₂(00⁰1) underlying the 4.26 μm IR emission. Future work will extend our simulations to blue jets at lower altitudes where our model predicts an important local heating in the TLE surrounding atmosphere.

Finally, we have developed a self-consistent kinetic model to analyze the atmospheric chemical disturbances caused by possible Saturnian upper atmospheric electric discharges. We have used our kinetic model to calculate the altitude and time-dependent behavior of the electron and ion densities together with the instantaneous and cumulative number of photons emitted by H₂ UV continuum and Fulcher bands originated by a halo-like event in Saturn's mesosphere. We found that H₃⁺ ions are rapidly produced

from the parent H_2^+ ions through the fast reaction $H_2^+ + H_2 \rightarrow H_3^+ + H$, so that H_3^+ becomes the dominant ion in all the scenarios considered. We also found that, after 4 ms, the concentration of the positive ion He^+ becomes the second largest (after H_3^+) when we use $M = 10^5$ C km with ambient electron density profiles (a) and $M = 10^6$ C km with profile (b). The maximum total number of UV and Fulcher photons from a possible Saturnian halo predicted with our full kinetic model are, respectively, 10^{25} and 10^{24} when $M = 10^6$ C km and electron density profile (b) are used.

It seems that detectable halos are unlikely in Saturn's atmosphere, but there is a possibility of sprites if the conventional breakdown field is exceeded below the transition altitude. The altitude of the event above the cloud tops could be estimated if images are taken toward the planet's limb. The lower boundary of a halo can be used to estimate the transition altitude. Such observations could be used to probe the local electron density.

5. CONCLUSIONS

Appendix A

Some constants for atmospheric sciences

Table A.1: Some constant for atmospheric sciences

Constants	
Speed of light	$c = 2.998 \times 10^8 \text{ m s}^{-1}$
Planck's constant	$h = 6.626 \times 10^{-34} \text{ J s}$
Boltzmann's constant	$k_B = 1.38 \times 10^{-23} \text{ J K}^{-1}$
Loschmidt's number	$L = 2.69 \times 10^{25} \text{ molecules m}^{-3}$
Vacuum permittivity	$\epsilon_0 = 8.854 \times 10^{-12} \text{ F m}^{-1}$
Elementary charge	$e = 1.602 \times 10^{-19} \text{ C}$
Electron mass	$m_e = 9.109 \times 10^{-31} \text{ kg}$
Heat capacity ratio	$\gamma (20^\circ\text{C, Dry air}) = 1.4$
Pi	$\pi = 3.141592$

A. SOME CONSTANTS FOR ATMOSPHERIC SCIENCES

Appendix B

Vibrational modes and statistical weights of CO₂

CO₂ is a linear and triatomic molecule with three normal vibrational modes:

- Symmetric stretch mode ν_1 ($\hbar\omega_1 = 0.17$ eV)
- Double degenerate symmetric bending mode ν_2 ($\hbar\omega_1 = 0.085$ eV)
- Asymmetric stretch mode ν_3 ($\hbar\omega_1 = 0.3$ eV)

The level of vibrational excitation of linear triatomic molecules is denoted as CO₂($\nu_1 \nu_2^{l_2} \nu_3$) showing the number of quanta in each mode (see p. 268 Fridman [2008]).

To calculate the statistical weights of the vibrational levels of CO₂ (see p. 488-489 Ochkin [2009]), we need the required number of normal vibrations differing in frequency that, for a linear molecule, are given by

$$n_v = 3N_a - 5 - l,$$

where N_a is the number of atoms in the molecule ($N_a(\text{CO}_2) = 3$) and l stands for the degenerate vibrations. In CO₂, we have $l = 1$, then $n_v = 3$. The normal vibration frequency ν_2 is doubly degenerate, that is, $d_{\nu_2} = 2$ and for the rest we have $d_{\nu_1} = d_{\nu_3} = 1$. The statistical weight of the CO₂ vibrational state ($\nu_1 \nu_2^{l_2} \nu_3$) is

$$g(\nu_1 \nu_2 \nu_3) = \prod_{n=1}^{n_v=3} \frac{(v_n + d_n - 1)!}{v_n! (d_n - 1)!}.$$

with $l_2 = \nu_2, \nu_2-2, \nu_2-4, \dots, 1$ or 0 .

B. VIBRATIONAL MODES AND STATISTICAL WEIGHTS OF CO₂

Table B.1: Statistical weights of vibrational levels of the ground electronic state of CO₂

$(\nu_1 \nu_2 \nu_3)$	g
(0 0 0)	1
(0 1 0)	2
(0 2 0)	3
(1 0 0)	1
(0 3 0)	4
(1 1 0)	2
(0 0 1)	1
(0 4 0)	5
(1 2 0)	3
(2 0 0)	1
(0 1 1)	2
(0 2 1)	3
(1 0 1)	1
(0 3 1)	4
(1 1 1)	2
(0 0 2)	1
(0 4 1)	5
(1 2 1)	3
(2 0 1)	1

Appendix C

Formation enthalpies of the chemical species considered

The potential energies ($Q_i = \Delta H_f$) of the species i required to calculate P_{chem} in the kinetic model are shown in the Table C.1. These energies correspond to the standard enthalpy of formation of the neutral species. For the ionic species, the energies have been calculated as follows

$$\Delta H_f(M^+) = \Delta H_f(M) + IE,$$

$$\Delta H_f(M^-) = \Delta H_f(M) - EA,$$

where $\Delta H_f(M)$ is the standard enthalpy of formation of the neutral specie, IE is the ionization energy, EA is the electronic affinity and $\Delta H_f(M^+)$ and $\Delta H_f(M^-)$ are the standard enthalpies of formation of the positive and negative ions, respectively. The ΔH_f of electronically, vibrationally and rotationally excited species is the addition of the potential energy of its ground neutral state to the excitation energy of the corresponding electronic, vibrational and rotational levels, respectively. If the standard enthalpy of formation of the species is negative, it indicates that the reaction of formation of the species is exothermic. The standard enthalpy of formation of the species will be positive for an endothermic reaction of formation. All species in their standard states (oxygen gas, nitrogen gas and argon gas) have a zero standard enthalpy of formation, as there is no change involved in their formation. The $\Delta H_f(M)$, IE and EA values have been obtained from Linstrom and Mallard [2015].

C. FORMATION ENTHALPIES OF THE CHEMICAL SPECIES CONSIDERED

Table C.1: Potential energies of the species i

i	Q_i (eV)
e^-	0.0
N	4.88
N(2D)	7.264
N(2P)	8.376
N $^+$	19.429
N ₂ (rot)	0.02
N ₂ (X $^1\Sigma_g^+$)	0.0
N ₂ (A $^3\Sigma_u^+$)	6.99
N ₂ (B $^3\Pi_g$)	7.35
N ₂ (W $^3\Sigma_g^+$)	7.36
N ₂ (B' $^3\Sigma_u^-$)	8.16
N ₂ (a' $^1\Sigma_u^-$)	8.4
N ₂ (a $^1\Pi_g$)	8.55
N ₂ (w $^1\Delta_u$)	8.89
N ₂ (C $^3\Pi_u$)	11.03
N ₂ (E $^3\Sigma_g^+$)	11.87
N ₂ (a'' $^1\Sigma_g^+$)	12.25
N ₂ (X $^1\Sigma_g^+$,v=1)	0.291
N ₂ (X $^1\Sigma_g^+$,v=2)	0.59
N ₂ (X $^1\Sigma_g^+$,v=3)	0.88
N ₂ (X $^1\Sigma_g^+$,v=4)	1.17
N ₂ (X $^1\Sigma_g^+$,v=5)	1.47
N ₂ (X $^1\Sigma_g^+$,v=6)	1.76
N ₂ (X $^1\Sigma_g^+$,v=7)	2.06
N ₂ (X $^1\Sigma_g^+$,v=8)	2.35
N ₂ $^+$	15.6
N ₂ $^+$ (A $^2\Pi_u$)	17.0
N ₂ $^+$ (B $^2\Sigma_u^+$)	18.8
N ₃ $^+$	11.06
N ₄ $^+$	14.6
O	2.56
O(1D)	4.527
O(1S)	6.75
O $^-$	1.122

O ⁺	16.17
O ₂ (X ³ Σ _g ⁻)	0.0
O ₂ (X ³ Σ _g ⁻ , v=1)	0.19
O ₂ (X ³ Σ _g ⁻ , v=2)	0.38
O ₂ (X ³ Σ _g ⁻ , v=3)	0.57
O ₂ (X ³ Σ _g ⁻ , v=4)	0.75
O ₂ (rot)	0.02
O ₂ (a ¹ Δ _g)	0.977
O ₂ (b ¹ Σ _g ⁺)	1.627
O ₂ (A ³ Σ _u ⁺)	4.5
O ₂ ⁻	-0.448
O ₂ ⁺	12.06
O ₃	1.478
O ₃ ⁻	-0.663
O ₄ ⁺	11.58
Ar	0.0
Ar(³ P)	11.55
Ar ⁺	15.759
NO	0.935
NO(A ² Σ ⁺)	6.39
NO ⁻	0.911
NO ⁺	10.195
NO ₂	0.343
NO ₂ ⁻	-1.93
NO ₂ ⁺	10.093
NO ₃	0.737
NO ₃ ⁻	-3.19
N ₂ O	0.85
N ₂ O ⁻	0.623
N ₂ O ⁺	13.74
N ₂ O ₅	0.117
N ₂ O ₂ ⁺	11.82
CO	-1.145
CO ₂ (00 ⁰ 0)	-4.077
CO ₂ (01 ¹ 0)	-3.997

C. FORMATION ENTHALPIES OF THE CHEMICAL SPECIES CONSIDERED

CO ₂ (02 ⁰ 0)	-3.917
CO ₂ (02 ² 0)	-3.911
CO ₂ (10 ⁰ 0)	-3.905
CO ₂ (03 ¹ 0)	-3.836
CO ₂ (03 ³ 0)	-3.827
CO ₂ (11 ¹ 0)	-3.818
CO ₂ (00 ⁰ 1)	-3.784
CO ₂ (04 ⁰ 0)	-3.760
CO ₂ (04 ² 0)	-3.755
CO ₂ (12 ⁰ 0)	-3.74479
CO ₂ (04 ⁴ 0)	-3.74471
CO ₂ (12 ² 0)	-3.733
CO ₂ (20 ⁰ 0)	-3.729
CO ₂ (01 ¹ 1)	-3.703
CO ₂ (02 ⁰ 1)	-3.681
CO ₂ (02 ² 1)	-3.673
CO ₂ (10 ⁰ 1)	-3.6616
CO ₂ (03 ¹ 1)	-3.6615
CO ₂ (03 ³ 1)	-3.648
CO ₂ (11 ¹ 1)	-3.641
CO ₂ (00 ⁰ 2)	-3.627
CO ₂ (04 ⁰ 1)	-3.621
CO ₂ (04 ² 1)	-3.615
CO ₂ (04 ⁴ 1)	-3.605
CO ₂ (12 ⁰ 1)	-3.601
CO ₂ (12 ² 1)	-3.592
CO ₂ (20 ⁰ 1)	-3.586
CO ₃ ⁻	-5.077

Appendix D

The correction factor of T_{gas}

Let's assume a collection of particles (atoms and/or molecules) in a radiation field characterized by the specific intensity I_ν . The specific intensity I_ν is related to the radiation energy density spectrum by

$$u_\nu = \frac{1}{c} \int_{4\pi} I_\nu d\Omega \quad (D.1)$$

with Ω being an element of solid angle about the direction Ω . The probability per unit time of induced emission into the solid angle $d\Omega$, corresponding to a transition from level i to level j is

$$B_{ij} I_{\nu_{ji}} d\Omega. \quad (D.2)$$

In a similar way, the probability per unit time of absorption from radiation propagating in the solid angle $d\Omega$ about the direction Ω , accompanied by a $j \rightarrow i$ transition is

$$B_{ji} I_{\nu_{ji}} d\Omega. \quad (D.3)$$

If there are n_i and n_j particles per unit volume in levels i and j , respectively, then the condition for a steady state between (spontaneous + stimulated) emission and absorption is

$$n_i \left(\frac{A_{ij}}{4\pi} + B_{ij} I_{\nu_{ji}} \right) = n_j B_{ji} I_{\nu_{ji}}. \quad (D.4)$$

Obtaining $I_{\nu_{ji}}$ from equation (D.4),

$$I_{\nu_{ji}} = \frac{\frac{A_{ij} B_{ij}}{4\pi}}{\left(\frac{B_{ji}}{B_{ij}} \right) \left(\frac{n_j}{n_i} - 1 \right)} \quad (D.5)$$

D. THE CORRECTION FACTOR OF T_{GAS}

Assuming Boltzmann equilibrium for the populations of n_j and n_i , that is, assuming the particles are in thermodynamic equilibrium

$$\frac{n_i}{n_j} = \frac{g_i}{g_j} \exp(-\epsilon_{ji}/k_B T_{gas}), \quad (D.6)$$

with $\epsilon_{ji} = |\epsilon_i - \epsilon_j|$. Then, the Boltzmann relation (D.6) is used as the condition for the radiation field to be in equilibrium with the matter. From (D.6) using (D.5), we obtain

$$I_{\nu_{ji}} = \frac{\frac{A_{ij}B_{ij}}{4\pi}}{\frac{g_j B_{ji}}{g_i B_{ij}} \exp(h\nu_{ji}/k_B T_{gas}) - 1}. \quad (D.7)$$

From equation (D.1)

$$I_{\nu_{ji}} = \frac{c}{4\pi} u_{\nu_{ji}}. \quad (D.8)$$

When the energy gap between levels i and j is much less than the thermal energy $k_B T_{gas}$, the value of $I_{\nu_{ji}}$ is given correctly classical theory (equation (D.1)) with

$$u_{\nu_{ji}} = \frac{8\pi\nu_{ji}^2 k_B T_{gas}}{c^3}. \quad (D.9)$$

Then, for $h\nu_{ji}/k_B T_{gas} \ll 1$, we have from equations (D.1), (D.7) and (D.9) that

$$\frac{2\nu_{ji}^2}{c^2} k_B T_{gas} = \frac{\frac{A_{ij}B_{ij}}{4\pi}}{\frac{g_j B_{ji}}{g_i B_{ij}} (1 + h\nu_{ji}/k_B T_{gas}) - 1}. \quad (D.10)$$

For equation (D.10) to be valid for all the values of $k_B T_{gas}$, consistent with $h\nu_{ji}/k_B T_{gas} \ll 1$, Einstein found that it was needed that

$$g_i B_{ji} = g_i B_{ij} \quad (D.11)$$

and

$$\frac{A_{ij}}{B_{ij}} = \frac{8\pi h\nu_{ji}^3}{c^2}. \quad (D.12)$$

Substituting (D.11) and (D.12) in equation (D.7) given the equilibrium spectral distribution of specific intensity $I_{\nu_{ji}}$

$$I_{\nu_{ji}} = \frac{2h\nu_{ji}^3/c^2}{\exp(h\nu_{ji}/k_B T_{gas}) - 1}, \quad (D.13)$$

related to the blackbody radiation energy density spectrum $u_{\nu_{ji}}$ in an enclosure. The energy absorbed per unit time in all j to i transitions from radiation traveling in the solid angle $d\Omega$ about Ω is

$$h\nu_{ji} B_{ji} I_{\nu_{ji}} d\Omega. \quad (D.14)$$

If the Einstein spontaneous emission probabilities (A_{ij}) are known, then

$$\frac{A_{ij}}{B_{ji}} = \frac{8\pi h\nu_{ji}^3}{c^2} \quad (\text{D.15})$$

with

$$B_{ij} = \frac{g_i}{g_j} B_{ji}, \quad (\text{D.16})$$

with g_j and g_i being the degeneration (or statistical weights) of emitting/absorbing levels (in diatomic molecules, the statistical weights of vibrational levels are 1). From (D.15) and (D.16)

$$\frac{A_{ij}g_i}{g_j B_{ji}} = \frac{8\pi h\nu_{ji}^3}{c^2}, \quad (\text{D.17})$$

then

$$B_{ji} = \frac{c^2}{8\pi h\nu_{ji}^3} A_{ij} \frac{g_i}{g_j}. \quad (\text{D.18})$$

Thus, using equations (D.14)-(D.18), the power density absorbed from radiation is

$$P_{abs} = \sum_j n_j h\nu_{ji} B_{ji} I_{\nu_{ji}}, \quad (\text{D.19})$$

with n_j being the lower absorbing level population in each transition considered. Substituting the equation (D.18) and (D.13) in (D.19), we obtain

$$P_{abs} = \sum_j n_j \frac{A_{ij} h\nu_{ji}}{4\pi} \frac{g_i}{g_j} \frac{1}{\exp(h\nu_{ji}/k_B T_{gas}) - 1}. \quad (\text{D.20})$$

The correction factor of the gas temperature (k_{corr}) used in the equation for P_{abs} is given by

$$P_{abs} = k_{corr} \sum_j n_j \frac{A_{ij} h\nu_{ji}}{4\pi N} \frac{g_i}{g_j} \frac{1}{\exp(\frac{h\nu_{ji}}{k_b T_{gas}^{bg}}) - 1},$$

where k_{corr} is an altitude-dependent fitting factor obtained in the thermal relaxation of the model by imposing the condition $T_{gas}(t = 0 \text{ s}) = T_{gas}(t = 10^6 \text{ s})$ (see Figure D.1).

D. THE CORRECTION FACTOR OF T_{GAS}

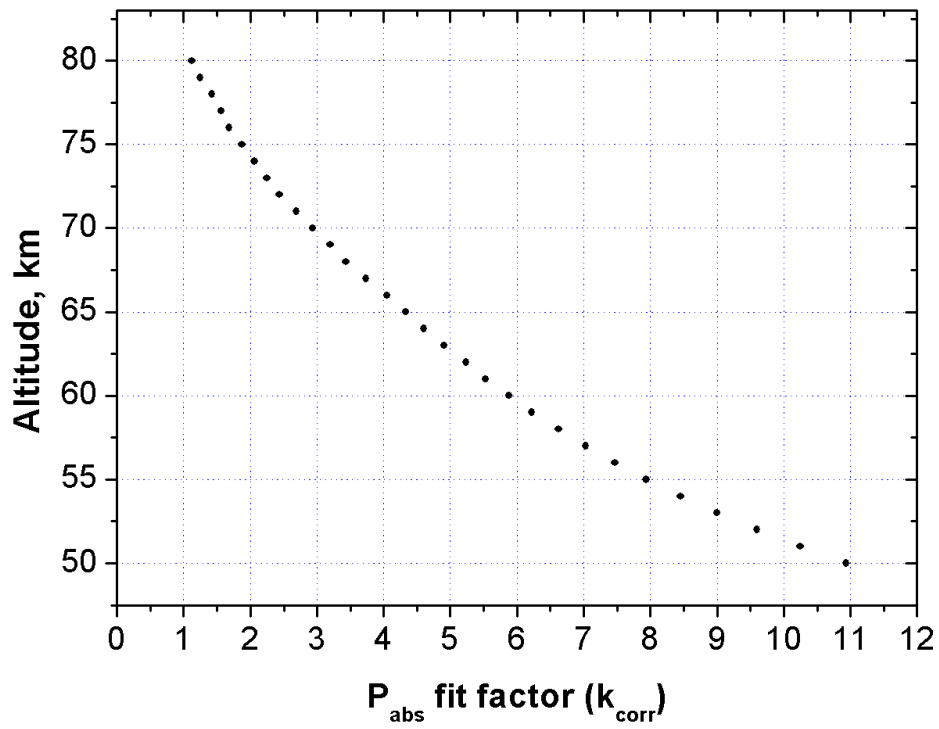


Figure D.1: Variation of the correction parameter (k_{corr}) with altitude taken from the thermal relaxation stage of the model.

Appendix E

Kinetic model for electrical discharges in the Earth's atmosphere

E.1 Chemical species

Table E.1: Ground neutrals considered

Ground neutrals
Ar
N, N ₂
O, O ₂ , O ₃
NO, NO ₂ , NO ₃ , N ₂ O, N ₂ O ₅
CO, CO ₂

Table E.2: Electrons and negative ions considered

Negative ions
e ⁻ , CO ₃ ⁻
O ⁻ , O ₂ ⁻ , O ₃ ⁻
NO ⁻ , NO ₂ ⁻ , NO ₃ ⁻ , N ₂ O ⁻

E. KINETIC MODEL FOR ELECTRICAL DISCHARGES IN THE EARTH'S ATMOSPHERE

Table E.3: Excited neutrals considered

Excited neutrals
Ar(³ P), NO(A ² Σ ⁺)
N(² D), N(² P)
N ₂ (A ³ Σ _u ⁺ , B ³ Π _g , W ³ Σ _g ⁺ , B' ³ Σ _u ⁻ , a' ¹ Σ _u ⁻ , a ¹ Π _g , w ¹ Δ _g , C ³ Π _u , E ³ Σ _g ⁺ , a'' ¹ Σ _g ⁺)
N ₂ (X ¹ Σ _g ⁺ , v = 1, ..., 8), N ₂ (rot)
O(¹ S), O(¹ D)
O ₂ (a ¹ Δ _g , b ¹ Σ _g ⁺ , A ³ Σ _u ⁺)
O ₂ (X ³ Σ _g ⁻ , v = 1, ..., 4), O ₂ (rot)
CO ₂ (v ₁ v ₂ ^l v ₃)

Table E.4: Positive ions considered

Positive ions
Ar ⁺
O ⁺ , O ₂ ⁺ , O ₄ ⁺
NO ⁺ , NO ₂ ⁺ , N ₂ O ⁺ , N ₂ O ₂ ⁺
N ⁺ , N ₂ ⁺ , N ₂ ⁺ (A ² Π _u , B ² Σ _u ⁺), N ₃ ⁺ , N ₄ ⁺

E.2 Types of reactions

Table E.5: Different types of reactions considered

Process	Name
$e + A \rightarrow A^+ + e + e$	Ionization
$e + AB \rightarrow A^+ + B + e + e$	Dissociative ionization
$e + AB \rightarrow A + B + e$	Dissociation
$e + A \rightarrow A^-$	Attachment
$e + A^+ \rightarrow A$	Recombination
$e + AB^+ \rightarrow A + B$	Dissociative recombination
$e + AB \rightarrow A^- + B$	Dissociative attachment
$A^- + B \rightarrow AB + e$	Associative detachment
$A^- + B^+ \rightarrow A + B$	Ion-Ion recombination
$A^- + B^* \rightarrow A + B + e$	Collisional detachment
$e + A \rightarrow B^* + C + e$	Electron-impact dissociative excitation
$h\nu + A \rightarrow A^*$	Photo-ionization
$A^*(\textit{metastable}) + B \rightarrow A + B^+ + e$	Penning ionization
$A^+ + B \rightarrow A + B^+$	Charge transfer
$A^{**} + B \rightarrow A^* + B$	Quenching
$A^* \rightarrow A + h\nu$	Radiative de-excitation
$e + A \rightarrow A + e$	Elastic collision
$e + A \rightarrow A^* + e$	Electron-impact excitation
$AB + C \rightarrow AC + B$	Substitution

E. KINETIC MODEL FOR ELECTRICAL DISCHARGES IN THE EARTH'S ATMOSPHERE

E.3 Reaction rates

The electron energy distribution function $f(\epsilon)$ gives us the most complete information about the state of the free electrons in the plasma. In the case of Local Thermodynamic Equilibrium (LTE), the electron energy distribution function will have a Maxwellian behavior

$$f(\epsilon) = A \exp\left(-\frac{\epsilon}{k_B T_e}\right), \quad (\text{E.1})$$

where T_e is the electron temperature, k_B is the Boltzmann's constant, $\epsilon = m_e v^2/2$ is the kinetic energy and A is the normalization parameter

$$A = \frac{2}{\sqrt{\pi}} (k_B T_e)^{-3/2} \quad (\text{E.2})$$

In general, the values of $f(\epsilon)$ are far from thermodynamic equilibrium due to the presence of electric fields. therefore we calculate the Electron Energy Distribution Function (EEDF) through the Boltzmann equation 2.3.

The electron scattering cross-sections determine the form of the EEDF and the rate coefficients for the processes involving free electrons. For inelastic processes, k_{snk} is the rate coefficient of the process $n \rightarrow k$ for the gas component s and k_{skn} is the rate coefficient for the inverse process, and we can calculate them as

$$k_{snk} = \sqrt{\frac{2}{m_e}} \int_0^\infty \sigma_{snk} \epsilon f(\epsilon) d\epsilon. \quad (\text{E.3})$$

The excitation/deexcitation rates for the electron impact processes are evaluated using the electron energy distribution function (EEDF) and their corresponding cross sections. When the cross sections are not available, the rates of electron driven mechanisms are calculated as

$$k_e = a \times T_e^b \times \exp(-c/T_e)$$

where T_e (in eV) is the electronic temperature. The excitation/deexcitation rates for the processes that include heavy species are parametrized as

$$k_h = d \times \left(\frac{300}{T_g}\right)^e \times \exp(-f/T_g)$$

being T_g (in K) the gas temperature. The $k_{e,h}$ units are cm^3s^{-1} and cm^6s^{-1} for two- and three-body processes, respectively. The general expression for the excitation/deexcitation rates of the processes ranging from 457 to 462, from 534 to 539, from

542 to 556 and from 571 to 578 are given as

$$k_{co2} = g \times (h + i \times \exp(-j/T_g^{1/3})).$$

For the processes ranging from 466 to 471 and from 557 to 570, the expression of the rates are given as

$$k_{co2} = g \times h \times \left(\frac{T_g}{300}\right)^i.$$

For the processes 540 and 541, the reaction rates are parametrized as

$$k_{co2} = g \times T_g,$$

and the reaction rates for other processes involving collisions of vibrationally excited CO₂ are parametrized as

$$k_{co2} = g \times h \times \exp(i/T_g + j/T_g^2).$$

The k_{co2} units are $\text{cm}^3 \text{s}^{-1}$. The rates of the return (backward) reactions in VV and VT processes have been calculated multiplying the direct reaction rate by $\exp(-E/k_B T_g)$, where E is the energy emitted/absorbed during the process depending on whether the process is exothermic or endothermic, and k_B is the Boltzmann constant.

The reaction rates of ionization due to cosmic rays are parametrized as

$$k_{cr} = k \times l,$$

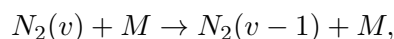
where $l = crc$ is an altitude-dependent factor obtained in the model electronic relaxation stage imposing $n_e(t = 0 \text{ s}) = n_e(t = 10^6 \text{ s})$ (see Figure E.1). The units of k_{cr} are s^{-1} .

The reaction rate of the process (80) is

$$k_f = a \times \left(\frac{300}{T_g}\right)^b$$

with T_g in Kelvin and k_f in $\text{cm}^3 \text{s}^{-1}$. The reaction rate of the process (402) is a polynomial fit performed on the *Rayment and Moruzzi* [1978] experimental data between 0 to 88 Td.

For the VT2 and VT3 processes of the type



E. KINETIC MODEL FOR ELECTRICAL DISCHARGES IN THE EARTH'S ATMOSPHERE

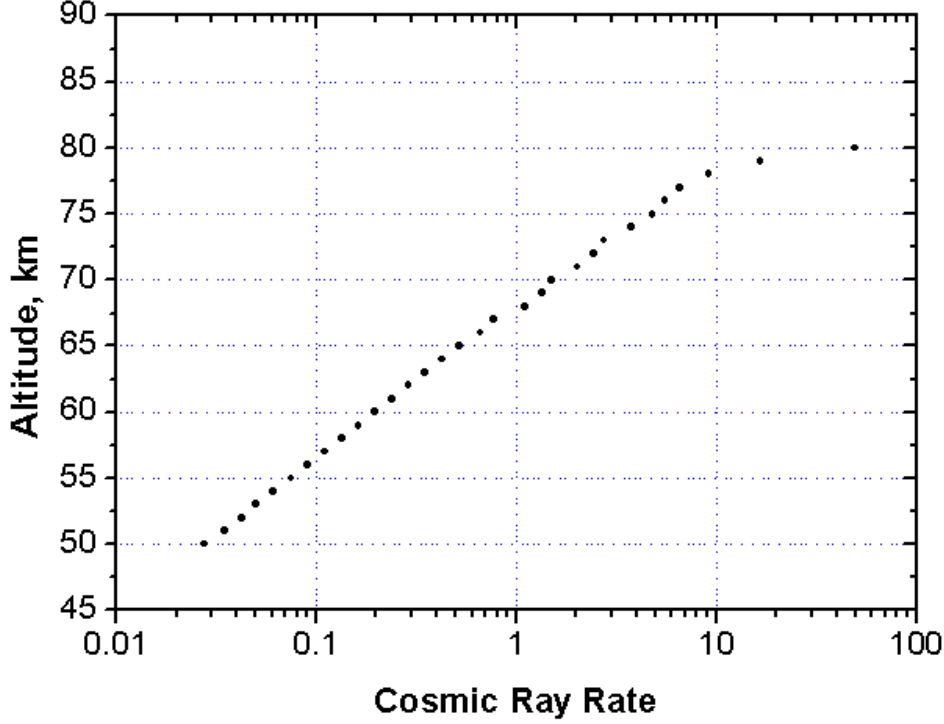


Figure E.1: Variation of the cosmic rays constant (CRC) with altitude taken from the electronic relaxation stage of the model.

with $M = N, O$ (from 137 to 151); the reaction rates are parametrized using an Arrhenius-type approximation of the form

$$k_{N_2} = d \times \exp\left(\frac{-e}{T_g}\right) + f \times \exp\left(\frac{-g}{T_g}\right)$$

with the units of T_g in Kelvin and k_{N_2} in $\text{cm}^3 \text{s}^{-1}$.

The reaction rate of the process (86) is taken from Kossyi et al. [1992] and it is given by

$$k_{86} = 1.07 \times 10^{-31} \times \left(\frac{300}{T_e}\right)^2 \times \exp\left(-\frac{70}{T_g}\right) \times \exp\left(\frac{1500 \times (T_e - T_g)}{T_e \times T_g}\right),$$

with the units of T_g and T_e in Kelvin and k_{86} in $\text{cm}^6 \text{s}^{-1}$.

The reaction rate of the process (152) is taken from Capitelli et al. [2000] and it is

given by

$$k_{152} = 1.1 \times 10^{-12} \times T_g \times \left(\frac{-218}{T_g^{1/3}} + \frac{690}{T_g} \right) \times \left(1 - \exp \left(-\frac{3375.19}{T_g} \right) \right)^{-1},$$

with the units of T_g in Kelvin and k_{153} in $\text{cm}^3 \text{s}^{-1}$.

The reaction rate of the process (153) is taken from Capitelli et al. [2000] and it is given by

$$k_{153} = 3.2 \times 10^{-15} \times \left(\frac{T_g}{300} \right)^{2.5},$$

with the units of T_g in Kelvin and k_{154} in $\text{cm}^3 \text{s}^{-1}$.

The reaction rate of the process (154) is taken from Capitelli et al. [2000] and it is given by

$$k_{154} = 2.05 \times 10^{-20} \times \exp \left(271 \times 10^{-4} \times T_g - 2.32 \times 10^{-5} \times T_g^2 \right),$$

with the units of T_g in Kelvin and k_{155} in $\text{cm}^3 \text{s}^{-1}$.

The reaction rate of the process (159) is taken from Capitelli et al. [2000] and it is given by

$$k_{159} = 1.35 \times 10^{-12} \times T_g \times \left(\frac{-137.9}{T_g^{1/3}} \right) \times \left(1 - \exp \left(-\frac{2203.76}{T_g} \right) \right)^{-1},$$

with the units of T_g in Kelvin and k_{159} in $\text{cm}^3 \text{s}^{-1}$.

The reaction rate of the process (160) is taken from Capitelli et al. [2000] and it is given by

$$k_{160} = 3.14 \times 10^{-12} \times T_g \times \left(\frac{-173.1}{T_g^{1/3}} + \frac{6.2 \times 10^5}{T_g^2} \right) \times \left(1 - \exp \left(-\frac{2203.76}{T_g} \right) \right)^{-1},$$

with the units of T_g in Kelvin and k_{160} in $\text{cm}^3 \text{s}^{-1}$. The processes in blue have only been included in the sprite streamer model.

E. KINETIC MODEL FOR ELECTRICAL DISCHARGES IN THE EARTH'S ATMOSPHERE

E.4 EEDF and cross section dependent processes

Table E.6: EEDF and cross section dependent processes

No.	Reaction	Ref.
1	$Ar + e \rightarrow Ar(^3P_2) + e$	Yamabe et al. [1983]
2	$Ar + e \rightarrow Ar^+ + 2e$	Yamabe et al. [1983]
3	$N_2 + e \rightleftharpoons N_2(v_1) + e$	Phelps and Pitchford [1985]
4	$N_2 + e \rightleftharpoons N_2(v_2) + e$	Phelps and Pitchford [1985]
5	$N_2 + e \rightleftharpoons N_2(v_3) + e$	Phelps and Pitchford [1985]
6	$N_2 + e \rightleftharpoons N_2(v_4) + e$	Phelps and Pitchford [1985]
7	$N_2 + e \rightleftharpoons N_2(v_5) + e$	Phelps and Pitchford [1985]
8	$N_2 + e \rightleftharpoons N_2(v_6) + e$	Phelps and Pitchford [1985]
9	$N_2 + e \rightleftharpoons N_2(v_7) + e$	Phelps and Pitchford [1985]
10	$N_2 + e \rightleftharpoons N_2(v_8) + e$	Phelps and Pitchford [1985]
11	$N_2 + e \rightarrow N_2(A^3\Sigma_u^+) + e$	Phelps and Pitchford [1985]
12	$N_2 + e \rightarrow N_2(a^1\Pi_g) + e$	Phelps and Pitchford [1985]
13	$N_2 + e \rightarrow N_2(a'^1\Sigma_u^-) + e$	Phelps and Pitchford [1985]
14	$N_2 + e \rightarrow N_2(a''^1\Sigma_g^+) + e$	Phelps and Pitchford [1985]
15	$N_2 + e \rightarrow N_2(B^3\Pi_g) + e$	Phelps and Pitchford [1985]
16	$N_2 + e \rightarrow N_2(B'^3\Sigma_u^-) + e$	Phelps and Pitchford [1985]
17	$N_2 + e \rightarrow N_2(C^3\Pi_u) + e$	Phelps and Pitchford [1985]
18	$N_2 + e \rightarrow N_2(E^3\Sigma_g^+) + e$	Phelps and Pitchford [1985]
19	$N_2 + e \rightarrow N_2(W^3\Delta_u) + e$	Phelps and Pitchford [1985]
20	$N_2 + e \rightarrow N_2(w^1\Delta_u) + e$	Phelps and Pitchford [1985]
21	$N_2 + e \rightarrow N_2(rot) + e$	Phelps and Pitchford [1985]
22	$N_2 + e \rightarrow N_2^+ + 2e$	Phelps and Pitchford [1985]
23	$N_2 + e \rightarrow N_2^+(B^2\Sigma_u^+) + 2e$	Phelps and Pitchford [1985]
24	$N_2 + e \rightarrow N_2^+(A^2\Pi_u) + 2e$	Shemansky and Broadfoot [1971]
25	$N_2 + e \rightarrow N + N(^2D) + e$	Phelps and Pitchford [1985]
26	$O_2 + e \rightleftharpoons O_2(v_1) + e$	Lawton and Phelps [1978]
27	$O_2 + e \rightleftharpoons O_2(v_2) + e$	Lawton and Phelps [1978]
28	$O_2 + e \rightleftharpoons O_2(v_3) + e$	Lawton and Phelps [1978]
29	$O_2 + e \rightleftharpoons O_2(v_4) + e$	Lawton and Phelps [1978]

E.4 EEDF and cross section dependent processes

No.	Reaction	Ref.
30	$O_2 + e \rightarrow O_2(A^3\Sigma_u^+) + e$	Lawton and Phelps [1978]
31	$O_2 + e \rightarrow O_2(a^1\Delta_g) + e$	Lawton and Phelps [1978]
32	$O_2 + e \rightarrow O_2(b^1\Sigma_g^+) + e$	Lawton and Phelps [1978]
33	$O_2 + e \rightarrow O_2^+ + 2e$	Lawton and Phelps [1978]
34	$O_2 + e \rightarrow O_2(rot) + e$	Lawton and Phelps [1978]
35	$O_2 + e \rightarrow O^- + O$	Lawton and Phelps [1978]
36	$O_2 + e \rightarrow O + O + e$	Lawton and Phelps [1978]
37	$O_2 + e \rightarrow O + O(^1D) + e$	Lawton and Phelps [1978]
38	$O_2 + e \rightarrow O + O(^1S) + e$	Lawton and Phelps [1978]
39	$O_2 + O_2 + e \rightarrow O_2^- + O_2$	Lawton and Phelps [1978]
40	$O_3 + e \rightarrow O^- + O_2$	Skalny et al. [1996]
41	$O_3 + e \rightarrow O_2^- + O$	Skalny et al. [1996]
42	$O + e \rightarrow O(^1D) + e$	Morgan [2000]
43	$O + e \rightarrow O(^1S) + e$	Morgan [2000]
44	$N_2O + e \rightarrow N_2 + O^-$	Hayashi [1987]
45	$N_2O + e \rightarrow N_2O^+ + 2e$	Hayashi [1987]
46	$NO + e \rightarrow NO^+ + 2e$	Phelps [1969]
47	$CO_2 + e \rightleftharpoons CO_2(01^10) + e$	Phelps [a]
48	$CO_2 + e \rightleftharpoons CO_2(00^01) + e$	Phelps [a]
49	$CO_2 + e \rightleftharpoons CO_2(02^00) + e$	Phelps [a]
50	$CO_2 + e \rightleftharpoons CO_2(02^20) + e$	Phelps [a]
51	$CO_2 + e \rightleftharpoons CO_2(10^00) + e$	Phelps [a]
52	$CO_2 + e \rightleftharpoons CO_2(03^10) + e$	Phelps [a]
53	$CO_2 + e \rightleftharpoons CO_2(03^30) + e$	Phelps [a]
54	$CO_2 + e \rightleftharpoons CO_2(11^10) + e$	Phelps [a]
55	$CO_2 + e \rightleftharpoons CO_2(04^00) + e$	Phelps [a]
56	$CO_2 + e \rightleftharpoons CO_2(04^20) + e$	Phelps [a]
57	$CO_2 + e \rightleftharpoons CO_2(12^00) + e$	Phelps [a]
58	$CO_2 + e \rightleftharpoons CO_2(04^40) + e$	Phelps [a]
59	$CO_2 + e \rightleftharpoons CO_2(12^20) + e$	Phelps [a]
60	$CO_2 + e \rightleftharpoons CO_2(20^00) + e$	Phelps [a]
61	$CO_2 + e \rightleftharpoons CO_2(01^11) + e$	Phelps [a]
62	$CO_2 + e \rightleftharpoons CO_2(02^01) + e$	Phelps [a]
63	$CO_2 + e \rightleftharpoons CO_2(02^21) + e$	Phelps [a]
64	$CO_2 + e \rightleftharpoons CO_2(10^01) + e$	Phelps [a]

E. KINETIC MODEL FOR ELECTRICAL DISCHARGES IN THE EARTH'S ATMOSPHERE

No.	Reaction	Ref.
65	$CO_2 + e \rightleftharpoons CO_2(03^1_1) + e$	Phelps [a]
66	$CO_2 + e \rightleftharpoons CO_2(03^3_1) + e$	Phelps [a]
67	$CO_2 + e \rightleftharpoons CO_2(11^1_1) + e$	Phelps [a]
68	$CO_2 + e \rightleftharpoons CO_2(00^0_2) + e$	Phelps [a]
69	$CO_2 + e \rightleftharpoons CO_2(04^0_1) + e$	Phelps [a]
70	$CO_2 + e \rightleftharpoons CO_2(04^2_1) + e$	Phelps [a]
71	$CO_2 + e \rightleftharpoons CO_2(04^4_1) + e$	Phelps [a]
72	$CO_2 + e \rightleftharpoons CO_2(12^0_1) + e$	Phelps [a]
73	$CO_2 + e \rightleftharpoons CO_2(12^2_1) + e$	Phelps [a]
74	$CO_2 + e \rightleftharpoons CO_2(20^0_1) + e$	Phelps [a]
75	$CO_2 + e \rightarrow CO + O^-$	Phelps [a]

E.5 Electronic temperature dependent processes

E.5.1 Ionization and dissociative ionization

Table E.7: Ionization and dissociative ionization processes

No.	Reaction	a	b	c	Ref.
76	$NO_2 + e \rightarrow NO_2^+ + 2e$	2.6E-9	0.5	10.0	Castillo [2004]
77	$NO + e \rightarrow O^+ + N + 2e$	2.9E-9	0.5	21.0	Castillo [2004]
78	$NO_2 + e \rightarrow NO^+ + O + 2e$	8.1E-9	0.5	12.9	Castillo [2004]
79	$O_2 + e \rightarrow O^+ + O + 2e$	4.2E-9	0.5	23.0	Castillo [2004]

E.5 Electronic temperature dependent processes

E.5.2 Dissociation

Table E.8: Dissociation processes

No.	Reaction	a	b	c	Ref.
80	$e + O_3 \rightarrow O_2 + O + e$	1.0E-8	0.5		Gudmundsson et al. [2001]
81	$e + NO \rightarrow N + O + e$	7.4E-9		6.50	Castillo [2004]
82	$e + NO_2 \rightarrow NO + O + e$	5.6E-9		3.11	Castillo [2004]
83	$e + N_2O \rightarrow N_2 + O + e$	1.4E-9		1.67	Castillo [2004]
84	$e + N_2O \rightarrow N_2 + O(^1D) + e$	1.2E-9		3.64	Castillo [2004]
85	$e + N_2O \rightarrow NO + N + e$	1.0E-10		4.93	Castillo [2004]

E.5.3 Attachment

Table E.9: Attachment processes

No.	Reaction	a	b	c	Ref.
86	$e + O_2 + N_2 \rightarrow O_2^- + N_2$				
87	$e + O + O_2 \rightarrow O^- + O_2$	1.0E-31			Capitelli et al. [2000]
88	$e + O + N_2 \rightarrow O^- + N_2$	1.0E-31			Capitelli et al. [2000]
89	$e + NO_2 \rightarrow O^- + NO$	3.0E-11			Kossyi et al. [1992]
90	$e + NO_2 \rightarrow NO_2^-$	1.0E-11			Kossyi et al. [1992]
91	$e + O_3 + O_2 \rightarrow O_3^- + O_2$	1.0E-31			Capitelli et al. [2000]
92	$e + NO + N_2 \rightarrow NO^- + N_2$	1.0E-30			Kossyi et al. [1992]

E. KINETIC MODEL FOR ELECTRICAL DISCHARGES IN THE EARTH'S ATMOSPHERE

E.5.4 Recombination

Table E.10: Recombination processes

No.	Reaction	a	b	c	Ref.
93	$e + N_2^+ \rightarrow N + N$	4.50E-8	-0.5		Kossyi et al. [1992]
94	$e + N_2^+ \rightarrow N + N(^2D)$	3.21E-8	-0.5		Kossyi et al. [1992]
95	$e + N_2^+ + O_2 \rightarrow N_2 + O_2$	2.49E-29	-1.5		Kossyi et al. [1992]
96	$e + O_2^+ \rightarrow O + O$	1.3006E-9	-0.7		Peverall et al. [2001]
97	$e + O_2^+ \rightarrow O + O(^1D)$	1.1334E-8	-0.7		Peverall et al. [2001]
98	$e + O_2^+ \rightarrow O(^1D) + O(^1D)$	4.645E-9	-0.7		Peverall et al. [2001]
99	$e + O_2^+ \rightarrow O(^1S) + O(^1D)$	1.3006E-9	-0.7		Peverall et al. [2001]
100	$e + NO^+ \rightarrow N + O$	1.66E-9	-1.5		Kossyi et al. [1992]
101	$e + NO^+ \rightarrow N(^2D) + O$	7.76E-9	-1.0		Kossyi et al. [1992]
102	$e + NO^+ + O_2 \rightarrow NO + O_2$	2.49E-29	-1.5		Kossyi et al. [1992]
103	$e + NO^+ + N_2 \rightarrow NO + N_2$	2.49E-29	-1.5		Kossyi et al. [1992]
104	$e + O_2^+ + O_2 \rightarrow O_2 + O_2$	2.49E-29	-1.5		Kossyi et al. [1992]
105	$e + N_4^+ \rightarrow N_2 + N + N$	3.13E-7	-0.41		Whitaker et al. [1981]
106	$e + N_4^+ \rightarrow N_2 + N_2$	3.21E-7	-0.5		Kossyi et al. [1992]
107	$e + O_4^+ \rightarrow O_2 + O + O$	2.30E-6			Kruger and Olander [1976]
108	$e + O_4^+ \rightarrow O_2 + O_2$	2.25E-7	-0.5		Kossyi et al. [1992]
109	$e + O^+ + N_2 \rightarrow O + N_2$	2.49E-29	-1.5		Kossyi et al. [1992]
110	$e + O^+ + e \rightarrow O + e$	7.18E-25	-4.5		Kossyi et al. [1992]
111	$e + O^+ + O_2 \rightarrow O + O_2$	2.49E-29	-1.5		Kossyi et al. [1992]
112	$e + N_2O^+ \rightarrow N_2 + O$	3.22E-8	-0.5		Castillo [2004]
113	$e + NO_2^+ \rightarrow NO + O$	3.22E-8	-0.5		Castillo [2004]
114	$e + N_2O_2^+ \rightarrow NO + NO$	3.61E-6	-0.5		Starikovskaia et al. [2001]
115	$e + N_2O_2^+ \rightarrow N_2 + O_2$	3.61E-6	-0.5		Starikovskaia et al. [2001]
116	$e + N_3^+ \rightarrow N_2 + N$	5.56E-7	-0.5		Starikovskaia et al. [2001]
117	$e + N_3^+ \rightarrow N_2(A^3\Sigma_u^+) + N$	6.91E-8	-0.5		Starikovskaia et al. [2001]
118	$e + N_3^+ \rightarrow N_2(B^3\Pi_g) + N$	6.91E-8	-0.5		Starikovskaia et al. [2001]
119	$e + e + N^+ \rightarrow e + N$	1.4E-8	-4.5		Kossyi et al. [1992]
120	$e + N^+ + O_2 \rightarrow N + O_2$	3.11E-23	-1.5		Kossyi et al. [1992]
121	$e + N^+ + N_2 \rightarrow N + N_2$	3.11E-23	-1.5		Kossyi et al. [1992]

E.6 Molecular nitrogen kinetics

E.6.1 Vibrational-Vibrational processes (VV)

Table E.11: Vibrational-Vibrational processes (VV)

No.	Reaction	d	e	f	$T_g(\text{K})$	Ref.
122	$N_2(v_1) + N_2(v_1) \rightleftharpoons N_2(v_2) + N_2$	3.0E-14			200	Cacciatore et al. [2005]
123	$N_2(v_1) + N_2(v_2) \rightleftharpoons N_2(v_3) + N_2$	4.0E-14			200	Cacciatore et al. [2005]
124	$N_2(v_1) + N_2(v_3) \rightleftharpoons N_2(v_4) + N_2$	5.0E-14			200	Cacciatore et al. [2005]
125	$N_2(v_1) + N_2(v_4) \rightleftharpoons N_2(v_5) + N_2$	5.6E-14			200	Cacciatore et al. [2005]
126	$N_2(v_1) + N_2(v_5) \rightleftharpoons N_2(v_6) + N_2$	6.0E-14			200	Cacciatore et al. [2005]
127	$N_2(v_1) + N_2(v_6) \rightleftharpoons N_2(v_7) + N_2$	5.6E-14			200	Cacciatore et al. [2005]
128	$N_2(v_1) + N_2(v_7) \rightleftharpoons N_2(v_8) + N_2$	5.0E-14			200	Cacciatore et al. [2005]

E.6.2 Vibrational-Translational processes (VT)

Table E.12: Vibrational-Translational processes (VT)

No.	Reaction	d	e	f	$T_g(\text{K})$	Ref.
129	$N_2(v_1) + N_2 \rightleftharpoons N_2 + N_2$	3.5E-21			500	Kurnosov et al. [2007]
130	$N_2(v_2) + N_2 \rightleftharpoons N_2(v_1) + N_2$	6.5E-21			500	Kurnosov et al. [2007]
131	$N_2(v_3) + N_2 \rightleftharpoons N_2(v_2) + N_2$	1.5E-20			500	Kurnosov et al. [2007]
132	$N_2(v_4) + N_2 \rightleftharpoons N_2(v_3) + N_2$	2.5E-20			500	Kurnosov et al. [2007]
133	$N_2(v_5) + N_2 \rightleftharpoons N_2(v_4) + N_2$	3.5E-20			500	Kurnosov et al. [2007]
134	$N_2(v_6) + N_2 \rightleftharpoons N_2(v_5) + N_2$	7.0E-20			500	Kurnosov et al. [2007]
135	$N_2(v_7) + N_2 \rightleftharpoons N_2(v_6) + N_2$	1.0E-19			500	Kurnosov et al. [2007]
136	$N_2(v_8) + N_2 \rightleftharpoons N_2(v_7) + N_2$	1.0E-19			500	Kurnosov et al. [2007]

E. KINETIC MODEL FOR ELECTRICAL DISCHARGES IN THE EARTH'S ATMOSPHERE

No.	Reaction	d	e	f	g	T_g (K)	Ref.
137	$N_2(v_2) + O \rightleftharpoons N_2(v_1) + O$	2.3E-13	1280	2.7E-11	10840	300	Capitelli et al. [2000]
138	$N_2(v_3) + O \rightleftharpoons N_2(v_2) + O$	2.3E-13	1280	2.7E-11	10840	300	Capitelli et al. [2000]
139	$N_2(v_4) + O \rightleftharpoons N_2(v_3) + O$	2.3E-13	1280	2.7E-11	10840	300	Capitelli et al. [2000]
140	$N_2(v_5) + O \rightleftharpoons N_2(v_4) + O$	2.3E-13	1280	2.7E-11	10840	300	Capitelli et al. [2000]
141	$N_2(v_6) + O \rightleftharpoons N_2(v_5) + O$	2.3E-13	1280	2.7E-11	10840	300	Capitelli et al. [2000]
142	$N_2(v_7) + O \rightleftharpoons N_2(v_6) + O$	2.3E-13	1280	2.7E-11	10840	300	Capitelli et al. [2000]
143	$N_2(v_8) + O \rightleftharpoons N_2(v_7) + O$	2.3E-13	1280	2.7E-11	10840	300	Capitelli et al. [2000]
144	$N_2(v_1) + N \rightleftharpoons N_2 + N$	2.3E-13	1280	2.7E-11	10840	300	Capitelli et al. [2000]
145	$N_2(v_2) + N \rightleftharpoons N_2(v_1) + N$	2.3E-13	1280	2.7E-11	10840	300	Capitelli et al. [2000]
146	$N_2(v_3) + N \rightleftharpoons N_2(v_2) + N$	2.3E-13	1280	2.7E-11	10840	300	Capitelli et al. [2000]
147	$N_2(v_4) + N \rightleftharpoons N_2(v_3) + N$	2.3E-13	1280	2.7E-11	10840	300	Capitelli et al. [2000]
148	$N_2(v_5) + N \rightleftharpoons N_2(v_4) + N$	2.3E-13	1280	2.7E-11	10840	300	Capitelli et al. [2000]
149	$N_2(v_6) + N \rightleftharpoons N_2(v_5) + N$	2.3E-13	1280	2.7E-11	10840	300	Capitelli et al. [2000]
150	$N_2(v_7) + N \rightleftharpoons N_2(v_6) + N$	2.3E-13	1280	2.7E-11	10840	300	Capitelli et al. [2000]
151	$N_2(v_8) + N \rightleftharpoons N_2(v_7) + N$	2.3E-13	1280	2.7E-11	10840	300	Capitelli et al. [2000]
152	$N_2(v_1) + CO_2 \rightleftharpoons N_2 + CO_2$						Capitelli et al. [2000]
153	$N_2(v_1) + O \rightleftharpoons N_2 + O$						Capitelli et al. [2000]
154	$N_2(v_1) + O_2 \rightleftharpoons N_2 + O_2(v_1)$						Capitelli et al. [2000]

E.7 Molecular oxygen kinetics

E.7.1 Vibrational-Translational processes (VT)

Table E.13: O₂ chemistry: vibrational-translational processes (VT)

No.	Reaction	d	e	f	$T_g(\mathbf{K})$	Ref.
155	$O_2(v_1) + O \rightleftharpoons O_2 + O$	4.5E-15				Capitelli et al. [2000]
156	$O_2(v_2) + O \rightleftharpoons O_2(v_1) + O$	4.5E-15				Capitelli et al. [2000]
157	$O_2(v_3) + O \rightleftharpoons O_2(v_2) + O$	4.5E-15				Capitelli et al. [2000]
158	$O_2(v_4) + O \rightleftharpoons O_2(v_3) + O$	4.5E-15				Capitelli et al. [2000]
159	$O_2(v_1) + O_2 \rightleftharpoons O_2 + O_2$					Capitelli et al. [2000]
160	$O_2(v_1) + Ar \rightleftharpoons O_2 + Ar$					Capitelli et al. [2000]

E. KINETIC MODEL FOR ELECTRICAL DISCHARGES IN THE EARTH'S ATMOSPHERE

E.8 Heavy particle kinetics

E.8.1 Electronically excited species

Table E.14: Electronically excited species

No.	Reaction	d	e	f	$T_g(\text{K})$	Ref.
161	$Ar(^3P_2) + N_2 \rightarrow Ar + N + N$	3.6E-11				Piper et al. [1973]
162	$Ar(^3P_2) + N_2 \rightarrow Ar + N_2(C^3\Pi_u)$	3.0E-11				Bouróne and Le Calvé [1973]
163	$Ar(^3P_2) + O_2 \rightarrow Ar + O + O$	2.1E-10				Piper et al. [1973]
164	$Ar(^3P_2) + CO_2 \rightarrow Ar + CO + O$	5.3E-10				Piper et al. [1973]
165	$Ar(^3P_2) + NO \rightarrow Ar + N + O$	2.2E-10				Piper et al. [1973]
166	$Ar(^3P_2) + N_2O \rightarrow Ar + NO + N$	4.4E-10				Piper et al. [1973]
167	$Ar(^3P_2) + N_2O \rightarrow Ar + N_2 + O$	4.4E-10				Piper et al. [1973]
168	$N(^2D) + O_2 \rightarrow NO + O$	1.5E-12	-0.5			Kossyi et al. [1992]
169	$N(^2D) + O_2 \rightarrow O(^1D) + NO$	6.0E-12	-0.5			Kossyi et al. [1992]
170	$N(^2D) + O \rightarrow N + O(^1D)$	4.0E-13				Capitelli et al. [2000]
171	$N(^2D) + N_2 \rightarrow N + N_2$	6.0E-15				Capitelli et al. [2000]
172	$N(^2D) + NO \rightarrow N_2 + O$	1.8E-10				Capitelli et al. [2000]
173	$N(^2D) + N_2O \rightarrow NO + N_2$	3.5E-12				Capitelli et al. [2000]
174	$N(^2P) + N \rightarrow N(^2D) + N$	1.8E-12				Capitelli et al. [2000]
175	$N(^2P) + O_2 \rightarrow NO + O$	2.6E-12				Capitelli et al. [2000]
176	$N(^2P) + N_2 \rightarrow N + N_2$	2.0E-18				Capitelli et al. [2000]
177	$N(^2P) + NO \rightarrow N_2 + O$	3.0E-11				Capitelli et al. [2000]
178	$N_2(a^1\Pi_g) + O_2 \rightarrow N_2 + O + O$	2.8E-11				Kossyi et al. [1992]
179	$N_2(a^1\Pi_g) + N_2 \rightarrow N_2 + N_2$	2.0E-13				Kossyi et al. [1992]
180	$N_2(a^1\Pi_g) + NO \rightarrow N_2 + N + O$	3.6E-10				Kossyi et al. [1992]
181	$N_2(a^1\Sigma_u^-) + N_2 \rightarrow N_2(B^3\Pi_g) + N_2$	2.0E-13				Kossyi et al. [1992]
182	$N_2(a^1\Sigma_u^-) + O_2 \rightarrow N_2 + O + O$	2.8E-11				Kossyi et al. [1992]
183	$N_2(a^1\Sigma_u^-) + O_2 \rightarrow N_2 + O + O(^1D)$	2.8E-11				Kossyi et al. [1992]
184	$N_2(a^1\Sigma_u^-) + NO \rightarrow N_2 + N + O$	3.6E-10				Kossyi et al. [1992]
185	$N_2(a^1\Sigma_u^-) + N_2(a^1\Sigma_u^-) \rightarrow N_4^+ + e$	2.0E-10				Kossyi et al. [1992]
186	$N_2(a^1\Sigma_u^-) + N_2(A^3\Sigma_u^+) \rightarrow N_4^+ + e$	5.0E-11				Kossyi et al. [1992]
187	$N_2(C^3\Pi_u) + N_2 \rightarrow N_2(a^1\Sigma_u^-) + N_2$	1.0E-11				Kossyi et al. [1992]
188	$N_2(C^3\Pi_u) + O_2 \rightarrow N_2 + O + O(^1S)$	3.0E-10				Capitelli et al. [2000]
189	$N_2(C^3\Pi_u) + N_2 \rightarrow N_2(B^3\Pi_g) + N_2$	1.0E-11				Kossyi et al. [1992]
190	$N_2(C^3\Pi_u) + O_2 \rightarrow N_2 + O + O(^1D)$	2.5E-10				Capitelli et al. [2000]
191	$N_2(B^3\Pi_g) + N_2 \rightarrow N_2 + N_2$	2.0E-12				Capitelli et al. [2000]
192	$N_2(B^3\Pi_g) + N_2 \rightarrow N_2(A^3\Sigma_u^+) + N_2$	1.0E-11				Capitelli et al. [2000]
193	$N_2(B^3\Pi_g) + O_2 \rightarrow N_2 + O + O$	3.0E-10				Capitelli et al. [2000]
194	$N_2(A^3\Sigma_u^+) + N_2 \rightarrow N_2 + N_2$	3.0E-18				Kossyi et al. [1992]
195	$N_2(A^3\Sigma_u^+) + O_2 \rightarrow N_2 + O + O$	2.54E-12				Kossyi et al. [1992]
196	$N_2(A^3\Sigma_u^+) + O_2 \rightarrow N_2O + O$	7.8E-14				Kossyi et al. [1992]
197	$N_2(A^3\Sigma_u^+) + O \rightarrow NO + N(^2D)$	7.0E-12				Capitelli et al. [2000]
198	$N_2(A^3\Sigma_u^+) + O \rightarrow N_2 + O(^1S)$	3.0E-11				Kossyi et al. [1992]
199	$N_2(A^3\Sigma_u^+) + N \rightarrow N_2 + N(^2P)$	5.0E-11				Capitelli et al. [2000]
200	$N_2(A^3\Sigma_u^+) + N_2O \rightarrow N_2 + N + NO$	1.0E-11				Kossyi et al. [1992]

E.8 Heavy particle kinetics

No.	Reaction	d	e	f	T_g (K)	Ref.
201	$N_2(A^3\Sigma_u^+) + N \rightarrow N_2 + N$	2.0E-11				Capitelli et al. [2000]
202	$N_2(A^3\Sigma_u^+) + NO \rightarrow N_2 + NO$	7.0E-11				Kossyi et al. [1992]
203	$N_2(A^3\Sigma_u^+) + NO \rightarrow N_2 + NO(A^2\Delta^+)$	8.75E-11				Simek [2003]
204	$N_2(A^3\Sigma_u^+) + N_2(A^3\Sigma_u^+) \rightarrow N_2(C^3\Pi_u) + N_2$	1.6E-10				Kossyi et al. [1992]
205	$N_2(A^3\Sigma_u^+) + N_2(A^3\Sigma_u^+) \rightarrow N_2(B^3\Pi_g) + N_2$	7.7E-11				Kossyi et al. [1992]
206	$N_2(A^3\Sigma_u^+) + O_2 \rightarrow N_2 + O_2(b^1\Sigma_g^+)$	7.5E-13				Kossyi et al. [1992]
207	$O(^1D) + N_2 \rightarrow O + N_2$	1.8E-11		-107		Kossyi et al. [1992]
208	$O(^1D) + N_2 \rightarrow O + N_2(v1)$	2.4E-11				Capitelli et al. [2000]
209	$O(^1D) + O_2 \rightarrow O + O_2(b^1\Sigma_g^+)$	2.56E-11		-67		Kossyi et al. [1992]
210	$O(^1D) + O_2 \rightarrow O + O_2$	6.4E-12		-67		Kossyi et al. [1992]
211	$O(^1D) + O_2 \rightarrow O + O_2(a^1\Delta_g)$	1.0E-12				Capitelli et al. [2000]
212	$O(^1D) + N_2O \rightarrow NO + NO$	7.2E-11				Kossyi et al. [1992]
213	$O(^1D) + N_2O \rightarrow N_2O + O$	1.0E-12				Starikovskaia et al. [2001]
214	$O(^1D) + N_2O \rightarrow N_2 + O_2$	4.9E-11				Castillo [2004]
215	$O(^1D) + NO_2 \rightarrow O_2 + NO$	3.0E-10				Castillo [2004]
216	$O(^1D) + NO \rightarrow O_2 + N$	1.7E-10				Kossyi et al. [1992]
217	$O(^1D) + O_3 \rightarrow O + O + O_2$	1.2E-10				Kossyi et al. [1992]
218	$O(^1D) + O_3 \rightarrow O + O_3$	2.41E-10				Linstrom and Mallard [2015]
219	$O(^1D) + O_3 \rightarrow O_2 + O_2$	2.4E-10				Kossyi et al. [1992]
220	$O(^1D) + CO_2 \rightarrow O + CO_2$	7.4E-11		-120	200-300	Linstrom and Mallard [2015]
221	$O(^1D) + CO \rightarrow CO_2$	7.3E-11			100-1200	Linstrom and Mallard [2015]
222	$O(^1S) + NO \rightarrow O + NO$	2.9E-10				Capitelli et al. [2000]
223	$O(^1S) + NO \rightarrow O(^1D) + NO$	5.1E-10				Capitelli et al. [2000]
224	$O(^1S) + O_2 \rightarrow O_2 + O$	4.3E-12	0	850		Kossyi et al. [1992]
225	$O(^1S) + O_2 \rightarrow O_2 + O(^1D)$	1.3E-12	0	850		Kossyi et al. [1992]
226	$O(^1S) + O_2(a^1\Delta_g) \rightarrow O_2 + O(^1D)$	3.6E-11				Kossyi et al. [1992]
227	$O(^1S) + O_2(a^1\Delta_g) \rightarrow O + O + O$	3.4E-11				Kossyi et al. [1992]
228	$O(^1S) + O_2(a^1\Delta_g) \rightarrow O + O_2(b^1\Sigma_g^+)$	1.3E-10				Kossyi et al. [1992]
229	$O(^1S) + O \rightarrow O(^1D) + O$	5.0E-11	0	301		Kossyi et al. [1992]
230	$O(^1S) + O \rightarrow O(^1D) + O(^1D)$	5.0E-11	0	301		Kossyi et al. [1992]
231	$O(^1S) + O_3 \rightarrow O_2 + O + O(^1D)$	2.9E-10				Kossyi et al. [1992]
232	$O(^1S) + O_3 \rightarrow O_2 + O_2$	2.9E-10				Kossyi et al. [1992]
233	$O(^1S) + CO_2 \rightarrow O + CO_2$	3.09E-13			300	Linstrom and Mallard [2015]
234	$O_2(a^1\Delta_g) + N \rightarrow O + NO$	2.0E-14	0	600		Kossyi et al. [1992]
235	$O_2(a^1\Delta_g) + O \rightarrow O + O_2$	7.0E-16				Kossyi et al. [1992]
236	$O_2(a^1\Delta_g) + O_2 \rightarrow O_2 + O_2$	2.2E-18	0.8			Kossyi et al. [1992]
237	$O_2(a^1\Delta_g) + N_2 \rightarrow O_2 + N_2$	1.4E-19				Atkinson et al. [2003]
238	$O_2(a^1\Delta_g) + NO \rightarrow O + NO_2$	4.88E-18				Linstrom and Mallard [2015]
239	$O_2(a^1\Delta_g) + O_3 \rightarrow O_2 + O_2 + O$	5.2E-11	0	2841	280-360	Linstrom and Mallard [2015]
240	$O_2(a^1\Delta_g) + NO \rightarrow O_2 + NO$	2.5E-11				Kossyi et al. [1992]
241	$O_2(b^1\Sigma_g^+) + N_2 \rightarrow O_2(a^1\Delta_g) + N_2$	4.9E-15		253		Kossyi et al. [1992]
242	$O_2(b^1\Sigma_g^+) + O_2 \rightarrow O_2(a^1\Delta_g) + O_2$	3.73E-16	2.4	241		Kossyi et al. [1992]
243	$O_2(b^1\Sigma_g^+) + O \rightarrow O_2 + O$	8.0E-14				Kossyi et al. [1992]
244	$O_2(b^1\Sigma_g^+) + O_3 \rightarrow O_2(a^1\Delta_g) + O_2(a^1\Delta_g) + O$	1.8E-11				Kossyi et al. [1992]
245	$O_2(b^1\Sigma_g^+) + NO \rightarrow O_2(a^1\Delta_g) + NO$	4.0E-14				Kossyi et al. [1992]
246	$NO(A^2\Sigma^+) + O_2 \rightarrow NO + O_2$	1.62E-10				Simek [2003]
247	$NO(A^2\Sigma^+) + N_2 \rightarrow NO + N_2(A^3\Sigma_u^+)$	5.0E-14				Thoman et al. [1992]
248	$N_2^+(A^2\Pi_u) + N_2 \rightarrow N_2^+ + N_2$	7.5E-10				Piper et al. [1985]

E. KINETIC MODEL FOR ELECTRICAL DISCHARGES IN THE EARTH'S ATMOSPHERE

No.	Reaction	d	e	f	T_g (K)	Ref.
249	$N_2^+(A^2\Pi_u) + O_2 \rightarrow N_2^+ + O_2$	6.2E-10				Piper et al. [1985]
250	$N_2^+(B^2\Sigma_u^+) + N_2 \rightarrow N_2^+ + N_2$	7.5E-11				Piper et al. [1985]
251	$N_2^+(B^2\Sigma_u^+) + O_2 \rightarrow N_2^+ + O_2$	6.2E-10				Piper et al. [1985]

E.8.2 Ground neutrals

Table E.15: Ground neutral species

No.	Reaction	d	e	f	T_g (K)	Ref.
252	$N + O_2 \rightarrow NO + O$	1.0E-11	0	3473	200-1000	Kossyi et al. [1992]
253	$N + NO_2 \rightarrow O + O + N_2$	9.1E-13				Capitelli et al. [2000]
254	$N + NO_2 \rightarrow O + N_2O$	3.0E-12				Capitelli et al. [2000]
255	$N + NO_2 \rightarrow O_2 + N_2$	7.0E-13				Capitelli et al. [2000]
256	$N + NO_2 \rightarrow NO + NO$	2.3E-13				Capitelli et al. [2000]
257	$NO_2 + NO_3 + O_2 \rightarrow N_2O_5 + O_2$	5.9E-29	-1.27			Starikovskaia et al. [2001]
258	$NO_2 + NO_3 + N_2 \rightarrow N_2O_5 + N_2$	5.9E-29	-1.27			Starikovskaia et al. [2001]
259	$NO_2 + NO_3 + NO \rightarrow N_2O_5 + NO$	5.9E-29	-1.27			Starikovskaia et al. [2001]
260	$NO_2 + NO_3 + N_2O_5 \rightarrow N_2O_5 + N_2O_5$	5.9E-29	-1.27			Starikovskaia et al. [2001]
261	$N_2O_5 + N_2 \rightarrow NO_2 + NO_3 + N_2$	2.1E-11	-4.4	11080		Capitelli et al. [2000]
262	$N_2O_5 + O_2 \rightarrow NO_2 + NO_3 + O_2$	2.1E-11	-4.4	11080		Capitelli et al. [2000]
263	$N_2O_5 + Ar \rightarrow NO_2 + NO_3 + Ar$	2.1E-11	-4.4	11080		Capitelli et al. [2000]
264	$N_2O_5 + O \rightarrow N_2 + O_2 + O_2 + O_2$	3.0E-16	0.5			Kossyi et al. [1992]
265	$NO_2 + O_3 \rightarrow NO_3 + O_2$	1.2E-13	0	2450	230-360	Capitelli et al. [2000]
266	$O + NO_2 + N_2 \rightarrow NO_3 + N_2$	8.9E-32	-2.0			Capitelli et al. [2000]
267	$O + NO_2 + O_2 \rightarrow NO_3 + O_2$	8.9E-32	-2.0			Capitelli et al. [2000]
268	$O + NO_3 \rightarrow NO_2 + O_2$	1.0E-11				Kossyi et al. [1992]
269	$NO + NO_3 \rightarrow NO_2 + NO_2$	1.11E-11				Capitelli et al. [2000]
270	$O + NO_2 \rightarrow O_2 + NO$	9.09E-12	0.18			Kossyi et al. [1992]
271	$N + O_3 \rightarrow NO + O_2$	2.0E-16				Kossyi et al. [1992]
272	$O + NO + N_2 \rightarrow NO_2 + N_2$	1.2E-31	-1.682		200-2500	Capitelli et al. [2000]
273	$O + NO + O_2 \rightarrow NO_2 + O_2$	9.3E-32	-1.682		200-2500	Capitelli et al. [2000]
274	$O + NO \rightarrow O_2 + N$	8.93E-13	1	19494.5	200-2500	Linstrom and Mallard [2015]
275	$O_3 + NO \rightarrow O_2 + NO_2$	4.3E-12	0	1560		Kossyi et al. [1992]
276	$N + N + N_2 \rightarrow N_2 + N_2$	8.27E-34	0	500		Kossyi et al. [1992]
277	$N + N + N \rightarrow N_2 + N$	3.31E-27	-1.5			Starikovskaia et al. [2001]
278	$O + O + N_2 \rightarrow O_2 + N_2$	6.49E-35	0	1039	190-4000	Capitelli et al. [2000]
279	$O + O + N \rightarrow O_2 + N$	3.2E-33	-0.41		290-4000	Capitelli et al. [2000]
280	$O + O_2 + O_2 \rightarrow O_3 + O_2$	7.6E-34	-1.9		200-4000	Capitelli et al. [2000]
281	$O + O_2 + N_2 \rightarrow O_3 + N_2$	5.8E-34	-2.8		200-4000	Capitelli et al. [2000]
282	$O + O_2 + O_3 \rightarrow O_3 + O_3$	1.5E-34	0	750		Starikovskaia et al. [2001]
283	$O + O_2 + O \rightarrow O_3 + O$	2.15E-34	0	345	200-4000	Capitelli et al. [2000]
284	$O + O_3 \rightarrow O_2 + O_2$	2.0E-11	0	2300	220-1000	Kossyi et al. [1992]
285	$N + O + N_2 \rightarrow NO + N_2$	1.0E-32	-0.5		200-4000	Capitelli et al. [2000]
286	$N + O + O_2 \rightarrow NO + O_2$	1.0E-32	-0.5		200-4000	Capitelli et al. [2000]

E.8 Heavy particle kinetics

No.	Reaction	d	e	f	T_g (K)	Ref.
287	$NO_2 + N_2 \rightarrow NO + O + N_2$	6.8E-6	-2	36180	200-4000	Capitelli et al. [2000]
288	$NO_2 + O_2 \rightarrow NO + O + O_2$	5.3E-6	-2	36180	200-4000	Capitelli et al. [2000]
289	$NO_2 + NO \rightarrow NO + NO + O$	5.3E-5	-2	36180	200-4000	Capitelli et al. [2000]
290	$NO_2 + NO_2 \rightarrow NO + O + NO_2$	4.0E-5	-2	36180	200-4000	Capitelli et al. [2000]
291	$NO_2 + Ar \rightarrow NO + O + Ar$	4.0E-6	-2	36180	200-4000	Capitelli et al. [2000]
292	$NO_3 + N_2 \rightarrow NO_2 + O + N_2$	3.1E-5	-2	25000	200-1500	Capitelli et al. [2000]
293	$NO_3 + O_2 \rightarrow NO_2 + O + O_2$	3.1E-5	-2	25000	200-1500	Capitelli et al. [2000]
294	$NO_3 + NO \rightarrow NO_2 + O + NO$	3.1E-5	-2	25000	200-1500	Capitelli et al. [2000]
295	$NO_3 + N \rightarrow NO_2 + O + N$	3.1E-4	-2	25000	200-1500	Capitelli et al. [2000]
296	$NO_3 + O \rightarrow NO_2 + O + O$	3.1E-4	-2	25000	200-1500	Capitelli et al. [2000]
297	$NO_3 + Ar \rightarrow NO_2 + O + Ar$	3.72E-5	-2	25000	200-1500	Capitelli et al. [2000]
298	$NO_3 + N_2 \rightarrow NO + O_2 + N_2$	6.2E-5	-2	25000	200-1500	Capitelli et al. [2000]
299	$NO_3 + O_2 \rightarrow NO + O_2 + O_2$	6.2E-5	-2	25000	200-1500	Capitelli et al. [2000]
300	$NO_3 + NO \rightarrow NO + O_2 + NO$	6.2E-5	-2	25000	200-1500	Capitelli et al. [2000]
301	$NO_3 + N \rightarrow NO + O_2 + N$	7.44E-4	-2	25000	200-1500	Capitelli et al. [2000]
302	$NO_3 + O \rightarrow NO + O_2 + O$	7.44E-4	-2	25000	200-1500	Capitelli et al. [2000]
303	$NO_3 + Ar \rightarrow NO + O_2 + Ar$	7.44E-5	-2	25000	200-1500	Capitelli et al. [2000]
304	$CO_2 + O \rightarrow CO + O_2$	2.81E-11	0	26474	300-2500	Linstrom and Mallard [2015]
305	$CO + O + N_2 \rightarrow CO_2 + N_2$	1.7E-33	0	1510	250-4000	Linstrom and Mallard [2015]
306	$CO + O_2 \rightarrow CO_2 + O$	4.2E-12	0	24000	300-6000	Linstrom and Mallard [2015]
307	$CO + NO_2 \rightarrow CO_2 + NO$	1.48E-10	0	16967	300-2000	Linstrom and Mallard [2015]

E. KINETIC MODEL FOR ELECTRICAL DISCHARGES IN THE EARTH'S ATMOSPHERE

E.9 Ionic kinetics

E.9.1 Ion-Ion recombination

Table E.16: Ion-Ion recombination processes

No.	Reaction	d	e	f	T_g (K)	Ref.
308	$N_2O_2^+ + O_2^- \rightarrow NO + NO + O_2$	1.0E-7				Starikovskaia et al. [2001]
309	$N_2O_2^+ + O_2^- \rightarrow N_2 + O_2 + O_2$	1.0E-7				Starikovskaia et al. [2001]
310	$N_2O_2^+ + O^- \rightarrow NO + NO + O$	1.0E-7				Starikovskaia et al. [2001]
311	$N_2O_2^+ + O^- \rightarrow N_2 + O + O_2$	1.0E-7				Starikovskaia et al. [2001]
312	$N_2O_2^+ + O_3^- \rightarrow NO + NO + O_3$	1.0E-7				Starikovskaia et al. [2001]
313	$N_2O_2^+ + O_3^- \rightarrow N_2 + O_2 + O_3$	1.0E-7				Starikovskaia et al. [2001]
314	$N_2O_2^+ + NO^- \rightarrow NO + NO + NO$	1.0E-7				Starikovskaia et al. [2001]
315	$N_2O_2^+ + NO^- \rightarrow NO + N_2 + O_2$	1.0E-7				Starikovskaia et al. [2001]
316	$N_2O_2^+ + NO_2^- \rightarrow NO + NO + NO_2$	1.0E-7				Starikovskaia et al. [2001]
317	$N_2O_2^+ + NO_2^- \rightarrow NO_2 + N_2 + O_2$	1.0E-7				Starikovskaia et al. [2001]
318	$N_2O_2^+ + NO_3^- \rightarrow NO + NO + NO_3$	1.0E-7				Starikovskaia et al. [2001]
319	$N_2O_2^+ + NO_3^- \rightarrow NO_3 + N_2 + O_2$	1.0E-7				Starikovskaia et al. [2001]
320	$N_3^+ + O^- \rightarrow N + N_2 + O$	1.0E-7				Starikovskaia et al. [2001]
321	$N_3^+ + O_3^- \rightarrow N + N_2 + O_3$	1.0E-7				Starikovskaia et al. [2001]
322	$N_3^+ + NO^- \rightarrow N + N_2 + NO$	1.0E-7				Starikovskaia et al. [2001]
323	$N_3^+ + NO_3^- \rightarrow N + N_2 + NO_3$	1.0E-7				Starikovskaia et al. [2001]
324	$O^- + N^+ \rightarrow O + N$	2.0E-7	0.5			Kossyi et al. [1992]
325	$O^- + NO^+ + O_2 \rightarrow NO_2 + O_2$	2.0E-25	-2.5			Capitelli et al. [2000]
326	$O^- + O_2^+ \rightarrow O + O_2$	2.0E-7	-0.5			Capitelli et al. [2000]
327	$O^- + O_2^+ + O_2 \rightarrow O_3 + O_2$	2.0E-25	-2.5			Capitelli et al. [2000]
328	$O_2^- + O_2^+ \rightarrow O_2 + O_2$	2.0E-7	-0.5			Capitelli et al. [2000]
329	$O_2^- + N^+ \rightarrow N + O_2$	2.0E-7	0.5			Kossyi et al. [1992]
330	$O_2^- + NO^+ \rightarrow O_2 + N + O$	1.0E-7				Capitelli et al. [2000]
331	$O_2^- + NO^+ + O_2 \rightarrow O_2 + O_2 + NO$	2.0E-25	-2.5			Capitelli et al. [2000]
332	$O_3^- + O^+ \rightarrow O_3 + O$	2.0E-7	-0.5			Capitelli et al. [2000]
333	$O_3^- + N^+ \rightarrow O_3 + N$	2.0E-7	0.5			Kossyi et al. [1992]
334	$O_3^- + O_2^+ \rightarrow O_3 + O_2$	2.0E-7	-0.5			Capitelli et al. [2000]
335	$O_3^- + O_2^+ \rightarrow O + O + O_3$	1.0E-7				Capitelli et al. [2000]
336	$O_3^- + NO^+ \rightarrow O_3 + NO$	2.0E-7	-0.5			Capitelli et al. [2000]
337	$NO^- + N^+ \rightarrow NO + N$	2.0E-7	0.5			Kossyi et al. [1992]
338	$NO_2^- + N^+ \rightarrow NO_2 + N$	2.0E-7	0.5			Kossyi et al. [1992]
339	$NO_3^- + N^+ \rightarrow NO_3 + N$	2.0E-7	0.5			Kossyi et al. [1992]
340	$NO_3^- + NO^+ \rightarrow NO_3 + N + O$	1.0E-7				Capitelli et al. [2000]
341	$NO_3^- + O_2^+ \rightarrow NO_3 + O + O$	1.0E-7				Capitelli et al. [2000]
342	$N_2O^- + N^+ \rightarrow N_2O + N$	2.0E-7	0.5			Kossyi et al. [1992]

E.9.2 Positive ions

Table E.17: Positive ion processes

No.	Reaction	d	e	f	$T_g(\text{K})$	Ref.
343	$Ar^+ + N_2 \rightarrow Ar + N_2^+$	1.1E-11				Lindinger et al. [1981]
344	$Ar^+ + O_2 \rightarrow Ar + O_2^+$	4.6E-11				Midey et al. [2002]
345	$N^+ + N_2 + N_2 \rightarrow N_3^+ + N_2$	9.0E-30		-400		Kossyi et al. [1992]
346	$N^+ + O + N_2 \rightarrow NO^+ + N_2$	1.0E-29				Kossyi et al. [1992]
347	$N^+ + O + O_2 \rightarrow NO^+ + O_2$	1.0E-29				Kossyi et al. [1992]
348	$N^+ + N + N_2 \rightarrow N_2^+ + N_2$	1.0E-29				Kossyi et al. [1992]
349	$N^+ + N + O_2 \rightarrow N_2^+ + O_2$	1.0E-29				Kossyi et al. [1992]
350	$N^+ + O_2 \rightarrow O_2^+ + N$	2.8E-10				Kossyi et al. [1992]
351	$N^+ + O_2 \rightarrow NO^+ + O$	2.5E-10				Kossyi et al. [1992]
352	$N^+ + O_2 \rightarrow O^+ + NO$	2.8E-11				Kossyi et al. [1992]
353	$N^+ + O \rightarrow O^+ + N$	1.0E-12				Kossyi et al. [1992]
354	$N^+ + O_3 \rightarrow NO^+ + O_2$	5.0E-10				Kossyi et al. [1992]
355	$N^+ + NO \rightarrow NO^+ + N$	8.0E-10				Kossyi et al. [1992]
356	$N^+ + NO \rightarrow N_2^+ + O$	3.0E-12				Kossyi et al. [1992]
357	$N^+ + NO \rightarrow O^+ + N_2$	1.0E-12				Kossyi et al. [1992]
358	$N^+ + N_2O \rightarrow NO^+ + N_2$	5.5E-10				Kossyi et al. [1992]
359	$N_2^+ + N_2 + N \rightarrow N_3^+ + N_2$	9.0E-30		-400		Capitelli et al. [2000]
360	$N_2^+ + O \rightarrow N_2 + O^+$	1.0E-11	-0.2			Kossyi et al. [1992]
361	$N_2^+ + O \rightarrow NO^+ + N$	1.3E-10	-0.5			Kossyi et al. [1992]
362	$N_2^+ + O_2 \rightarrow N_2 + O_2^+$	6.0E-11	-0.5			Kossyi et al. [1992]
363	$N_2^+ + O_3 \rightarrow O_2^+ + O + N_2$	1.0E-10				Capitelli et al. [2000]
364	$N_2^+ + N_2O \rightarrow N_2O^+ + N_2$	5.0E-10				Capitelli et al. [2000]
365	$N_2^+ + N_2O \rightarrow NO^+ + N + N_2$	4.0E-10				Capitelli et al. [2000]
366	$N_2^+ + NO \rightarrow NO^+ + N_2$	3.3E-10				Kossyi et al. [1992]
367	$N_2^+ + N_2 + N_2 \rightarrow N_4^+ + N_2$	5.2E-29	-2.2			Capitelli et al. [2000]
368	$N_3^+ + N_2(A^3\Sigma_u^+) \rightarrow N_3^+ + N_2$	3.0E-10				Starikovskaia et al. [2001]
369	$N_3^+ + O_2 \rightarrow O_2^+ + N + N_2$	2.3E-11				Kossyi et al. [1992]
370	$N_3^+ + O_2 \rightarrow NO_2^+ + N_2$	4.4E-11				Kossyi et al. [1992]
371	$N_3^+ + N \rightarrow N_2^+ + N_2$	6.6E-11				Kossyi et al. [1992]
372	$N_3^+ + NO \rightarrow NO^+ + N + N_2$	7.0E-11				Kossyi et al. [1992]
373	$N_3^+ + NO \rightarrow N_2 + N_2O^+$	7.0E-11				Starikovskaia et al. [2001]
374	$N_4^+ + O_2 \rightarrow O_2^+ + N_2 + N_2$	2.5E-10				Capitelli et al. [2000]
375	$N_4^+ + O \rightarrow O^+ + N_2 + N_2$	2.5E-10				Capitelli et al. [2000]

E. KINETIC MODEL FOR ELECTRICAL DISCHARGES IN THE EARTH'S ATMOSPHERE

No.	Reaction	d	e	f	$T_g(\text{K})$	Ref.
376	$O^+ + N_2 \rightarrow NO^+ + N$	3.0E-12				Kossyi et al. [1992]
377	$O^+ + O_2 \rightarrow O_2^+ + O$	2.0E-11	-0.5			Capitelli et al. [2000]
378	$O^+ + O_3 \rightarrow O_2^+ + O_2$	1.0E-10				Capitelli et al. [2000]
379	$O^+ + NO \rightarrow NO^+ + O$	2.4E-11				Capitelli et al. [2000]
380	$O^+ + NO \rightarrow O_2^+ + N$	3.0E-12				Capitelli et al. [2000]
381	$O^+ + N_2O \rightarrow NO^+ + NO$	2.3E-10				Capitelli et al. [2000]
382	$O^+ + N_2O \rightarrow O_2^+ + N_2$	2.0E-11				Capitelli et al. [2000]
383	$O^+ + N_2O \rightarrow N_2O^+ + O$	2.2E-11				Capitelli et al. [2000]
384	$O^+ + NO_2 \rightarrow NO_2^+ + O$	1.6E-9				Capitelli et al. [2000]
385	$O_2^+ + N \rightarrow NO^+ + O$	1.2E-10				Kossyi et al. [1992]
386	$O_2^+ + N_2 \rightarrow NO^+ + NO$	1.0E-17				Kossyi et al. [1992]
387	$O_2^+ + NO_2 \rightarrow NO^+ + O_3$	1.0E-11				Capitelli et al. [2000]
388	$O_2^+ + NO_2 \rightarrow NO_2^+ + O_2$	6.6E-10				Capitelli et al. [2000]
389	$O_2^+ + NO \rightarrow NO^+ + O_2$	4.4E-10				Kossyi et al. [1992]
390	$O_2^+ + O_2 + O_2 \rightarrow O_4^+ + O_2$	2.4E-30	-3.2			Kossyi et al. [1992]
391	$O_2^+ + N_2 + N_2 \rightarrow N_2O_2^+ + N_2$	9.0E-31	-2			Kossyi et al. [1992]
392	$O_4^+ + O_2(a^1\Delta_g) \rightarrow O_2^+ + O_2 + O_2$	1.0E-10				Kossyi et al. [1992]
393	$O_4^+ + O_2(b^1\Sigma_g^+) \rightarrow O_2^+ + O_2 + O_2$	1.0E-10				Kossyi et al. [1992]
394	$O_4^+ + N_2 \rightarrow N_2O_2^+ + O_2$	4.6E-12	2.5	2650		Capitelli et al. [2000]
395	$O_4^+ + NO \rightarrow NO^+ + O_2 + O_2$	1.0E-10				Kossyi et al. [1992]
396	$O_4^+ + O \rightarrow O_2^+ + O_3$	3.0E-10				Kossyi et al. [1992]
397	$O_4^+ + O_2 \rightarrow O_2^+ + O_2 + O_2$	3.3E-6	-4	5030		Kossyi et al. [1992]
398	$NO_2^+ + NO \rightarrow NO^+ + NO_2$	2.9E-10				Capitelli et al. [2000]
399	$N_2O^+ + NO \rightarrow NO^+ + N_2O$	2.9E-10				Capitelli et al. [2000]
400	$N_2O_2^+ + N_2 \rightarrow O_2^+ + N_2 + N_2$	1.1E-6	-5.3	2357		Capitelli et al. [2000]
401	$N_2O_2^+ + O_2 \rightarrow O_4^+ + N_2$	1.0E-10				Capitelli et al. [2000]

E.9.3 Negative ions

Table E.18: Negative ion processes

No.	Reaction	d	e	f	T_g (K)	Ref.
402	$O^- + N_2 \rightarrow N_2O + e$	$(1.156E-12 \times (E/N)^2)/(1892.2 + (E/N)^2)$				Rayment and Moruzzi [1978]
403	$O^- + O_2 \rightarrow O_3 + e$	5.0E-15				Kossyi et al. [1992]
404	$O^- + O \rightarrow O_2 + e$	5.0E-10				Kossyi et al. [1992]
405	$O^- + N_2(A^3\Sigma_u^+) \rightarrow O + N_2 + e$	2.2E-9				Kossyi et al. [1992]
406	$O^- + O_2(a^1\Delta_g) \rightarrow O_3 + e$	3.0E-10				Kossyi et al. [1992]
407	$O^- + O_3 \rightarrow O_2 + O_2 + e$	5.3E-10				Kossyi et al. [1992]
408	$O^- + NO \rightarrow NO_2 + e$	2.6E-10				Kossyi et al. [1992]
409	$O^- + N_2O \rightarrow NO^- + NO$	2.1E-10				Kossyi et al. [1992]
410	$O^- + NO_2 \rightarrow NO_2^- + O$	1.2E-9				Kossyi et al. [1992]
411	$O^- + O_2 + O_2 \rightarrow O_3^- + O_2$	1.1E-30	-1			Kossyi et al. [1992]
412	$O^- + O_3 \rightarrow O_3^- + O$	5.3E-10				Kossyi et al. [1992]
413	$O^- + O_2(a^1\Delta_g) \rightarrow O_2^- + O$	1.0E-10				Capitelli et al. [2000]
414	$O^- + N_2(B^3\Pi_g) \rightarrow O + N_2 + e$	1.9E-9				Capitelli et al. [2000]
415	$O^- + CO \rightarrow CO_2 + e$	6.0E-10	-0.32			Bortner and Baurer [1972]
416	$O^- + CO_2 + Ar \rightarrow CO_3^- + Ar$	3.1E-28	-0.5			Brasseur and Solomon [1986]
417	$O^- + CO_2 + CO_2 \rightarrow CO_3^- + CO_2$	3.1E-28	-0.5			Brasseur and Solomon [1986]
418	$O_2^- + O \rightarrow O^- + O_2$	3.3E-10				Kossyi et al. [1992]
419	$O_2^- + O \rightarrow O_3 + e$	1.5E-10				Kossyi et al. [1992]
420	$O_2^- + O_2 \rightarrow O_2 + O_2 + e$	2.7E-18	0.5	5590		Kossyi et al. [1992]
421	$O_2^- + O_2(a^1\Delta_g) \rightarrow O_2 + O_2 + e$	2.0E-10				Kossyi et al. [1992]
422	$O_2^- + O_2(b^1\Sigma_g^+) \rightarrow O_2 + O_2 + e$	3.6E-10				Kossyi et al. [1992]
423	$O_2^- + N_2 \rightarrow O_2 + N_2 + e$	1.9E-12	0.5	4990		Capitelli et al. [2000]
424	$O_2^- + N \rightarrow NO_2 + e$	5.0E-10				Kossyi et al. [1992]
425	$O_2^- + NO_2 \rightarrow O_2 + NO_2^-$	8.0E-10				Kossyi et al. [1992]
426	$O_2^- + O_3 \rightarrow O_2 + O_3^-$	4.0E-10				Kossyi et al. [1992]
427	$O_2^- + N_2(A^3\Sigma_u^+) \rightarrow O_2 + N_2 + e$	2.1E-9				Capitelli et al. [2000]
428	$O_2^- + N_2(B^3\Pi_g) \rightarrow O_2 + N_2 + e$	2.5E-9				Capitelli et al. [2000]
429	$O_3^- + O \rightarrow O_2^- + O_2$	2.5E-10				Kazil [2002]
430	$O_3^- + O \rightarrow O_2 + O_2 + e$	1.4E-10				Kossyi et al. [1992]
431	$O_3^- + NO \rightarrow NO_3^- + O$	1.0E-11				Kossyi et al. [1992]
432	$O_3^- + NO_2 \rightarrow O_3 + NO_2^-$	7.0E-10				Kossyi et al. [1992]
433	$O_3^- + NO_2 \rightarrow NO_3^- + O_2$	2.0E-11				Kossyi et al. [1992]
434	$O_3^- + NO \rightarrow O_2 + NO_2^-$	2.6E-11				Capitelli et al. [2000]
435	$O_3^- + O_3 \rightarrow O_2 + O_2 + O_2 + e$	1.0E-10				Kazil [2002]
436	$O_3^- + CO_2 \rightarrow CO_3^- + O_2$	5.5E-10	0.5			Brasseur and Solomon [1986]

E. KINETIC MODEL FOR ELECTRICAL DISCHARGES IN THE EARTH'S ATMOSPHERE

No.	Reaction	d	e	f	T_g (K)	Ref.
437	$NO^- + O_2 \rightarrow O_2^- + NO$	5.0E-10				Kossyi et al. [1992]
438	$NO^- + NO_2 \rightarrow NO_2^- + NO$	7.4E-16				Kossyi et al. [1992]
439	$NO^- + N_2O \rightarrow NO_2^- + N_2$	2.8E-14				Kossyi et al. [1992]
440	$NO^- + CO_2 \rightarrow NO + CO_2 + e$	8.3E-12			193-506	Albritton [1978]
441	$NO^- + CO \rightarrow NO + CO + e$	5.0E-13			193-506	Albritton [1978]
442	$NO^- + N_2O \rightarrow NO + N_2O + e$	5.1E-12			193-506	Albritton [1978]
443	$NO^- + NO \rightarrow NO + NO + e$	5.0E-12			285-506	Albritton [1978]
444	$NO_2^- + O_3 \rightarrow O_2 + NO_3^-$	1.8E-11				Kossyi et al. [1992]
445	$NO_2^- + NO_2 \rightarrow NO_3^- + NO$	4.0E-12				Capitelli et al. [2000]
446	$NO_2^- + NO_3 \rightarrow NO_2 + NO_3^-$	5.0E-10				Capitelli et al. [2000]
447	$NO_3^- + NO \rightarrow NO_2^- + NO_2$	3.0E-15				Capitelli et al. [2000]
448	$CO_3^- + O \rightarrow O_2^- + CO_2$	1.1E-10	0.5			Brasseur and Solomon [1986]
449	$CO_3^- + NO \rightarrow NO_2^- + CO_2$	1.1E-11	0.5			Brasseur and Solomon [1986]
450	$CO_3^- + NO_2 \rightarrow NO_3^- + CO_2$	2.0E-10	0.5			Brasseur and Solomon [1986]

E.10 Carbon dioxide kinetics

E.10.1 Vibrational-Translational processes (VT)

Table E.19: Vibrational-Translational processes

No.	Reaction	g	h	i	j	T_g (K)	Ref.
451	$CO_2(00^01) + CO_2 \rightleftharpoons CO_2(02^00) + CO_2$	0.18	7.3E-14	-850.3	86523	300	Lepoutre et al. [1977]
452	$CO_2(00^01) + CO_2 \rightleftharpoons CO_2(02^20) + CO_2$	0.18	7.3E-14	-850.3	86523	300	Lepoutre et al. [1977]
453	$CO_2(00^01) + CO_2 \rightleftharpoons CO_2(10^00) + CO_2$	0.18	7.3E-14	-850.3	86523	300	Lepoutre et al. [1977]
454	$CO_2(00^01) + CO_2 \rightleftharpoons CO_2(03^10) + CO_2$	0.82	7.3E-14	-850.3	86523	300	Lepoutre et al. [1977]
455	$CO_2(00^01) + CO_2 \rightleftharpoons CO_2(03^30) + CO_2$	0.82	7.3E-14	-850.3	86523	300	Lepoutre et al. [1977]
456	$CO_2(00^01) + CO_2 \rightleftharpoons CO_2(11^10) + CO_2$	0.82	7.3E-14	-850.3	86523	300	Lepoutre et al. [1977]
457	$CO_2(00^01) + N_2 \rightleftharpoons CO_2(02^00) + N_2$	0.1	2.2E-15	1.14E-10	76.75	300	López-Valverde [1990]
458	$CO_2(00^01) + N_2 \rightleftharpoons CO_2(02^20) + N_2$	0.1	2.2E-15	1.14E-10	76.75	300	López-Valverde [1990]
459	$CO_2(00^01) + N_2 \rightleftharpoons CO_2(10^00) + N_2$	0.1	2.2E-15	1.14E-10	76.75	300	López-Valverde [1990]
460	$CO_2(00^01) + N_2 \rightleftharpoons CO_2(03^10) + N_2$	0.9	2.2E-15	1.14E-10	76.75	300	López-Valverde [1990]
461	$CO_2(00^01) + N_2 \rightleftharpoons CO_2(03^30) + N_2$	0.9	2.2E-15	1.14E-10	76.75	300	López-Valverde [1990]
462	$CO_2(00^01) + N_2 \rightleftharpoons CO_2(11^10) + N_2$	0.9	2.2E-15	1.14E-10	76.75	300	López-Valverde [1990]
463	$CO_2(00^01) + CO \rightleftharpoons CO_2(03^10) + CO$	1.0	1.7E-14	-448.3	53636	300	Starr and Hancock [1975]
464	$CO_2(00^01) + CO \rightleftharpoons CO_2(03^30) + CO$	1.0	1.7E-14	-448.3	53636	300	Starr and Hancock [1975]
465	$CO_2(00^01) + CO \rightleftharpoons CO_2(11^10) + CO$	1.0	1.7E-14	-448.3	53636	300	Starr and Hancock [1975]
466	$CO_2(00^01) + O \rightleftharpoons CO_2(02^00) + O$	0.1	2.0E-13	0.5		300	Buchwald and Hunten [1975]
467	$CO_2(00^01) + O \rightleftharpoons CO_2(02^20) + O$	0.1	2.0E-13	0.5		300	Buchwald and Hunten [1975]
468	$CO_2(00^01) + O \rightleftharpoons CO_2(10^00) + O$	0.1	2.0E-13	0.5		300	Buchwald and Hunten [1975]
469	$CO_2(00^01) + O \rightleftharpoons CO_2(03^10) + O$	0.9	2.0E-13	0.5		300	Buchwald and Hunten [1975]
470	$CO_2(00^01) + O \rightleftharpoons CO_2(03^30) + O$	0.9	2.0E-13	0.5		300	Buchwald and Hunten [1975]
471	$CO_2(00^01) + O \rightleftharpoons CO_2(11^10) + O$	0.9	2.0E-13	0.5		300	Buchwald and Hunten [1975]

E.10 Carbon dioxide kinetics

No.	Reaction	g	h	i	j	T_g (K)	Ref.
472	$CO_2(01^10) + CO_2 \rightleftharpoons CO_2 + CO_2$	1.0	4.2E-12	-2988	303930	300	López-Valverde [1990]
473	$CO_2(02^00) + CO_2 \rightleftharpoons CO_2(01^10) + CO_2$	2.5	4.2E-12	-2988	303930	300	López-Valverde [1990]
474	$CO_2(02^20) + CO_2 \rightleftharpoons CO_2(01^10) + CO_2$	2.5	4.2E-12	-2988	303930	300	López-Valverde [1990]
475	$CO_2(10^00) + CO_2 \rightleftharpoons CO_2(01^10) + CO_2$	2.5	4.2E-12	-2988	303930	300	López-Valverde [1990]
476	$CO_2(03^10) + CO_2 \rightleftharpoons CO_2(02^00) + CO_2$	3.75	4.2E-12	-2988	303930	300	López-Valverde [1990]
477	$CO_2(03^10) + CO_2 \rightleftharpoons CO_2(02^20) + CO_2$	3.75	4.2E-12	-2988	303930	300	López-Valverde [1990]
478	$CO_2(03^10) + CO_2 \rightleftharpoons CO_2(10^00) + CO_2$	3.75	4.2E-12	-2988	303930	300	López-Valverde [1990]
479	$CO_2(03^30) + CO_2 \rightleftharpoons CO_2(02^00) + CO_2$	3.75	4.2E-12	-2988	303930	300	López-Valverde [1990]
480	$CO_2(03^30) + CO_2 \rightleftharpoons CO_2(02^20) + CO_2$	3.75	4.2E-12	-2988	303930	300	López-Valverde [1990]
481	$CO_2(03^30) + CO_2 \rightleftharpoons CO_2(10^00) + CO_2$	3.75	4.2E-12	-2988	303930	300	López-Valverde [1990]
482	$CO_2(11^10) + CO_2 \rightleftharpoons CO_2(02^00) + CO_2$	3.75	4.2E-12	-2988	303930	300	López-Valverde [1990]
483	$CO_2(11^10) + CO_2 \rightleftharpoons CO_2(02^20) + CO_2$	3.75	4.2E-12	-2988	303930	300	López-Valverde [1990]
484	$CO_2(11^10) + CO_2 \rightleftharpoons CO_2(10^00) + CO_2$	3.75	4.2E-12	-2988	303930	300	López-Valverde [1990]
485	$CO_2(01^10) + N_2 \rightleftharpoons CO_2 + N_2$	1.0	2.1E-12	-2659	223052	300	López-Valverde [1990]
486	$CO_2(02^00) + N_2 \rightleftharpoons CO_2(01^10) + N_2$	2.5	2.1E-12	-2659	223052	300	López-Valverde [1990]
487	$CO_2(02^20) + N_2 \rightleftharpoons CO_2(01^10) + N_2$	2.5	2.1E-12	-2659	223052	300	López-Valverde [1990]
488	$CO_2(10^00) + N_2 \rightleftharpoons CO_2(01^10) + N_2$	2.5	2.1E-12	-2659	223052	300	López-Valverde [1990]
489	$CO_2(03^10) + N_2 \rightleftharpoons CO_2(02^00) + N_2$	3.75	2.1E-12	-2659	223052	300	López-Valverde [1990]
490	$CO_2(03^10) + N_2 \rightleftharpoons CO_2(02^20) + N_2$	3.75	2.1E-12	-2659	223052	300	López-Valverde [1990]
491	$CO_2(03^10) + N_2 \rightleftharpoons CO_2(10^00) + N_2$	3.75	2.1E-12	-2659	223052	300	López-Valverde [1990]
492	$CO_2(03^30) + N_2 \rightleftharpoons CO_2(02^00) + N_2$	3.75	2.1E-12	-2659	223052	300	López-Valverde [1990]
493	$CO_2(03^30) + N_2 \rightleftharpoons CO_2(02^20) + N_2$	3.75	2.1E-12	-2659	223052	300	López-Valverde [1990]
494	$CO_2(03^30) + N_2 \rightleftharpoons CO_2(10^00) + N_2$	3.75	2.1E-12	-2659	223052	300	López-Valverde [1990]
495	$CO_2(11^10) + N_2 \rightleftharpoons CO_2(02^00) + N_2$	3.75	2.1E-12	-2659	223052	300	López-Valverde [1990]
496	$CO_2(11^10) + N_2 \rightleftharpoons CO_2(02^20) + N_2$	3.75	2.1E-12	-2659	223052	300	López-Valverde [1990]
497	$CO_2(11^10) + N_2 \rightleftharpoons CO_2(10^00) + N_2$	3.75	2.1E-12	-2659	223052	300	López-Valverde [1990]
498	$CO_2(01^10) + CO \rightleftharpoons CO_2 + CO$	1.0	2.1E-12	-2659	223052	300	López-Valverde [1990]
499	$CO_2(02^00) + CO \rightleftharpoons CO_2(01^10) + CO$	2.5	2.1E-12	-2659	223052	300	López-Valverde [1990]
500	$CO_2(02^20) + CO \rightleftharpoons CO_2(01^10) + CO$	2.5	2.1E-12	-2659	223052	300	López-Valverde [1990]
501	$CO_2(10^00) + CO \rightleftharpoons CO_2(01^10) + CO$	2.5	2.1E-12	-2659	223052	300	López-Valverde [1990]
502	$CO_2(03^10) + CO \rightleftharpoons CO_2(02^00) + CO$	3.75	2.1E-12	-2659	223052	300	López-Valverde [1990]
503	$CO_2(03^10) + CO \rightleftharpoons CO_2(02^20) + CO$	3.75	2.1E-12	-2659	223052	300	López-Valverde [1990]
504	$CO_2(03^10) + CO \rightleftharpoons CO_2(10^00) + CO$	3.75	2.1E-12	-2659	223052	300	López-Valverde [1990]
505	$CO_2(03^30) + CO \rightleftharpoons CO_2(02^00) + CO$	3.75	2.1E-12	-2659	223052	300	López-Valverde [1990]
506	$CO_2(03^30) + CO \rightleftharpoons CO_2(02^20) + CO$	3.75	2.1E-12	-2659	223052	300	López-Valverde [1990]
507	$CO_2(03^30) + CO \rightleftharpoons CO_2(10^00) + CO$	3.75	2.1E-12	-2659	223052	300	López-Valverde [1990]
508	$CO_2(11^10) + CO \rightleftharpoons CO_2(02^00) + CO$	3.75	2.1E-12	-2659	223052	300	López-Valverde [1990]
509	$CO_2(11^10) + CO \rightleftharpoons CO_2(02^20) + CO$	3.75	2.1E-12	-2659	223052	300	López-Valverde [1990]
510	$CO_2(11^10) + CO \rightleftharpoons CO_2(10^00) + CO$	3.75	2.1E-12	-2659	223052	300	López-Valverde [1990]

E. KINETIC MODEL FOR ELECTRICAL DISCHARGES IN THE EARTH'S ATMOSPHERE

No.	Reaction	g	h	i	j	T_g (K)	Ref.
511	$CO_2(01^1_0) + O \rightleftharpoons CO_2 + O$	1.0	3.0E-12			300	López-Valverde [1990]
512	$CO_2(02^0_0) + O \rightleftharpoons CO_2(01^1_0) + O$	2.0	3.0E-12			300	López-Valverde [1990]
513	$CO_2(02^2_0) + O \rightleftharpoons CO_2(01^1_0) + O$	2.0	3.0E-12			300	López-Valverde [1990]
514	$CO_2(10^0_0) + O \rightleftharpoons CO_2(01^1_0) + O$	2.0	3.0E-12			300	López-Valverde [1990]
515	$CO_2(03^1_0) + O \rightleftharpoons CO_2(02^0_0) + O$	3.4	3.0E-12			300	López-Valverde [1990]
516	$CO_2(03^1_0) + O \rightleftharpoons CO_2(02^2_0) + O$	3.4	3.0E-12			300	López-Valverde [1990]
517	$CO_2(03^1_0) + O \rightleftharpoons CO_2(10^0_0) + O$	3.4	3.0E-12			300	López-Valverde [1990]
518	$CO_2(03^3_0) + O \rightleftharpoons CO_2(02^0_0) + O$	3.4	3.0E-12			300	López-Valverde [1990]
519	$CO_2(03^3_0) + O \rightleftharpoons CO_2(02^2_0) + O$	3.4	3.0E-12			300	López-Valverde [1990]
520	$CO_2(03^3_0) + O \rightleftharpoons CO_2(10^0_0) + O$	3.4	3.0E-12			300	López-Valverde [1990]
521	$CO_2(11^1_0) + O \rightleftharpoons CO_2(02^0_0) + O$	3.4	3.0E-12			300	López-Valverde [1990]
522	$CO_2(11^1_0) + O \rightleftharpoons CO_2(02^2_0) + O$	3.4	3.0E-12			300	López-Valverde [1990]
523	$CO_2(11^1_0) + O \rightleftharpoons CO_2(10^0_0) + O$	3.4	3.0E-12			300	López-Valverde [1990]
524	$CO_2(10^0_1) + CO_2 \rightleftharpoons CO_2(02^0_1) + CO_2$	1.0	1.6E-12			300	Orr and Smith [1987]
525	$CO_2(10^0_1) + N_2 \rightleftharpoons CO_2(02^0_1) + N_2$	1.0	1.6E-12			300	Orr and Smith [1987]
526	$CO_2(10^0_1) + CO_2 \rightleftharpoons CO_2(02^2_1) + CO_2$	1.0	5.0E-12			300	Orr and Smith [1987]
527	$CO_2(10^0_1) + N_2 \rightleftharpoons CO_2(02^0_1) + N_2$	1.0	5.0E-12			300	Orr and Smith [1987]
528	$CO_2(02^2_0) + CO_2 \rightleftharpoons CO_2(02^0_1) + CO_2$	1.0	5.0E-12			300	Orr and Smith [1987]
529	$CO_2(02^2_0) + N_2 \rightleftharpoons CO_2(02^0_1) + N_2$	1.0	5.0E-12			300	Orr and Smith [1987]
530	$CO_2(10^0_1) + O_2 \rightleftharpoons O_2 + CO_2(02^0_1)$	1.0	2.0E-11			300	López-Puertas and Taylor [1989]
531	$CO_2(10^0_1) + O_2 \rightleftharpoons O_2 + CO_2(02^2_1)$	2.0	2.4E-12			300	López-Puertas and Taylor [1989]
532	$CO_2(02^2_1) + N_2 \rightleftharpoons O_2 + CO_2(02^0_1)$	1.0	2.4E-12			300	López-Puertas and Taylor [1989]
533	$CO_2(02^2_1) + O_2 \rightleftharpoons O_2 + CO_2(02^0_1)$	1.0	2.4E-12			300	López-Puertas and Taylor [1989]
534	$CO_2(00^0_1) + O_2 \rightleftharpoons O_2 + CO_2(03^1_0)$	1.0	2.3E-15	1.54E-10	76.75	300	López-Puertas et al. [1986]
535	$CO_2(00^0_1) + O_2 \rightleftharpoons O_2 + CO_2(03^3_0)$	1.0	2.3E-15	1.54E-10	76.75	300	López-Puertas et al. [1986]
536	$CO_2(00^0_1) + O_2 \rightleftharpoons O_2 + CO_2(11^1_0)$	1.0	2.3E-15	1.54E-10	76.75	300	López-Puertas et al. [1986]
537	$CO_2(00^0_1) + O_2 \rightleftharpoons O_2 + CO_2(02^0_0)$	1.0	2.3E-15	1.54E-10	76.75	300	López-Puertas et al. [1986]
538	$CO_2(00^0_1) + O_2 \rightleftharpoons O_2 + CO_2(02^2_0)$	1.0	2.3E-15	1.54E-10	76.75	300	López-Puertas et al. [1986]
539	$CO_2(00^0_1) + O_2 \rightleftharpoons O_2 + CO_2(10^0_0)$	1.0	2.3E-15	1.54E-10	76.75	300	López-Puertas et al. [1986]
540	$CO_2(00^0_1) + NO \rightleftharpoons NO + CO_2(11^1_0)$	1.09E-16					Bauer et al. [1987]
541	$CO_2(00^0_1) + N_2O \rightleftharpoons N_2O + CO_2(11^1_0)$	6.34E-16					Bauer et al. [1987]

E.10 Carbon dioxide kinetics

E.10.2 Vibrational-Vibrational processes (VV)

Table E.20: Vibrational-Vibrational processes

No.	Reaction	g	h	i	j	$T_g(\text{K})$	Ref.
542	$CO_2(02^00) + CO_2 \rightleftharpoons CO_2(01^10) + CO_2(01^10)$	1.0	2.5E-11			300	Orr and Smith [1987]
543	$CO_2(02^20) + CO_2 \rightleftharpoons CO_2(01^10) + CO_2(01^10)$	1.0	2.5E-11			300	Orr and Smith [1987]
544	$CO_2(10^00) + CO_2 \rightleftharpoons CO_2(01^10) + CO_2(01^10)$	1.0	2.5E-11			300	Orr and Smith [1987]
545	$CO_2(03^10) + CO_2 \rightleftharpoons CO_2(02^00) + CO_2(01^10)$	6.0	2.5E-11			300	López-Valverde [1990]
546	$CO_2(03^30) + CO_2 \rightleftharpoons CO_2(02^20) + CO_2(01^10)$	6.0	2.5E-11			300	López-Valverde [1990]
547	$CO_2(03^10) + CO_2 \rightleftharpoons CO_2(10^00) + CO_2(01^10)$	6.0	2.5E-11			300	López-Valverde [1990]
548	$CO_2(03^30) + CO_2 \rightleftharpoons CO_2(02^00) + CO_2(01^10)$	6.0	2.5E-11			300	López-Valverde [1990]
549	$CO_2(03^30) + CO_2 \rightleftharpoons CO_2(02^20) + CO_2(01^10)$	6.0	2.5E-11			300	López-Valverde [1990]
550	$CO_2(03^30) + CO_2 \rightleftharpoons CO_2(10^00) + CO_2(01^10)$	6.0	2.5E-11			300	López-Valverde [1990]
551	$CO_2(11^10) + CO_2 \rightleftharpoons CO_2(02^00) + CO_2(01^10)$	6.0	2.5E-11			300	López-Valverde [1990]
552	$CO_2(11^10) + CO_2 \rightleftharpoons CO_2(02^00) + CO_2(01^10)$	6.0	2.5E-11			300	López-Valverde [1990]
553	$CO_2(11^10) + CO_2 \rightleftharpoons CO_2(02^00) + CO_2(01^10)$	6.0	2.5E-11			300	López-Valverde [1990]
554	$CO_2(00^01) + CO_2 \rightleftharpoons CO_2(02^00) + CO_2(01^10)$	1.0	3.6E-13	-1660	176948	300	Lepoutre et al. [1977]
555	$CO_2(00^01) + CO_2 \rightleftharpoons CO_2(02^20) + CO_2(01^10)$	1.0	3.6E-13	-1660	176948	300	Lepoutre et al. [1977]
556	$CO_2(00^01) + CO_2 \rightleftharpoons CO_2(10^00) + CO_2(01^10)$	1.0	3.6E-13	-1660	176948	300	Lepoutre et al. [1977]
557	$CO_2(01^11) + N_2 \rightleftharpoons N_2(v_1) + CO_2(01^10)$	1.0	5.0E-13	-0.5		300	Inoue and Tsuchiya [1975]
558	$CO_2(02^01) + N_2 \rightleftharpoons N_2(v_1) + CO_2(02^00)$	1.0	5.0E-13	-0.5		300	Inoue and Tsuchiya [1975]
559	$CO_2(02^21) + N_2 \rightleftharpoons N_2(v_1) + CO_2(02^20)$	1.0	5.0E-13	-0.5		300	Inoue and Tsuchiya [1975]
560	$CO_2(10^01) + N_2 \rightleftharpoons N_2(v_1) + CO_2(10^00)$	1.0	5.0E-13	-0.5		300	Inoue and Tsuchiya [1975]
561	$CO_2(03^11) + N_2 \rightleftharpoons N_2(v_1) + CO_2(03^10)$	1.0	5.0E-13	-0.5		300	Inoue and Tsuchiya [1975]
562	$CO_2(03^31) + N_2 \rightleftharpoons N_2(v_1) + CO_2(03^30)$	1.0	5.0E-13	-0.5		300	Inoue and Tsuchiya [1975]
563	$CO_2(11^11) + N_2 \rightleftharpoons N_2(v_1) + CO_2(11^10)$	1.0	5.0E-13	-0.5		300	Inoue and Tsuchiya [1975]
564	$CO_2(00^02) + N_2 \rightleftharpoons N_2(v_1) + CO_2(00^01)$	1.0	5.0E-13	-0.5		300	Inoue and Tsuchiya [1975]
565	$CO_2(04^01) + N_2 \rightleftharpoons N_2(v_1) + CO_2(04^00)$	1.0	5.0E-13	-0.5		300	Inoue and Tsuchiya [1975]
566	$CO_2(04^21) + N_2 \rightleftharpoons N_2(v_1) + CO_2(04^20)$	1.0	5.0E-13	-0.5		300	Inoue and Tsuchiya [1975]
567	$CO_2(04^41) + N_2 \rightleftharpoons N_2(v_1) + CO_2(04^40)$	1.0	5.0E-13	-0.5		300	Inoue and Tsuchiya [1975]
568	$CO_2(12^01) + N_2 \rightleftharpoons N_2(v_1) + CO_2(12^00)$	1.0	5.0E-13	-0.5		300	Inoue and Tsuchiya [1975]
569	$CO_2(12^21) + N_2 \rightleftharpoons N_2(v_1) + CO_2(12^20)$	1.0	5.0E-13	-0.5		300	Inoue and Tsuchiya [1975]
570	$CO_2(20^01) + N_2 \rightleftharpoons N_2(v_1) + CO_2(20^00)$	1.0	5.0E-13	-0.5		300	Inoue and Tsuchiya [1975]
571	$CO_2 + N_2(v_1) \rightleftharpoons N_2 + CO_2(00^01)$	3.96E-13	1.0				Moore et al. [1967]
572	$CO_2 + N_2(v_2) \rightleftharpoons N_2(v_1) + CO_2(00^01)$	3.96E-13	1.0				Moore et al. [1967]
573	$CO_2 + N_2(v_3) \rightleftharpoons N_2(v_2) + CO_2(00^01)$	3.96E-13	1.0				Moore et al. [1967]
574	$CO_2 + N_2(v_4) \rightleftharpoons N_2(v_3) + CO_2(00^01)$	3.96E-13	1.0				Moore et al. [1967]
575	$CO_2 + N_2(v_5) \rightleftharpoons N_2(v_4) + CO_2(00^01)$	3.96E-13	1.0				Moore et al. [1967]
576	$CO_2 + N_2(v_6) \rightleftharpoons N_2(v_5) + CO_2(00^01)$	3.96E-13	1.0				Moore et al. [1967]
577	$CO_2 + N_2(v_7) \rightleftharpoons N_2(v_6) + CO_2(00^01)$	3.96E-13	1.0				Moore et al. [1967]
578	$CO_2 + N_2(v_8) \rightleftharpoons N_2(v_7) + CO_2(00^01)$	3.96E-13	1.0				Moore et al. [1967]

E. KINETIC MODEL FOR ELECTRICAL DISCHARGES IN THE EARTH'S ATMOSPHERE

E.11 Ionization processes due to galactic cosmic rays

Table E.21: Galactic cosmic rays ionization

No.	Reaction	k	l	Ref.
579	$N_2 + h\nu \rightarrow N_2^+ + e$	5.85E-18	crc	Yelinov et al. [2009]
580	$O_2 + h\nu \rightarrow O_2^+ + e$	1.54E-18	crc	Yelinov et al. [2009]
581	$N_2 + h\nu \rightarrow N^+ + N + e$	1.85E-18	crc	Yelinov et al. [2009]
582	$O_2 + h\nu \rightarrow O^+ + O + e$	7.6E-19	crc	Yelinov et al. [2009]

E.12 Rotational deexcitation processes

Table E.22: Rotational deexcitation processes

No.	Reaction	k	l	Ref.
583	$N_2(rot) + N_2 \rightarrow N_2 + N_2$	1.02E-10		Capitelli et al. [2000]
584	$O_2(rot) + O_2 \rightarrow O_2 + O_2$	5.35E-10		Capitelli et al. [2000]

E.13 Radiative decay processes

Table E.23: Radiative decay processes

No.	Reaction	A(s ⁻¹)	Ref.
585	$CO_2(01^10) \rightarrow CO_2 + h\nu$	1.564	García-Comas
586	$CO_2(02^00) \rightarrow CO_2(01^10) + h\nu$	1.21	García-Comas
587	$CO_2(02^20) \rightarrow CO_2(01^10) + h\nu$	3.153	García-Comas
588	$CO_2(10^00) \rightarrow CO_2(01^10) + h\nu$	2.08	García-Comas
589	$CO_2(03^10) \rightarrow CO_2(02^00) + h\nu$	2.052	García-Comas
590	$CO_2(03^10) \rightarrow CO_2(02^20) + h\nu$	0.529	García-Comas
591	$CO_2(03^10) \rightarrow CO_2(10^00) + h\nu$	0.0302	García-Comas
592	$CO_2(03^10) \rightarrow CO_2 + h\nu$	9.644E-4	García-Comas
593	$CO_2(03^30) \rightarrow CO_2(02^20) + h\nu$	4.778	García-Comas
594	$CO_2(03^30) \rightarrow CO_2 + h\nu$	2.381E-7	García-Comas
595	$CO_2(11^10) \rightarrow CO_2 + h\nu$	6.6E-3	García-Comas
596	$CO_2(11^10) \rightarrow CO_2(02^00) + h\nu$	0.0152	García-Comas
597	$CO_2(11^10) \rightarrow CO_2(02^20) + h\nu$	1.202	García-Comas
598	$CO_2(11^10) \rightarrow CO_2(10^00) + h\nu$	2.547	García-Comas
599	$CO_2(00^01) \rightarrow CO_2(02^00) + h\nu$	0.2	García-Comas
600	$CO_2(00^01) \rightarrow CO_2 + h\nu$	450.0	García-Comas
601	$CO_2(00^01) \rightarrow CO_2(10^00) + h\nu$	0.35	García-Comas
602	$CO_2(04^00) \rightarrow CO_2(01^10) + h\nu$	8.866E-4	García-Comas
603	$CO_2(04^00) \rightarrow CO_2(03^10) + h\nu$	2.746	García-Comas
604	$CO_2(04^00) \rightarrow CO_2(11^10) + h\nu$	5.03E-3	García-Comas
605	$CO_2(04^00) \rightarrow CO_2(00^01) + h\nu$	3.073E-6	García-Comas
606	$CO_2(04^20) \rightarrow CO_2(01^10) + h\nu$	1.469E-3	García-Comas
607	$CO_2(04^20) \rightarrow CO_2(03^10) + h\nu$	3.472	García-Comas
608	$CO_2(04^20) \rightarrow CO_2(03^30) + h\nu$	4.982E-1	García-Comas
609	$CO_2(04^20) \rightarrow CO_2(01^11) + h\nu$	1.575E-2	García-Comas
610	$CO_2(12^00) \rightarrow CO_2(01^10) + h\nu$	2.275E-4	García-Comas
611	$CO_2(12^00) \rightarrow CO_2(03^10) + h\nu$	1.343	García-Comas

E. KINETIC MODEL FOR ELECTRICAL DISCHARGES IN THE EARTH'S ATMOSPHERE

No.	Reaction	A(s ⁻¹)	Ref.
612	$CO_2(12^0_0) \rightarrow CO_2(11^1_0) + h\nu$	7.013E-1	García-Comas
613	$CO_2(12^0_0) \rightarrow CO_2(00^0_1) + h\nu$	1.878E-4	García-Comas
614	$CO_2(04^4_0) \rightarrow CO_2(03^3_0) + h\nu$	5.866	García-Comas
615	$CO_2(12^2_0) \rightarrow CO_2(01^1_0) + h\nu$	2.293E-2	García-Comas
616	$CO_2(12^2_0) \rightarrow CO_2(03^1_0) + h\nu$	6.103E-2	García-Comas
617	$CO_2(12^2_0) \rightarrow CO_2(03^3_0) + h\nu$	9.958E-2	García-Comas
618	$CO_2(12^2_0) \rightarrow CO_2(11^1_0) + h\nu$	3.949	García-Comas
619	$CO_2(20^0_0) \rightarrow CO_2(01^1_0) + h\nu$	2.948E-2	García-Comas
620	$CO_2(20^0_0) \rightarrow CO_2(03^1_0) + h\nu$	3.272E-2	García-Comas
621	$CO_2(20^0_0) \rightarrow CO_2(11^1_0) + h\nu$	4.266	García-Comas
622	$CO_2(01^1_1) \rightarrow CO_2(01^1_0) + h\nu$	4.117E+2	García-Comas
623	$CO_2(01^1_1) \rightarrow CO_2(03^1_0) + h\nu$	4.398E-1	García-Comas
624	$CO_2(01^1_1) \rightarrow CO_2(11^1_0) + h\nu$	3.565E-1	García-Comas
625	$CO_2(01^1_1) \rightarrow CO_2(00^0_1) + h\nu$	1.451	García-Comas
626	$CO_2(02^0_1) \rightarrow CO_2 + h\nu$	1.088E+1	García-Comas
627	$CO_2(02^0_1) \rightarrow CO_2(02^0_0) + h\nu$	4.008E+2	García-Comas
628	$CO_2(02^0_1) \rightarrow CO_2(10^0_0) + h\nu$	4.008E-1	García-Comas
629	$CO_2(02^0_1) \rightarrow CO_2(04^0_0) + h\nu$	7.379E-1	García-Comas
630	$CO_2(02^0_1) \rightarrow CO_2(12^0_0) + h\nu$	4.318E-1	García-Comas
631	$CO_2(02^0_1) \rightarrow CO_2(20^0_0) + h\nu$	9.068E-3	García-Comas
632	$CO_2(02^0_1) \rightarrow CO_2(01^1_0) + h\nu$	1.263	García-Comas
633	$CO_2(02^2_1) \rightarrow CO_2 + h\nu$	3.963E-4	García-Comas
634	$CO_2(02^2_1) \rightarrow CO_2(02^2_0) + h\nu$	3.989E+2	García-Comas
635	$CO_2(02^2_1) \rightarrow CO_2(04^2_0) + h\nu$	4.325E-1	García-Comas
636	$CO_2(02^2_1) \rightarrow CO_2(12^2_0) + h\nu$	3.262E-1	García-Comas
637	$CO_2(02^2_1) \rightarrow CO_2(01^1_1) + h\nu$	2.877	García-Comas
638	$CO_2(10^0_1) \rightarrow CO_2 + h\nu$	1.735E+1	García-Comas
639	$CO_2(10^0_1) \rightarrow CO_2(02^0_0) + h\nu$	1.704E-1	García-Comas
640	$CO_2(10^0_1) \rightarrow CO_2(10^0_0) + h\nu$	3.98E+2	García-Comas
641	$CO_2(10^0_1) \rightarrow CO_2(04^0_0) + h\nu$	9.511E-4	García-Comas
642	$CO_2(10^0_1) \rightarrow CO_2(12^0_0) + h\nu$	6.237E-1	García-Comas
643	$CO_2(10^0_1) \rightarrow CO_2(20^0_0) + h\nu$	5.543E-1	García-Comas
644	$CO_2(10^0_1) \rightarrow CO_2(01^1_1) + h\nu$	1.639	García-Comas

E.13 Radiative decay processes

No.	Reaction	A(s ⁻¹)	Ref.
645	$CO_2(03^11) \rightarrow CO_2(01^10) + h\nu$	1.008E+1	García-Comas
646	$CO_2(03^11) \rightarrow CO_2(03^10) + h\nu$	3.907E+2	García-Comas
647	$CO_2(03^11) \rightarrow CO_2(11^10) + h\nu$	1.988E-1	García-Comas
648	$CO_2(03^11) \rightarrow CO_2(00^01) + h\nu$	9.012E-4	García-Comas
649	$CO_2(03^11) \rightarrow CO_2(02^01) + h\nu$	1.91	García-Comas
650	$CO_2(03^11) \rightarrow CO_2(02^21) + h\nu$	5.551E-1	García-Comas
651	$CO_2(03^11) \rightarrow CO_2(10^01) + h\nu$	2.827E-2	García-Comas
652	$CO_2(03^31) \rightarrow CO_2(03^30) + h\nu$	3.847E+2	García-Comas
653	$CO_2(03^31) \rightarrow CO_2(02^21) + h\nu$	4.135	García-Comas
654	$CO_2(11^11) \rightarrow CO_2(01^10) + h\nu$	1.752E+1	García-Comas
655	$CO_2(11^11) \rightarrow CO_2(03^10) + h\nu$	4.651E-2	García-Comas
656	$CO_2(11^11) \rightarrow CO_2(11^10) + h\nu$	3.869E+2	García-Comas
657	$CO_2(11^11) \rightarrow CO_2(00^01) + h\nu$	6.242E-3	García-Comas
658	$CO_2(11^11) \rightarrow CO_2(02^01) + h\nu$	1.063E-1	García-Comas
659	$CO_2(11^11) \rightarrow CO_2(02^21) + h\nu$	2.987E-1	García-Comas
660	$CO_2(11^11) \rightarrow CO_2(10^01) + h\nu$	2.104	García-Comas
661	$CO_2(00^02) \rightarrow CO_2(01^10) + h\nu$	7.307E-4	García-Comas
662	$CO_2(00^02) \rightarrow CO_2(00^01) + h\nu$	4.126E+2	García-Comas
663	$CO_2(00^02) \rightarrow CO_2(02^01) + h\nu$	4.109E-1	García-Comas
664	$CO_2(00^02) \rightarrow CO_2(10^01) + h\nu$	4.063E-1	García-Comas
665	$CO_2(04^01) \rightarrow CO_2 + h\nu$	1.567E-1	García-Comas
666	$CO_2(04^01) \rightarrow CO_2(02^00) + h\nu$	1.705E+1	García-Comas
667	$CO_2(04^01) \rightarrow CO_2(10^00) + h\nu$	1.498E-1	García-Comas
668	$CO_2(04^01) \rightarrow CO_2(04^00) + h\nu$	3.814E+2	García-Comas
669	$CO_2(04^01) \rightarrow CO_2(12^00) + h\nu$	4.571E-1	García-Comas
670	$CO_2(04^01) \rightarrow CO_2(20^00) + h\nu$	1.056E-2	García-Comas
671	$CO_2(04^01) \rightarrow CO_2(01^11) + h\nu$	1.242E-3	García-Comas
672	$CO_2(04^01) \rightarrow CO_2(03^11) + h\nu$	2.768	García-Comas
673	$CO_2(04^01) \rightarrow CO_2(11^11) + h\nu$	4.822E-3	García-Comas
674	$CO_2(04^21) \rightarrow CO_2 + h\nu$	3.247E-5	García-Comas
675	$CO_2(04^21) \rightarrow CO_2(02^20) + h\nu$	9.901	García-Comas
676	$CO_2(04^21) \rightarrow CO_2(04^20) + h\nu$	4.774E+2	García-Comas
677	$CO_2(04^21) \rightarrow CO_2(12^20) + h\nu$	1.129E-1	García-Comas

E. KINETIC MODEL FOR ELECTRICAL DISCHARGES IN THE EARTH'S ATMOSPHERE

No.	Reaction	A(s ⁻¹)	Ref.
678	$CO_2(04^21) \rightarrow CO_2(01^11) + h\nu$	1.006E-3	García-Comas
679	$CO_2(04^21) \rightarrow CO_2(03^11) + h\nu$	3.351	García-Comas
680	$CO_2(04^21) \rightarrow CO_2(03^31) + h\nu$	4.968E-1	García-Comas
681	$CO_2(04^21) \rightarrow CO_2(11^11) + h\nu$	1.382E-2	García-Comas
682	$CO_2(04^41) \rightarrow CO_2(04^40) + h\nu$	3.695E+2	García-Comas
683	$CO_2(04^41) \rightarrow CO_2(03^31) + h\nu$	5.664	García-Comas
684	$CO_2(12^01) \rightarrow CO_2 + h\nu$	7.169E-1	García-Comas
685	$CO_2(12^01) \rightarrow CO_2(02^00) + h\nu$	2.138E+1	García-Comas
686	$CO_2(12^01) \rightarrow CO_2(10^00) + h\nu$	1.486E+1	García-Comas
687	$CO_2(12^01) \rightarrow CO_2(04^00) + h\nu$	1.347E-1	García-Comas
688	$CO_2(12^01) \rightarrow CO_2(12^00) + h\nu$	3.75E+2	García-Comas
689	$CO_2(12^01) \rightarrow CO_2(20^00) + h\nu$	4.229E-1	García-Comas
690	$CO_2(12^01) \rightarrow CO_2(03^11) + h\nu$	1.194	García-Comas
691	$CO_2(12^01) \rightarrow CO_2(11^11) + h\nu$	7.268E-1	García-Comas
692	$CO_2(12^21) \rightarrow CO_2 + h\nu$	3.97E-5	García-Comas
693	$CO_2(12^21) \rightarrow CO_2(02^20) + h\nu$	1.801E+1	García-Comas
694	$CO_2(12^21) \rightarrow CO_2(04^20) + h\nu$	1.308E-2	García-Comas
695	$CO_2(12^21) \rightarrow CO_2(12^20) + h\nu$	3.747E+2	García-Comas
696	$CO_2(12^21) \rightarrow CO_2(01^11) + h\nu$	2.426E-2	García-Comas
697	$CO_2(12^21) \rightarrow CO_2(03^11) + h\nu$	6.489E-2	García-Comas
698	$CO_2(12^21) \rightarrow CO_2(03^31) + h\nu$	9.08E-1	García-Comas
699	$CO_2(12^21) \rightarrow CO_2(11^11) + h\nu$	3.76	García-Comas
700	$CO_2(20^01) \rightarrow CO_2 + h\nu$	2.363E-1	García-Comas
701	$CO_2(20^01) \rightarrow CO_2(02^00) + h\nu$	3.832E-1	García-Comas
702	$CO_2(20^01) \rightarrow CO_2(10^00) + h\nu$	2.877E+1	García-Comas
703	$CO_2(20^01) \rightarrow CO_2(12^00) + h\nu$	1.128E-1	García-Comas
704	$CO_2(20^01) \rightarrow CO_2(20^00) + h\nu$	3.749E+2	García-Comas
705	$CO_2(20^01) \rightarrow CO_2(01^11) + h\nu$	3.261E-2	García-Comas
706	$CO_2(20^01) \rightarrow CO_2(03^11) + h\nu$	3.443E-2	García-Comas
707	$CO_2(20^01) \rightarrow CO_2(11^11) + h\nu$	3.433	García-Comas
708	$N_2(A^3\Sigma_u^+) \rightarrow N_2(X^1\Sigma_g^+) + h\nu$	0.5	Capitelli et al. [2000]
709	$N_2(B^3\Pi_g) \rightarrow N_2(A^3\Sigma_u^+) + h\nu$	1.34E+5	Capitelli et al. [2000]
710	$N_2(C^3\Pi_u) \rightarrow N_2(B^3\Pi_g) + h\nu$	2.45E+7	Capitelli et al. [2000]

No.	Reaction	A(s ⁻¹)	Ref.
711	$N_2(W^3\Delta_u) \rightarrow N_2(X^1\Sigma_g^+) + h\nu$	0.154	Capitelli et al. [2000]
712	$N_2(B'^3\Sigma_u^-) \rightarrow N_2(B^3\Pi_g) + h\nu$	3.4E+4	Capitelli et al. [2000]
713	$N_2(E^3\Sigma_g^+) \rightarrow N_2(A^3\Sigma_u^+) + h\nu$	1.2E+3	Capitelli et al. [2000]
714	$N_2(E^3\Sigma_g^+) \rightarrow N_2(B^3\Pi_g) + h\nu$	3.46E+2	Capitelli et al. [2000]
715	$N_2(E^3\Sigma_g^+) \rightarrow N_2(C^3\Pi_u) + h\nu$	1.73E+3	Capitelli et al. [2000]
716	$N_2(a''^1\Sigma_g^+) \rightarrow N_2(X^1\Sigma_g^+) + h\nu$	2.86E+5	Kam and Pipkin [1991]
717	$N_2(a'^1\Sigma_u^-) \rightarrow N_2(X^1\Sigma_g^+) + h\nu$	1.0E+2	Capitelli et al. [2000]
718	$N_2(a^1\Pi_g) \rightarrow N_2(X^1\Sigma_g^+) + h\nu$	8.55E+3	Capitelli et al. [2000]
719	$N_2(a^1\Pi_g) \rightarrow N_2(a'^1\Sigma_u^-) + h\nu$	1.3E+2	Capitelli et al. [2000]
720	$N_2(w^1\Delta_u) \rightarrow N_2(a^1\Pi_g) + h\nu$	1.51E+3	Capitelli et al. [2000]
721	$N_2^+(A^2\Pi_u) \rightarrow N_2^+(X^2\Sigma_g^+) + h\nu$	4.64E+4	Gilmore et al. [1992]
722	$N_2^+(B^2\Sigma_u^+) \rightarrow N_2^+(X^2\Sigma_g^+) + h\nu$	1.14E+7	Gilmore et al. [1992]
723	$NO(A^2\Sigma^+) \rightarrow NO(X^2\Pi_r) + h\nu$	5.0E+6	Radzig and Smirnov [1985]
724	$O(^1D) \rightarrow O + h\nu$	5.1E-3	Wiese et al. [1966]
725	$O(^1S) \rightarrow O(^1D) + h\nu$	1.34	Wiese et al. [1966]
726	$O_2(A^3\Sigma_u^+) \rightarrow O_2(X^3\Sigma_g^-) + h\nu$	1.1E+1	Bates [1988]
727	$O_2(a^1\Delta_g) \rightarrow O_2(X^3\Sigma_g^-) + h\nu$	3.307E-4	Krupenie [1972]
728	$O_2(b^1\Sigma_g^+) \rightarrow O_2(X^3\Sigma_g^-) + h\nu$	8.2E-2	Krupenie [1972]
729	$O_2(b^1\Sigma_g^+) \rightarrow O_2(a^1\Delta_g) + h\nu$	1.7E-3	Krupenie [1972]

E. KINETIC MODEL FOR ELECTRICAL DISCHARGES IN THE EARTH'S ATMOSPHERE

E.14 Processes only included in the model of halos

Table E.24: Processes only included in the model of halos

No.	Reaction	Rate	Ref.
730	$N + NO \rightarrow N_2 + O$	$k = 3.51\text{E-}11 \exp(-49.84/T_g)$	Linstrom and Mallard [2015]
731	$N_2(a^1\Pi_g) + N_2(a^1\Pi_g) \rightarrow N_2 + N_2^+ + e$	$k = 2.0\text{E-}10$	Starikovskaia et al. [2001]
732	$N_2^+(A^2\Pi_u) + N_2 \rightarrow N_2^+ + N_2$	$k = 7.5\text{E-}10$	Piper et al. [1985]
733	$N_2(rot) + N_2 \rightleftharpoons N_2 + N_2$	$k = 7.77\text{E-}7$	Capitelli et al. [2000]
734	$N_2(rot) + O_2 \rightleftharpoons N_2 + O_2$	$k = 7.77\text{E-}7$	Capitelli et al. [2000]
735	$O_2(rot) + N_2 \rightleftharpoons O_2 + N_2$	$k = 5.45\text{E-}7$	Capitelli et al. [2000]
736	$O_2(rot) + O_2 \rightleftharpoons O_2 + O_2$	$k = 5.45\text{E-}7$	Capitelli et al. [2000]

Appendix F

Kinetic model for electrical discharges in Saturn's atmosphere

F.1 Species

Table F.1: Ground neutrals considered

Ground neutrals
He
H, H ₂

Table F.2: Excited neutrals considered

Excited neutrals
He(2s ² ³ S), He ₂ (a ³ Σ _u ⁺)
H(2s ² S), H(2p ² P), H(3), H(4), H(5)
H ₂ (B ¹ Σ _u ⁺ , c ³ Π _u , a ³ Σ _g ⁺ , C ¹ Π _u , d ³ Π _u)
H ₂ (X ¹ Σ _g ⁺ , v = 1, ..., 9)

F. KINETIC MODEL FOR ELECTRICAL DISCHARGES IN SATURN'S ATMOSPHERE

Table F.3: Electrons and negative ions considered

Negative ions
e^-
H^{-1}

Table F.4: Positive ions considered

Positive ions
HeH^+
He^+, He_2^+
H^+, H_2^+, H_3^+

F.2 Reaction rates

The rate coefficients for the direct electron-impact collisions for which we have the corresponding cross sections, are evaluated using the calculated EEDF and the equation (E.3). When the cross section is not available, the rates of the electronic processes are given as

$$k_e = a \times T_e^b \times \exp(-c/T_e) \quad (F.1)$$

where T_e is the electron temperature in eV. The rate coefficients of the kinetic processes involving heavy species (neutrals and ions) are parametrized as

$$k_h = d \times \left(\frac{T_g}{300}\right)^e \times \exp(-f/T_g) \quad (F.2)$$

where T_g is the ambient gas temperature in K. The units of $k_{e,h}$ are $\text{cm}^3 \text{s}^{-1}$ and $\text{cm}^6 \text{s}^{-1}$ for two- and three-body reactions, respectively. For radiative decay processes, the magnitudes A (in s^{-1}), λ (in nm) and κ are the Einstein coefficient of spontaneous radiative de-excitation, the emission wavelength and the optical thickness ($0 \leq \kappa \leq 1$) assumed.

F.3 EEDF and cross section dependent processes

Table F.5: EEDF and cross section dependent processes

No.	Reaction	Ref.
1	$He(1S) + e \rightleftharpoons He(3S) + e$	Lis
2	$He(1S) + e \rightarrow He^+ + e + e$	Lis
3	$H_2(X^1\Sigma_g^+) + e \rightarrow H_2(B^1\Sigma_u^+) + e$	Phelps [b]
4	$H_2(X^1\Sigma_g^+) + e \rightarrow H_2(c^3\Pi_u) + e$	Phelps [b]
5	$H_2(X^1\Sigma_g^+) + e \rightarrow H_2(a^3\Sigma_g^+) + e$	Phelps [b]
6	$H_2(X^1\Sigma_g^+) + e \rightarrow H_2(C^1\Pi_u) + e$	Phelps [b]
7	$H_2(X^1\Sigma_g^+) + e \rightarrow H_2(d^3\Pi_u) + e$	Phelps [b]
8	$H_2(X^1\Sigma_g^+) + e \rightarrow H(1s^2S) + H(1s^2S) + e$	Phelps [b]
9	$H_2(X^1\Sigma_g^+) + e \rightarrow H(2s^2S) + H(1s^2S) + e$	Phelps [b]
10	$H_2(X^1\Sigma_g^+) + e \rightarrow H(2p^2P) + H(1s^2S) + e$	Phelps [b]
11	$H_2(X^1\Sigma_g^+) + e \rightarrow H(3) + H(1s^2S) + e$	Phelps [b]
12	$H_2(X^1\Sigma_g^+) + e \rightarrow H(4) + H(1s^2S) + e$	H2L
13	$H_2(X^1\Sigma_g^+) + e \rightarrow H(5) + H(1s^2S) + e$	H2L
14	$H_2(X^1\Sigma_g^+) + e \rightarrow H_2^+ + e + e$	Phelps [b]
15	$H_2(B^1\Sigma_u^+) + e \rightarrow H_2^+ + e + e$	The same CS as used in reaction (14)
16	$H_2(c^3\Pi_u) + e \rightarrow H_2^+ + e + e$	The same CS as used in reaction (14)
17	$H_2(a^3\Sigma_g^+) + e \rightarrow H_2^+ + e + e$	The same CS as used in reaction (14)
18	$H_2(C^1\Pi_u) + e \rightarrow H_2^+ + e + e$	The same CS as used in reaction (14)
19	$H_2(d^3\Pi_u) + e \rightarrow H_2^+ + e + e$	The same CS as used in reaction (14)
20	$H_2(X^1\Sigma_g^+, v=0) + e \rightleftharpoons H_2(X^1\Sigma_g^+, v=1) + e + e$	Phelps [b]
21	$H_2(X^1\Sigma_g^+, v=0) + e \rightleftharpoons H_2(X^1\Sigma_g^+, v=2) + e + e$	Phelps [b]
22	$H_2(X^1\Sigma_g^+, v=0) + e \rightleftharpoons H_2(X^1\Sigma_g^+, v=3) + e + e$	Phelps [b]
23	$H_2(X^1\Sigma_g^+, v=1) + e \rightleftharpoons H_2(X^1\Sigma_g^+, v=2) + e + e$	The same CS as used in reaction (20)
24	$H_2(X^1\Sigma_g^+, v=2) + e \rightleftharpoons H_2(X^1\Sigma_g^+, v=3) + e + e$	The same CS as used in reaction (20)
25	$H_2(X^1\Sigma_g^+, v=3) + e \rightleftharpoons H_2(X^1\Sigma_g^+, v=4) + e + e$	The same CS as used in reaction (20)
26	$H_2(X^1\Sigma_g^+, v=4) + e \rightleftharpoons H_2(X^1\Sigma_g^+, v=5) + e + e$	The same CS as used in reaction (20)
27	$H_2(X^1\Sigma_g^+, v=5) + e \rightleftharpoons H_2(X^1\Sigma_g^+, v=6) + e + e$	The same CS as used in reaction (20)
28	$H_2(X^1\Sigma_g^+, v=6) + e \rightleftharpoons H_2(X^1\Sigma_g^+, v=7) + e + e$	The same CS as used in reaction (20)
29	$H_2(X^1\Sigma_g^+, v=7) + e \rightleftharpoons H_2(X^1\Sigma_g^+, v=8) + e + e$	The same CS as used in reaction (20)
30	$H_2(X^1\Sigma_g^+, v=8) + e \rightleftharpoons H_2(X^1\Sigma_g^+, v=9) + e + e$	The same CS as used in reaction (20)
31	$H(1s^2S) + e \rightarrow H(2s^2S) + e$	HLi
32	$H(1s^2S) + e \rightarrow H(2p^2P) + e$	HLi
33	$H(1s^2S) + e \rightarrow H(3) + e$	HLi
34	$H(1s^2S) + e \rightarrow H(4) + e$	HLi
35	$H(1s^2S) + e \rightarrow H(5) + e$	HLi
36	$H_2(X^1\Sigma_g^+, v=0) + e \rightarrow H + H^-$	Bardsley and Wadehra [1979]
37	$H_2(X^1\Sigma_g^+, v=1) + e \rightarrow H + H^-$	Bardsley and Wadehra [1979]
38	$H_2(X^1\Sigma_g^+, v=2) + e \rightarrow H + H^-$	Bardsley and Wadehra [1979]
39	$H_2(X^1\Sigma_g^+, v=3) + e \rightarrow H + H^-$	Bardsley and Wadehra [1979]
40	$H_2(X^1\Sigma_g^+, v=4) + e \rightarrow H + H^-$	Bardsley and Wadehra [1979]
41	$H_2(X^1\Sigma_g^+, v=5) + e \rightarrow H + H^-$	Bardsley and Wadehra [1979]
42	$H_2(X^1\Sigma_g^+, v=6) + e \rightarrow H + H^-$	Bardsley and Wadehra [1979]
43	$H_2(X^1\Sigma_g^+, v=7) + e \rightarrow H + H^-$	Bardsley and Wadehra [1979]

F. KINETIC MODEL FOR ELECTRICAL DISCHARGES IN SATURN'S ATMOSPHERE

No.	Reaction	Ref.
44	$H_2(X^1\Sigma_g^+, v=8) + e \rightarrow H + H^-$	Bardsley and Wadehra [1979]
45	$H_2(X^1\Sigma_g^+, v=9) + e \rightarrow H + H^-$	Bardsley and Wadehra [1979]
46	$H(1s^2S) + e \rightarrow H^+ + e + e$	Bray and Ralchenko
47	$H(2s^2S) + e \rightarrow H^+ + e + e$	The same CS as used in reaction (46)
48	$H(2p^2P) + e \rightarrow H^+ + e + e$	The same CS as used in reaction (46)

F.4 Electronic temperature dependent processes

F.4.1 Ionization process

Table F.6: Ionization process

No.	Reaction	a	b	c	Ref.
49	$He_2^* + e \rightarrow He_2^+ + e + e$	9.75E-10	0.71	3.4	Liu et al. [2010]

F.4.2 Dissociation processes

Table F.7: Dissociation processes

No.	Reaction	a	b	c	Ref.
50	$H_2 + e \rightarrow H + H + e$	1.7527E-7	-1.2366	12.5924	Méndez et al. [2006]
51	$H_2^+ + e \rightarrow H^+ + H + e$	1.0702E-7	0.04876	9.69028	Méndez et al. [2006]
52	$H_2^+ + e \rightarrow H^+ + H^+ + e + e$	2.1202E-9	0.31394	23.2988	Méndez et al. [2006]
53	$H_3^+ + e \rightarrow H_2^+ + H + e$	4.8462E-7	-0.04975	19.1656	Méndez et al. [2006]
54	$He_2(a^3\Sigma_u^+) + e \rightarrow He + He + e$	3.8E-9			Liu et al. [2010]

F.4.3 Attachment and dissociative attachment processes

Table F.8: Attachment and dissociative attachment processes

No.	Reaction	a	b	c	Ref.
55	$H + e \rightarrow H^-$	3.46E-16	0.5		Liu et al. [2010]
56	$He_2^+ + e \rightarrow H^+ + H^-$	2.17E-10	-0.2	0.2	Liu et al. [2010]

F.4.4 Excitation/De-excitation processes

Table F.9: Excitation/de-excitation processes

No.	Reaction	a	b	c	Ref.
57	$H(2s^2S) + e \rightarrow H(2p^2P) + e$	6.0E-5			Seaton [1955]
58	$H(2p^2P) + e \rightarrow H(2s^2S) + e$	2.0E-5			Seaton [1955]
59	$H(2s^2S) + e \rightarrow H(3) + e$	1.68E-6	0.1013	1.9	Liu et al. [2010]
60	$H(2p^2P) + e \rightarrow H(3) + e$	1.68E-6	0.1013	1.9	Liu et al. [2010]

F.4.5 Detachment process

Table F.10: Detachment process

No.	Reaction	a	b	c	Ref.
61	$H^- + e \rightarrow H + e + e$	2.32E-8	2.0	0.13	Liu et al. [2010]

F. KINETIC MODEL FOR ELECTRICAL DISCHARGES IN SATURN'S ATMOSPHERE

F.4.6 Recombination and dissociative recombination processes

Table F.11: Recombination and dissociative recombination processes

No.	Reaction	a	b	c	Ref.
62	$H_2^+ + e \rightarrow H(3) + H$	5.33E-8	-0.4		Mitchell [1990]
63	$H_2^+ + e \rightarrow H(2s^2S) + H$	0.21E-8	-0.4		Mitchell [1990]
64	$H_3^+ + e \rightarrow H + H + H$	0.75E-8	-0.8		Mitchell [1990]
65	$H_3^+ + e \rightarrow H_2 + H$	0.75E-8	-0.8		Mitchell [1990]
66	$He_2^+ + e \rightarrow He(^3S) + He$	5.38E-11	-1		Alves et al. [1992]
67	$He^+ + e \rightarrow He(^3S)$	6.76E-13	-0.5		Liu et al. [2010]
68	$He^+ + e + e \rightarrow He(^3S) + e$	1.31E-28	-4.4		Liu et al. [2010]
69	$He^+ + He + e \rightarrow He(^3S) + He$	1.15E-30	-2.0		Liu et al. [2010]
70	$He_2^+ + e + e \rightarrow He(^3S) + He + e$	2.80E-20			Liu et al. [2010]
71	$He_2^+ + e + e \rightarrow He_2(a^3\Sigma_u^+) + e$	1.20E-21			Liu et al. [2010]
72	$He_2^+ + He + e \rightarrow He(^3S) + He + He$	3.50E-27	-0.8		Liu et al. [2010]
73	$He_2^+ + He + e \rightarrow He_2(a^3\Sigma_u^+) + He$	1.50E-27			Liu et al. [2010]
74	$HeH^+ + e \rightarrow He + H$	1.10E-9	-0.6		Liu et al. [2010]
75	$H^+ + e \rightarrow H$	2.62E-13	-0.		Liu et al. [2010]
76	$H^+ + e + e \rightarrow H + e$	8.8E-27	-4.5		Liu et al. [2010]
77	$H_3^+ + e \rightarrow H^+ + H + H + e$	1.8E-8	0.95	10.5	Liu et al. [2010]

F.5 Heavy particle kinetics

F.5.1 Ground neutral processes

Table F.12: Ground neutral processes

No.	Reaction	d	e	f	Ref.
78	$H + H \rightarrow H_2$	6.04E-33	-1		Liu et al. [2010]
79	$H + H + He \rightarrow H_2 + He$	5.80E-33	-1		Liu et al. [2010]
80	$H + H + H \rightarrow H_2 + H$	6.00E-31	-1		Liu et al. [2010]
81	$H + H + H_2 \rightarrow H_2 + H_2$	8.10E-33	-0.6		Liu et al. [2010]

F.5.2 Electronically excited neutral including Penning ionization processes

Table F.13: Electronically excited neutral including Penning ionization processes

No.	Reaction	d	e	f	Ref.
82	$H_2(d^3\Pi_u) + H_2 \rightarrow H_2(a^3\Sigma_g^+) + H_2$	1.2E-9			Bretagne et al. [1981]
83	$H_2(a^3\Sigma_g^+) + H_2 \rightarrow H_2 + H_2$	1.7E-10			Bretagne et al. [1981]
84	$He(^3S) + He + He \rightarrow He_2(a^3\Sigma_u^+) + He$	2.00E-34			Liu et al. [2010]
85	$He_2(a^3\Sigma_u^+) + H_2 \rightarrow He + He + H_2$	1.50E-15			Liu et al. [2010]
86	$He(^3S) + H_2 \rightarrow H(2p^2P) + H + He$	1.40E-11			Liu et al. [2010]
87	$He + H(3) \rightarrow H + He$	1.00E-11			Liu et al. [2010]
88	$H(2p^2P) + H_2 \rightarrow H + H + H$	2.1E-11			Liu et al. [2010]
89	$H(2s^2S) + H_2 \rightarrow H + H + H$	2.1E-11			Liu et al. [2010]
90	$H(3) + H_2 \rightarrow H + H_2$	2.0E-9			Liu et al. [2010]
91	$He(^3S) + He(^3S) \rightarrow He + He^+ + e$	8.7E-10	0.5		Liu et al. [2010]
92	$He(^3S) + He(^3S) \rightarrow He_2^+ + e$	1.03E-9	0.5		Liu et al. [2010]
93	$He(^3S) + He_2(a^3\Sigma_u^+) \rightarrow He^+ + He + He + e$	5.0E-10			Liu et al. [2010]
94	$He(^3S) + He_2(a^3\Sigma_u^+) \rightarrow He_2^+ + He + e$	2.0E-9			Liu et al. [2010]
95	$He(^3S) + H \rightarrow H^+ + He + e$	1.1E-9			Liu et al. [2010]
96	$He(^3S) + H_2 \rightarrow H_2^+ + He + e$	2.9E-11			Liu et al. [2010]
97	$He(^3S) + H_2 \rightarrow H + HeH^+ + e$	3.0E-12			Liu et al. [2010]
98	$He_2(a^3\Sigma_u^+) + He_2(a^3\Sigma_u^+) \rightarrow He^+ + He + He + He + e$	3.0E-10			Liu et al. [2010]
99	$He_2(a^3\Sigma_u^+) + He_2(a^3\Sigma_u^+) \rightarrow He_2^+ + He + He + e$	1.2E-9			Liu et al. [2010]
100	$He_2(a^3\Sigma_u^+) + H \rightarrow He + He + H^+ + e$	2.2E-10			Liu et al. [2010]
101	$He_2(a^3\Sigma_u^+) + H_2 \rightarrow H_2^+ + He + He + e$	2.2E-10			Liu et al. [2010]

F. KINETIC MODEL FOR ELECTRICAL DISCHARGES IN SATURN'S ATMOSPHERE

F.5.3 Vibrational-vibrational processes (VV)

Table F.14: Vibrational-vibrational processes

No.	Reaction	d	e	f	Ref.
102	$H_2(v=1) + H_2(v=1) \rightarrow H_2(v=2) + H_2$	9.3E-15			Capitelli et al. [1994]
103	$H_2(v=1) + H_2(v=2) \rightarrow H_2(v=3) + H_2$	1.7E-14			Capitelli et al. [1994]
104	$H_2(v=1) + H_2(v=3) \rightarrow H_2(v=4) + H_2$	2.6E-14			Capitelli et al. [1994]
105	$H_2(v=1) + H_2(v=4) \rightarrow H_2(v=5) + H_2$	3.3E-14			Capitelli et al. [1994]
106	$H_2(v=1) + H_2(v=5) \rightarrow H_2(v=6) + H_2$	3.2E-14			Capitelli et al. [1994]
107	$H_2(v=1) + H_2(v=6) \rightarrow H_2(v=7) + H_2$	2.5E-14			Capitelli et al. [1994]
108	$H_2(v=1) + H_2(v=7) \rightarrow H_2(v=8) + H_2$	1.6E-14			Capitelli et al. [1994]
109	$H_2(v=1) + H_2(v=8) \rightarrow H_2(v=9) + H_2$	9.5E-15			Capitelli et al. [1994]

F.5.4 Vibrational-translational processes (VT)

Table F.15: Vibrational-translational processes

No.	Reaction	d	e	f	Ref.
110	$H_2(v=1) + H_2 \rightarrow H_2 + H_2$	1.6E-16			Capitelli et al. [1994]
111	$H_2(v=2) + H_2 \rightarrow H_2(v=1) + H_2$	7.8E-16			Capitelli et al. [1994]
112	$H_2(v=3) + H_2 \rightarrow H_2(v=2) + H_2$	3.0E-15			Capitelli et al. [1994]
113	$H_2(v=4) + H_2 \rightarrow H_2(v=3) + H_2$	1.0E-14			Capitelli et al. [1994]
114	$H_2(v=5) + H_2 \rightarrow H_2(v=4) + H_2$	3.2E-14			Capitelli et al. [1994]
115	$H_2(v=6) + H_2 \rightarrow H_2(v=5) + H_2$	1.0E-13			Capitelli et al. [1994]
116	$H_2(v=7) + H_2 \rightarrow H_2(v=6) + H_2$	3.3E-13			Capitelli et al. [1994]
117	$H_2(v=8) + H_2 \rightarrow H_2(v=7) + H_2$	1.1E-12			Capitelli et al. [1994]
118	$H_2(v=9) + H_2 \rightarrow H_2(v=8) + H_2$	3.3E-12			Capitelli et al. [1994]

F.6 Ionic kinetics

F.6.1 Ion-Ion recombination processes

Table F.16: Ion-Ion recombination processes

No.	Reaction	d	e	f	Ref.
119	$H^- + H^+ \rightarrow H + H$	3.900E-07			Fridman [2008]
120	$He^+ + H^- \rightarrow H + He$	2.3E-7	-0.5		Liu et al. [2010]
121	$HeH^+ + H^- \rightarrow H_2 + He$	1.0E-7			Liu et al. [2010]
122	$He_2^+ + H^- \rightarrow H + He + He$	1.0E-7			Liu et al. [2010]
123	$H^+ + H^- \rightarrow H(2s^2S) + H$	9.0E-11	0.83		Liu et al. [2010]
124	$H^+ + H^- \rightarrow H(2s^2P) + H$	9.0E-11	0.83		Liu et al. [2010]
125	$H^+ + H^- \rightarrow H(3) + H$	1.8E-7	-0.5		Liu et al. [2010]
126	$H_2^+ + H^- \rightarrow H + H_2$	2.0E-7	-0.5		Liu et al. [2010]
127	$H_3^+ + H^- \rightarrow H_2 + H_2$	2.0E-7	-0.5		Liu et al. [2010]

F. KINETIC MODEL FOR ELECTRICAL DISCHARGES IN SATURN'S ATMOSPHERE

F.6.2 Positive ion processes

Table F.17: Positive ion processes

No.	Reaction	d	e	f	Ref.
128	$H^+ + H_2 \rightarrow H_2^+ + H$	1.19E-22			Méndez et al. [2006]
129	$H_2^+ + H \rightarrow H^+ + H_2$	6.4E-10			Liu et al. [2010]
130	$H_2^+ + H_2 \rightarrow H_3^+ + H$	2.0E-9			Capitelli et al. [2000]
131	$He^+ + He + He \rightarrow He_2^+ + He$	1.4E-31	-0.6		Alves et al. [1992]
132	$He^+ + H \rightarrow H^+ + He$	1.9E-15			Liu et al. [2010]
133	$He^+ + H \rightarrow HeH^+$	1.58E-15	-0.3		Liu et al. [2010]
134	$He^+ + H_2 \rightarrow H^+ + H + He$	3.7E-14			Liu et al. [2010]
135	$He^+ + H_2 \rightarrow H_2^+ + He$	7.2E-15			Liu et al. [2010]
136	$HeH^+ + H \rightarrow H_2^+ + He$	9.1E-10			Liu et al. [2010]
137	$HeH^+ + H_2 \rightarrow H_3^+ + He$	1.5E-9			Liu et al. [2010]
138	$He_2^+ + H \rightarrow H^+ + He + He$	3.5E-10			Liu et al. [2010]
139	$He_2^+ + H_2 \rightarrow HeH^+ + H + He$	1.76E-10			Liu et al. [2010]
140	$H^+ + He \rightarrow HeH^+$	8.4E-19	-4.5		Liu et al. [2010]
141	$H^+ + H + H_2 \rightarrow H_2^+ + H_2$	1.0E-34			Liu et al. [2010]
142	$H^+ + H_2 + He \rightarrow H_3^+ + He$	1.5E-29			Liu et al. [2010]
143	$H_2^+ + He \rightarrow HeH^+ + H$	1.3E-10			Liu et al. [2010]

F.6.3 Negative ion processes

Table F.18: Negative ion processes

No.	Reaction	d	e	f	Ref.
144	$H^- + H \rightarrow H_2 + e$	1.800E-9			Capitelli et al. [2000]
145	$H^- + He \rightarrow He + H + e$	8.0E-12	0.5		Liu et al. [2010]

F.7 Radiative decay processes

Table F.19: Radiative decay processes

No.	Reaction	A(s ⁻¹)	λ(nm)	κ	Ref.
146	$H(2p^2P) \rightarrow H + h\nu$	4.69E+8	121.56	1	Wiese et al. [1966]
147	$H(3) \rightarrow H + h\nu$	5.57E+7	102.57	1	Wiese et al. [1966]
148	$H(4) \rightarrow H + h\nu$	1.27E+7	79.25	1	Wiese et al. [1966]
149	$H(5) \rightarrow H + h\nu$	4.12E+8	94.97	1	Wiese et al. [1966]
150	$H(3) \rightarrow H(2s^2S) + h\nu$	2.24E+7	656.27	1	Wiese et al. [1966]
151	$H(3) \rightarrow H(2p^2P) + h\nu$	6.31E+6	656.28	1	Wiese et al. [1966]
152	$H(4) \rightarrow H(2s^2S) + h\nu$	9.66E+6	486.13	1	Wiese et al. [1966]
153	$H(4) \rightarrow H(2p^2P) + h\nu$	2.57E+6	486.13	1	Wiese et al. [1966]
154	$H(5) \rightarrow H(2s^2S) + h\nu$	4.95E+6	434.04	1	Wiese et al. [1966]
155	$H(5) \rightarrow H(2p^2P) + h\nu$	9.42E+6	434.04	1	Wiese et al. [1966]
156	$H(4) \rightarrow H(3) + h\nu$	8.98E+6	1875.10	1	Wiese et al. [1966]
157	$H(5) \rightarrow H(3) + h\nu$	2.20E+6	1281.81	1	Wiese et al. [1966]
158	$H(5) \rightarrow H(4) + h\nu$	2.70E+6	4051.20	1	Wiese et al. [1966]
159	$H_2(d^3\Pi_u) \rightarrow H_2(a^3\Sigma_g^+) + h\nu$	3.33E+7	612.00	1	Bretagne et al. [1981]
160	$H_2(a^3\Sigma_g^+) \rightarrow H + H + h\nu$	8.77E+7	400.00	1	Bretagne et al. [1981]

**F. KINETIC MODEL FOR ELECTRICAL DISCHARGES IN
SATURN'S ATMOSPHERE**

References

- H₂ IST-Lisbon Electron Impact Cross Section Database in LxCat. URL <http://fr.lxcat.net/home/>. 239
- H IST-Lisbon Electron Impact Cross Section Database in LxCat. URL <http://fr.lxcat.net/home/>. 239
- Helium IST-Lisbon Electron Impact Cross Section Database in LxCat. URL <http://fr.lxcat.net/home/>. 239
- T. Adachi, H. Fukunishi, Y. Takahashi, Y. Hiraki, R.-R. Hsu, H.-T. Su, A. B. Chen, S. B. Mende, H. U. Frey, and L. C. Lee. Electric field transition between the diffuse and streamer regions of sprites estimated from ISUAL/array photometer measurements. *Geophys. Res. Lett.*, 33:L17803, 2006. doi: 10.1029/2006GL026495. 112
- T. Adachi, Y. Hiraki, K. Yamamoto, Y. Takahashi, H. Fukunishi, R.-R. Hsu, H.-T. Su, A. B. Chen, S. B. Mende, H. U. Frey, and L. C. Lee. Electric fields and electron energies in sprites and temporal evolutions of lightning charge moment. *J. Phys. D*, 41(23):234010, 2008. doi: 10.1088/0022-3727/41/23/234010. 112
- D. L. Albritton. *At. Data Nucl. Data Tables*, volume 22. 1978. 226
- L. L. Alves, G. Gousset, and C. M. Ferreira. A collisional-radiative model for microwave discharges in helium at low and intermediate pressures. *J. Phys. D: Appl. Phys.*, 25:1713, 1992. doi: 10.1088/0022-3727/25/12/007. 242, 246
- R. A. Armstrong, J. A. Shorter, M. J. Taylor, D. M. Suszcynsky, W. A. Lyons, and L. S. Jeong. Photometric measurements in the SPRITES '95 and '96 campaigns of nitrogen second positive (399.8 nm) and first negative (427.8 nm) emissions. *J. Atm. Sol.-Terr. Phys.*, 60:787, 1998. doi: 10.1016/S1364-6826(98)00026-1. 27, 113
- R. A. Armstrong, D. M. Suszcynsky, W. A. Lyons, and T. E. Nelson. Multi-color photometric measurements of ionization and energies in sprites. *Geophys. Res. Lett.*, 27:653, 2000. doi: 10.1029/1999GL003672. 27, 113
- E. Arnone, A. Kero, B. M. Dinelli, C.-F. Enell, N. F. Arnold, E. Papandrea, C. J. Rodger, M. Carlotti, M. Ridolfi, and E. Turunen. Seeking sprite-induced signatures in remotely sensed middle atmosphere NO₂. *Geophys. Res. Lett.*, 35:L05807, 2008. doi: 10.1029/2007GL031791. 115, 134
- R. Atkinson, D. L. Baulch, R. A. Cox, J. N. Crowley, R. F. Hampson, R. G. Hynes, M. E. Jenkin, M. J. Rossi, and J. Troe. Evaluated kinetic and photochemical data for atmospheric chemistry: Part 1 gas phase reactions of O_x, HO_x, NO_x and SO_x species. *Atmospheric Chemistry & Physics Discussions*, 3:6179, 2003. 219
- S. K. Atreya. *Atmospheres and Ionospheres of the Outer Planets and their Satellites*. New York, 1986. 173
- S. K. Atreya and A. S. Wong. Coupled clouds and chemistry of the giant planets - A case for multiprobes. *Space Sci. Rev.*, 116 (1-2):121-136, jan 2005. doi: 10.1007/s11214-005-1951-5. 173
- K. H. Baines, A. A. Simon-Miller, G. S. Orton, H. A. Weaver, A. Lunsford, T. W. Momary, J. Spencer, A. F. Cheng, D. C. Reuter, D. E. Jennings, G. R. Gladstone, J. Moore, S. A. Stern, L. A. Young, H. Throop, P. Yanamandra-Fisher, B. M. Fisher, J. Hora, and M. E. Ressler. Polar Lightning and Decadal-Scale Cloud Variability on Jupiter. *Science*, 318:226, oct 2007. doi: 10.1126/science.1147912. 166
- J. N. Bardsley and J. M. Wadehra. Dissociative attachment and vibrational excitation in low-energy collisions of electrons with H₂ and D₂. *Phys Rev. A*, 20:1398, 1979. doi: 10.1103/PhysRevA.20.1398. 176, 239, 240
- C. P. Barrington-Leigh, U. S. Inan, M. Stanley, and S. A. Cummer. Sprites triggered by negative lightning discharges. *Geophys. Res. Lett.*, 26:3605, 1999. doi: 10.1029/1999GL010692. 111
- C. P. Barrington-Leigh, U. S. Inan, and M. Stanley. Identification of sprites and elves with intensified video and broadband array photometry. *J. Geophys. Res.*, 106:1741, 2001. doi: 10.1029/2000JA000073. 25, 112
- D. R. Bates. Transition probabilities of the bands of the oxygen systems of the nightglow. *Planet. Space Sci.*, 36:869-873, 1988. doi: 10.1016/0032-0633(88)90092-X. 235
- S. H. Bauer, J. F. Caballero, R. Curtis, and J. R. Wiesenfeld. Vibrational relaxation rates of CO₂(001) with various collisions partners for 300 K. *J. Chem. Phys.*, 91:1778-1785, 1987. doi: 10.1021/j100291a020. 228
- T. F. Bell, V. P. Pasko, and U. S. Inan. Runaway electrons as a source of Red Sprites in the mesosphere. *Geophys. Res. Lett.*, 22:2127, 1995. doi: 10.1029/95GL02239. 111
- T. F. Bell, S. C. Reising, and U. S. Inan. Intense continuing currents following positive cloud-to-ground lightning associated with red sprites. *Geophys. Res. Lett.*, 25:1285, 1998. doi: 10.1029/98GL00734. 114
- E. A. Bering, III, L. Bhusal, J. R. Benbrook, J. A. Garrett, A. P. Jackson, E. M. Wescott, D. R. Moudry, D. D. Sentman, H. C. Stenbaek-Nielsen, and W. A. Lyons. The results from the 1999 sprites balloon campaign. *Adv. Space Res.*, 34:1782, 2004. doi: 10.1016/j.asr.2003.05.043. 112
- L. Bhusal, E. A. Bering, III, J. R. Benbrook, J. A. Garrett, A. M. Paredes, E. M. Wescott, D. R. Moudry, D. D. Sentman, H. C. Stenbaek-Nielsen, and W. A. Lyons. Statistics and properties of transient luminous events found in the 1999 Sprites Balloon Campaign. *Adv. Space Res.*, 34:1811, 2004. doi: 10.1016/j.asr.2003.05.045. 112
- C. Biloiu, X. Sun, Z. Harvey, and E. Scime. An alternative method for gas temperature determination in nitrogen plasmas: Fits of the bands of the first positive system (B³Π_g → A³Σ_u). *J. Appl. Phys.*, 101:073303, 2007. doi: 10.1063/1.2537448. 28, 96

REFERENCES

- E. Blanc, T. Farges, R. Roche, D. Brebion, T. Hua, A. Labarthe, and V. Melnikov. Nadir observations of sprites from the International Space Station. *J. Geophys. Res. (Space Phys)*, 109:A02306, 2004. doi: 10.1029/2003JA009972. 112
- D. J. Boccippio, E. R. Williams, S. J. Heckman, W. A. Lyons, I. T. Baker, and R. Boldi. Sprites, ELF Transients, and Positive Ground Strokes. *Science*, 269:1088, 1995. doi: 10.1126/science.269.5227.1088. 111
- W. L. Boeck, O. H. Jr. Vaughan, R. Blakeslee, B. Vonnegut, and M. Brook. Lightning induced brightening in the air-glow layer. *Geophys. Res. Lett.*, 19:99–102, 1992. doi: 10.1029/91GL03168. 20
- W. L. Boeck, O. H. Vaughan, R. J. Blakeslee, B. Vonnegut, M. Brook, and J. McKune. Observations of lightning in the stratosphere. *J. Geophys. Res.*, 100:1465, 1995. doi: 10.1029/94JD02432. 16, 112
- W. L. Boeck, O. H. Vaughan, R. J. Blakeslee, B. Vonnegut, and M. Brook. The role of the space shuttle videotapes in the discovery of sprites, jets and elves. *J. Atm. Sol.-Terr. Phys.*, 60:669, 1998. doi: 10.1016/S1364-6826(98)00025-X. 112
- J. Bór. Optically perceptible characteristics of sprites observed in Central Europe in 20072009. *Journal of Atmospheric and Terrestrial Physics*, 92:151–177, 2013. doi: 10.1016/j.jastp.2012.10.008. 112
- M. H. Bortner and T. Baurer. *Defense nuclear agency reaction rate handbook 2nd edn.* 1972. 225
- W. J. Borucki and J. A. Magalhães. Analysis of Voyager 2 images of Jovian lightning. *Icarus*, 96:1–14, mar 1992. doi: 10.1016/0019-1035(92)90002-O. 166
- M. Bouróné and J. Le Calvé. De-excitation cross section of metastable argon by various atoms and molecules. *J. Chem. Phys.*, 58:1452–1458, 1973. doi: 10.1063/1.1679379. 218
- G. Brasseur and S. Solomon. *Aeronomy of the middle atmosphere 2nd edn.* 1986. 225, 226
- I. Bray and Y. Ralchenko. Electron Impact Cross Section Database. URL <http://atom.curtin.edu.au/CCC-WWW/>. 240
- J. Bretagne, J. Godart, and V. Puech. Time-resolved study of the H₂ continuum at low pressures. *J. Phys. B: At. Mol. Phys.*, 14:L761–L765, 1981. doi: 10.1088/0022-3700/14/23/002. 243, 247
- C. E. R. Bruce and R. H. Golde. The lightning discharge. *Journal of the Institution of Electrical Engineers. Part II: Power Engineering*, 88:487–505, 1941. doi: 10.1049/ji-2.1941.0065. 171, 173
- M. I. Buchwald and D. M. Hunten. Vibrational relaxation of CO₂(001) by atoms. *J. Chem. Phys.*, 62:2828–2832, 1975. doi: 10.1063/1.430819. 226
- E. Bucselá, J. Morrill, M. Heavner, C. Siefing, S. Berg, D. Hampton, D. Moudry, E. Wescott, and D. Sentman. N₂(B³Π_g) and N₂⁺(A²Π_u) vibrational distributions observed in sprites. *J. Atm. Sol.-Terr. Phys.*, 65:583, 2003. doi: 10.1016/S1364-6826(02)00316-4. xxi, 30, 69, 93, 97, 105, 106, 108, 109, 113, 186
- A. Budo. Über die Triplett-Bandentermformel für den allgemeinen intermediären Fall und Anwendung derselben auf die B³Π-C³Π-Terme des N₂-Molekuls. *Z. Phys.*, 96:219, 1935. doi: 10.1007/BF01341523. 96
- M. Cacciatore, A. Kurnosov, and A. Napartovich. Vibrational energy transfer in N₂-N₂ collisions: A new semiclassical study. *J. Chem. Phys.*, 123:174315, 2005. doi: 10.1063/1.2101445. 215
- M. Capitelli, R. Celiberto, and M. Cacciatore. Needs for Cross Sections in Plasma Chemistry. *Adv. Atom. Mol. Opt. Phys.*, 33:321, 1994. doi: 10.1016/S1049-250X(08)60040-3. 244
- M. Capitelli, C. M. Ferreira, B. F. Gordiets, and A. I. Osipov. *Plasma Kinetics in Atmospheric Gases*. Springer Verlag, Berlin, Germany, 2000. doi: 10.1007/978-3-662-04158-1. 208, 209, 213, 216, 217, 218, 219, 220, 221, 222, 223, 224, 225, 226, 230, 234, 235, 236, 246
- D. C. Cartwright. Vibrational populations of the excited states of N₂ under auroral conditions. *J. Geophys. Res.*, 83:517, 1978. doi: 10.1029/JA083iA02p00517. 30, 186
- M. Castillo. *Spectrometry and kinetics of cold plasmas of nitrogen oxides and air*. PhD thesis, 2004. 212, 213, 214, 219
- M. Castillo, V. J. Herrero, and I. Tanarro. Characterization of modeling of the steady state and transients of modulated hollow cathode discharges of nitric oxide. *Plasma Sour. Sci. Technol.*, 11:368–376, 2002. doi: 10.1088/0963-0252/11/4/302. 85
- M. Castillo, V. J. Herrero, I. Méndez, and I. Tanarro. Time resolved diagnostics and kinetic modeling of a modulated hollow cathode discharge of NO₂. *Plasma Sour. Sci. Technol.*, 13:39–47, 2004a. doi: 10.1088/0963-0252/13/1/005. 85, 86
- M. Castillo, V. J. Herrero, I. Méndez, and I. Tanarro. Spectrometric and kinetic study of a modulated glow air discharge. *Plasma Sour. Sci. Technol.*, 13:343–350, 2004b. doi: 10.1088/0963-0252/13/2/022. 85, 86
- M. Castillo, I. Méndez, A. M. Islyaikin, V. J. Herrero, and I. Tanarro. Low-Pressure DC air plasmas. Investigation of neutral and ion chemistry. *J. Phys. Chem. A*, 109:6255, 2005. doi: 10.1021/JP051318M. 98
- R. Celiberto, R. K. Janev, A. Laricchiuta, M. Capitelli, J. M. Wadehra, and D. E. Atems. CROSS SECTION DATA FOR ELECTRON-IMPACT INELASTIC PROCESSES OF VIBRATIONALLY EXCITED MOLECULES OF HYDROGEN AND ITS ISOTOPES. *Atom. Data Nucl. Data Tables*, 77(2):161, 2001. doi: 10.1006/adnd.2000.0850. 176
- A. B. Chen, C.-L. Kuo, Y.-J. Lee, H.-T. Su, R.-R. Hsu, J.-L. Chern, H. U. Frey, S. B. Mende, Y. Takahashi, H. Fuku-nishi, Y.-S. Chang, T.-Y. Liu, and L.-C. Lee. Global distributions and occurrence rates of transient luminous events. *J. Geophys. Res. (Space Phys)*, 113:A08306, 2008. doi: 10.1029/2008JA013101. 112
- M. Cho and M. J. Rycroft. Computer simulation of the electric field structure and optical emission from cloud-top to the ionosphere. *J. Atm. Sol.-Terr. Phys.*, 60:871, 1998. doi: 10.1016/S1364-6826(98)00017-0. 26, 111

REFERENCES

- M. Cho and M. J. Rycroft. Non-uniform ionization of the upper atmosphere due to the electromagnetic pulse a horizontal lightning discharge. *J. Atmos. Sol. Terr. Phys.*, 63: 559–580, 2001. doi: 10.1016/S1364-6826(00)00235-2. 26
- I. B. Cohen. *Benjamin Franklin's Experiments: A New Edition of Franklin's Experiments and Observations on Electricity*. Cambridge, MA, 1941. 10
- B. J. Conrath and D. Gautier. Saturn Helium Abundance: A Reanalysis of Voyager Measurements. *Icarus*, 144:124–134, mar 2000. doi: 10.1006/icar.1999.6265. 174
- A. F. Cook, II, T. C. Duxbury, and G. E. Hunt. First results on Jovian lightning. *Nature*, 280:794, aug 1979. doi: 10.1038/280794a0. 166
- S. A. Cummer and M. Füllekrug. Unusually intense continuing current in lightning produces delayed mesospheric breakdown. *Geophys. Res. Lett.*, 28:495, 2001. doi: 10.1029/2000GL012214. 37, 114
- S. A. Cummer, N. Jaugey, J. Li, W. A. Lyons, T. E. Nelson, and E. A. Gerken. Submillisecond imaging of sprite development and structure. *Geophys. Res. Lett.*, 33:L04104, 2006. doi: 10.1029/2005GL024969. 112
- C. L. da Silva and V. P. Pasko. Infrasonic acoustic waves generated by fast air heating in sprite cores. *Geophys. Res. Lett.*, 41:1789–1795, 2014. doi: 10.1002/2013GL059164. 119, 122
- T. de los Arcos, C. Domingo, V.J. Herrero, M. Sanz, A. Schulz, and I. Tamarro. Diagnostic and kinetic modeling of a hollow cathode N₂O discharge. *J. Phys. Chem. A*, 102:6282–6291, 1998. doi: 10.1021/jp981749n. 85, 86, 98
- I. de Pater, L. A. Sromovsky, P. M. Fry, H. B. Hammel, C. Baranec, and K. Sayanagi. Record-breaking Storm Activity on Uranus in 2014. *Icarus*, 2015. doi: 10.1016/j.icarus.2014.12.037. xxv, 167
- S. J. Desch, W. J. Borucki, C. T. Russell, and A. Bar-Nun. Progress in planetary lightning. *Rep. Prog. Phys.*, 65:955–997, jun 2002. doi: 10.1088/0034-4885/65/6/202. 166
- E. M. Dewan, R. H. Picard, R. R. O'Neil, H. A. Gardiner, J. Gibson, J. D. Mill, E. Richards, M. Kendra, and W. O. Gallery. MSX satellite observations of thunderstorm-generated gravity waves in mid-wave infrared images of the upper stratosphere. *Geophys. Res. Lett.*, 25:939–942, 1998. doi: 10.1029/98GL00640. 26
- D. Dubrovin, S. Nijdam, E. M. van Veldhuizen, U. Ebert, Y. Yair, and C. Price. Sprite discharges on Venus and Jupiter-like planets: A laboratory investigation. *J. Geophys. Res. (Space Phys)*, 115:A00E34, 2010. doi: 10.1029/2009JA014851. 169
- D. Dubrovin, A. Luque, F. J. Gordillo-Vázquez, Y. Yair, F. C. Parra-Rojas, U. Ebert, and C. Price. Impact of lightning on the lower ionosphere of Saturn and possible generation of halos and sprites. *Icarus*, 241:313–328, oct 2014. doi: 10.1016/j.icarus.2014.06.025. xxvi, 172, 174
- J. R. Dwyer. The initiation of lightning by runaway air breakdown. *Geophys. Res. Lett.*, 32:L20808, 2005. doi: 10.1029/2005GL023975. 18
- J. R. Dwyer and M. A. Uman. The physics of lightning. *Phys. Rep.*, 534:147–241, 2014. doi: 10.1016/j.physrep.2013.09.004. xii, 11, 12, 13
- J. R. Dwyer, D. M. Smith, and S. A. Cummer. High-Energy Atmospheric Physics: Terrestrial Gamma-Ray Flashes and Related Phenomena. *Space Sci. Rev.*, 173:133–196, 2012. doi: 10.1007/s11214-012-9894-0. 22
- U. A. Dyudina, A. D. Del Genio, A. P. Ingersoll, C. C. Porco, R. A. West, A. R. Vasavada, and J. M. Barbara. Lightning on Jupiter observed in the H_α line by the Cassini imaging science subsystem. *Icarus*, 172:24–36, nov 2004. doi: 10.1016/j.icarus.2004.07.014. 166
- U. A. Dyudina, A. P. Ingersoll, S. P. Ewald, C. C. Porco, G. Fischer, W. S. Kurth, and R. A. West. Detection of visible lightning on Saturn. *Geophys. Res. Lett.*, 37:L09205, may 2010. doi: 10.1029/2010GL043188. 168, 171, 173
- U. A. Dyudina, A. P. Ingersoll, S. P. Ewald, C. C. Porco, G. Fischer, and Y. Yair. Saturn's visible lightning, its radio emissions, and the structure of the 2009–2011 lightning storms. *Icarus*, 226:1020–1037, sep 2013. doi: 10.1016/j.icarus.2013.07.013. xxv, 168, 171, 173
- D. Ehrenreich, G. Tinetti, A. Lecavelier des Etangs, A. Vidal-Madjar, and F. Selsis. The transmission spectrum of Earth-size transiting planets. *Astronomy and Astrophysics*, 448:379–393, 2006. doi: 10.1051/0004-6361/20053861. xi, 5
- C.-F. Enell, E. Arnone, T. Adachi, O. Chanrion, P. T. Verronen, A. Seppälä, T. Neubert, T. Ulich, E. Turunen, Y. Takahashi, and R.-R. Hsu. Parameterisation of the chemical effect of sprites in the middle atmosphere. *Annales Geophysicae*, 26:13, 2008. doi: 10.5194/angeo-26-13-2008. 115, 134
- W. H. Everett. Rocket lightning. *Nature*, 68:599, 1903. doi: 10.1038/068599c0. 15
- A. A. Evtushenko, F. A. Kuterin, and E. A. Mareev. A model of sprite influence on the chemical balance of mesosphere. *Journal of Atmospheric and Terrestrial Physics*, 102:298–310, 2013. doi: 10.1016/j.jastp.2013.06.005. 115
- T. Farges, E. Blanc, A. Le Pichon, T. Neubert, and T. H. Allin. Identification of infrasound produced by sprites during the Sprite2003 campaign. *Geophys. Res. Lett.*, 32:L01813, 2005. doi: 10.1029/2004GL021212. 115
- W. M. Farrell, M. L. Kaiser, G. Fischer, P. Zarka, W. S. Kurth, and D. A. Gurnett. Are Saturn electrostatic discharges really superbolts? A temporal dilemma. *Geophys. Res. Lett.*, 34:L06202, mar 2007. doi: 10.1029/2006GL028841. 171
- R. F. Fernsler and H. L. Rowland. Models of lightning-produced sprites and elves. *J. Geophys. Res.*, 101:29653, 1996. doi: 10.1029/96JD02159. 26
- M. C. Festou and S. K. Atreya. Voyager ultraviolet stellar occultation measurements of the composition and thermal profiles of the Saturnian upper atmosphere. *Geophys. Res. Lett.*, 9 (10):1147–1150, oct 1982. doi: 10.1029/GL009i010p01147. xxvi, 175

REFERENCES

- G. Fischer, M. D. Desch, P. Zarka, M. L. Kaiser, D. A. Gurnett, W. S. Kurth, W. Macher, H. O. Rucker, A. Lecacheux, W. M. Farrell, and B. Cecconi. Saturn lightning recorded by Cassini/RPWS in 2004. *Icarus*, 183: 135–152, jul 2006. doi: 10.1016/j.icarus.2006.02.010. 171
- G. Fischer, W. S. Kurth, U. A. Dyudina, M. L. Kaiser, P. Zarka, A. Lecacheux, A. P. Ingersoll, and D. A. Gurnett. Analysis of a giant lightning storm on Saturn. *Icarus*, 190:528–544, oct 2007. doi: 10.1016/j.icarus.2007.04.002. 171
- G. Fischer, D. A. Gurnett, W. S. Kurth, F. Akalin, P. Zarka, U. A. Dyudina, W. M. Farrell, and M. L. Kaiser. Atmospheric Electricity at Saturn. *Space Sci. Rev.*, 137:271–285, jun 2008. doi: 10.1007/s11214-008-9370-z. 168
- G. Fischer, W. S. Kurth, D. A. Gurnett, P. Zarka, U. A. Dyudina, A. P. Ingersoll, S. P. Ewald, C. C. Porco, A. Wesley, C. Go, and M. Delcroix. A giant thunderstorm on Saturn. *Nature*, 475:75–77, dec 2011. doi: 10.1038/nature10205. xxv, 168
- G. J. Fishman, P. N. Bhat, R. Mallozzi, J. M. Horack, T. Koshut, C. Kouveliotou, G. N. Pendleton, C. A. Meegan, R. B. Wilson, W. S. Paciesas, S. J. Goodman, and H. J. Christian. Discovery of Intense Gamma-Ray Flashes of Atmospheric Origin. *Science*, 264:1313, 1994. doi: 10.1126/science.264.5163.1313. 18, 22
- A. Flitti and S. Pancheshnyi. Gas heating in fast pulsed discharges in N₂-O₂ mixtures. *European Physical Journal Applied Physics*, 45(2):021001, 2009. doi: 10.1051/epjap/2009011. 184
- R. C. Franz, R. J. Nemzek, and J. R. Winckler. Television Image of a Large Upward Electrical Discharge Above a Thunderstorm System. *Science*, 249:48, 1990. doi: 10.1126/science.249.4964.48. 15
- A. Fridman. *Plasma Chemistry*. New York, 2008. 193, 245
- H. Fukunishi, Y. Takahashi, M. Kubota, K. Sakanoi, U. S. Inan, and W. A. Lyons. Elves: Lightning-induced transient luminous events in the lower ionosphere. *Geophys. Res. Lett.*, 23:2157, 1996. doi: 10.1029/96GL01979. 20
- M. Füllekrug, R. Roussel-Dupré, E. M. D. Symbalisty, O. Chanrion, A. Odzimek, O. van der Velde, and T. Neubert. Relativistic runaway breakdown in low-frequency radio. *J. Geophys. Res. (Space Phys)*, 115:A00E09, 2010. doi: 10.1029/2009JA014468. 111
- M. Galand, L. Moore, B. Charnay, I. Müller-Wodarg, and M. Mendillo. Solar primary and secondary ionization at Saturn. *J. Geophys. Res.*, 114(A6):A06313, 2009. doi: 10.1029/2008JA013981. 23, 174
- W. R. Gameraota, S. A. Cummer, J. Li, H. C. Stenbaek-Nielsen, R. K. Haaland, and M. G. McHarg. Comparison of sprite initiation altitudes between observations and models. *J. Geophys. Res. (Space Phys)*, 116:A02317, 2011. doi: 10.1029/2010JA016095. xiii, 22, 37, 40, 41, 42, 51
- M. L. García-Comas. Personal communication. 231, 232, 233, 234
- D. Gautier, B. Conrath, M. Flasar, R. Achterberg, P. Schinder, A. Kliore, Cassini CIRS, and Radio Science Teams. The helium to hydrogen ratio in Saturn’s atmosphere from Cassini CIRS and radio science measurement. In *36th COSPAR Scientific Assembly*, volume 36 of *COSPAR Meeting*, page 867, 2006. URL <http://adsabs.harvard.edu/abs/2006cosp...36..867G>. Provided by the SAO/NASA Astrophysics Data System. 174
- E. Gerken and U. Inan. Streamers and Diffuse Glow Observed in Upper Atmospheric Electrical Discharges. *IEEE Trans. Plasma Sci.*, 33:282, 2005. doi: 10.1109/TPS.2005.845010. 112
- E. A. Gerken and U. S. Inan. Observations of decameter-scale morphologies in sprites. *J. Atm. Sol.-Terr. Phys.*, 65:567, 2003. doi: 10.1016/S1364-6826(02)00333-4. 112
- E. A. Gerken, U. S. Inan, and C. P. Barrington-Leigh. Telescopic imaging of sprites. *Geophys. Res. Lett.*, 27:2637, 2000. doi: 10.1029/2000GL000035. 112
- F. R. Gilmore, R. R. Laher, and P. J. Espy. Franck-Condon Factors, r-Centroids, Electronic Transition Moments, and Einstein Coefficients for Many Nitrogen and Oxygen Band Systems. *J. Phys. Chem. Ref. Data*, 21:1005, 1992. doi: 10.1063/1.555910. 94, 235
- F. J. Gordillo-Vázquez. Air plasma kinetics under the influence of sprites. *J. Phys. D*, 41(23):234016, 2008. doi: 10.1088/0022-3727/41/23/234016. 22, 26, 27, 30, 115, 131, 135, 152, 153, 176
- F. J. Gordillo-Vázquez. Vibrational kinetics of air plasmas induced by sprites. *J. Geophys. Res. (Space Phys)*, 115: A00E25, 2010. doi: 10.1029/2009JA014688. 22, 30, 97, 105, 106, 115, 176, 186
- F. J. Gordillo-Vázquez and A. Luque. Electrical conductivity in sprite streamer channels. *Geophys. Res. Lett.*, 37: L16809, 2010. doi: 10.1029/2010GL044349. 114
- F. J. Gordillo-Vázquez, A. Luque, and M. Simek. Spectrum of sprite halos. *J. Geophys. Res. (Space Phys)*, 116:A09319, 2011. doi: 10.1029/2011JA016652. xxi, 30, 97, 105, 106, 108, 113, 151, 186
- F. J. Gordillo-Vázquez, A. Luque, and M. Simek. Near infrared and ultraviolet spectra of TLEs. *J. Geophys. Res. (Space Phys)*, 117:A05329, 2012. doi: 10.1029/2012JA017516. xxi, 30, 97, 105, 106, 108, 109, 113, 151, 186
- J. T. Gudmundsson, I. G. Kouznetsov, K. K. Patel, and M. A. Lieberman. Electronegativity of low-pressure high-density oxygen discharges. *J. Phys. D*, 34:1100, 2001. doi: 10.1088/0022-3727/34/7/312. 213
- D. A. Gurnett, W. S. Kurth, I. H. Cairns, and L. J. Granroth. Wistlers in Neptune’s magnetosphere-Evidence of atmospheric lightning. *J. Geophys. Res.*, 95:20967–20976, 1990. doi: 10.1029/JA095iA12p20967. 167
- D. A. Gurnett, W. S. Kurth, A. Roux, R. Gendrin, C. F. Kennel, and S. J. Bolton. Lightning and plasma wave observations from the Galileo flyby of Venus. *Science*, 253: 1522, 1991. doi: 10.1126/science.253.5027.1522. 165

REFERENCES

- D. A. Gurnett, P. Zarka, R. Manning, W. S. Kurth, G. B. Hospodarsky, T. F. Averkamp, M. L. Kaiser, and W. M. Farrell. Non-detection at Venus of high-frequency radio signals characteristic of terrestrial lightning. *Nature*, 409: 313, 2001. 166
- G. J. M. Hagelaar and L. C. Pitchford. Solving the Boltzmann equation to obtain electron transport coefficients and rate coefficients for fluid models. *Plasma Sour. Sci. Technol.*, 14:722, 2005. doi: 10.1088/0963-0252/14/4/011. 32, 118
- D. L. Hampton, M. J. Heavner, E. M. Wescott, and D. D. Sentman. Optical spectral characteristics of sprites. *Geophys. Res. Lett.*, 23:89, 1996. doi: 10.1029/95GL03587. 27, 93, 112
- M. Hayashi. *Swarm Studies and Inelastic Electron-Molecule collisions*. Pitchford, L. C. and McKoy, B. V. and Chutjian, A. and Trajmar, S., 1987. 211
- M. J. Heavner. *Optical Spectroscopic Observations of Sprites, Blue Jets, and Elves: Inferred Microphysical Processes and their Macrophysical Implications*. PhD thesis, University of Alaska Fairbanks, 2000. URL http://talus-and-heavner.com/rs/MattHeavner_PhDThesis_May2000.pdf. 18, 21, 113
- M. J. Heavner, J. S. Morrill, C. Siefing, D. D. Sentman, D. R. Moudry, E. M. Wescott, and E. J. Bucsel. Near-ultraviolet and blue spectral observations of sprites in the 320-460 nm region: N₂ (2PG) emissions. *J. Geophys. Res. (Space Phys)*, 115:A00E44, 2010. doi: 10.1029/2009JA014858. 113
- C. Helling, M. Jardine, S. Witte, and D. A. Diver. Extraterrestrial lightning in atmospheric dust clouds. Nantes, France, 2011. EPSC-DSP Joint Meeting. 169
- G Herzberg. *Molecular Spectra and Molecular Structure I. Spectra of Diatomic Molecules*. Van Nostrand Reinhold Co., New York, USA, 1950. 23, 29, 89, 90, 94, 96, 98
- Y. Hiraki, L. Tong, H. Fukunishi, K. Nanbu, Y. Kasai, and A. Ichimura. Generation of metastable oxygen atom O(¹D) in sprite halos. *Geophys. Res. Lett.*, 31:L14105, 2004. doi: 10.1029/2004GL020048. 26, 71, 114
- Y. Hiraki, Y. Kasai, and H. Fukunishi. Chemistry of sprite discharges through ion-neutral reactions. *Atmospheric Chemistry & Physics*, 8:3919, 2008. 115
- K. O. Hirschfelder, C. F. Curtis, and R. Byron. *Molecular theory of gases and liquids*. 1954. 86
- W. Hu, S. A. Cummer, and W. A. Lyons. Testing sprite initiation theory using lightning measurements and modeled electromagnetic fields. *J. Geophys. Res. (Atmos.)*, 112: D13115, 2007. doi: 10.1029/2006JD007939. xiii, 22, 32, 36, 119
- D M. Hunten, F. E. Roach, and J. W. Chamberlain. A photometric unit for the airglow and aurora. *J. Atmos. Terr. Phys.*, 8:345-346, 1956. doi: 10.1016/0021-9169(56)90111-8. 61, 146
- U. S. Inan, T. F. Bell, and J. V. Rodriguez. Heating and ionization of the lower ionosphere by lightning. *Geophys. Res. Lett.*, 18:705-708, 1991. doi: 10.1029/91GL00364. 20
- G. Inoue and S. Tsuchiya. Vibration-vibration energy transfer of CO₂(00⁰1) with N₂ and CO at low temperatures. *J. Phys. Soc. Jpn.*, 39:479, 1975. doi: 10.1143/JPSJ.39.479. 229
- A. Jehl, T. Farges, and E. Blanc. Color pictures of sprites from non-dedicated observation on board the International Space Station. *J. Geophys. Res.*, 118:454-461, 2013. doi: 10.1029/2012JA018144. 112
- M. L. Kaiser, M. D. Desch, W. M. Farrell, and P. Zarka. Restrictions on the characteristics of Neptunian lightning. *J. Geophys. Res.*, 96(S01):19043-19047, 1991. 167
- A. W. Kam and F. M. Pipkin. Measurement of the lifetime of the metastable aⁿ1Σ_g⁺ state of N₂. *Phys. Rev. A*, 43:3279, 1991. doi: 10.1103/PhysRevA.43.3279. 235
- T. Kanmae, H. C. Stenbaek-Nielsen, and M. G. McHarg. Altitude resolved sprite spectra with 3 ms temporal resolution. *Geophys. Res. Lett.*, 34:L07810, 2007. doi: 10.1029/2006GL028608. xxi, 30, 93, 97, 105, 106, 108, 109, 186
- J. Kazil. *The University of Bern atmospheric ion model: time-dependent ion modeling in the stratosphere, mesosphere and lower thermosphere*. PhD thesis, University of Bern, 2002. 225
- A. J. Kliore, A. F. Nagy, E. A. Marouf, A. Anabtawi, E. Barbinis, D. U. Fleischman, and D. S. Kahan. Mid-latitude and high-latitude electron density profiles in the ionosphere of Saturn obtained by Cassini radio occultation observations. *J. Geophys. Res.*, 114:A04315, 2009. doi: 10.1029/2008JA013900. 174
- I. A. Kossyi, A. Y. Kostinsky, A. A. Matveyev, and V. P. Silakov. Kinetic scheme of the non-equilibrium discharge in nitrogen-oxygen mixtures. *Plasma Sour. Sci. Technol.*, 1:207, 1992. doi: 10.1088/0963-0252/1/3/011. 208, 213, 214, 218, 219, 220, 222, 223, 224, 225, 226
- I. Kovacs. *Rotational Structure in the Spectra of Diatomic Molecules*. New York, 1969. 95
- P. R. Krehbiel, J. A. Riousset, V. P. Pasko, R. J. Thomas, W. Rison, M. A. Stanley, and H. E. Edens. Upward electrical discharges from thunderstorms. *Nature Geoscience*, 1:233, 2008. doi: 10.1038/ngeo162. 18
- V. Kruger and D. R. Olander. Oxygen radiolysis by modulated molecular beam mass spectrometry. *J. Phys. Chem.*, 80:1676-1684, 1976. doi: 10.1021/j100556a005. 214
- P. H. Krupenie. The spectrum of Molecular Oxygen. *J. Phys. Chem. Ref. Data.*, 1(2), 1972. doi: 10.1063/1.3253101. 235
- L. V. Ksanfomaliti. Discovery of frequent lightning discharges in clouds on Venus. *Nature*, 284:244-246, 1980. doi: 10.1038/284244a0. xxv, 165, 166
- S. Kumar, A. Kumar, and C. J. Rodger. Subionospheric early VLF perturbations observed at Suva: VLF detection of red sprites in the day? *J. Geophys. Res. (Space Phys)*, 113:A03311, 2008. doi: 10.1029/2007JA012734. 115
- C.-L. Kuo, R. R. Hsu, A. B. Chen, H. T. Su, L. C. Lee, S. B. Mende, H. U. Frey, H. Fukunishi, and Y. Takahashi. Electric fields and electron energies inferred from the ISUAL recorded sprites. *Geophys. Res. Lett.*, 32:L19103, 2005. doi: 10.1029/2005GL023389. 112, 114

REFERENCES

- A. Kurnosov, A. Napartovich, S. Shnyrev, and M. Cacciatore. Vibrational energy exchanges in nitrogen: Application of new rate constants for kinetic modeling. *J. Phys. Chem. A*, 111:7057–7065, 2007. doi: 10.1021/jp071657a. 215
- B. Lavrov, M. Osiac, A. Pipa, and J. Ropke. On the spectroscopic detection of neutral species in a low-pressure plasma containing boron and hydrogen. *Plasma Sour. Sci. Technol.*, 12:576, 2003. doi: 10.1088/0963-0252/12/4/309. 27
- S. A. Lawton and A. V. Phelps. Excitation of the $b^1\Sigma_g^+$ state of O_2 by low energy electrons. *J. Chem. Phys.*, 69:1055, 1978. doi: 10.1063/1.436700. 210, 211
- E. H. Lay, C. J. Rodger, R. H. Holzworth, M. Cho, and J. N. Thomas. Temporal-spatial modeling of electron density enhancement due to successive lightning strokes. *J. Geophys. Res.*, 115:A00E59, 2010. doi: 10.1029/2009JA014756. 26
- Y. S. Lee and G. G. Shepherd. Summer high-latitude mesospheric observations of supersonic bursts and $O(1S)$ emission rate with the UARS WINDII instrument and the association with sprites, meteors, and lightning. *J. Geophys. Res.*, 115:A00E26, 2010. doi: 10.1029/2009JA014731. 114, 137
- F. Lepoutre, G. Louis, and H. Marceau. Collisional relaxation in CO_2 between 180 K and 400 K measured by the spectrophone method. *Chem. Phys. Lett.*, 48:509–615, 1977. doi: 10.1016/0009-2614(77)85082-3. 226, 229
- I. N. Levine. *Physical Chemistry*. 1978. 86
- W. Lindinger, F. Howorka, P. Lukac, S. Kuhn, H. Villinger, E. Alge, and H. Ramler. Charge transfer of $Ar^+ + N_2 \rightleftharpoons N_2^+ + Ar$ at near thermal energies. *Phys. Rev. A*, 23:2319–2326, 1981. doi: 10.1103/PhysRevA.23.2319. 223
- P. J. Linstrom and W. G. Mallard, editors. *NIST Chemistry WebBook*. NIST Standard Reference Database Number 69, National Institute of Standards and Technology, Gaithersburg MD, 20899, 2015. URL <http://webbook.nist.gov>. 195, 219, 220, 221, 236
- B. Little, C. D. Anger, A. P. Ingersoll, A. R. Vasavada, D. A. Senske, H. H. Breneman, W. J. Borucki, and The Galileo SSI Team. Galileo Images of Lightning on Jupiter. *Icarus*, 142:306, 1999. doi: 10.1006/icar.1999.6195. 166
- D. X. Liu, P. Bruggeman, F. Iza, M. Z. Rong, and M. G. Kong. Global model of low-temperature atmospheric-pressure He + H_2O plasmas. *Plasma Sour. Sci. Technol.*, 19:025018, 2010. doi: 10.1088/0963-0252/19/2/025018. 240, 241, 242, 243, 245, 246
- N. Liu. Model of sprite luminous trail caused by increasing streamer current. *Geophys. Res. Lett.*, 37:L04102, 2010. doi: 10.1029/2009GL042214. 122
- N. Liu. Multiple ion species fluid modeling of sprite halos and the role of electron detachment of O^- in their dynamics. *J. Geophys. Res.*, 117:A03308, 2012. doi: 10.1029/2011JA017062. 40
- N. Liu and V. P. Pasko. Molecular nitrogen LBH band system far-UV emissions of sprite streamers. *Geophys. Res. Lett.*, 32:L05104, 2005. doi: 10.1029/2004GL022001. 113
- N. Liu and V. P. Pasko. Modeling studies of $NO-\gamma$ emissions of sprites. *Geophys. Res. Lett.*, 34:L16103, 2007. doi: 10.1029/2007GL030352. 113
- N. Liu, V. P. Pasko, D. H. Burkhardt, H. U. Frey, S. B. Mende, H.-T. Su, A. B. Chen, R.-R. Hsu, L.-C. Lee, H. Fukunishi, and Y. Takahashi. Comparison of results from sprite streamer modeling with spectrophotometric measurements by ISUAL instrument on FORMOSAT-2 satellite. *Geophys. Res. Lett.*, 33:L01101, 2006. doi: 10.1029/2005GL024243. 112, 113
- N. Liu, V. P. Pasko, H. U. Frey, S. B. Mende, H.-T. Su, A. B. Chen, R.-R. Hsu, and L.-C. Lee. Assessment of sprite initiating electric fields and quenching altitude of a $^1\Pi_g$ state of N_2 using sprite streamer modeling and ISUAL spectrophotometric measurements. *J. Geophys. Res. (Space Phys)*, 114:A00E02, 2009. doi: 10.1029/2008JA013735. 112
- M. López-Puertas. *Emisiones del CO_2 en 4.26 y 15 μm en las atmósferas de los planetas interiores*. PhD thesis, Universidad de Granada, 1982. 118
- M. López-Puertas and F. W. Taylor. Carbon dioxide 4.3 μm emission in the Earth's atmosphere: A comparison between NIMBUS 7 SAMS measurements and non-local thermodynamic equilibrium radiative transfer calculations. *J. Geophys. Res.*, 94:13045, 1989. doi: 10.1029/JD094iD10p13045. 228
- M. López-Puertas, R. Rodrigo, J. J. López-Moreno, and F. W. Taylor. A non-LTE radiative transfer model for infrared bands in the middle atmosphere. II. CO_2 (2.7 and 4.3 μm) and water vapour (6.3 μm) bands and $N_2(v1)$ and $O_2(v1)$ vibrational levels. *Journal of Atmospheric and Terrestrial Physics*, 48:749–764, 1986. doi: 10.1016/0021-9169(86)90023-1. 228
- M. A. López-Valverde. *Emisiones infrarrojas en la atmosfera de Marte*. PhD thesis, Universidad de Granada, 1990. 226, 227, 228, 229
- A. Luque and U. Ebert. Sprites in varying air density: Charge conservation, glowing negative trails and changing velocity. *Geophys. Res. Lett.*, 37:L06806, 2010. doi: 10.1029/2009GL041982. 23, 121, 122, 187
- A. Luque and F. J. Gordillo-Vázquez. Modeling and analysis of $N_2(B^3\Pi_g)$ and $N_2(C^3\Pi_u)$ vibrational distributions in sprites. *J. Geophys. Res. (Space Phys)*, 116:A02306, 2011. doi: 10.1029/2010JA015952. xxi, 30, 97, 105, 106, 108, 113, 186
- A. Luque and F. J. Gordillo-Vázquez. Mesospheric electric breakdown and delayed sprite ignition caused by electron detachment. *Nature Geoscience*, 4, 2012. doi: 10.1038/ngeo1314. 30, 33, 34, 37, 40, 45, 114, 126
- A. Luque, V. Ratushnaya, and U. Ebert. Positive and negative streamers in ambient air: modelling evolution and velocities. *J. Phys. D*, 41(23):234005, 2008. doi: 10.1088/0022-3727/41/23/234005. 23, 121
- A. Luque, D. Dubrovin, F. J. Gordillo-Vázquez, U. Ebert, F. C. Parra-Rojas, Y. Yair, and C. Price. Coupling between atmospheric layers in gaseous giant planets due to lightning-generated electromagnetic pulses. *J. Geophys. Res.: Space Physics*, 119:8705–8720, 2014. doi: 10.1002/2014JA020457. xxvi, 170, 175

REFERENCES

- W. A. Lyons. Sprite observations above the U.S. High Plains in relation to their parent thunderstorm systems. *J. Geophys. Res.*, 101:29641, 1996. doi: 10.1029/96JD01866. 112
- W. A. Lyons, M. Stanley, T. E. Nelson, and M. Taylor. Sprites, elves, halos, trolls and blue starters above the STEPS domain. *Eos. Trans. Am. Geophys. Union*, 81:F131, 2000. 21
- W. A. Lyons, T. E. Nelson, R. A. Armstrong, V. P. Pasko, and M. A. Stanley. Upward Electrical Discharges From Thunderstorm Tops. *Bulletin of the American Meteorological Society*, 84:445, 2003. doi: 10.1175/BAMS-84-4-445. 17, 21
- D. R. MacGorman and W. D. Rust. *The Electrical Nature of Storms*. New York, 1998. 10
- J. A. Magalhães and W. J. Borucki. Spatial distribution of visible lightning on Jupiter. *Nature*, 349:311–313, 1991. doi: 10.1038/349311a0. 166
- W. J. Markiewicz, D. V. Titov, S. S. Limaye, H. U. Keller, N. Ignatiev, R. Jaumann, N. Thomas, H. Michalik, R. Moissl, and P. Russo. Morphology and dynamics of the upper cloud layer of Venus. *Nature*, 450:633, 2007. doi: 10.1038/nature06320. 169
- D. R. Marsh, M. J. Mills, D. E. Kinnison, J. F. Lamarque, N. Calvo, and L. M. Polvani. Climate change from 1850 to 2005 simulated in CESM1(WACCM). *Journal of Climate*, 26(19):7372–7391, 2013. doi: 10.1175/JCLI-D-12-00558.1. 119
- R. A. Marshall and U. S. Inan. High-speed telescopic imaging of sprites. *Geophys. Res. Lett.*, 32:L05804, 2005. doi: 10.1029/2004GL021988. 112
- R. A. Marshall and U. S. Inan. High-speed measurements of small-scale features in sprites: Sizes and lifetimes. *Radio Science*, 41:RS6S43, 2006. doi: 10.1029/2005RS003353. 112
- R. A. Marshall and U. S. Inan. Possible direct cloud-to-ionosphere current evidenced by sprite-initiated secondary TLEs. *Geophys. Res. Lett.*, 34:L05806, 2007. doi: 10.1029/2006GL028511. 21
- R. A. Marshall, U. S. Inan, and T. W. Chevalier. Early VLF perturbations caused by lightning EMP-driven dissociative attachment. *Geophys. Res. Lett.*, 35:L21807, 2008. doi: 10.1029/2008GL035358. 26
- R. S. Massey and D. N. Holden. Phenomenology of transionospheric pulse pairs. *Radio Science*, 30:1645–1689, 1995. doi: 10.1029/95RS01563. 22
- E. McDaniel. *Atomic Collisions, Electron and Photon Projectiles*. New York, 1989. 86
- M. G. McHarg, H. C. Stenbaek-Nielsen, and T. Kammer. Observations of streamer formation in sprites. *Geophys. Res. Lett.*, 34:L06804, 2007. doi: 10.1029/2006GL027854. 112
- S. Mende, H. Frey, R. R. Hsu, H. T. Su, A. Chen, L. C. Lee, H. Fukunishi, and Y. Takahashi. . In *EOS Trans. Am. Geophys. Union 85 (Fall Meet. Suppl.)*, 2004. 113, 151
- S. B. Mende, R. L. Rairden, G. R. Swenson, and W. A. Lyons. Sprite spectra; N₂ 1 PG band identification. *Geophys. Res. Lett.*, 22:2633, 1995. doi: 10.1029/95GL02827. 27, 93, 112
- S. B. Mende, H. U. Frey, R. R. Hsu, H. T. Su, A. B. Chen, L. C. Lee, D. D. Sentman, Y. Takahashi, and H. Fukunishi. D region ionization by lightning-induced electromagnetic pulses. *J. Geophys. Res. (Space Phys)*, 110:A11312, 2005. doi: 10.1029/2005JA011064. 112
- I. Méndez, F. J. Gordillo-Vázquez, V. J. Herrero, and I. Tanarro. Atom and ion chemistry in low pressure hydrogen DC plasmas. *J. Phys. Chem. A*, 110:6060–6066, 2006. doi: 10.1021/jp057182+. 98, 240, 246
- A. J. Midey, S. Williams, T. M. Miller, P. T. Larsen, and A. A. Viggiano. Investigation of the Reaction of O₃⁺ with N₂ and O₂ from 100 to 298 K. *J. Phys. Chem. A*, 106:11739–11742, 2002. doi: 10.1021/jp020311r. 223
- G. M. Milikh, D. A. Usikov, and J. A. Valdivia. Model of infrared emission from sprites. *J. Atm. Sol-Terr. Phys.*, 60:895, 1998. doi: 10.1016/S1364-6826(98)80009-6. 113
- E. Mishin. Ozone layer perturbation by a single blue jet. *Geophys. Res. Lett.*, 24:1919, 1997. doi: 10.1029/97GL01890. 114
- J. B. A. Mitchell. THE DISSOCIATIVE RECOMBINATION OF MOLECULAR IONS. *Phys. Rep.*, 186:215–248, 1990. doi: 10.1016/0370-1573(90)90159-Y. 242
- F. Mokler, C. Helling, and M. Jardine. Lightning in Brown Dwarfs? In *COOL STARS, STELLAR SYSTEMS AND THE SUN*, volume 1094, pages 533–536, Cambridge, 2009. 15th Cambridge Workshop on Cool Stars, Stellar Systems and the Sun. 169
- C. B. Moore, R. E. Wood, B. L. Hu, and J. T. Yardley. Vibrational energy transfer in CO₂ lasers. *J. Chem. Phys.*, 46:4222–4231, 1967. doi: 10.1063/1.1840527. 229
- C. B. Moore, K. B. Eack, G. D. Aulich, and W. Rison. Energetic radiation associated with lightning stepped-leaders. *Geophys. Res. Lett.*, 28:2141, 2001. doi: 10.1029/2001GL013140. 18
- L. Moore, M. Mendillo, I. Müller-Wodarg, and D. Murr. Modeling of global variations and ring shadowing in Saturn’s ionosphere. *Icarus*, 172(2):503–520, 2004. doi: 10.1016/j.icarus.2004.07.007. 23, 174
- W. L. Morgan. Electron collision data for plasma chemistry modeling. *Adv. At. Mol. Opt. Phys.*, 43:79–110, 2000. doi: 10.1016/S1049-250X(08)60122-6. 211
- J. Morrill, E. Bucsela, C. Siefring, M. Heavner, S. Berg, D. Moudry, S. Slinker, R. Fernsler, E. Wescott, D. Sentman, and D. Osborne. Electron energy and electric field estimates in sprites derived from ionized and neutral N₂ emissions. *Geophys. Res. Lett.*, 29(10):1462, 2002. doi: 10.1029/2001GL014018. 27, 113
- J. S. Morrill and W. M. Benesch. Auroral N₂ emissions and the effect of collisional processes on N₂ triplet state vibrational populations. *J. Geophys. Res.*, 101:261, 1996. doi: 10.1029/95JA02835. 30, 186

REFERENCES

- J. S. Morrill, E. J. Bucseles, V. P. Pasko, S. L. Berg, M. J. Heavner, D. R. Moudry, W. M. Benesch, E. M. Wescott, and D. D. Sentman. Time resolved N_2 triplet state vibrational populations and emissions associated with red sprites. *J. Atm. Sol.-Terr. Phys.*, 60:811, 1998. doi: 10.1016/S1364-6826(98)00031-5. 69, 93, 112, 113
- J. I. Moses and S. F. Bass. The effects of external material on the chemistry and structure of Saturn's ionosphere. *J. Geophys. Res.*, 105:7013–7052, 2000. doi: 10.1029/1999JE001172. 174
- G. D. Moss, V. P. Pasko, N. Liu, and G. Veronis. Monte Carlo model for analysis of thermal runaway electrons in streamer tips in transient luminous events and streamer zones of lightning leaders. *J. Geophys. Res. (Space Phys)*, 111:A02307, 2006. doi: 10.1029/2005JA011350. 18
- D. Moudry, H. Stenbaek-Nielsen, D. Sentman, and E. Wescott. Imaging of elves, halos and sprite initiation at 1ms time resolution. *J. Atm. Sol.-Terr. Phys.*, 65:509, 2003. doi: 10.1016/S1364-6826(02)00323-1. 112
- D. R. Moudry. *The dynamics and morphology of sprites*. PhD thesis, University of Alaska, 2003. xxii, 21, 126, 127
- D. R. Moudry, H. C. Stenbaek-Nielsen, D. D. Sentman, and E. M. Wescott. Velocities of sprite tendrils. *Geophys. Res. Lett.*, 29(20):1992, 2002. doi: 10.1029/2002GL015682. 27
- R. S. Mulliken. The interpretation of band spectra. Parts I, IIa, IIb. *Reviews of Modern Physics*, 2(1):60–115, 1930. doi: 10.1103/RevModPhys.2.506. 96
- Y. Naghizadeh-Kashani, Y. Cressault, and A. Gleizes. Net emission coefficient of air thermal plasmas. *J. Phys. D: Appl. Phys.*, 35:2925–2934, 2002. doi: 10.1088/0022-3727/35/22/306. 96
- A. F. Nagy, A. J. Kliore, M. Mendillo, S. Miller, L. Moore, J. I. Moses, I. Müller-Wodarg, and D. Shemansky. *Upper atmosphere and ionosphere of Saturn*. In: *Saturn from Cassini-Huygens*. 2009. 177
- T. Neubert. On Sprites and their exotic kin. *Science*, 300:747, 2003. doi: 10.1126/science.1083006. 111
- V. N. Ochkin. *Spectroscopy of Low Temperature Plasma*. Wiley-VCH Verlag GmbH and Co., Weinheim, mar 2009. 193
- B. J. Orr and I. W. M. Smith. Collision-induced vibrational energy transfer in small polyatomic molecules. *J. Phys. Chem.*, 91:6106–6119, 1987. doi: 10.1021/j100308a013. 228, 229
- S. Pancheshnyi, M. Nudnova, and A. Starikovskii. Development of a cathode-directed streamer discharge in air at different pressures: Experiment and comparison with direct numerical simulation. *Phys. Rev. E*, 71(1):016407, 2005. doi: 10.1103/PhysRevE.71.016407. 122
- S. Pancheshnyi, B. Eismann, G. J. M. Hagelaar, and L. C. Pitchford. Zdblaskin: Zero-dimensional plasma kinetics. <http://www.zdblaskin.laplace.univ-tlse.fr/>, 2008. 32, 118
- F. C. Parra-Rojas, A. Luque, and F. J. Gordillo-Vázquez. Chemical and electrical impact of lightning on the Earth mesosphere: The case of sprite halos. *J. Geophys. Res.*, 118:1–25, 2013a. doi: 10.1002/jgra.50449. 22, 114, 116, 119, 176
- F. C. Parra-Rojas, M. Passas, E. Carrasco, A. Luque, I. Tanarro, M. Simek, and F. J. Gordillo-Vázquez. Spectroscopic diagnostics of laboratory air plasmas as a benchmark for spectral rotational (gas) temperature determination in TLEs. *J. Geophys. Res.*, 118:4649–4661, 2013b. doi: 10.1002/jgra.50433. 22, 113
- F.C. Parra-Rojas, A. Luque, and F. J. Gordillo-Vázquez. Chemical and thermal impact of sprite streamers in the Earth mesosphere. *Submitted to J. Geophys. Res.*, 2015. 23, 176
- V. P. Pasko. Atmospheric physics: Electric jets. *Nature*, 423:927, 2003. doi: 10.1038/423927a. 18, 111
- V. P. Pasko and H. C. Stenbaek-Nielsen. Diffuse and streamer regions of sprites. *Geophys. Res. Lett.*, 29(10):1440, 2002. doi: 10.1029/2001GL014241. 112
- V. P. Pasko, U. S. Inan, Y. N. Taranenko, and T. F. Bell. Heating, ionization and upward discharges in the mesosphere due to intense quasi-electrostatic thundercloud fields. *Geophys. Res. Lett.*, 22:365, 1995. doi: 10.1029/95GL00008. 111
- V. P. Pasko, U. S. Inan, and T. F. Bell. Sprites as luminous columns of ionization produced by quasi-electrostatic thundercloud fields. *Geophys. Res. Lett.*, 23:649, 1996. doi: 10.1029/96GL00473. 25
- V. P. Pasko, U. S. Inan, T. F. Bell, and Y. N. Taranenko. Sprites produced by quasi-electrostatic heating and ionization in the lower ionosphere. *J. Geophys. Res.*, 102:4529, 1997. doi: 10.1029/96JA03528. 26, 113
- V. P. Pasko, U. S. Inan, and T. F. Bell. Spatial structure of sprites. *Geophys. Res. Lett.*, 25:2123, 1998. doi: 10.1029/98GL01242. 18, 112
- V. P. Pasko, M. A. Stanley, J. D. Mathews, U. S. Inan, and T. G. Wood. Electrical discharge from a thundercloud top to the lower ionosphere. *Nature*, 416:152–154, 2002. doi: 10.1038/416152a. xii, 18, 19
- M. Passas, J. Sánchez, A. Luque, and F. J. Gordillo-Vázquez. Transient Upper Atmospheric Plasmas: Sprites and Halos. *IEEE Transactions on Plasma Science*, 42, 2014. doi: 10.1109/TPS.2014.2329320. 113
- M. Pätzold, B. Häusler, M. K. Bird, S. Tellmann, R. Mattei, S. W. Asmar, V. Dehant, W. Eidel, T. Imamura, R. A. Simpson, and G. L. Tyler. The structure of Venus' middle atmosphere and ionosphere. *Nature*, 450:657, 2007. doi: 10.1038/nature06239. 169
- R. Peverall, S. Rosén, J. R. Peterson, M. Larsson, A. Al-Khalili, L. Viktor, J. Semaniak, R. Bobbenkamp, A. Le Padellec, A. N. Maurellis, and W. J. van der Zande. Dissociative recombination and excitation of O_2^+ : Cross sections, product yields and implications for studies of ionospheric airglows. *J. Chem. Phys.*, 114:6679, 2001. doi: 10.1063/1.1349079. 214
- A. V. Phelps. CO_2 electron cross sections. <http://jilawwww.colorado.edu/avp/>, a. 211, 212
- A. V. Phelps. H_2 Phelps Electron Impact Cross Section Database in LxCat, b. URL <http://fr.lxcat.net/home/>. 239

REFERENCES

- A. V. Phelps. NO electron cross sections. <http://jilawww.colorado.edu/avp/>, 1969. 211
- A. V. Phelps and L. C. Pitchford. Anisotropic scattering of electrons by N_2 and its effect on electron transport. *Phys. Rev. A*, 31:2932, 1985. doi: 10.1103/PhysRevA.31.2932. 210
- R. H. Picard, U. S. Inan, V. P. Pasko, J. R. Winick, and P. P. Wintersteiner. Infrared glow above thunderstorms? *Geophys. Res. Lett.*, 24:2635, 1997. doi: 10.1029/97GL02753. 113
- L. G. Piper. State-to-state $N_2(A^3\Sigma_u^+)$ energy pooling reactions. II. The formation and quenching of $N_2(B^3\Pi_g, v=1-12)$. *J. Chem. Phys.*, 88:6911, 1988. doi: 10.1063/1.454388. 28, 30
- L. G. Piper. The excitation of $N_2(B^3\Pi_g, v=1-12)$ in the reaction between $N_2(A^3\Sigma_u^+)$ and $N_2(X, v \geq 5)$. *J. Chem. Phys.*, 91:864, July 1989. doi: 10.1063/1.457138. 30
- L. G. Piper, J. E. Velazco, and D. W. Setser. Quenching cross sections for electronic energy transfer reactions between metastable argon atoms and noble gases and small molecules. *J. Chem. Phys.*, 59:3323–3340, 1973. doi: 10.1063/1.1680477. 218
- L. G. Piper, B. D. Green, W. A. M. Blumberg, and S. J. Wolnik. N_2^+ Meinel band quenching. *J. Chem. Phys.*, 82:3139, 1985. doi: 10.1063/1.448211. 219, 220, 236
- A. A. Radzig and B. M. Smirnov. *Reference Data on Atoms, Molecules and Ions*. 1985. 235
- R. L. Rairden and S. B. Mende. Time resolved sprite imagery. *Geophys. Res. Lett.*, 22:3465, 1995. doi: 10.1029/95GL03332. 112
- Y. P. Raizer. *Gas Discharge Physics*. Springer-Verlag, Berlin, Germany, 1991. 112
- Y. P. Raizer, G. M. Milikh, M. N. Shneider, and S. V. Novakovski. Long streamers in the upper atmosphere above thundercloud. *J. Phys. D*, 31:3255, 1998. doi: 10.1088/0022-3727/31/22/014. 112
- V. A. Rakov and M. A. Uman. *Lightning*. 2003. 14
- S. W. Rayment and J. L. Moruzzi. Electron detachment studies between O- ions and nitrogen. *International Journal of Mass Spectrometry and Ion Physics*, 26(3):321 – 326, 1978. ISSN 0020-7381. doi: 10.1016/0020-7381(78)80033-3. 225
- N. O. Renno, A. S. Wong, S. K. Atreya, I. de Pater, and M. Roos-Serote. Electrical discharges and broadband radio emission by Martian dust devils and dust storms. *Geophys. Res. Lett.*, 30:2140, 2003. doi: 10.1029/2003GL017879. 166
- C. J. Rodger, A. Seppälä, and M. A. Clilverd. Significance of transient luminous events to neutral chemistry: Experimental measurements. *Geophys. Res. Lett.*, 35:L07803, 2008. doi: 10.1029/2008GL033221. 115
- F. Roux, F. Michaud, and J. Verges. High-resolution Fourier spectrometry of $^{14}N_2$ infrared emission spectrum: Extensive analysis of the $B^3\Pi_g-A^3\Sigma_u^+$ system. *J. Mol. Spectrosc.*, 97:253, 1983. doi: 10.1016/0022-2852(83)90266-7. 96
- F. Roux, F. Michaud, and M. Vervloet. Investigation of the rovibrational levels of the $B^3\Pi_g$ state of $^{14}N_2$ molecule above the dissociation limit $N(^4S) + N(^4S)$ by Fourier transform spectrometry. *Can. J. Phys.*, 68:1257, 1990. doi: 10.1139/p90-181. 96
- C. T. Russell, T. L. Zhang, M. Delva, W. Magnes, R. J. Strangeway, and H. Y. Wei. Lightning on Venus inferred from whistler-mode waves in the ionosphere. *Nature*, 450:661, 2007. doi: 10.1038/nature05930. 166
- A. Sánchez-Lavega, T. del Río-Gaztelurrutia, R. Hueso, J. M. Gómez-Forrellad, J. F. Sanz-Requena, J. Legarreta, E. García-Melendo, F. Colas, J. Lecacheux, L. N. Fletcher, D. Barrado-Navascués, D. Parker, and the International Outer Planet Watch Team. Deep winds beneath Saturn's upper clouds from a seasonal long-lived planetary-scale storm. *Nature*, 475:71–73, 2011. doi: 10.1038/nature10203. 173
- K. M. Sayanagi, U. A. Dyudina, S. P. Ewald, G. Fischer, A. P. Ingersoll, W. S. Kurth, G. D. Muro, C. C. Porco, and R. A. West. Dynamics of Saturn's great storm of 2010-2011 from Cassini ISS and RPWS. *Icarus*, 223:460–478, 2013. doi: 10.1016/j.icarus.2012.12.013. 168
- M. J. Seaton. Cross Sections for 2s-2p Transitions in H and 3s-3p Transitions in Na Produced by Electron and by Proton Impact. *Proc. Phys. Soc. (London)*, 68:457, 1955. doi: 10.1088/0370-1298/68/6/301. 241
- D. D. Sentman. Electrical Breakdown Parameters For Neutral Atmospheres of the Solar System. In *ISUAL workshop proceedings*, number 08-013-0016, 2004. 168
- D. D. Sentman and H. C. Stenbaek-Nielsen. Chemical effects of weak electric fields in the trailing columns of sprite streamers. *Plasma Sour. Sci. Technol.*, 18(3):034012, 2009. doi: 10.1088/0963-0252/18/3/034012. 115
- D. D. Sentman and E. M. Wescott. Red sprites and blue jets: Thunderstorm-excited optical emissions in the stratosphere, mesosphere, and ionosphere. *Physics of Plasmas*, 2:2514, 1995. doi: 10.1063/1.871213. 114
- D. D. Sentman, E. M. Wescott, D. L. Osborne, D. L. Hampton, and M. J. Heavner. Preliminary results from the Sprites94 aircraft campaign: 1. Red sprites. *Geophys. Res. Lett.*, 22:1205, 1995. doi: 10.1029/95GL00583. 112, 113
- D. D. Sentman, E. M. Wescott, R. H. Picard, J. R. Winick, H. C. Stenbaek-Nielsen, E. M. Dewan, D. R. Moudry, F. T. Sao Sabbas, M. J. Heavner, and J. Morrill. Simultaneous observations of mesospheric gravity waves and sprites generated by a midwestern thunderstorm. *J. Atm. Sol.-Terr. Phys.*, 65:537, 2003. doi: 10.1016/S1364-6826(02)00328-0. 26
- D. D. Sentman, H. C. Stenbaek-Nielsen, M. G. McHarg, and J. S. Morrill. Correction to "Plasma chemistry of sprite streamers". *J. Geophys. Res. (Atmos.)*, 113:D14399, 2008a. doi: 10.1029/2008JD010634. 119
- D. D. Sentman, H. C. Stenbaek-Nielsen, M. G. McHarg, and J. S. Morrill. Plasma chemistry of sprite streamers. *J. Geophys. Res. (Atmos.)*, 113:D11112, 2008b. doi: 10.1029/2007JD008941. 26, 32, 114, 131, 135, 152
- X. M. Shao, E. H. Lay, and A. R. Jacobson. Reduction of electron density in the night-time lower ionosphere in response to a thunderstorm. *Nature Geoscience*, 6, 2012. doi: 10.1038/NNGEO1668. 114

REFERENCES

- X. M. Shao, E. H. Lay, and R. Jacobson. Reduction of electron density in the night-time lower ionosphere in response to a thunderstorm. *Nature Geoscience*, 6:29–33, 2013. doi: 10.1038/NNGEO1668. 25, 45
- D. E. Shemansky and A. L. Broadfoot. Excitation of N_2 and N_2^+ system by electrons- II excitation cross sections and N_2 1PG low pressure afterglow. *J. Quant. Spectrosc. Radiat. Transfer.*, 11:1401–1439, 1971. 210
- M. Simek. On the use of the numerical simulations of the first positive system of N_2 : III. numerical thermometer on $(v',0)$ bands, $v' = 0-3$. *Research Report IPPCZ-345*, pages 1–31, 1994. 91, 92, 93, 94
- M. Simek. Determination of $N_2(A^3\Sigma_u^+)$ metastable density produced by nitrogen streamers at atmospheric pressure: 1. Design of diagnostic method. *Plasma Sour. Sci. Technol.*, 12:421, 2003. doi: 10.1088/0963-0252/12/3/318. 219
- M. Simek and S. DeBenedictis. On the use of the numerical simulation of the first positive system of n_2 : II. fast t_{rot} estimation from the partially resolved (3,0) band. *Plasma Chem. Plasma Proc.*, 15:451–463, 1995. 23, 29, 90, 91, 92, 93, 94, 95
- J. D. Skalny, S. Matejcik, A. Kiendler, A. Stamatovic, and T. D Mrk. Dissociative electron attachment to ozone using a high-resolution crossed beams technique. *Chem. Phys. Lett.*, 255:112–118, 1996. doi: 10.1016/0009-2614(96)00341-7. 211
- B. A. Smith, L. A. Soderblom, T. V. Johnson, A. P. Ingersoll, S. A. Collins, Shoemaker. E. M., G. E. Hunt, H. Masursky, Carr. M. H., M. E. Davies, A. F. Cook II, J. Boyce, G. E. Danielson, T. Owen, C. Sagan, R. F. Beebe, J. Veverka, R. G. Strom, J. F. McCauley, D. Morrison, G. A. Briggs, and V. E. Suomi. The Jupiter System Through the Eyes of Voyager 1. *Science*, 204:951–957+960–972, 1979. doi: 10.1126/science.204.4396.951. xxv, 166, 167
- D. A. Smith, R. S. Massey, K. C. Wiens, K. B. Eack, X. M. Shao, D. N. Holden, and P. E. Argo. Observations and inferred physical characteristics of compact intracloud discharges. In *Proc. 11th Int. Conf. on Atmospheric Electricity*, pages 6–9, Guntersville, Alabama, 1999. 15
- D. M. Smith, L. I. Lopez, R. P. Lin, and C. P. Barrington-Leigh. Terrestrial Gamma-Ray Flashes Observed up to 20 MeV. *Science*, 307:1085, 2005. doi: 10.1126/science.1107466. 18
- M. Stanley, P. Krehbiel, M. Brook, C. Moore, W. Rison, and B. Abrahams. High speed video of initial sprite development. *Geophys. Res. Lett.*, 26:3201, 1999. doi: 10.1029/1999GL010673. 112
- M. Stanley, M. Brook, P. Krehbiel, and S. A. Cummer. Detection of daytime sprites via a unique sprite ELF signature. *Geophys. Res. Lett.*, 27:871, 2000. doi: 10.1029/1999GL010769. 115
- S. M. Starikovskaia, A. Y. Starikovskii, and D. V. Zatsepin. Hydrogen oxidation in a stoichiometric hydrogen-air mixture in the fast ionization wave. *Combustion Theory Modelling*, 5:97, 2001. doi: 10.1088/1364-7830/5/1/306. 214, 219, 220, 222, 223, 236
- D. F. Starr and J. K. Hancock. Vibrational energy transfer in CO_2-CO mixtures from 163 to 406 K. *J. Chem. Phys.*, 63:4730–4734, 1975. doi: 10.1063/1.431259. 226
- H. C. Stenbaek-Nielsen and M. G. McHarg. High time-resolution sprite imaging: observations and implications. *J. Phys. D*, 41(23):234009, 2008. doi: 10.1088/0022-3727/41/23/234009. 23, 112, 122
- H. C. Stenbaek-Nielsen, D. R. Moudry, E. M. Wescott, D. D. Sentman, and F. T. Sao Sabbas. Sprites and possible mesospheric effects. *Geophys. Res. Lett.*, 27:3829, 2000. doi: 10.1029/2000GL003827. 114
- H. C. Stenbaek-Nielsen, M. G. McHarg, T. Kanmae, and D. D. Sentman. Observed emission rates in sprite streamer heads. *Geophys. Res. Lett.*, 34:L11105, 2007. doi: 10.1029/2007GL029881. 112, 153
- H. C. Stenbaek-Nielsen, T. Kanmae, M. G. McHarg, and R. Haaland. High-Speed Observations of Sprite Streamers. *Surv. Geophys.*, 34:769–795, 2013. doi: 10.1007/s10712-013-9224-4. 112, 121, 147
- H. T. Su, R. R. Hsu, A. B. Chen, Y. C. Wang, W. S. Hsiao, W. C. Lai, L. C. Lee, M. Sato, and H. Fukunishi. Gigantic jets between a thundercloud and the ionosphere. *Nature*, 423:974, 2003. doi: 10.1038/nature01759. 18
- D. M. Suszcynsky, R. Roussel-Dupré, W. A. Lyons, and R. A. Armstrong. Blue-light imagery and photometry of sprites. *J. Atm. Sol.-Terr. Phys.*, 60:801, 1998. doi: 10.1016/S1364-6826(98)00027-3. 27
- Y. N. Taranenkov, U. S. Inan, and T. F. Bell. The interaction with the lower ionosphere of electromagnetic pulses from lightning: Heating, attachment and ionization. *Geophys. Res. Lett.*, 20(23):1539–1542, 1993. doi: 10.1029/93GL02838. 26, 114
- M. J. Taylor and M. A. Hapgood. Identification of a thunderstorm as a source of a short period gravity waves in the upper atmospheric nightglow emission. *Planet. Space Sci.*, 36:975–985, 1988. doi: 10.1016/0032-0633(88)90035-9. 26
- M. J. Taylor, M. A. Bailey, P. D. Pautet, S. A. Cummer, N. Jaugey, J. N. Thomas, N. N. Solorzano, F. Sao Sabbas, R. H. Holzworth, O. Pinto, and N. J. Schuch. Rare measurements of a sprite with halo event driven by a negative lightning discharge over Argentina. *Geophys. Res. Lett.*, 35:L14812, 2008. doi: 10.1029/2008GL033984. 111
- J. W. Thoman, Jr., J. A. Gray, J. L. Durant, Jr., and P. H. Paul. Collisional electronic quenching of $NO(A^2\Sigma^+)$ by N_2 from 300 to 4500 K. *J. Chem. Phys.*, 97:8156, 1992. doi: 10.1063/1.463437. 219
- H. Toynbee. Meteorological phenomena. *Nature*, 33:245, 1886. doi: 10.1038/033245d0. 15
- M. A. Uman. *The Lightning Discharge*. London, 2001. xii, 13, 18
- J. A. Vallance. *Aurora*. Dordrecht, The Netherlands, 1974. 28
- O. H. Vaughan, R. Blakeslee, W. L. Boeck, B. Vonnegut, M. Brook, and J. McKune. A Cloud-to-Space Lightning as Recorded by the Space Shuttle Payload-Bay TV Cameras. *Monthly Weather Review*, 120:1459, 1992. doi: 10.1175/1520-0493(1992)120(1459:ACTSLA)2.0.CO;2. 112

REFERENCES

- J. M. Wallace and P. V. Hobbs. *Atmospheric Science: An Introductory Survey*. Academic Press, Inc., New York, USA, 2006. xxix, 3, 6
- J. W. Warwick, J. B. Pearce, D. R. Evans, T. D. Carr, J. J. Schauble, J. K. Alexander, M. L. Kaiser, M. D. Desch, M. Pedersen, A. Lecacheux, G. Daigne, A. Boischoit, and C. H. Barrow. Planetary Radio Astronomy Observations from Voyager 1 Near Saturn. *Science*, 212:239–243, 1981. doi: 10.1126/science.212.4491.239. 168
- E. M. Wescott, D. Sentman, D. Osborne, D. Hampton, and M. Heavner. Preliminary results from the Sprites94 aircraft campaign: 2. Blue jets. *Geophys. Res. Lett.*, 22:1209, 1995. doi: 10.1029/95GL00582. 16, 17
- E. M. Wescott, D. D. Sentman, M. J. Heavner, D. L. Hampton, D. L. Osborne, and O. H. Vaughan. Blue starters: Brief upward discharges from an intense Arkansas thunderstorm. *Geophys. Res. Lett.*, 23:2153, 1996. doi: 10.1029/96GL01969. 17, 18
- E. M. Wescott, D. D. Sentman, M. J. Heavner, D. L. Hampton, and O. H. Vaughan. Blue Jets: their relationship to lightning and very large hailfall, and their physical mechanisms for their production. *J. Atm. Sol.-Terr. Phys.*, 60: 713, 1998. doi: 10.1016/S1364-6826(98)00018-2. 17, 18
- E. M. Wescott, D. D. Sentman, H. C. Stenbaek-Nielsen, P. Huet, M. J. Heavner, and D. R. Moudry. New evidence for the brightness and ionization of blue starters and blue jets. *J. Geophys. Res.*, 106:21549, 2001. doi: 10.1029/2000JA000429. 17, 27
- M. Whitaker, M. A. Biondi, and R. Johnsen. Electron-temperature dependence of dissociative recombination of electrons with $N_2^+-N_2$ dimer ions. *Phys. Rev. A*, 24:743–745, 1981. doi: 10.1103/PhysRevA.24.743. 214
- E. E. Whiting, A. Schadee, J. B. Tatum, J. T. Hougen, and R. W. Nicholls. Recommended conventions for defining transition moments and intensity factors in diatomic molecular spectra. *J. Mol. Spectrosc.*, 80:249, 1980. doi: 10.1016/0022-2852(80)90137-X. 94, 95
- W. L. Wiese, M. W. Smith, and B. M. Glennon. Atomic Transition Probabilities: Hydrogen through Neon. In *NSRDS-NBS 4*, volume 1 of *Washington, DC: National Bureau of Standards*, 1966. 235, 247
- E. Williams, C. L. Kuo, J. Bór, G. Sători, R. Newsome, T. Adachi, R. Boldi, A. Chen, E. Downes, R. R. Hsu, W. Lyons, M. M. F. Saba, M. Taylor, and H. T. Su. Resolution of the sprite polarity paradox: The role of halos. *Radiation Science*, 47:RS2002, 2012. doi: 10.1029/2011RS004794. 38, 77
- C. T. R. Wilson. On some determinations of the sign and magnitude of electric discharges in lightning flashes. *Proc. R. Soc. Lon. Ser. A*, 221:73–115, 1920. doi: 10.1098/rspa.1916.0040. 10
- C. T. R. Wilson. Investigations on Lightning Discharges and on the Electric Field of Thunderstorms. *Royal Society of London Philosophical Transactions Series A*, 221:73, 1921. doi: 10.1098/rsta.1921.0003. 10
- C. T. R. Wilson. The electric field of a thundercloud and some of its effects. *Proc. Phys. Soc. London*, 37:32D, 1925. doi: 10.1088/1478-7814/37/1/314. 15
- C. T. R. Wilson. A Theory of Thundercloud Electricity. *Royal Society of London Proceedings Series A*, 236:297, 1956. doi: 10.1098/rspa.1956.0137. 15
- J. R. Winckler, W. A. Lyons, T. E. Nelson, and R. J. Nemzek. New high-resolution ground-based studies of sprites. *J. Geophys. Res.*, 101:6997, 1996. doi: 10.1029/95JD03443. 112
- H. Winkler and J. Nothold. The chemistry of daytime sprite streamers - a model study. *Atmospheric Chemistry and Physics*, 14:3545–3556, 2014. doi: 10.5194/acp-14-3545-2014. 116
- Y. Yair. New results on planetary lightning. *Adv. Space Res.*, 50(3):293–310, 2012. doi: 10.1016/j.asr.2012.04.013. 165
- Y. Yair, Z. Levin, and S. Tzivion. Microphysical processes and dynamics of a Jovian thundercloud. *Icarus*, 114:278, 1995. doi: 10.1006/icar.1995.1062. 166, 173
- Y. Yair, P. Israelevich, A. D. Devir, M. Moalem, C. Price, J. H. Joseph, Z. Levin, B. Ziv, A. Sternlieb, and A. Teller. New observations of sprites from the space shuttle. *J. Geophys. Res. (Atmos.)*, 109:D15201, 2004. doi: 10.1029/2003JD004497. 112
- Y. Yair, G. Fischer, F. Simões, N. Renno, and P. Zarka. Updated Review of Planetary Atmospheric Electricity. *Space Sci. Rev.*, 137:29, 2008. doi: 10.1007/s11214-008-9349-9. 166
- Y. Yair, Y. Takahashi, R. Yaniv, U. Ebert, and Y. Goto. A study of the possibility of sprites in the atmospheres of other planets. *J. Geophys. Res. (Planets)*, 114:E09002, 2009. doi: 10.1029/2008JE003311. xxv, 168, 169, 170
- C. Yamabe, S. J. Buckman, and A. V. Phelps. Measurement of free-free emission from low-energy-electron collisions with Ar. *Phys. Rev. A*, 27:1345–1352, 1983. doi: 10.1103/PhysRevA.27.1345. 210
- P. I. Y. Yelinov, A. Mishev, and L. Mateev. Model for induced ionization by galactic cosmic rays in the Earth atmosphere and ionosphere. *Adv. Space Res.*, 44:1002, 2009. doi: 10.1016/j.asr.2009.06.006. 119, 230
- J. Yue, S. L. Vadas, C. Y. She, T. Nakamura, S. C. Reising, H. L. Liu, P. Stamus, D. A. Krueger, W. Lyons, and T. Li. Concentric gravity waves in the mesosphere generated by deep convective plumes in the lower atmosphere near Fort Collins, Colorado. *J. Geophys. Res.*, 114:D06104, 2009. doi: 10.1029/2008JD011244. 26
- R. S. Zuelsdorf, R. J. Strangeway, C. T. Russell, C. Casler, H. J. Christian, and R. C. Franz. Trans-Ionospheric pulse pairs (TIPPs): Their geographic distributions and seasonal variations. *Geophys. Res. Lett.*, 24:3165–3168, 1997. doi: 10.1029/97GL02949. 22

Declaration

I herewith declare that I have produced this paper without the prohibited assistance of third parties and without making use of aids other than those specified; notions taken over directly or indirectly from other sources have been identified as such. This paper has not previously been presented in identical or similar form to any other Spanish or foreign examination board.

The thesis work was conducted from 2010 to 2015 under the supervision of Dr. Francisco J. Gordillo Vázquez and Dr. Alejandro Luque.

Granada, May 4, 2015

Curriculum Vitae

Personal information

Date of birth: 21 Sep. 1980

Place of birth: Cuevas del Almanzora, Almería, Spain

Nationality: Spanish

Education and employment

2010-2015: PhD Studies at the Instituto de Astrofísica de Andalucía (IAA-CSIC) and University of Granada

Granada, Spain

Dissertation: “Electrical discharges in upper planetary atmospheres: thermal and chemical effects”

2010-2011: M. Sc. degree at the University of Granada

Granada, Spain

Dissertation: “CO₂ and nitrogen oxides kinetics in air plasmas produced by sprites and halos in Earth’s mesosphere”

2008: Research fellow at Dinámica Fundación

Madrid, Spain

Dissertation: “Rotations of solids with intrinsic angular momentum”

2003-2009: B.S. in Physics at the University of La Laguna
San Cristobal de la Laguna, Tenerife, Spain
Diploma thesis: “Physical parameters of galactic O-type stars
and study of their possible HII region”

Short stays

Sep. 2013 - Dic. 2013: Pulsed Plasmas Departament at the Institute of
Plasma Physics
Prague, Czech Republic
Dissertation: “Spectroscopy of air plasmas at low
pressure as analogous to sprite streamers”

Mar. 2012 - Apr. 2012: Instituto de Estructura de la Materia, (IEM-CSIC)
Madrid, Spain
Dissertation: “Spectroscopic diagnostics of air plas-
mas for rotational temperature determination in
TLEs”

Ago. 2011 - Sep. 2011: Centre National de la Recherche Scientifique (CNRS)
Toulouse, France
Dissertation: “Simulations of fast heating on sprite
streamer channels”

Publications

Journal papers

- **Parra-Rojas F.C.**, Luque A. & Gordillo-Vázquez F.J., *Chemical and thermal impact of sprite streamers in the Earth mesosphere*, Submitted to J. Geophys. Res. - Space Physics, 2015.
- Luque A., Dubrovin D., Gordillo-Vázquez F.J., Yair Y., **Parra-Rojas F.C.**, Ebert U. & Price C., *Coupling between atmospheric layers in gaseous giant planets due to lightning-generated electromagnetic pulses*, J. Geophys. Res. - Space Physics, Vol. 119, 8705-8720. doi:10.1002/2014JA020457, 2014.
- Dubrovin D., Luque A., Gordillo-Vázquez F.J., Yair Y., **Parra-Rojas F.C.**, Ebert U. & Price C., *Impact of lightning on the lightning ionosphere of Saturn and possible generation of TLEs*, Icarus, Vol. 241, 313-328. doi:10.1016/j.icarus.2014.06.025, 2014.
- **Parra-Rojas F.C.**, Passas M., Carrasco E., Luque A., Tanarro I., Simek M. & Gordillo-Vázquez F.J., *Spectroscopy diagnostics of laboratory air plasmas as a benchmark for spectral rotational (gas) temperature determination in TLEs*, J. Geophys. Res. - Space Physics, Vol. 118, 4649-4661. doi:10.1002/jgra.50433, 2013.
- **Parra-Rojas F.C.**, Luque A. & Gordillo-Vázquez F.J., *Chemical and electrical impact of lightning on the Earth mesosphere: the case of Sprite Halos*, J. Geophys. Res. - Space Physics, Vol. 118, 1-25. doi:10.1002/jgra.50449, 2013.

Conference proceedings

- **Parra-Rojas F.C.**, Luque A. & Gordillo-Vázquez F.J., *Gas heating and chemical impact of sprite streamers in the Earth mesosphere*, 2nd. TEA-IS summer school, Collioure, France, 2014.
- **Parra-Rojas F.C.**, Luque A. & Gordillo-Vázquez F.J., *Chemical and electrical impact of lightning on the Earth atmosphere: the case of Sprite Halos*, XXXI Int. Conf. Phenomena in ionized gases (ICPIG), Granada, Spain, 2013.
- **Parra-Rojas F.C.**, Passas M., Carrasco E., Luque A., Tanarro I., Simek M. & Gordillo-Vázquez F.J., *Spectroscopy diagnostics of laboratory air plasmas as a benchmark for spectral rotational (gas) temperature determination in TLEs*, XXXI Int. Conf. Phenomena in ionized gases (ICPIG), Granada, Spain, 2013.
- Passas M., Sánchez J., **Parra-Rojas F.C.**, Luque A. and Gordillo-Vázquez F.J., *GRAnada Sprite Spectrograph and Polarimeter*, XXXI Int. Conf. Phenomena in ionized gases (ICPIG), Granada, Spain, 2013.
- **Parra-Rojas F.C.**, Passas M., Carrasco E., Luque A. Tanarro I., Simek M. & Gordillo-Vázquez F.J., *Diagnostics of hollow cathode low pressure air discharges as a tool for understanding Halo spectral features in the Earth mesosphere*, 1st. TEA-IS summer school, Torremolinos, Spain, 2012.
- **Parra-Rojas F.C.**, Luque A. & Gordillo-Vázquez F.J., *Kinetics of CO₂ and nitrogen oxides in air plasmas produced by the action of sprites and halos in the Earth mesosphere*, 1st. TEA-IS summer school, Torremolinos, Spain, 2012.

Others

- Gordillo-Vázquez F.J., Luque A., **Parra-Rojas F.C.** & Passas M., *Plasmas en atmósferas planetarias*, Revista Española de Física, Vol. 35, pp. 3, 2011.

Presentations

2015

- **Parra-Rojas F.C.**, Luque A. & Gordillo-Vázquez F.J., *Chemical and thermal influence of sprite streamers in the upper atmosphere of the Earth*, XXXII Int. Conf. Phenomena in ionized gases (ICPIG), 26-31 Jul. 2015, Iasi, Romania [Poster presentation + conference proceedings]
- **Parra-Rojas F.C.**, Luque A. & Gordillo-Vázquez F.J., *Gas heating and chemical impact of sprite streamers in the Earth mesosphere*, IV Encuentro de Ciencias Planetarias y Exploración del Sistema Solar, 8-10 Jun. 2015, Alicante, Spain [Oral + poster presentation]
- **Parra-Rojas F.C.**, Luque A., Gordillo-Vázquez F.J., *Influence of sprite streamers in the mesospheric chemical and thermal balance*, TEA-IS meeting, 18 Apr. 2015, Vienna, Austria [Oral presentation]
- **Parra-Rojas F.C.**, Luque A., Gordillo-Vázquez F.J., *Influence of sprite streamers in the mesospheric chemical and thermal balance*, EGU General Assabily, 13-17 Apr. 2013, Vienna, Austria [Poster presentation]

2014

- **Parra-Rojas F.C.**, Luque A. & Gordillo-Vázquez F.J., *Gas heating and chemical impact of sprite streamers in the Earth mesosphere*, 2nd. TEA-IS summer school, 23-27 Jun. 2014, Collioure, France [Oral + poster presentation + conference proceedings]

2013

- **Parra-Rojas F.C.**, Luque A. & Gordillo-Vázquez F.J., *Chemical and electrical impact of lightning on the Earth atmosphere: the case of Sprite Halos*, XXXI Int. Conf. Phenomena in ionized gases (ICPIG), 14-19 Jul. 2013, Granada, Spain [Poster presentation + conference proceedings]
- **Parra-Rojas F.C.**, Passas M., Carrasco E., Luque A., Tanarro I., Simek M. & Gordillo-Vázquez F.J., *Spectroscopy diagnostics of laboratory air plasmas as a benchmark for spectral rotational (gas) temperature determination in TLEs*, XXXI Int. Conf. Phenomena in ionized gases (ICPIG), 14-19 Jul. 2013, Granada, Spain [Poster presentation + conference proceedings]
- Passas M., Sánchez J., **Parra-Rojas F.C.**, Luque A. and Gordillo-Vázquez F.J., *GRAnada Sprite Spectrograph and Polarimeter*, XXXI Int. Conf. Phenomena in ionized gases (ICPIG), 14-19 Jul. 2013, Granada, Spain [Poster presentation + conference proceedings]
- **Parra-Rojas F.C.**, Luque A., Gordillo-Vázquez F.J., *Impacto electroquímico de rayos en la mesosfera terrestre y su posible extensión a otras atmósferas planetarias con actividad eléctrica*, III Encuentro de Ciencias Planetarias y Exploración del Sistema Solar, 19-21 Jun. 2013, Madrid, Spain [Oral + poster presentation]
- **Parra-Rojas F.C.**, Luque A., Gordillo-Vázquez F.J., *Chemical and electrical impact of lightning in the Earth mesosphere: the case of Sprite Halos*, EGU General Assabbly, 7-12 Apr. 2013, Vienna, Austria [Poster presentation]
- **Parra-Rojas F.C.**, Luque A., Gordillo-Vázquez F.J., *Chemical and electrical impact of lightning in the Earth mesosphere: the case of Sprite Halos*, TEA-IS meeting, 10 Apr. 2013, Vienna, Austria [Oral presentation]

2012

- **Parra-Rojas F.C.**, Passas M., Carrasco E., Luque A. Tanarro I., Simek M. & Gordillo-Vázquez F.J., *Diagnostics of hollow cathode low pressure air discharges as a tool for understanding Halo spectral features in the Earth mesosphere*, 1st. TEA-IS summer school, 18-22 Jun. 2012 Torremolinos, Spain [Poster presentation + conference proceedings]
- **Parra-Rojas F.C.**, Luque A. & Gordillo-Vázquez F.J., *Kinetics of CO₂ and nitrogen oxides in air plasmas produced by the action of sprites and halos in the Earth mesosphere*, 1st. TEA-IS summer school, 18-22 Jun. 2012 Torremolinos, Spain [Oral + Poster presentation + conference proceedings]

2011

- **Parra-Rojas F.C.**, Luque A. & Gordillo-Vázquez F.J., *CO₂ kinetics in air plasmas produced by the action of sprites and halos in the Earth mesosphere*, TEA-IS workshop, 10-14 Oct. 2011, Leiden, The Netherlands [Poster presentation]
- **Parra-Rojas F.C.**, Luque A. & Gordillo-Vázquez F.J., *CO₂ kinetics in air plasmas produced by the action of sprites and halos in the Earth mesosphere*, Biennial of RSEF, 19-23 Sep. 2011, Santander, Spain [Poster presentation]